Advanced Contacts for Crystalline Silicon Solar Cells

James Bullock

February 2016

A thesis submitted for the degree of

Doctor of Philosophy of

The Australian National University

Australian National University

Confidentiality statement

This document contains a significant quantity of unpublished work currently in preparation or under consideration for publication. As such, this document and the information in it are provided in confidence for the sole purpose of doctorate thesis examination and may not be disclosed to any third party or used for any other purpose without the express written permission of James Bullock.

Thesis declaration

I certify that this thesis does not incorporate without acknowledgement any material submitted for a degree or diploma in any university and that, to the best of my knowledge, it does not contain any material previously published or written by another person except where due reference is made in the text. The work in this thesis is my own, except for the contributions made by others as described in the Acknowledgements.

James Bullock

February 2016

Publication declaration

On behalf of all co-authors, I certify that all the papers listed in the main body of this *Thesis by Compilation* were written by James Bullock as part of his Ph.D research. In all cases he contributed the majority of the work, both experimental and theoretical, and as the primary author, he wrote most of the text in these papers and prepared the corresponding graphs and figures.

Professor Andres Cuevas

February 2016

Abstract

Mainstream dopant-diffused crystalline silicon (*c*-Si) solar cells have reached a point in their development where losses at the directly-metalized, heavily-doped regions have a significant, and often limiting effect on device performance. The conventional wisdom on addressing this issue is to drastically reduce the percentage of the contacted surface area–to less than 1% in some cases–significantly increasing the complexity of fabrication. An alternative approach is to focus on addressing the losses at the metal / *c*-Si interface by implementing novel 'carrier-selective' contacting structures. This approach to solar cell contacting has the potential to increase the output power whilst significantly simplifying cell architectures and fabrication procedures. This thesis is centered on the conceptual and experimental development of a number of advanced contacting structures for *c*-Si solar cells, collectively referred to here as 'heterocontacts'. The 'carrier-selectivity' of the contact, that is, how well it collects just one of the two carriers (whilst preserving the other), is used as a universal concept for comparing different contacting strategies, including mainstream contacts based on direct metallization of heavily doped *c*-Si.

To provide a foundation on this topic the initial section of the thesis discusses the concept and theory of carrier-selectivity. This is complemented with an in depth literature review of current state-of-the-art contacting practices for *c*-Si solar cells. This provides a reference frame with which to compare the three experimental chapters that follow.

In the first experimental chapter it is shown that a suitable initial stepping stone towards advancing solar *c*-Si cell contacts is to combine the benefits of conventional dopant-diffused regions with those of heterocontacts. A number of such hybrid systems are demonstrated and optimized at the contact level through multiple dedicated studies focused on using thin silicon oxide (SiO_x), aluminum oxide (AlO_x) or hydrogenated amorphous silicon (*a*-Si:H) passivating interlayers. These interlayers are shown to reduce carrier recombination at the contact surface by up to two orders of magnitude. In a later study we develop and demonstrate a novel *a*-Si:H enhanced Al / SiO_x / *c*-Si(n^+) heterocontact concept. This structure is also explored at the solar cell level, yielding an efficiency of 21% in the initial stages of development – equivalent to that of an analogous cell made with the conventional directly metallized partial contact technique.

In the succeeding chapter, the logical next stage in the development of such a concept is explored, that is, to completely remove the heavily doped surface regions, instead using the heterocontacts exclusively to separate electrons and holes. It is demonstrated that this can be achieved using materials with extreme work functions. For the collection of holes, sub-stoichiometric molybdenum oxide MoO_x is utilized, favored for its transparency and large work function. Over multiple studies, it is demonstrated that MoO_x heterocontact systems, both with and without passivating interlayers can be used to effectively collect holes on both n and p-type *c*-Si absorbers. This enables its application to a number of novel solar cells architectures, most prominently a novel MoO_x partial rear contact cell attaining conversion efficiencies over 20% in the initial proof-of-concept stage.

In the final experimental chapter, a complementary electron heterocontact system is developed, based on a low work function LiF_x / Al electrode. This is shown to provide

excellent electron collection characteristics, both with and without *a*-Si:H passivating interlayers. The exceptional contact characteristics enabled by this heterocontact allow the demonstration of a first-of-its-kind n-type partial rear contact cell already with an efficiency above 20% in its first demonstration.

To conclude the thesis and demonstrate its premise, a novel *c*-Si cell is developed without the use of dopants. This cell, referred to as the dopant free asymmetric heterocontact (DASH) cell, combines the previously mentioned MoO_x based hole contacts and LiF_x based electron heterocontacts, both with passivating *a*-Si:H interlayers. A conversion efficiency of 19.4% is attained for this proof-of-concept device— an improvement by more than 5 percent absolute from the previous DASH cell record and more importantly the first demonstration of such a concept to be competitive with conventional cell designs.

Contents

Confidentiality statement .... **i**

Thesis declaration .... **iii**

Publication declaration .... **v**

Abstract .... **vii**

1. Introduction **1**

1.1 Introduction to carrier-selectivity 1

1.2 Quantifying carrier-selectivity 3

1.3 State-of-the-art directly metalized doped silicon contacts 7

Collecting electrons 9

'Blocking' holes 11

1.4 Heterocontacts 16

Manipulating surface carrier concentrations 16

Introducing asymmetries in conductivity at the heterocontact 22

Combining heterocontacts with surface doping 25

1.5 Successful demonstration of heterocontacts 26

1.6 Thesis outline 37

2. Electron and hole selective contacts on highly doped surface regions **41**

2.1 Foreword 41

2.2 First author manuscripts 45

Passivation of aluminium–n^+ silicon contacts for solar cells by ultrathin Al_2O_3 and SiO_2 dielectric layers 45

Amorphous silicon passivated contacts for diffused junction silicon solar cells 57

Amorphous Silicon Enhanced Metal-Insulator-Semiconductor Contacts for Silicon Solar Cells 77

Simple silicon solar cells featuring an a-Si:H enhanced rear MIS contact 105

3 Molybdenum oxide hole-selective contacts for *c*-Si solar cells 105

3.1 Foreword 119

3.2 First author manuscripts 123

Molybdenum Oxide MoO_x: A Versatile Hole Contact For Silicon Solar Cells 123

n- and p-type silicon solar cells with molybdenum oxide hole contacts 139

Proof-of-concept p-type silicon solar cells with molybdenum oxide local rear contacts 147

4 Alkali metal salt electron-selective contacts for *c*-Si solar cells 157

4.1 Foreword 157

4.2 First author manuscripts 159

Lithium fluoride based electron contacts for high efficiency n-type crystalline silicon solar cells 159

Efficient silicon solar cells with dopant-free asymmetric heterocontacts 179

5 Conclusion **209**

6 List of Publications **217**

Journal papers 217

Conference papers 220

Appendices **223**

Appendix 1: Carrier-selectivity parameters and simulation details 223

Carrier-selectivity parameters 223

Simulation details 226

Appendix 2: Additional first author manuscripts 227

Passivated Contacts to n^+ and p^+ Silicon Based on Amorphous Silicon and Thin Dielectrics 227

Imaging the recombination current pre-factor J_0 of heavily doped surface regions; a comparison of low and high injection Photoluminescence techniques 241

Enhanced rear-side reflection and firing-stable surface passivation of silicon solar cells with capping polymer films. 259

Appendix 3: Additional relevant manuscripts 269

p^+nn^+ silicon solar cell with a full-area rear MIS passivated contact 269

1. Introduction

1.1 Introduction to carrier-selectivity

The basic functioning of crystalline silicon (*c*-Si) solar cells can be separated into two interrelated processes, as depicted in Figure 1a. Firstly, photons impinging on the cell are coupled into the *c*-Si absorber. Those photons with sufficient energy to overcome *c*-Si's energy gap generate an electron-hole pair. Maximising the total amount and concentration of photo-excited electrons and holes is equivalent to increasing the upper-limit current density and voltage of the solar cell. In the second process, which dictates how much of that current and voltage can be accessed, photo-excited carriers are

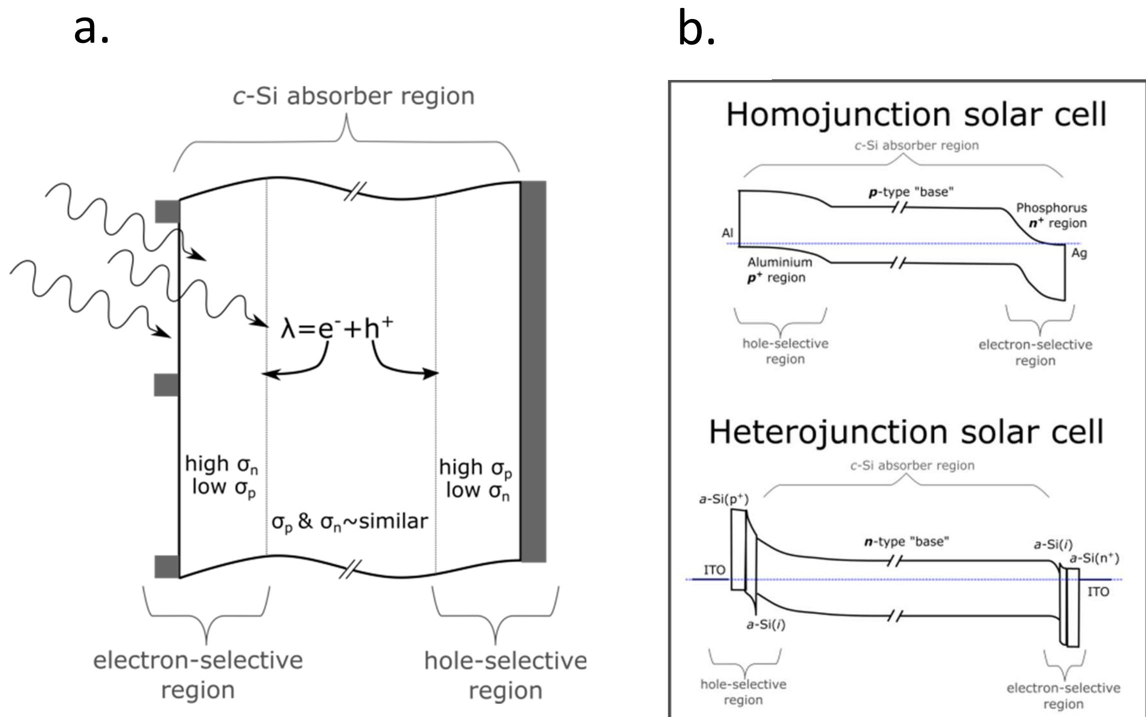

Figure 1: (a) schematic representation of the basic processes required for a solar cell to function (b) examples of conventional solar cell structures; top: p-type dopant diffused solar cell, bottom: n-type silicon heterojunction solar cell.

separated at opposite electron and hole 'selective' regions and passed on to the metal electrodes to drive an external load.

While selectivity in these regions can be realised using a diverse range of techniques and electronic structures [1], currently more than 90% of commercially available *c*-Si solar cells achieve carrier-selectivity via doping in the near-surface regions of the *c*-Si absorber [2]. By controlling the dopant type and concentration, large asymmetries in the conductivity presented to electrons and holes can be achieved. These heavily doped surface regions, commonly called homojunctions, are typically formed by thermal diffusion, ion implantation, or via rapid melt-recrystallization processes, most of which were inherited from the microelectronics industry. This approach has proven very effective at carrier separation, as exemplified by ~25% efficiency devices demonstrated in the late 90's [3], and has now become the workhorse of the solar industry, particularly the standard screen printed p-type cell architecture [2] (a representative energy band diagram of which is shown in Figure 1b). However, as discussed below, the high doping concentrations also introduce a number of fundamental losses and technological issues, which hinder further reduction of the cost-to-performance ratio for this technology. A long recognised strategy to remove these issues and progress forward is to instead use heterocontacts to achieve carrier-selectivity. The modern archetype of the heterocontact concept is the silicon heterojunction (SHJ) cell, also depicted in Figure 1b, popularised by Sanyo/ Panasonic as the "*heterojunction with intrinsic thin layer*" or HIT solar cell [4,5]. The merits of this heterocontact system have recently been conclusively demonstrated, surpassing the homojunction technologies and claiming the world record efficiency for single junction *c*-Si cells [6]. In addition to the SHJ cell, the last 4 years have seen a dramatic increase in the development of new, and revisitation of old, heterocontact systems to replace the heavily doped homojunctions of *c*-Si solar cells. This introduction

chapter explores some of the theory surrounding, and surveys some of the different cell structures utilised in achieving, carrier-selectivity in *c*-Si solar cells. A particular emphasis is placed on newly developed heterocontact systems and some of the advantages they exhibit.

1.2 Quantifying carrier-selectivity

The central aim of carrier-selectivity can be simply thought of as maximising the flux of one carrier through a virtual surface, henceforth called the *collected* carrier, whilst minimising the flux of the other, here called the *blocked* carrier, as depicted in Figure 2a. These fluxes are governed by both the conductivity σ and gradient in electrochemical potential grad(η) for electrons and holes. As such, an appropriate design rule for carrier-selectivity is to provide a suitably high conductivity to the collected carrier and a much (much) lower conductivity to the blocked carrier as they travel towards the contact. Unfortunately, these parameters are difficult to extract experimentally and instead results have generally been presented as a pair of equilibrium parameters; the contact recombination factor J_{0c} (to represent the flux of the blocked carrier) and the contact resistivity ρ_c (to represent the interface resistance to collected carriers).

It is important to note, that the impact of these two parameters have on carrier selectivity is quite different. To demonstrate this Figure 2b presents the results of simulations which highlight the impact that these two parameters impart. This simulation, performed using *Quokka* [7], focuses on a full-area rear electron-selective contact of an otherwise perfect solar cell. Further details of the simulation inputs can be found in Appendix 1. The relationship between operating voltage and ρ_c is approximately linear, which means that it is insignificant for a sufficiently low value of ρ_c. A pessimistic

estimate of a ρ_c induced voltage drop, based on J_g – the maximum possible current that can flow through the contact interface for a full area contact, is given by the product J_g ρ_c. It can be quickly realised that the influence of ρ_c on a full-area contacted silicon solar cell is minimal below ~0.14 Ωcm^2, given that the voltage drop would be less than 6 mV, that is, about 1% of typical values for the maximum power voltage. This influence can clearly be seen in the simulation of Figure 1b, where the efficiency contours are seen to begin bending downward at this ρ_c value. On the other hand, the impact of the J_{0c} on the cell performance is approximately logarithmic, meaning a decreasing J_{0c} will indefinitely improve cell voltage, as seen in Figure 1b, until another recombination mechanism dominates (for example intrinsic bulk recombination as to be discussed later).

The impact of the above two metrics can be crudely combined in the form of the contact 'upper-limit' maximum power voltage, imposed by the contact's recombination and resistance behaviour, given by,

$$V_{C,UL} = V_t ln\left(\frac{J_g}{J_{0c}}\right) - J_g \rho_c, \quad (1)$$

where a standardised reference value for J_g must be incorporated (see Appendix 1 for details and an alternative metric). We recommend a value of 43.31 mA/cm^2 calculated in Ref. [8] as a suitable figure. Whilst the proposed V_{UL} parameter is unphysical (and unattainable), as it comprises open and short circuit components, it may act as a suitable and accessible metric for carrier-selectivity. This is demonstrated in Figure 2b where contours of V_{UL} are overlayed on the simulations showing near perfect trend alignment with the efficiency contours. The slight departure between the numerical simulation and analytical model in the low J_{0c} region arises due to the increasing influence of Auger recombination in the bulk of the wafer, which Equation 1 does not account for. This is also the reason for departure between V_{UL} and attainable voltages for *c*-Si devices at very

low ρ_c and J_{0c} (If the user so wishes, this can be crudely accounted for by adding an additional intrinsic recombination term into equation 1).

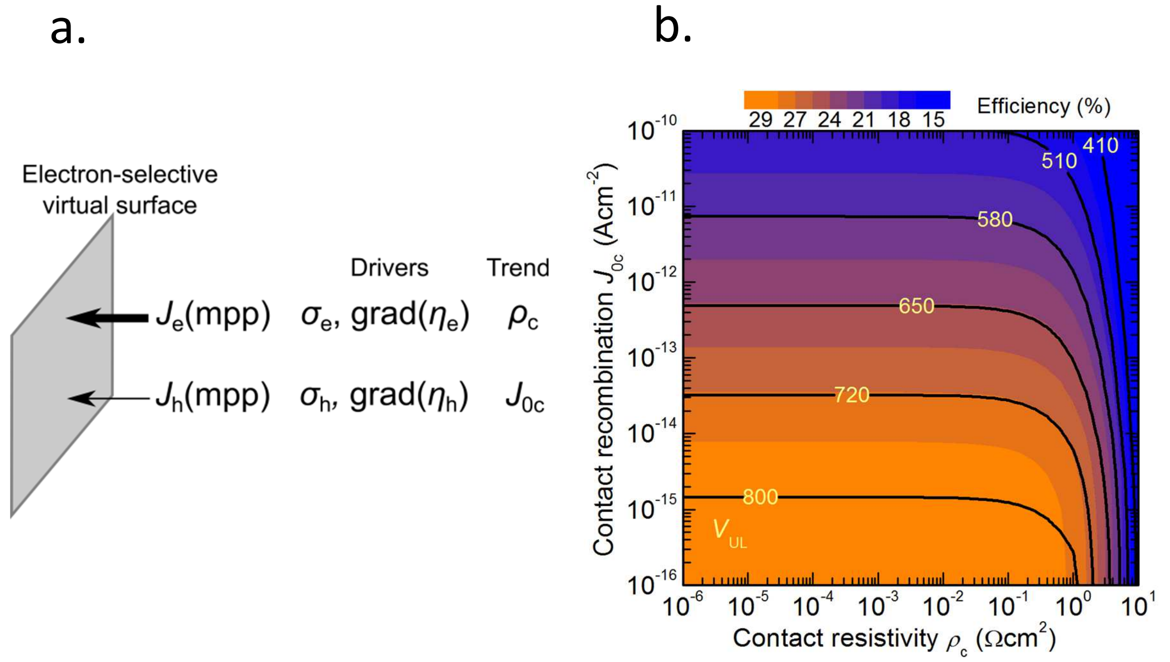

Figure 2: (a) representation of a carrier-selective virtual surface. (b) simplified simulation performed in Quokka, highlighting the impact of J_{0c} and ρ_c on the cells carrier selectivity and efficiency.

In addition to the above parameters, the contact fraction adds a further complicating component to carrier-selectivity. A common approach to reducing contact recombination is to reduce the percentage of the solar cell's surface which is contacted – to less than 1% in some cases. The remaining non-contacted area can then be passivated by state-of-the-art dielectric films which exhibit femto-amp scale recombination factors [9], and favourable optical properties when applied to *c*-Si [10]. As such, in many conventional structures using partial rear contacts, the non-contacted regions have a negligible flux of both electrons and holes flowing to the surface in those regions. From a carrier-selectivity perspective, confining the contact fraction increases the resistance presented to both the collected carrier (which is bad) and the blocked carrier (which is good). In doing so, the relative impact that these two parameters have on the carrier-

selectivity are traded off. This is generally permissible given their relative effects on solar cell performance, as can be seen in Figure 2b. This is at odds with many other electronic devices which have a stronger reliance on ρ_c.

The importance of considering contact confinement when talking about carrier-selectivity is highlighted in Figure 3a which shows the impact that contact fraction has on efficiency for four different contact systems which all have approximately the same optimum efficiency (~28%) and V_{UL}, despite orders of magnitude difference in the J_{0c} and ρ_c values. Essentially, the contact fraction provides an additional tool with which to achieve the best carrier-selectivity from a given contact system, but it must also be balanced with the increased complexity in the fabrication for small area contact fractions. Shown in Figure 3b, is a modification of the earlier contour plot, where for every

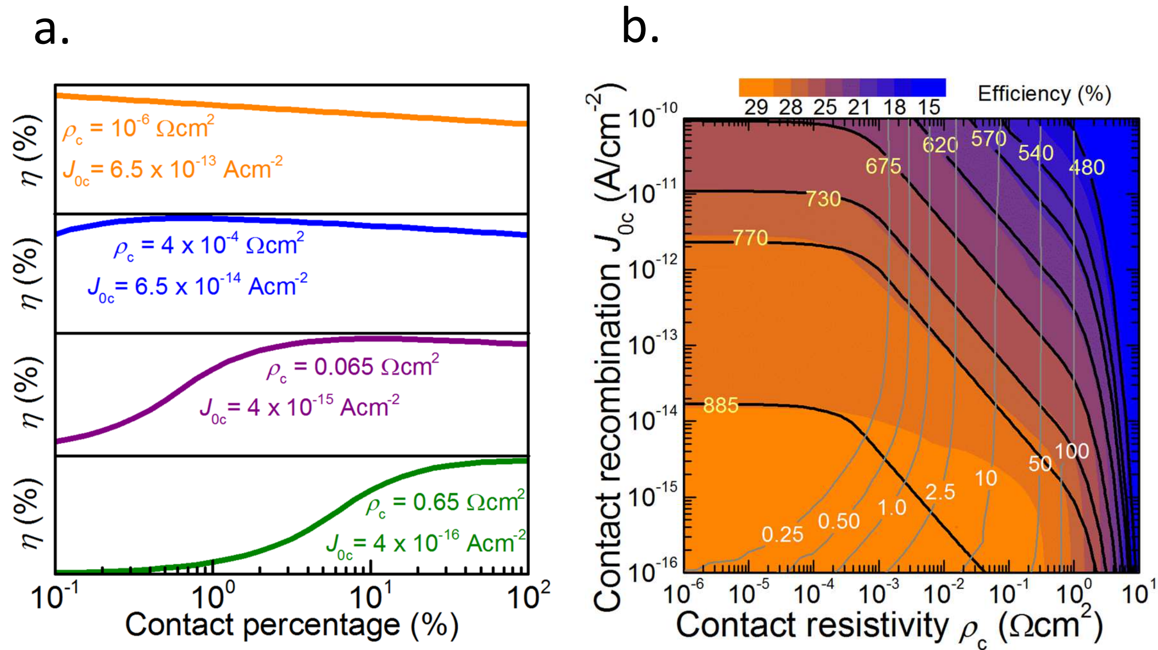

Figure 3: (a) efficiency as a function of rear contact fraction for a series of cells with the same optimised efficiency (~28%) and V_{UL}, showing that contact fraction plays a role in the carrier-selectivity of a contact system. (b) Quokka simulations showing the optimum contact fraction (dotted lines) and resultant idealized efficiency (coloured contours) as a function of the rear contact J_{0c} and ρ_c.

combination of ρ_c and J_{0c} the optimum contact fraction (dotted lines) is found and the resultant efficiency is calculated (coloured contours). The experimentalist can superimpose J_{0c} and ρ_c values corresponding to a new contact system on such a plot to determine: *i*, what is the best contact fraction to use and; *ii*, how does the contact system compare to others in terms of carrier-selectivity. The earlier described V_{UL} metric can be modified to approximately take into consideration the partial contact fraction,

$$V_{UL} = V_t ln\left(\frac{J_g}{m_f J_{0c} + (1 - m_f) J_{0p}}\right) - \frac{J_g \rho_c}{m_f} \quad (2)$$

where additional terms for the rear contact fraction m_f and recombination in the non-contacted, surface passivated regions J_{0p} are included. The J_{0p} value must be included as the recombination in the non-contacted regions can affect the carrier-selectivity. As shown in Figure 3b, the amended V_{UL} parameter can be seen to still maintain some validity when a variable contact fraction is used. Again, the departure between the simulations and model at low J_{0c} is partially associated with an increased contribution of Auger recombination from the bulk of the absorber. In a separate Quokka simulation (not shown), with Auger recombination removed, closer trend alignment between efficiency and V_{UL} was obtained.

1.3 State-of-the-art directly metalized doped silicon contacts

All conventional *c*-Si solar cells require a pair of external metal contacts to convey the potential and current developed within the cell to the load. According to ideal Schottky-Mott theory, when *c*-Si and a metal, with a difference in chemical potential are brought together, a perfectly balancing electrical potential will develop – forming a flat

electrochemical potential across the interface. The large electron density in metals result in a charge screening length generally less than 1 Å and, therefore, the majority of the balancing electric potential falls within the *c*-Si. This theory suggests that choosing metals with small (large) chemical potential values relative to *c*-Si would promote electron (hole) accumulation at the interface, as depicted in the energy band diagram of Figure 4a. Such carrier accumulation would in turn favour the transport and collection of electrons (holes). Nevertheless, this is seldom achieved in practice as the metal / *c*-Si interface is known to suffer from Fermi level pinning (FLP). Consequently, in most cases a large barrier to the majority carrier, known as a Schottky barrier (typically ~0.7 eV on n-type *c*-Si, ~0.4 eV on p-type *c*-Si) is formed at the interface (as shown in Figure 4b). This occurs largely independent of the metal's chemical potential, commonly producing rectifying behaviour [11]. In addition, the metal / *c*-Si interface is known to be extremely recombination active, owing to a large density of states within the *c*-Si band gap which promote Shockley-Read-Hall recombination. The extent of this process is such that the surface recombination rate is limited only by the speed at which carriers diffuse to the surface from the bulk of the *c*-Si wafer – known as the diffusivity limit, with a corresponding J_{0c} of ~1 $nAcm^{-2}$ for lowly doped *c*-Si [12]. These issues have prevented the success of simple *c*-Si cells which use direct metal contacts to achieve carrier-selectivity (commonly known as Schottky

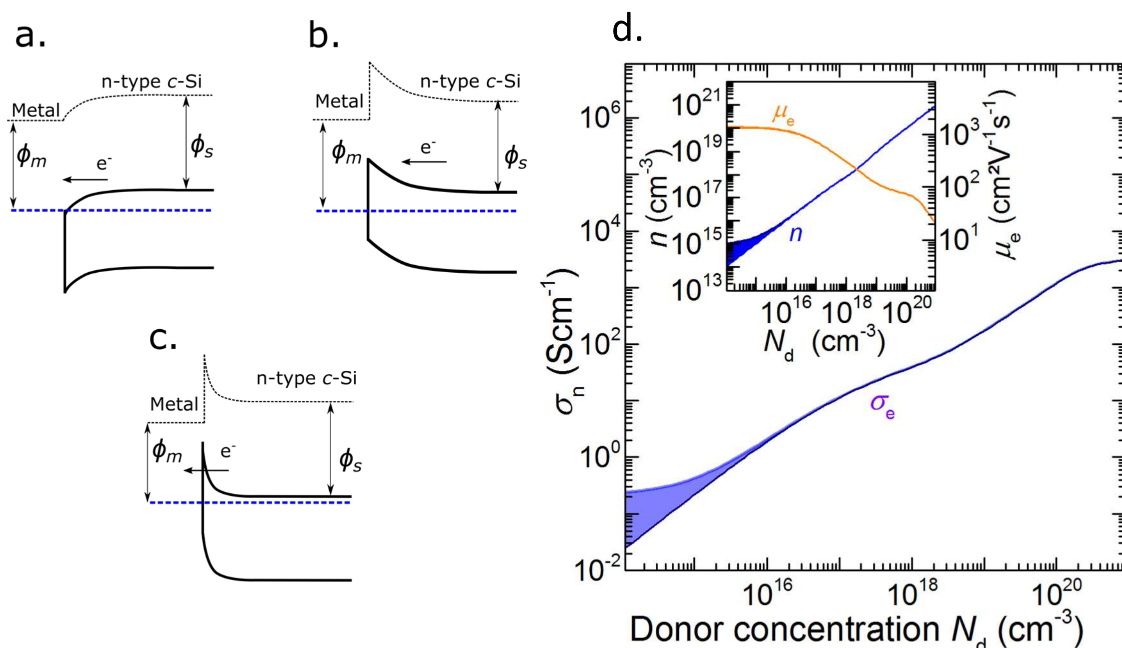

Figure 4: electronic band schematics showing (a) ideal behaviour, (b) experimental behaviour and (c) the result of heavily doping the surface, for a directly metal contacted n-type *c*-Si surface. (d) increase in electron conductivity σ_e as a function of phosphorus dopant concentration. Inset shows a large increase in carrier concentration and small decrease in mobility as a consequence of increased doping. Modelling details: mobility tool (with default settings) at *PVlighthouse.com.*

barrier solar cells) and instead the more complicated process of heavily doping the near surface regions has been favoured. In this approach, the two surfaces of a *c*-Si wafer are typically doped to a concentration of at least 10^{18} cm^{-3}, with phosphorus to produce n-type behaviour for collecting electrons on one side and aluminium or boron to create p-type for collecting holes on the other. Heavy doping promotes both improved transport of the collected carrier and a reduced flux of the blocked carrier – greatly enhancing the carrier-selectivity. For the sake of brevity, the following discussion is centred on the electron collection side formed by heavy phosphorus doping, an equal (but opposite) situation is true for hole collection via boron or aluminium doping.

Collecting electrons

For the collected electrons, as shown in Figure 4d, the increase in phosphorus doping causes a significant increase in electron conductivity σ_e. This occurs as the

increase in electron concentration, *n,* with doping is far greater that the decrease in carrier mobility, μ_e. This conductivity is largely unaffected by one sun illumination when the phosphorus doping concentration is above 10^{16} cm^{-3}. This characteristic is particularly useful when the collected carrier has to travel laterally through the cell to reach the metal contacts, as is commonly the case on the front-side. In addition, for phosphorus concentrations greater than 10^{19} cm^{-3}, the density of fixed dopant ions is high enough to reduce the width of any surface potential barrier at the metal / *c*-Si interface to the scale of nanometres. At such barrier thicknesses quantum mechanical tunnelling can occur, as shown schematically in Figure 4c, and the rectifying behaviour of the metal / *c*-Si interface is resultantly nullified [11]. To demonstrate this effect, Figure 5 presents a compilation of currently achievable metal-silicon ρ_c values for both p and n-type surfaces as a function of doping concentration. Within this compilation a number of different metallisation techniques are highlighted including the industry standard screen-printing process [13–21], as well as advanced processes based on fine-line printing [13,22,23], plating [24–26], and physical vapour deposition (PVD) [12,27–33]. As a further reference, lines representing the theoretical $\rho_c(N_{dope})$ are also included. These lines are based on image force corrected thermionic-emission (TE), thermionic-field-emission (TFE) and field-emission (FE) analytical models of ρ_c for metal-silicon interfaces, following the approach in Ref. [11]. Evident in Figure 5 is an absence of data points for low phosphorus surface concentrations. This is due to the large barrier known to exist at n-type silicon-metal interfaces and it can be seen that contact can only be formed when the dopant density is sufficiently high to allow tunnelling based mechanisms. Conversely p-type *c*-Si, which is known to host a smaller surface barrier, can produce workable contact resistivities even with surface concentrations below 10^{17} cm^{-3}, where conduction is dominated by thermionic emission. This has been demonstrated practically in a number of existing p-

type cells which utilise direct partial rear contacts to moderately doped p-type *c*-Si [34–36]. Technology-wise, it can be seen on both p and n-type surfaces the conventional screen-printed technologies produce the highest ρ_c values, likely associated with a lower percentage of physical contact to the *c*-Si surface, and the PVD technologies produce the lowest ρ_c values.

'Blocking' holes

In addition to increasing the conductivity presented to the electrons, these highly doped regions have the opposite effect for holes. In thermal equilibrium the electron concentration n_o, fixed by the high phosphorus dopant concentration, induces a low hole concentration p_o, through the law of mass-action,

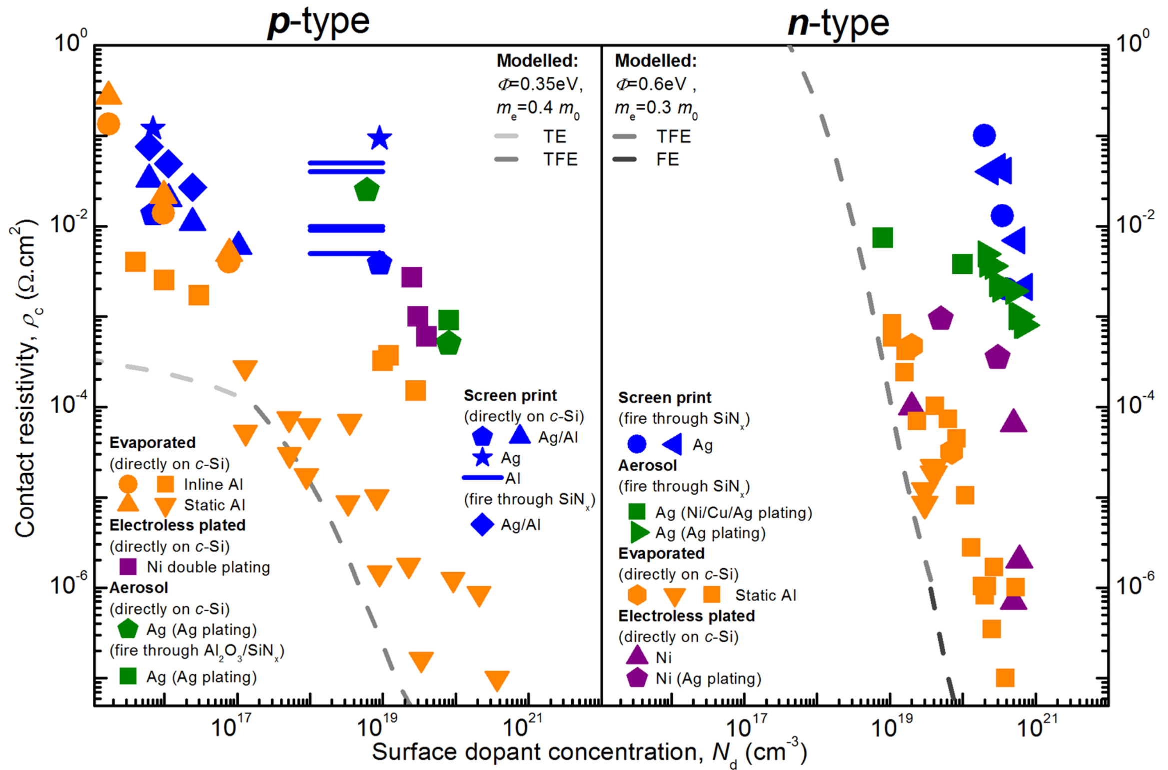

Figure 5: Compilation of measured ρ_c values resultant from a number of different metallisation techniques on p and n–type *c*-Si. Dashed lines indicate modelled TE, TFE and FE contact resistivities. Of significant uncertainty in this analysis are the surface concentration values of the screen printed aluminium contacts. In this compilation they are presented as having surface dopant concentrations in the 10^{18} – 10^{19} cm^{-3} range, in line with saturation limit of aluminium in *c*-Si at ~ 3×10^{18} cm^{-3}. Most measurements were made using the transfer length method (TLM) or similar, some however were obtained using different techniques and hence may not be directly comparable.

$$n_o p_o = n_i^2, \quad (3)$$

where n_i represents the intrinsic carrier concentration. This influence still holds to an extent under illumination, modified by an exponential term (assuming Boltzmann statistics) representative of the departure from equilibrium,

$$np = n_i^2 \exp\left(\frac{V}{V_t} - 1\right), \quad (4)$$

where V and V_t represent the cell's voltage and the thermal voltage, respectively. As can be seen from Equation 4, within the heavily doped region where the electron concentration is already very high, a much lower excess hole concentration is required to support the same voltage, compared to a lightly doped region. This is also shown in the contour plot of Figure 6a. The lower hole concentration (for a given voltage) reduces the rate of Shockley-Read-Hall surface recombination, as it is the rate limiting species. The electron and hole concentrations in a typical phosphorus diffusion with an 'infinite' surface recombination velocity is shown in Figure 6b. The upper and lower bounds of the shaded regions represent the carrier profiles under light (100 mW/cm^2, at the maximum power point) and dark conditions. The excess carrier concentration is seen to clearly be lower in the more heavily doped side of the *pn* junction, even when Auger and surface recombination are removed – as shown by the dashed lines. This effect can also be seen in Figure 7 which provides a compilation of the different experimentally determined J_{0c} values of directly metalized n and p-type surface regions, taken from different sources in the literature [37–43]. An easily measured and commonly used quantity to compare against the J_{0c} is the sheet resistance of the diffused region R_{sh}. This reflects the R_{sh} presented to the collected carrier, but at the same time it is roughly proportional to the blocked carrier

conductivity. In both plots, as expected, the J_{0c} increases with larger R_{sh}, in line with a higher conductivity towards the blocked carriers.

The above mentioned trends for the collected and blocked carriers would suggest that the easiest route towards improving the selectivity of diffused contacts would be to increase the concentration (and depth) of the doped regions. Unfortunately, this also invokes a number of detrimental heavy doping effects, a summary of which is presented in Table 1. Perhaps the most significant amongst these effects is Auger recombination, which is evident in the modelling of the total recombination in the diffused region presented in Figure 7. The modelling shows an increase in total J_{0c} at very low R_{sh} values. This is caused by an increasing Auger recombination contribution which is more significant than the decrease in surface recombination. This results in a lowest achievable

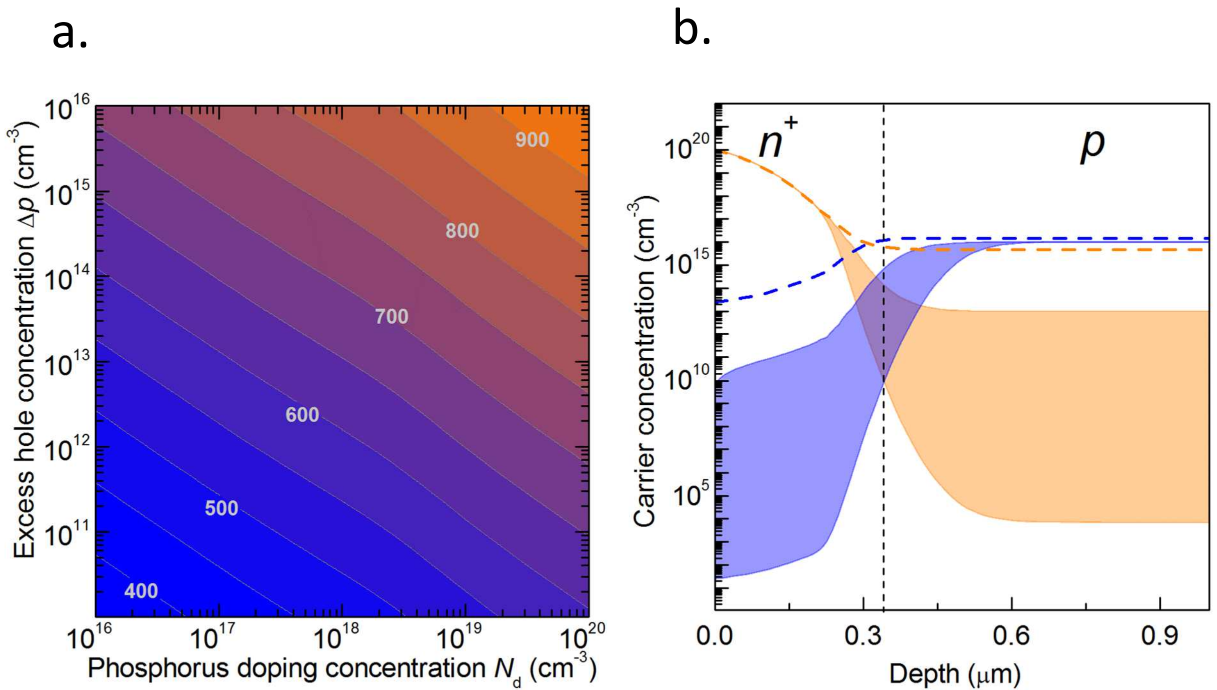

Figure 6: (a) contour plot of the voltage as a function of excess hole concertation for a range of different phosphorus doping concentrations. (b) electron (orange) and hole (blue) profiles at a realistic phosphorus diffused surface ($N_{surf} = 10^{20}$ cm^{-3}, depth~350 nm), obtained using the simulation tool *PC1D*. The surface recombination was set to 5×10^6 cm/s to mimic direct metallisation. The upper and lower bounds of the shaded region show the expected behaviour under light (100 mW/cm^2, at the maximum power point of 540 mV) and dark conditions. The dashed profiles are simulated from an identical phosphorus diffused region without Auger or surface recombination, showing that the hole concertation is still lower in the phosphorus diffused region than in the bulk of the wafer.

metal-contacted diffused region J_{0c} of ~350 fAcm^{-2} for both phosphorus and boron diffusions [38,39] and slightly higher, ~400 fAcm^{-2} for aluminium alloyed p$^+$ regions [42] (due mostly to a lower solubility limit [44,45]). A reasonable correlation between modelled and measured J_{0c} trends is clearly seen.

A further important restriction to this approach is presented by non-contacted regions contiguous to the metal contacts. As the optimised heavily doped region has a large component of Auger recombination, passivating the surface in the non-contacted regions provides only a small reduction in J_{0c}. Hence either a compromise needs to be made between contacted and non-contacted regions in terms of the desired dopant profile, or the heavy diffusion has to be applied only locally under the contacts introducing significant complexity to fabrication.

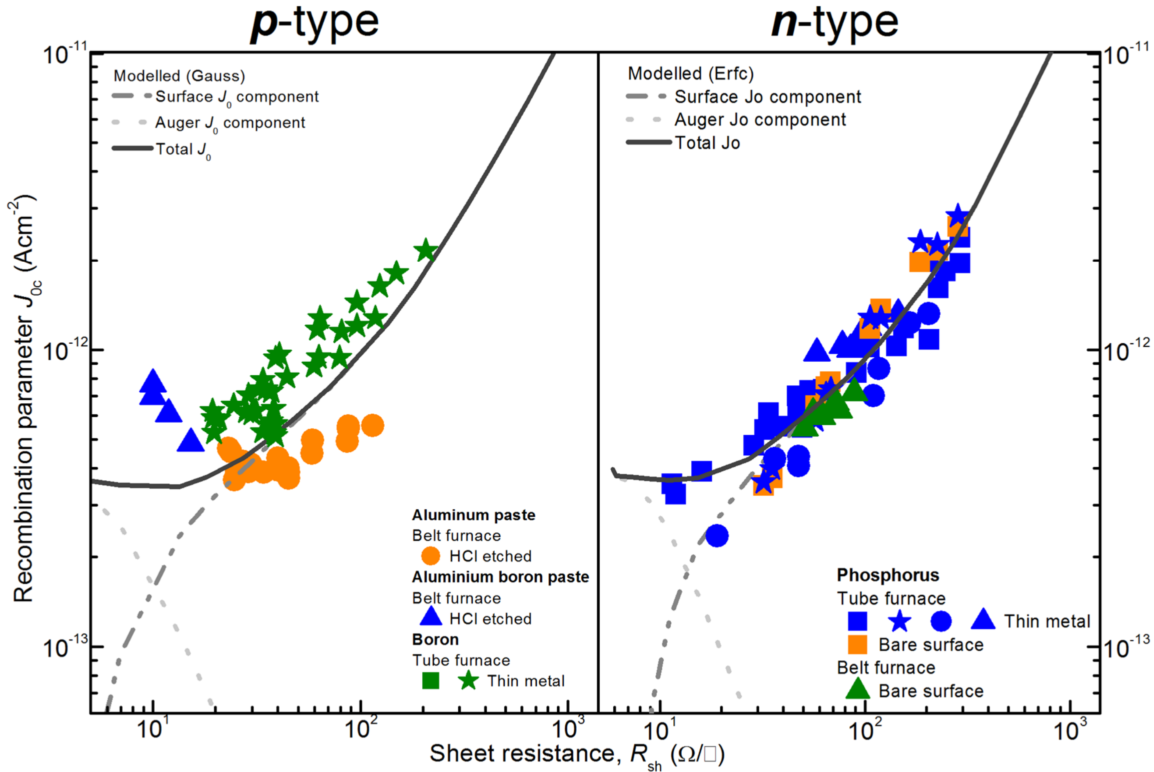

Figure 7: Compilation of measured J_{0c} parameters as a function of the sheet resistance of the underlying diffusion profile for phosphorus, boron and aluminium dopant profiles. J_{0c} values from different references have been extracted using different intrinsic carrier concentrations n_i and hence cannot strictly be directly compared, these J_{0c} have been corrected to an n_i value of 8.95×10^9 cm^{-3} where possible. The modelling was performed using simulation tool *EDNA*, with an error function to model the phosphorus diffusion and a Gaussian function to model the boron diffusion. A SRV of 5×10^6 cm/s was chosen to mimic the directly metalized surface. Depth factors and surface concentrations were varied incrementally to obtain a range on differing dopant 'dose' surfaces.

Table 1: Common loss mechanisms in heavily doped silicon.

Category	Loss mechanism	Cause	Ref.
Optical	Parasitic free carrier absorption, reduced J_{sc}	Heavy doping	[46]
	Parasitic window layer absorption, reduces J_{sc}	Narrow bandgap window layers (eg. Doped *a*-Si:H and *poly*-Si)	[47]
Recombination	Auger and radiative recombination, reduces V_{oc}	Heavy doping	[9]
	SRH recombination, reduces V_{oc}	Dopant precipitates (eg. phosphorus clusters)	[48]
		Dopant complexes (eg. Boron-oxygen defects)	[49]
	Surface SRH recombination, reduces V_{oc}	High surface dopant concentration (currently debated)	[50]
	Bulk and surface recombination, reduces V_{oc}	Band gap narrowing, increased minority carrier concentration	[39]
Transport	Resistive losses, reduces *FF* (especially lateral R_s)	Dopant and carrier scattering, low majority carrier mobility	[51]
	Low minority carrier diffusion length, reduces J_{sc}	Dopant and carrier scattering, low minority carrier mobility	[51]

1.4 Heterocontacts

The increasing obstructiveness of the abovementioned fundamental and practical losses has prompted a reassessment of the contribution that the contacts make towards carrier-selectivity. This has primarily been focused on the development of different contacting systems, applied to the surfaces of the *c*-Si absorber, which are selective towards just the collected carrier, referred to collectively as heterocontacts here, but also known as 'carrier-selective contacts' or 'passivating contacts'. Many of these systems are based on old ideas [4,52–54], assisted by significant advancements made in surface passivation understanding and techniques in recent years [9]. Others are borrowed from standard structures in other absorber type devices, particularly from organic electronics, where doping is not so easily achieved and hence heterocontacts have been actively developed [55,56]. A large diversity in the structure of these heterocontacts has arisen due to a wide range of different ways to achieve carrier-selectivity. These can be broadly divided into two areas, which are commonly implemented simultaneously; manipulating surface carrier concentration profiles within the absorber and creating asymmetries in conductivity through the electronic structure of the heterocontact.

Manipulating surface carrier concentrations

The formation of a surface potential ψ_s which alters the surface carrier concentrations, n_s and p_s, can arise due to a number of different mechanisms. Among these, the most accessible when fabricating heterocontacts are *i.* chemical potential differences (commonly known as work function differences) between the semiconductor and the heterocontact; and *ii.* a fixed charge density within one of the heterocontact films. These two elements can alter the magnitude and polarity of ψ_s resulting in four possible surface carrier concentration conditions: accumulation, flat-band, depletion and inversion.

For heterocontacts, inversion and accumulation conditions are the most relevant as they provide significant asymmetry in the two carrier concentrations at the surface, similar to the case of the surface dopant profile discussed in the section above. That is, a ψ_s that favours the build-up of the collected carrier in turn increases the conductivity *en route* to the contact surface and can, to a small degree, assist in lateral transport [57,58]. Conversely, the same ψ_s would result in a low surface concentration for the blocked carrier relative to the concentration within the bulk, due to the law of mass action (Equation 3 and 4). This lower blocked carrier concentration in turn reduces the rate of Shockley-Read-Hall surface recombination.

To first look at this situation under ideal conditions, Figure 8a presents the changing n_s and p_s as a function of the ψ_s for a lightly doped n-type wafer ($N_D = 10^{14}$ cm^{-3}). These $n_s(\psi_s)$ and $p_s(\psi_s)$ trends were calculated using the approach outlined by Walstra and Sah [59], and the Fermi-Dirac (FD) integral approximations suggested in Ref [60]. Also highlighted in this figure are the regions of depletion, accumulation and inversion – showing the strong asymmetries in carrier concentration present in the latter two. Figure 8a is representative of equilibrium conditions; under illumination the situation is more complicated and ψ_s will decrease [61]. However, a large asymmetry in the surface carrier concentrations can still exist at one sun if the initial ψ_s is sufficiently strong. To investigate this effect, the above FD based $n_s(\psi_s)$ and $p_s(\psi_s)$ equations are combined with the iterative approach of Girisch *et al.* [62]. This is used to model the change in ψ_s with illumination, represented by a bulk excess carrier density Δn, under the influence of either a metal work function $q\phi_m$ or a fixed charge density Q_f. A detailed description of this approach can be found in the paper by Girisch *et al.*, or in a number of other studies specifically focused on *c*-Si photovoltaics [61,63,64]. Provided in Figure 8b are plots which show the change in the p_s/n_s ratio as a function of $q\phi_m$ (in the top plot) and Q_f (in the

bottom plot) for a range of different Δn levels. In these plots it can be seen that significant carrier concentration asymmetries can be maintained under illumination with relatively

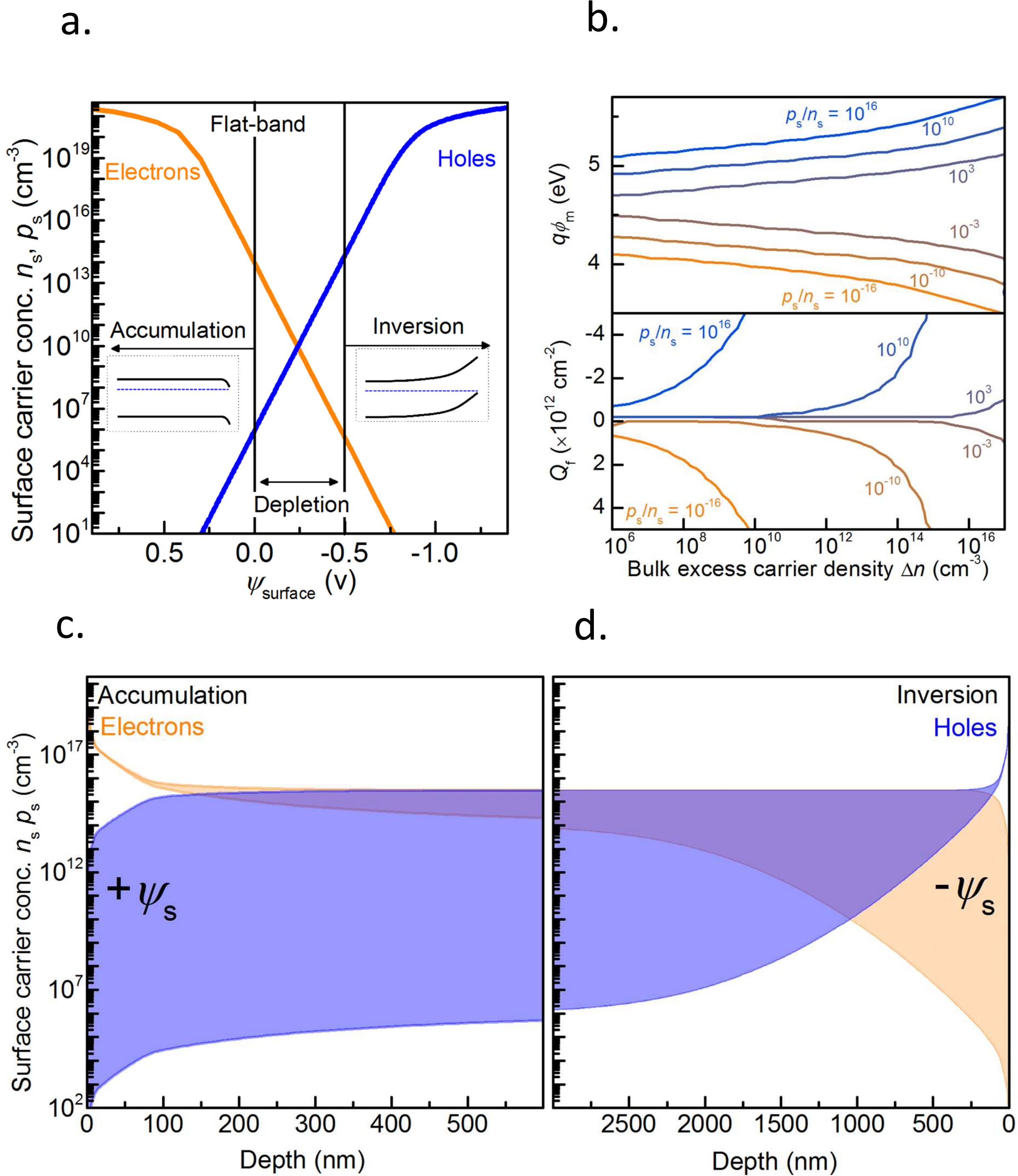

Figure 8: (a) electron (orange) and hole (blue) surface concentrations calculated as a function of surface potential, using Fermi Dirac-statistics, for a lowly doped ($N_D = 10^{14}$ cm^{-3}) n-type *c*-Si wafer. Band diagrams of inversion and accumulation conditions are also provided. (b) effect of excess carrier density on the p_s/n_s ratio for surfaces with an applied work function (top) and fixed charge density (bottom). (c) and (d) show simulations, performed in *PC1D*, of the spatial carrier profile for accumulation and inversion conditions resultant when applying surface potentials of 0.35 eV and -0.8 eV, respectively, to a lowly doped ($N_D = 10^{14}$ cm^{-3}) n-type *c*-Si wafer.

modest values of $\phi_{m,}$ and Q_f.

To demonstrate this explicitly, an example of how manipulating ψ_s can lead to carrier-selectivity is shown in Figures 8c and d, which utilises the simulation tool *PC1D* to plot the electron and hole carrier profiles of a lowly doped n-type wafer when positive (equilibrium ψ_s = 0.35 V) and negative (equilibrium ψ_s = -0.8 V) surface potentials are present on the left and right most surfaces, suitable for the collection of electrons and holes, respectively. Again the upper and lower bounds of the shaded regions represent light ($\Delta n = 10^{15}$ cm^{-3}) and dark conditions, respectively. In the absence of surface traps, the above ψ_s values permit a simulated device efficiency of ~29% under one sun conditions, in line with the intrinsic efficiency limit of *c*-Si (assuming perfect optics and an intrinsic bulk lifetime). In reality, departures from the ideal behaviour assumed in Figure 8 are expected. We also note that the approach of Grisch *et al.* requires the assumption of flat quasi Fermi energies through the surface regions, a factor which is not strictly true in the case of a heterocontact nor in the case of extremely high surface recombination [61].

In getting as close as possible to the ideal situation presented in Figure 8 there are some design rules and considerations that can be implemented. The major departures from the ideal case stem from the nature of the heterocontact interface with the *c*-Si absorber, which dictates much of the recombination and resistive behaviour of the heterocontact. As discussed already, reducing recombination is of primary importance and creating asymmetries in carrier concentration is only one component. Effective reduction in recombination also requires a minimisation of the surface trap concentration and their effectiveness at capturing the blocked carrier. The trap concentration can vary by orders of magnitude depending on how the *c*-Si surface is treated. For example, the

directly metallised c-Si surface is known to host an extremely high concentration of surface traps, likely above 10^{13} cm^{-2} [11]. Fortunately, focused surface passivation research in the last 15 years has shown that a reduction in the interface trap density to 10^9-10^{11} cm^{-2}, that is, 1 trap for every ~10,000 surface atoms, is achievable using a number of interlayer films with the assistance of hydrogenation [65–68]. The trap's effectiveness at capturing the blocked carrier is also dependent on the interface, primarily through the electron and hole capture cross sections c_e and c_h.

In a related manner, the nature of the interface also dictates how effectively we can manipulate the ψ_s using the metal work function. For example, when a metal is used directly, the interface is known to suffer from Fermi level pinning (FLP) to c-Si's charge neutrality level (CNL) and hence the ψ_s cannot be well controlled [27]. Whilst the precise molecular origin of FLP remains an open discussion within the broader scientific community [27,69–71], from a practical perspective, by inserting thin interlayers, as thin as 3Å [70], between the outer metal contact and the c-Si, the effects of Fermi level pinning (and also surface recombination) can be reduced [72–75]. In this instance, part of the metal / c-Si work function difference will now fall across the interlayer; bringing into relevance the thickness of this interlayer and its dielectric constant. It is noted that for some heterocontacts, due the angstrom scale of interlayer thickness, the characteristics of this interlayer, including the dielectric constant, may not be reflected by the bulk properties of such films [76]. In addition to the above case, a semiconductor with a desirable work function, for example doped polycrystalline silicon (*poly*-Si) or molybdenum oxide, can also be used in the place of the metal. In such a case, part of the balancing electric potential will also fall across this semiconductor unless it is degenerately doped or has a very large density of chargeable states. The use of an outer semiconductor rather than a metal has also been shown to reduce the effects of Fermi level pinning [77], and can be

considered particularly beneficial if it also acts as an additional source of molecular hydrogen to assist in reducing the density of surface traps [78,79]. Even with an interlayer, in many instances the Fermi level remains partially pinned to the CNL of the passivating interlayer (provided the interlayer has a wider band gap [71]). The degree of pinning is empirically quantified by the pinning factor S, taking a value between 0 and 1 (where 1 signifies no pinning). Nevertheless, a number of heterocontact systems have now been demonstrated on *c*-Si with pinning factors close to 1, including SiO_2 [77]. Furthermore, as demonstrated in Chapters 3 and 4, the availability of materials with extreme work function values can overcome many of these issues.

The use of a fixed charge density to manipulate the ψ_s at the heterocontact also requires consideration of a number of additional effects to those discussed above. The fixed charge density is commonly described as a thin sheet of immobile charges within an insulating film close to its interface with *c*-Si. These are generally attributed to particular molecular configurations which either have a permanent fixed charge or can be charged by carriers from the underlying *c*-Si substrate [63]. The location of this charge is usually taken to be contained within the first few nanometres [57,63], and hence in cases where an interlayer must be kept extremely thin to allow direct tunnelling, they may not develop the ‘full charge’ measured on thicker films. In addition, the analysis in Figure 8 assumed that the fixed charge density is mirrored solely in the *c*-Si wafer, an assumption which is valid in many regions of a solar cell. However, in the case of the heterocontact, given that a metallic or very conductive film is likely to be placed on top of the thin interlayer, a large percentage of the charge will instead be mirrored in this conductive layer – reducing the ψ_s within the *c*-Si [64].

Whilst important, the above commonly found departutures from the ideal case are not prohibitive, and as demonstrated in the examples to follow and in Chapters 3 and 4 of this thesis, carrier-selectivity can be achieved using these strategies.

Introducing asymmetries in conductivity at the heterocontact

In addition to controlling the population of carriers at the *c*-Si contact surface, carrier-selectivity can also be introduced or further assisted through the band structure of the heterocontact itself. It has long been recognised that an ideal *c*-Si solar cell would comprise two wide band-gap heterocontacts, asymmetrically straddled on either side of a *c*-Si wafer. In such a system ideally the collected carrier of each heterocontact experiences no barrier *en route* to the outer metal contact whilst the blocked carrier experiences an unsurmountable barrier for carrier transport, leading to obvious carrier-selectivity. In reality, a perfect implementation of this approach is yet to be demonstrated and typically selectivity is achieved by film stacks [78–80], each layer of which performs a specific function. Whilst excellent passivation (limiting the flux of the blocked carrier) is achievable, typically small barriers to the collected carrier are unavoidable. Fortunately, as discussed above, *c*-Si solar cells with full-area contacts can tolerate relatively high ρ_c values reducing the impact of such barriers. A number of mechanisms have been used to describe transport through these barriers, however in this case a simple thermionic emission model is used, following the approach in Ref. [11]. Figure 9a shows the thermionic emission ρ_c as a function of the barrier height presented to the collected carrier at the heterocontact for cell temperatures of 25 °C, 45 °C and 65°C. Included in this plot are two lines representative of upper and lower relevance for *c*-Si solar cells. The line at 0.5 Ωcm^2 represents an upper-limit for full-area contacts before the ρ_c starts to significantly detract from the cell's performance. The line at 2×10^{-7} Ωcm^2 can be treated

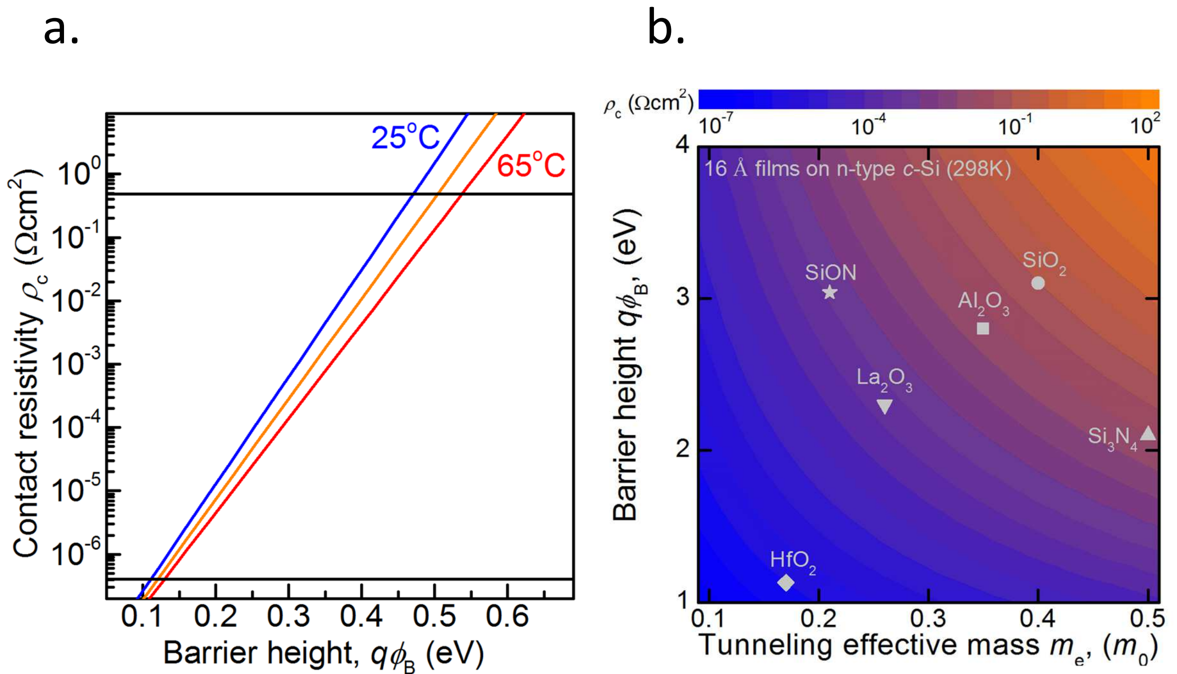

Figure 9: (a) thermionic emission ρ_c as a function of barrier height ϕ_B for a number of temperatures relevant to the operation of silicon solar cells. (b) direct tunnelling ρ_c for electrons in the conduction band as a function of electron tunnelling effective mass and barrier height of the interlayer. As a reference a range of empirical values for common interlayers (within the microelectronics community) are superimposed on this plot.

as a lower-limit, below which the ρ_c does not impact the cell significantly even for small area contacts. It can be seen that barriers below 0.15 eV have no effect on cell performance, and those above ~0.5 eV are prohibitively high for efficient silicon solar cells. The strong effect of cell temperature on the ρ_c can also be seen. It is interesting to note that solar cells with thermionic barriers may have better temperature response than conventional diffused contact solar cells [81], an important consideration given that standard module temperatures during operation are typically around ~45°C – significantly higher than standard measurement conditions of 25°C [81].

In many cases, the use of wide band gap passivating interlayers is desired for their excellent temperature stability and passivation characteristics. In such a case, barrier heights greater than 0.5 eV are introduced and hence transport cannot occur via thermionic emission. However, conduction can still occur through the barrier if it is

sufficiently thin. Again, a wide variety of different techniques can describe conduction thought such barriers, particularly if defects are involved [82]. In this case simple direct quantum mechanical tunnelling is used to describe such conduction. A previously introduced figure of merit specific to the collection of one carrier via the tunnelling process [43],

$$f = d\sqrt{m^{*}_{(e,h)}\Phi_{eff(C,V)}}\,.,\tag{3}$$

shows that carrier-selectivity can be achieved by creating a significant asymmetry in, for example, the barrier heights and tunnelling effective masses presented to electron in the conduction band and holes in the valence band. Also to be noted here is that, while it is not feasible to present a different barrier thickness to the two carriers, the extreme dependence of tunnelling on thickness favours an interlayer which can achieve surface passivation using very thin layers. As an example of direct tunnelling, Figure 9b provides a contour plot of the changing electron tunnelling ρ_c as a function of the electron effective mass and barrier height of the conduction band for a 16 Å interlayer, following the approach in Ref. [11]. It should be emphasised that this plot represents only the contribution of the direct tunnelling process to the ρ_c and that other effects (for example barriers at the *c*-Si surface) would change the ρ_c. Superimposed on this plot are empirical values for interlayers commonly implemented in the microelectronic industry [77,83], most of which are known to provide excellent passivation to *c*-Si when applied as thicker films [65–67,84]. In designing electron-selective heterocontacts the ability of these layers to block holes would also have to be considered. In addition, as discussed above, for cases where the work function of an outer material was used to change surface carrier concentrations, the dielectric constant (and thickness) of the interlayer would also have to be factored into the relative merits of the heterocontact system.

A number of other strategies have been suggested to achieve selectivity at the heterocontact including the asymmetric mobility heterocontact [1], and the introduction of carrier selective defects into a passivating film [85]. However, both of these ideas remain at the concept stage.

Combining heterocontacts with surface doping

Given the current dominance of directly metalized, surface diffusion processes, particularly phosphorus doping processes, rather than removing surface doping completely, a rational alternative might be to dramatically lighten the surface doping profiles and replace the direct metal contacts with passivating heterocontacts. This hybrid stratergy would combine some of the benefits of both methods of carrier-selectivity. By significantly lightening the dopant concentration, heavy-doping effects could be minimised at the same time as reducing surface barriers and recombination and still allowing the phosphorus gettering process. This hybrid doping / selective contact approach is already implemented in many *poly*-Si type contacts [86], which experience some in-diffusion from the doped layers during high temperature annealing. In this context, compared to direct metallisation, the use of a passivating heterocontact can be viewed as a trade-off between ρ_c and $J_{0,}$ modulated, for example, by the interlayer thickness. This still introduces significant benefits in terms of carrier-selectivity and can be regarded as an alternative to the localised doping approaches by reducing the required trade-off between contacted and non-contacted regions in terms of the underlying dopant profile. It also frees up restrictions on the choice of metal – allowing the use of cheaper, easily deposited, lower resistance or more optically suitable metals.

1.5 Successful demonstration of heterocontacts

Provided below is a brief description of current state-of-the-art heterocontact systems for *c*-Si solar cells, some of which are discussed in greater detail in the chapters to follow.

The earliest successful demonstration of heterocontacts for *c*-Si solar cells appears to be that of the metal insulator semiconductor (MIS) contacts utilised in *c*-Si MIS-inversion layer cells in the 1970's [53,87–89]. A diverse range of such devices was demonstrated with different metal and interlayer combinations [90,91], but typically Al and SiO_x were the most successful. The SiO_x passivating interlayer was grown both chemically and thermally, with higher temperature oxides exhibiting greater device stability [92]. This standard *c*-Si(p) / SiO_x / Al design relied on both the low metal work function and fixed charges on the cell's front-side films to assist in carrier-selectivity. The principal benefits of this technology is the simplicity of design, low temperature fabrication and resultant low cost. However, despite reaching a conversion efficiency of 19.6% [93], focus was instead shifted to a parallel stream of research that combined MIS heterocontacts and dopant diffused surfaces, commonly known as the metal-insulator-*np* or MINP cells [94]. This architecture held the world record efficiency for a short period in the 1980's [95], and is still in use today [96], expanding in some cases to alternative passivating layers, fabrication procedures and different underlying dopant species [43,97–99], all of which are explored in Chapter 2.

A closely related family of heterocontacts, initially demonstrated as suitable for *c*-Si solar cells in the 1980's and 90's [4,52,54], involve the use of doped-silicon outer semiconductors, separated from the *c*-Si absorber by silicon-based passivating interlayers. These architectures are currently the most popular and successful heterocontact options

available. One variant of which is the world record holding SHJ solar cell [6], outlined in the introduction section of this chapter (see Figure 1b). In general, the outer phosphorus and boron doped silicon layers can be amorphous *a*-Si [100], microcrystalline *μ*-Si [101], or polycrystalline *poly*-Si [86,102], and have been demonstrated using a wide variety of deposition techniques (for example sputtering [103], PECVD [86,100,104], LPCVD [101], hot wire CVD [106]) and doping practices (for example, *in situ* [97,105], thermal [86,105], ion implantation [102,107]). The passivating interlayers are typically either intrinsic *a*-Si:H [100], silicon carbide SiC_x [108], silicon nitride SiN_x [109], or silicon oxide SiO_x [78,79,86,110,111]. This heterocontact technology is characterised by unmatched V_{oc}'s [5], whilst typically conveying higher, but acceptable, contact resistivities [112,113]. A number of such heterocontacts have now been demonstrated on *c*-Si solar cells with efficiencies at and around 25% [5,78,110], both within industry and research laboratories. The most commonly ascribed shortcoming of this approach is the parasitic absorption occurring in the doped-silicon films [47], which do not support carrier lifetimes long enough to allow carrier collection. In addition, the variants featuring *a*-Si:H layers are sensitive to temperatures above 200°C. However, a suitable low temperature back-end process has been developed, reducing the impact of this temperature instability. In recent years, research in this field has focused on reducing absorption via thinning of the films, carbon and oxygen incorporation [108,111], or crystallisation of the silicon based layers to increase their transparency [101]. In addition, the issue can be circumvented by switching to more advanced architectures which avoid the use of such layers on the top surface, for example, interdigitated back contact [6], or tandem based devices [114].

An alternative approach, to address the issues of absorption in the doped-silicon layers, and in some cases simplify the fabrication procedure, is to substitute these films with other, less absorptive materials which perform the same function. This is a rapidly

expanding area of research within the *c*-Si community. In its current state promising heterocontacts have been demonstrated using a range of different materials including, most prominently metal oxides, alkali and alkaline earth metal salts, organic polymers and carbon based nanomaterials. These materials can generally be deposited using simple low temperature techniques – introducing potential reductions in fabrication costs.

The largest sub-group is that based on the metal oxides. For the collection of electrons, a number of n-type metal oxides with demonstrated passivation of *c*-Si surfaces (TiO_x [115,116], TaO_x [117], GaO_x [118], ZnO_x [119] etc.), and favourable theoretical band alignment, are being explored, some of which were previously identified in earlier relevant research [90,120,121]. Of particular promise is TiO_x, already demonstrating electron-selectivity on *c*-Si both with [122], and without passivating interlayers [116,123–125], as discussed in Chapter 3. As for the hole heterocontacts, while some attention has been paid to the p-type oxides in this application (for example, NiO_x [74], and CuO_x), most research in recent years has focused on the high work function n-type transition metal oxides MoO_x[81,126–133], WO_x[128,130,132], and VO_x[128,132], also identified as useful for *c*-Si solar cells in the past [90]. These films, which exhibit work functions above 6.5 eV in the ideal case [134], have been trialled as heterocontacts to *c*-Si both with, and without, passivating interlayers. In particular, MoO_x has recently been integrated into modified PRC and SHJ cells attaining efficiencies above 20% and 22% respectively [80,135], further details of which will be provided in Chapter 3. Similar to the SHJ cells, these layers also suffer from instability at relatively low temperatures [80,130], requiring specialised low temperature processing.

Another alternative, inherited from the organic electronic community [136], is the use of thin alkali and alkaline earth metal salt interlayers to enhance electron extraction,

including LiF [122,133,137–139], KF [122], CsF [122], $CsCO_3$ [140], and MgF_2 [141]. When these layers are integrated under a metal electrode, most commonly Al, low work function values can be obtained, as low as ~2.5 eV in some cases, promoting the collection of electrons from the adjacent *c*-Si surface. The applicability of this technique to *c*-Si solar cells has recently been demonstrated, in some cases with *a*-Si:H passivating interlayers [122,141] to assist in reducing the blocked carrier flux to the surface. In particular, LiF has recently been integrated as an electron contact into dopant-free, asymmetric heterocontact (DASH) and PRC cells with efficiencies around 20%, as discussed in Chapter 4.

Two final subcategories of heterocontacts for *c*-Si solar cells are those formed by carbon nanomaterials, and organic polymer films. The carbon based heterocontacts, namely graphene [142], graphene oxide [143], and carbon nanotubes [144], utilised for collecting holes, remain at an early development stage, with device efficiencies of 15% and below. The formation of organic / *c*-Si heterocontacts, most commonly for the collection of holes, has been achieved using a wide range of organic hole collecting layers including 1,1-bis[(di-4-tolylamino)phenyl]cyclohexane (TAPC) [145], poly(3,4-ethylenedioxythiophene) :poly(styrenesulfonate) (PEDOT:PSS) [124,146,147], and 2,2′,7,7′-Tetrakis-(N,N-di-4-methoxyphenylamino)-9,9′-spirobifluorene (Spiro-OMeTAD) [148]. PEDOT:PSS remains the most promising candidate, with demonstrated efficiencies over 20% when implemented as the hole contact in p-type *c*-Si cells, and slightly lower for n-type [147].

To conclude this introduction chapter, Figure 10 compiles a range of experimentally determined J_{0c} and ρ_c values for different carrier-selectivity systems; including heterocontacts, directly metalized heavily doped contacts and 'hybrid' heterocontacts on heavily doped regions. These are superimposed on an identical carrier-

selectivity plot to that presented earlier in Figure 3b, to compare their relative carrier-selectivity. In this plot, directly metalized dopant-diffused contacts are shown by hollow points. The leftmost of these directly metalized data points are representative of solar cells which employ localised doped regions such as the passivated emitter rear locally diffused (PERL) type solar cells. It can be seen that such systems are characterised by low ρ_c and high J_{0c} requiring that they are applied only to a very small area. Conversely, the heterocontacts, primarily situated on the right of the plot, are characterised by low J_{0c} and high ρ_c. It is interesting to note that these two disparate selective-contact systems approximately occupy the same region of carrier-selectivity–suggesting both currently have similar ultimate efficiency potential. Resultantly, factors such as fabrication cost/complexity and cell environmental stability will likely be more important considerations for future solar cell manufacturers.

.

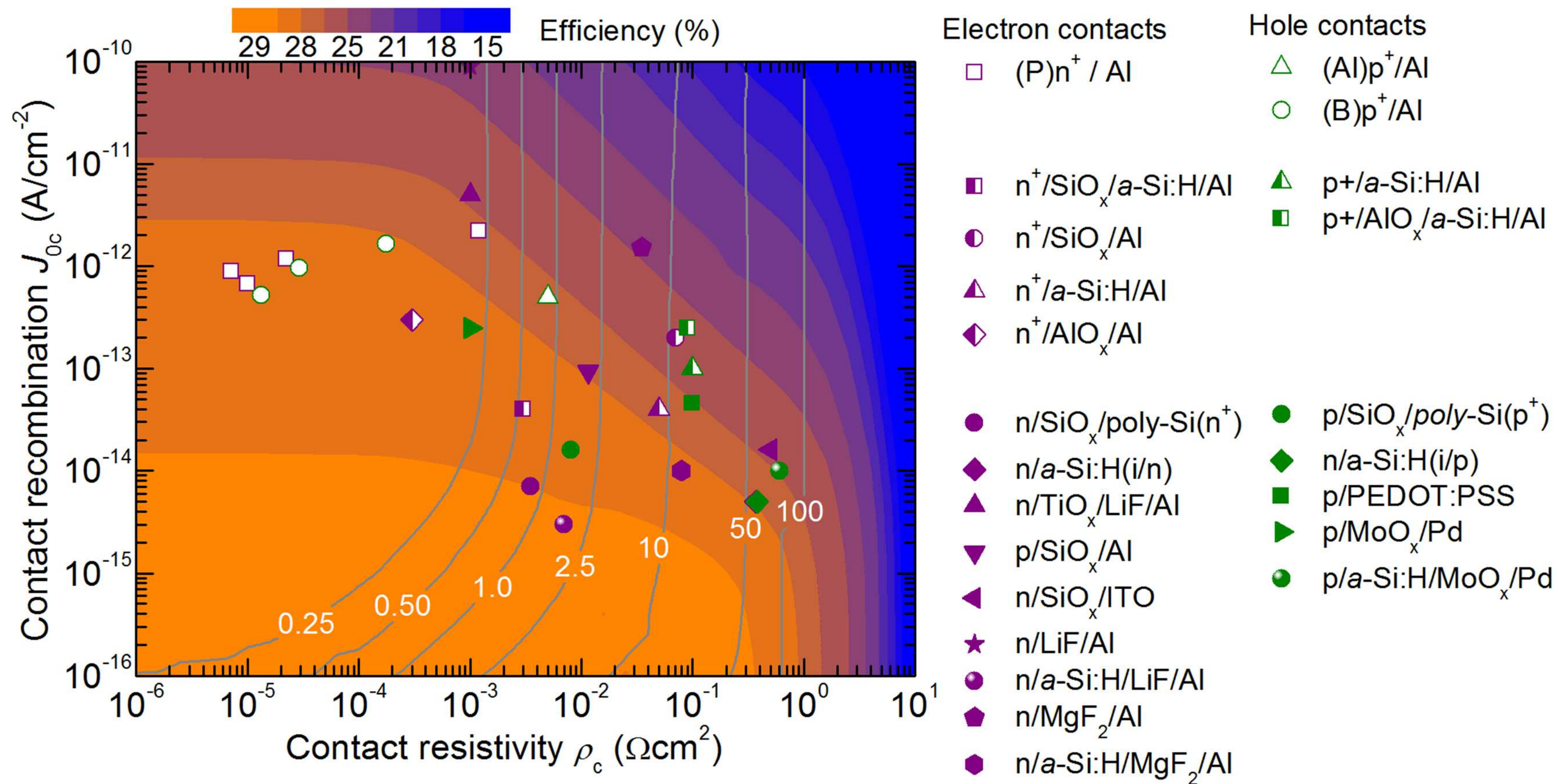

Figure 10: Compilation of experimentally determined ρ_c and J_{0c} values for different carrier-selectivity systems. Data points for electron (purple) and hole (green) directly metalized heavily doped surfaces (hollow), hybrid heterocontacts on highly doped surfaces (half full) and heterocontacts on lightly doped surfaces (filled) are included. It is noted that the *poly*-Si contacts have been classed as heterocontacts on lightly doped surfaces here despite the fact that they may form a light dopant profile at the *c*-Si surface. These results are overlayer over efficiency simulations (coloured contours) with optimised contact fractions (grey lines).

References

[1] U. Wurfel, A. Cuevas, P. Wurfel, *Photovolt. IEEE J. Of* **2015**, *5*, 461.
[2] *International Technology Roadmap for Photovoltaic (ITRPV), 2014 Results, Revision 1, July 2015*, **n.d.**
[3] J. Zhao, A. Wang, M. A. Green, *Prog. Photovolt. Res. Appl.* **1999**, *7*, 471.
[4] M. Tanaka, M. Taguchi, T. Matsuyama, T. Sawada, S. Tsuda, S. Nakano, H. Hanafusa, Y. Kuwano, *Jpn. J. Appl. Phys.* **1992**, *31*, 3518.
[5] M. Taguchi, A. Yano, S. Tohoda, K. Matsuyama, Y. Nakamura, T. Nishiwaki, K. Fujita, E. Maruyama, *Photovolt. IEEE J. Of* **2014**, *4*, 96.
[6] K. Masuko, M. Shigematsu, T. Hashiguchi, D. Fujishima, M. Kai, N. Yoshimura, T. Yamaguchi, Y. Ichihashi, T. Mishima, N. Matsubara, T. Yamanishi, T. Takahama, M. Taguchi, E. Maruyama, S. Okamoto, *Photovolt. IEEE J. Of* **November**, 1433.
[7] A. Fell, *Electron Devices IEEE Trans. On* **2013**, *60*, 733.
[8] A. Richter, M. Hermle, S. W. Glunz, *IEEE J. Photovolt.* **2013**, *3*, 1184.
[9] A. Richter, S. W. Glunz, F. Werner, J. Schmidt, A. Cuevas, *Phys. Rev. B* **2012**, *86*, 165202.
[10] K. O. Davis, K. Jiang, C. Demberger, H. Zunft, H. Haverkamp, D. Habermann, W. V. Schoenfeld, *IEEE J. Photovolt.* **2013**, *3*, 641.
[11] S. M. Sze, K. K. Ng, *Physics of Semiconductor Devices*, John Wiley & Sons, **2006**.
[12] C. Mader, J. Muller, S. Eidelloth, R. Brendel, *Sol. Energy Mater. Sol. Cells* **2012**, *107*, 272.
[13] M. Hörteis, Fine-Line Printed Contacts on Crystalline Silicon Solar Cells, Fraunhofer Institut für Solare Energiesysteme, **2009**.
[14] A. Mette, New Concepts for Front Side Metallization of Industrial Silicon Solar Cells, Fraunhofer-Institut für Solare Energiesysteme, **2007**.
[15] G. Schubert, Thick Film Metallisation of Crystalline Silicon Solar Cells Mechanisms, Models and Applications, Universität Konstanz, **2006**.
[16] A. Rohatgi, S. Narasimha, D. S. Ruby, in *Proc. 2nd World Conf. Photovolt. Sol. Energy Convers.*, **1998**.
[17] S. Riegel, F. Mutter, G. Hahn, B. Terheiden, *Energy Procedia* **2011**, *8*, 533.
[18] E. Urrejola, K. Peter, H. Plagwitz, G. Schubert, *J. Appl. Phys.* **2010**, *107*, 124516.
[19] S. Gatz, T. Dullweber, R. Brendel, *IEEE J. Photovolt.* **2011**, *1*, 37.
[20] L. Jaime, in *Sol. Energy* (Ed.: R. D), InTech, **2010**.
[21] C. Kranz, B. Lim, U. Baumann, T. Dullweber, *Energy Procedia* **2015**, *67*, 64.
[22] S. Binder, J. Bartsch, M. Glatthaar, S. Glunz, *Energy Procedia* **2012**, *21*, 32.
[23] A. Richter, S. Henneck, J. Benick, M. Hörteis, M. Hermle, S. Glunz, *Proc. 25th Eur. Photovolt. Sol. Energy Conf. Valencia Spain* **2010**.
[24] S. Braun, E. Emre, B. Raabe, G. Hahn, Valencia, Spain, **2010**, pp. 1892 – 1895.
[25] M. Rauer, A. Mondon, C. Schmiga, J. Bartsch, M. Glatthaar, S. W. Glunz, *Energy Procedia* **2013**, *38*, 449.
[26] S. Seren, S. Braun, Y. Schiele, G. Hahn, B. Terheiden, Frankfurt, Germany, **2012**.
[27] D. K. Schroder, D. L. Meier, *IEEE Trans. Electron Devices* **1984**, *31*, 637.
[28] A. Richter, J. Benick, A. Kalio, J. Seiffe, M. Hörteis, M. Hermle, S. W. Glunz, *Energy Procedia* **2011**, *8*, 479.
[29] J. Bullock, D. Yan, A. Cuevas, B. Demaurex, A. Hessler-Wyser, S. De Wolf, in *Photovolt. Spec. Conf. PVSC 2014 IEEE 40th*, **2014**, pp. 3442–3447.
[30] H. Plagwitz, M. Schaper, A. Wolf, R. Meyer, J. Schmidt, B. Terheiden, R. Brendel, Barcelona, Spain, **2005**.
[31] H. Plagwitz, M. Nerding, N. Ott, H. P. Strunk, R. Brendel, *Prog. Photovolt. Res. Appl.* **2004**, *12*, 47.
[32] W. Y. H. Anita, A Novel Rear Contacting Technique for Buried Contact Solar Cells, University of New South Wales, **2004**.
[33] F. Heinemeyer, C. Mader, D. Münster, T. Dullweber, R. Brendel, **n.d.**
[34] A. W. Blakers, A. Wang, A. M. Milne, J. Zhao, M. A. Green, *Appl. Phys. Lett.* **1989**, *55*, 1363.
[35] R. Hezel, K. Jaeger, *J. Electrochem. Soc.* **1989**, *136*, 518.
[36] S. W. Glunz, H. Mackel, J. Nekarda, A. Cuevas, in *22nd Eur. Photovolt. Sol. Energy Conf. Exhib.*, Milan, Italy, **2007**.
[37] A. Cuevas, P. A. Basore, G. Giroult-Matlakowski, C. Dubois, *J. Appl. Phys.* **1996**, *80*, 3370.
[38] D. Yan, A. Cuevas, *J. Appl. Phys.* **2013**, *114*, DOI http://dx.doi.org/10.1063/1.4816694.
[39] D. Yan, A. Cuevas, *J. Appl. Phys.* **2014**, *116*, DOI http://dx.doi.org/10.1063/1.4902066.
[40] M. J. Kerr, Surface, Emitter and Bulk Recombination in Silicon and Development of Silicon Nitride Passivated Solar Cell, The Australian National University, **2002**.
[41] M. J. Kerr, J. Schmidt, A. Cuevas, J. H. Bultman, *J. Appl. Phys.* **2001**, *89*, 3821.
[42] R. Woehl, P. Gundel, J. Krause, K. Ruhle, F. D. Heinz, M. Rauer, C. Schmiga, M. C. Schubert, W. Warta, D. Biro, *IEEE Trans. Electron Devices* **2011**, *58*, 441.

[43] J. Bullock, A. Cuevas, D. Yan, B. Demaurex, A. Hessler-Wyser, S. De Wolf, *J. Appl. Phys.* **2014**, *116*, DOI http://dx.doi.org/10.1063/1.4900539.
[44] P. Lolgen, W. C. Sinke, C. Leguijt, A. W. Weeber, P. F. A. Alkemade, L. A. Verhoef, *Appl. Phys. Lett.* **1994**, *65*, 2792.
[45] P. Lolgen, C. Leguijt, J. A. Eikelboom, R. A. Steeman, W. C. Sinke, L. A. Verhoef, P. F. A. Alkemade, E. Algra, in *Conf. Rec. Twenty Third IEEE Photovolt. Spec. Conf. 1993*, **1993**, pp. 236–242.
[46] S. C. Baker-Finch, K. R. McIntosh, D. Yan, K. C. Fong, T. C. Kho, *J. Appl. Phys.* **2014**, *116*, DOI http://dx.doi.org/10.1063/1.4893176.
[47] Z. C. Holman, A. Descoeudres, L. Barraud, F. Z. Fernandez, J. P. Seif, S. De Wolf, C. Ballif, *Photovolt. IEEE J. Of* **2012**, *2*, 7.
[48] B. Min, H. Wagner, A. Dastgheib-Shirazi, A. Kimmerle, H. Kurz, P. P. Altermatt, *Phys. Status Solidi RRL Rapid Res. Lett.* **2014**, *8*, 680.
[49] J. Schmidt, A. Cuevas, *J. Appl. Phys.* **1999**, *86*, 3175.
[50] R. R. King, R. A. Sinton, R. M. Swanson, *Electron Devices IEEE Trans. On* **1990**, *37*, 365.
[51] D. B. M. Klaassen, *Solid-State Electron.* **1992**, *35*, 953.
[52] J. Y. Gan, R. M. Swanson, in *Conf. Rec. Twenty First IEEE Photovolt. Spec. Conf. 1990*, **1990**, pp. 245–250 vol.1.
[53] R. B. Godfrey, M. A. Green, *Appl. Phys. Lett.* **1979**, *34*, 790.
[54] E. Yablonovitch, T. Gmitter, R. M. Swanson, Y. H. Kwark, *Appl. Phys. Lett.* **1985**, *47*, 1211.
[55] L.-M. Chen, Z. Xu, Z. Hong, Y. Yang, *J. Mater. Chem.* **2010**, *20*, 2575.
[56] H. Zhou, Q. Chen, G. Li, S. Luo, T. Song, H.-S. Duan, Z. Hong, J. You, Y. Liu, Y. Yang, *Science* **2014**, *345*, 542.
[57] F. Werner, Y. Larionova, D. Zielke, T. Ohrdes, J. Schmidt, *J. Appl. Phys.* **2014**, *115*, DOI http://dx.doi.org/10.1063/1.4865962.
[58] B. Kuhlmann, A. G. Aberle, R. Hezel, G. Heiser, *IEEE Trans. Electron Devices* **2000**, *47*, 2167.
[59] S. V. Walstra, R. .-Y. Sah, *IEEE Trans. Electron Devices* **1997**, *44*, 1136.
[60] P. V. Halen, D. L. Pulfrey, *J. Appl. Phys.* **1985**, *57*, 5271.
[61] S. Dauwe, Low Temperature Surface Passivation of Crystalline Silicon and Its Application to the Rear Side of Solar Cells, Institut fur SolarenergieforschungHarneln, **2004**.
[62] R. B. M. Girisch, R. P. Mertens, R. F. De Keersmaecker, *IEEE Trans. Electron Devices* **1988**, *35*, 203.
[63] A. G. Aberle, *Crystalline Silicon Solar Cells: Advanced Surface Passivation and Analysis*, Centre For Photovoltaic Engineering, University Of New South Wales, **1999**.
[64] S. J. Robinson, S. R. Wenham, P. P. Altermatt, A. G. Aberle, G. Heiser, M. A. Green, *J. Appl. Phys.* **1995**, *78*, 4740.
[65] Y. Wan, K. R. McIntosh, A. F. Thomson, A. Cuevas, *IEEE J. Photovolt.* **2013**, *3*, 554.
[66] G. Dingemans, N. M. Terlinden, D. Pierreux, H. B. Profijt, M. C. M. van de Sanden, W. M. M. Kessels, *Electrochem. Solid-State Lett.* **2011**, *14*, H1.
[67] A. G. Aberle, S. W. Glunz, A. W. Stephens, M. A. Green, *Prog. Photovolt. Res. Appl.* **1994**, *2*, 265.
[68] S. D. Wolf, M. Kondo, *Appl. Phys. Lett.* **2007**, *90*, 042111.
[69] R. T. Tung, *Appl. Phys. Rev.* **2014**, *1*, 011304.
[70] W. Mönch, *J. Appl. Phys.* **2012**, *111*, 073706.
[71] J. Robertson, *J. Vac. Sci. Technol. A* **2013**, *31*, 050821.
[72] Z. Liu, M. Kobayashi, B. C. Paul, Z. Bao, Y. Nishi, in *Electron Devices Meet. IEDM 2009 IEEE Int.*, **2009**, pp. 1–4.
[73] D. Connelly, C. Faulkner, P. A. Clifton, D. E. Grupp, *Appl. Phys. Lett.* **2006**, *88*, 012105.
[74] R. Islam, G. Shine, K. C. Saraswat, *Appl. Phys. Lett.* **2014**, *105*, 182103.
[75] B. E. Coss, W.-Y. Loh, H. C. Floresca, M. J. Kim, P. Majhi, R. M. Wallace, J. Kim, R. Jammy, *Appl. Phys. Lett.* **2011**, *99*, 102108.
[76] A. Schenk, G. Heiser, *J. Appl. Phys.* **1997**, *81*, 7900.
[77] Y.-C. Yeo, T.-J. King, C. Hu, *J. Appl. Phys.* **2002**, *92*, 7266.
[78] J. B. Heng, J. Fu, B. Kong, Y. Chae, W. Wang, Z. Xie, A. Reddy, K. Lam, C. Beitel, C. Liao, C. Erben, Z. Huang, Z. Xu, *Photovolt. IEEE J. Of* **2014**, *PP*, 1.
[79] F. Feldmann, M. Bivour, C. Reichel, M. Hermle, S. W. Glunz, *Sol. Energy Mater. Sol. Cells* **2014**, *120*, 270.
[80] J. Geissbühler, J. Werner, S. Martin de Nicolas, L. Barraud, A. Hessler-Wyser, M. Despeisse, S. Nicolay, A. Tomasi, B. Niesen, S. De Wolf, C. Ballif, *Appl. Phys. Lett.* **2015**, *107*.
[81] C. Battaglia, S. M. de Nicolas, S. De Wolf, X. Yin, M. Zheng, C. Ballif, A. Javey, *Appl. Phys. Lett.* **2014**, *104*.
[82] F.-C. Chiu, *Adv. Mater. Sci. Eng.* **2014**, *2014*, e578168.
[83] Yee Chia Yeo, Qiang Lu, Wen Chin Lee, Tsu-Jae King, Chenming Hu, Xiewen Wang, Xin Guo, T. P. Ma, *IEEE Electron Device Lett.* **2000**, *21*, 540.
[84] F. Lin, B. Hoex, Y. H. Koh, J. J. Lin, A. G. Aberle, *Energy Procedia* **2012**, *15*, 84.
[85] Y. Liu, P. Stradins, H. Deng, J. Luo, S.-H. Wei, *Appl. Phys. Lett.* **2016**, *108*, 022101.
[86] D. Yan, A. Cuevas, J. Bullock, Y. Wan, C. Samundsett, *Sol. Energy Mater. Sol. Cells* **2015**, *142*, 75.
[87] J. P. Ponpon, P. Siffert, *J. Appl. Phys.* **1976**, *47*, 3248.
[88] D. L. Pulfrey, *Electron Devices IEEE Trans. On* **1978**, *25*, 1308.

[89] M. A. Green, R. B. Godfrey, *Appl. Phys. Lett.* **1976**, *29*, 610.
[90] J. Shewchun, D. Burk, M. B. Spitzer, *IEEE Trans. Electron Devices* **1980**, *27*, 705.
[91] K. K. Ng, H. C. Card, *IEEE Trans. Electron Devices* **1980**, *27*, 716.
[92] M. Grauvogl, R. Hezel, *Prog. Photovolt. Res. Appl.* **1998**, *6*, 15.
[93] R. Hezel, R. Meyer, A. Metz, *Sol. Energy Mater. Sol. Cells* **2001**, *65*, 311.
[94] M. A. Green, A. W. Blakers, Z. R. Willison, T. Szpitalak, E. M. Keller, E. Gauja, P. J. Hart, in *Proc. 15th Photovolt. Spec. Conf. Kissimmee FL*, **1981**.
[95] M. A. Green, *Prog. Photovolt. Res. Appl.* **2009**, *17*, 183.
[96] J. Schmidt, A. Merkle, R. Brendel, B. Hoex, M. C. M. van de Sanden, W. M. M. Kessels, *Prog. Photovolt. Res. Appl.* **2008**, *16*, 461.
[97] J. Bullock, D. Yan, A. Cuevas, *Phys. Status Solidi RRL Rapid Res. Lett.* **2013**, *7*, 946.
[98] D. Zielke, J. H. Petermann, F. Werner, B. Veith, R. Brendel, J. Schmidt, *Phys. Status Solidi RRL Rapid Res. Lett.* **2011**, *5*, 298.
[99] J. Bullock, A. Cuevas, C. Samundsett, D. Yan, J. McKeon, Y. Wan, *Sol. Energy Mater. Sol. Cells* **2015**, *138*, 22.
[100] A. Descoeudres, Z. C. Holman, L. Barraud, S. Morel, S. De Wolf, C. Ballif, *Photovolt. IEEE J. Of* **2013**, *3*, 83.
[101] H. Wernerus, M. Bivour, L. Kroely, M. Hermle, W. Wolke, *Energy Procedia* **2014**, *55*, 310.
[102] U. Romer, R. Peibst, T. Ohrdes, B. Lim, J. Krugener, T. Wietler, R. Brendel, *IEEE J. Photovolt.* **2015**, *5*, 507.
[103] X. Zhang, S. Hargreaves, Y. Wan, A. Cuevas, *Phys. Status Solidi RRL – Rapid Res. Lett.* **2014**, *8*, 231.
[104] P. Stradins, S. Essig, W. Nemeth, B. G. Lee, D. Young, A. Norman, Y. Liu, J.-W. Luo, E. Warren, A. Dameron, V. LaSalvia, M. Page, A. Rohatgi, A. Upadhyaya, B. Rounsaville, Y.-W. Ok, S. Glunz, J. Benick, F. Feldmann, M. Hermle, *Passivated Tunneling Contacts to N-Type Wafer Silicon and Their Implementation into High Performance Solar Cells: Preprint*, National Renewable Energy Laboratory (NREL), Golden, CO., **2014**.
[105] U. Römer, R. Peibst, T. Ohrdes, B. Lim, J. Krügener, E. Bugiel, T. Wietler, R. Brendel, *Sol. Energy Mater. Sol. Cells* **2014**, *131*, 85.
[106] Q. Wang, M. R. Page, E. Iwaniczko, Y. Q. Xu, L. Roybal, R. Bauer, B. To, H.-C. Yuan, A. Duda, Y. F. Yan, in *33rd IEEE Photovolt. Spec. Conf. 2008 PVSC 08*, **2008**, pp. 1–5.
[107] F. Feldmann, R. Müller, C. Reichel, M. Hermle, *Phys. Status Solidi RRL – Rapid Res. Lett.* **2014**, *08*, 767.
[108] M. Boccard, Z. C. Holman, *J. Appl. Phys.* **2015**, *118*, 065704.
[109] D. Yan, A. Cuevas, Y. Wan, J. Bullock, *Phys. Status Solidi RRL – Rapid Res. Lett.* **2015**, *9*, 617.
[110] A. Moldovan, F. Feldmann, M. Zimmer, J. Rentsch, J. Benick, M. Hermle, *Sol. Energy Mater. Sol. Cells* **2015**, *142*, 123.
[111] T. Mueller, S. Schwertheim, M. Scherff, W. R. Fahrner, *Appl. Phys. Lett.* **2008**, *92*, 033504.
[112] S.-Y. Lee, H. Choi, H. Li, K. Ji, S. Nam, J. Choi, S.-W. Ahn, H.-M. Lee, B. Park, *Sol. Energy Mater. Sol. Cells* **2014**, *120, Part A*, 412.
[113] R. Gogolin, M. Turcu, R. Ferre, J. Clemens, N.-P. Harder, R. Brendel, J. Schmidt, *Photovolt. IEEE J. Of* **2014**, *4*, 1169.
[114] J. Werner, C.-H. Weng, A. Walter, L. Fesquet, J. P. Seif, S. De Wolf, B. Niesen, C. Ballif, *J. Phys. Chem. Lett.* **2016**, *7*, 161.
[115] B. Liao, B. Hoex, A. G. Aberle, D. Chi, C. S. Bhatia, *Appl. Phys. Lett.* **2014**, *104*, 253903.
[116] J. Jhaveri, S. Avasthi, G. Man, W. E. McClain, K. Nagamatsu, A. Kahn, J. Schwartz, J. C. Sturm, in *Photovolt. Spec. Conf. PVSC 2013 IEEE 39th*, **2013**, pp. 3292–3296.
[117] Y. Wan, J. Bullock, A. Cuevas, *Sol. Energy Mater. Sol. Cells* **2015**, *142*, 42.
[118] T. G. Allen, A. Cuevas, *Appl. Phys. Lett.* **2014**, *105*, 031601.
[119] S. Smit, D. Garcia-Alonso, S. Bordihn, M. S. Hanssen, W. M. M. Kessels, *Sol. Energy Mater. Sol. Cells* **2014**, *120, Part A*, 376.
[120] A. K. Ghosh, C. Fishman, T. Feng, *J. Appl. Phys.* **1978**, *49*, 3490.
[121] H. Kobayashi, H. Mori, T. Ishida, Y. Nakato, *J. Appl. Phys.* **1995**, *77*, 1301.
[122] J. Bullock, M. Hettick, J. Geissbühler, A. J. Ong, T. Allen, C. M. Sutter-Fella, T. Chen, H. Ota, E. W. Schaler, S. De Wolf, C. Ballif, A. Cuevas, A. Javey, *Nat. Energy* **2016**, 15031.
[123] S. Avasthi, W. E. McClain, G. Man, A. Kahn, J. Schwartz, J. C. Sturm, *Appl. Phys. Lett.* **2013**, *102*, DOI http://dx.doi.org/10.1063/1.4803446.
[124] K. A. Nagamatsu, S. Avasthi, G. Sahasrabudhe, G. Man, J. Jhaveri, A. H. Berg, J. Schwartz, A. Kahn, S. Wagner, J. C. Sturm, *Appl. Phys. Lett.* **2015**, *106*.
[125] X. Yang, K. Weber, in *Photovolt. Spec. Conf. PVSC 2015 IEEE 42nd*, **2015**, pp. 1–4.
[126] C. Battaglia, X. Yin, M. Zheng, I. D. Sharp, T. Chen, S. McDonnell, A. Azcatl, C. Carraro, B. Ma, R. Maboudian, R. M. Wallace, A. Javey, *Nano Lett.* **2014**, *14*, 967.
[127] J. Bullock, A. Cuevas, T. Allen, C. Battaglia, *Appl. Phys. Lett.* **2014**, *105*, DOI http://dx.doi.org/10.1063/1.4903467.
[128] Z. Liang, M. Su, Y. Zhou, L. Gong, C. Zhao, K. Chen, F. Xie, W. Zhang, J. Chen, P. Liu, W. Xie, *Phys Chem Chem Phys* **2015**, *17*, 27409.
[129] B. Macco, M. F. J. Vos, N. F. W. Thissen, A. A. Bol, W. M. M. Kessels, *Phys. Status Solidi RRL – Rapid Res. Lett.* **2015**, *9*, 393.
[130] M. Bivour, J. Temmler, H. Steinkemper, M. Hermle, *Sol. Energy Mater. Sol. Cells* **2015**.

[131] J. Bullock, D. Yan, A. Cuevas, Y. Wan, C. Samundsett, *Energy Procedia* **2015**, *77*, 446.
[132] L. G. Gerling, S. Mahato, A. Morales-Vilches, G. Masmitja, P. Ortega, C. Voz, R. Alcubilla, J. Puigdollers, *Sol. Energy Mater. Sol. Cells* **2016**, *145, Part 2*, 109.
[133] H.-D. Um, N. Kim, K. Lee, I. Hwang, J. H. Seo, K. Seo, *Nano Lett.* **2016**, *16*, 981.
[134] J. Meyer, S. Hamwi, M. Kroger, W. Kowalsky, T. Riedl, A. Kahn, *Adv. Mater.* **2012**, *24*, 5408.
[135] J. Bullock, C. Samundsett, A. Cuevas, D. Yan, Y. Wan, T. Allen, *Photovolt. IEEE J. Of* **2015**, *5*, 1591.
[136] L. S. Hung, C. W. Tang, M. G. Mason, *Appl. Phys. Lett.* **1997**, *70*, 152.
[137] Y. Zhang, R. Liu, S.-T. Lee, B. Sun, *Appl. Phys. Lett.* **2014**, *104*.
[138] F.-H. Hsu, N.-F. Wang, Y.-Z. Tsai, C.-Y. Wu, Y.-S. Cheng, M.-H. Chien, M.-P. Houng, *Thin Solid Films* **2014**, *573*, 159.
[139] D. Xu, X. Yu, L. Zuo, D. Yang, *RSC Adv.* **2015**, *5*, 46480.
[140] Y. Zhang, W. Cui, Y. Zhu, F. Zu, L. Liao, S.-T. Lee, B. Sun, *Energy Env. Sci* **2015**, *8*, 297.
[141] Y. Wan, C. Samundsett, J. Bullock, D. Yan, T. Allen, P. Zheng, X. Zhang, J. Cui, J. McKeon, A. Cuevas, in *Submitt. 43rd IEEE PVSC*, Portland, Oregon, **2016**.
[142] X. Zhang, C. Xie, J. Jie, X. Zhang, Y. Wu, W. Zhang, *J Mater Chem A* **2013**, *1*, 6593.
[143] M. Ono, Z. Tang, R. Ishikawa, T. Gotou, K. Ueno, H. Shirai, *Appl. Phys. Express* **2012**, *5*, 032301.
[144] E. Shi, L. Zhang, Z. Li, P. Li, Y. Shang, Y. Jia, J. Wei, K. Wang, H. Zhu, D. Wu, S. Zhang, A. Cao, *Sci. Rep.* **2012**, *2*, DOI 10.1038/srep00884.
[145] P. Yu, C.-Y. Tsai, J.-K. Chang, C.-C. Lai, P.-H. Chen, Y.-C. Lai, P.-T. Tsai, M.-C. Li, H.-T. Pan, Y.-Y. Huang, C.-I. Wu, Y.-L. Chueh, S.-W. Chen, C.-H. Du, S.-F. Horng, H.-F. Meng, *ACS Nano* **2013**, *7*, 10780.
[146] D. Zielke, A. Pazidis, F. Werner, J. Schmidt, *Sol. Energy Mater. Sol. Cells* **2014**, *131*, 110.
[147] D. Zielke, C. Niehaves, W. Lövenich, A. Elschner, M. Hörteis, J. Schmidt, *Energy Procedia* **2015**, *77*, 331.
[148] L. He, C. Jiang, Rusli, D. Lai, H. Wang, *Appl. Phys. Lett.* **2011**, *99*, 021104.

1.6 Thesis outline

The work in this thesis is primarily centred on the conceptual and experimental development of a number of different carrier-selective heterocontact systems for *c*-Si solar cells. The majority of the experimental work is conducted at the contact level and, in the cases where these contacts showed excellent potential, they were further developed at the cell level. This thesis is formatted in the Australian National University's *Thesis by Compilation* style. Each chapter contains a brief introduction to the subtopic, followed by a compilation of first author papers relevant this subtopic. A brief outline of the thesis chapters is provided below.

Chapter 1 explores the concept of carrier-selectivity, outlining different strategies for separating carriers and the relative benefits and shortcomings of such approaches. It also includes a general review of the literature in this field of research.

Chapter 2 focuses on the application of thin interlayers to enhance the selectivity of phosphorus and boron diffused regions in *c*-Si solar cells. These 'hybrid' contact systems implement SiO_x, AlO_x and *a*-Si:H interlayers to assist in surface passivation. The investigation proceeds from relatively straightforward approaches, which show moderate performance improvements, to a completely novel approach—the *a*-Si:H enhanced MIS contact—which leads to large improvements. The latter is then successfully implemented as a rear contact of 21% efficient solar cell with a simple architecture. The papers that compose this part of the thesis are:

- James Bullock, Di Yan, and Andrés Cuevas, "*Passivation of aluminum–n^+silicon contacts for solar cells by ultrathin Al_2O_3 and SiO_2 dielectric layers*", Physica Status Solidi: Rapid Research Letters, 7, No. 11, 946–949, 2013.
- James Bullock, Di Yan, Yimao Wan, Andres Cuevas, Benedicte Demaurex, Aïcha Hessler-Wyser and Stefaan De Wolf, "*Amorphous silicon passivated contacts for diffused junction silicon* solar cells", Journal of Applied Physics, 115, 163703, 2014.

- James Bullock, Di Yan, Andres Cuevas, Benedicte Demaurex, Aïcha Hessler-Wyser and Stefaan De Wolf, "*Amorphous Silicon Enhanced Metal-Insulator-Semiconductor Contacts for Silicon Solar Cells*", Journal of Applied Physics, 116, 163706, 2014
- James Bullock, Andres Cuevas, Christian Samundsett, Di Yan, Josephine McKeon and Yimao Wan, "*Simple silicon solar cells featuring an a-Si:H enhanced rear MIS contact*", Solar Energy Materials and Solar Cells, Volume 138, Pages 22–25, 2015.

Chapter 3 explores the use of molybdenum oxide MoO_x based hole contacts to lightly doped n- and p-type *c*-Si. The benefits of using this material in *c*-Si solar cells has only recently been realised, and detailed characterisation of the contact and recombination properties of this interface is necessary to assess its real potential. After an initial characterisation of its general applicability to *c*-Si solar cells, MoO_x based hole contacts are trialled in both simple full-area contact devices and more sophisticated cells with partial rear contacts. The papers presented in this part of the thesis are:

- James Bullock, Andres Cuevas, Thomas G. Allen, Corsin Battaglia, "*Molybdenum Oxide MoO_x: A Versatile Hole Contact For Silicon Solar Cells*" Applied Physics Letters, 105, 232109, 2014.
- James Bullock, Di Yan, Andres Cuevas, Yimao Wan and Christian Samundsett, "*n- and p-type silicon solar cells with molybdenum oxide hole contacts*" Energy Procedia, Volume 77, Pages 446–450, 2015.
- James Bullock, Christian Samundsett, Andrés Cuevas, Di Yan, Yimao Wan and Thomas Allen, "*Proof-of-concept p-type silicon solar cells with molybdenum oxide partial rear contacts*" IEEE Journal of Photovoltaics, vol. 5, no. 6, 2015.

Chapter 4 examines the use of alkali metal salt interlayers for electron contacts to n and p-type *c*-Si. In particular, the use of LiF_x to form low resistance contacts to lightly doped n-type *c*-Si is demonstrated in a first-of-its-kind n-type partial rear contact cell–without the need for a phosphorus diffusion. In the final section of this chapter a novel *a*-Si:H / LiF_x / Al heterocontact is developed and combined with a MoO_x based hole contact

to fabricate a high-efficiency dopant-free *c*-Si solar cell. The papers presented in this part of the thesis are:

- James Bullock**,** Peiting Zheng, Quentin Jeangros, Mahmut Tosun, Mark Hettick, Carolin Sutter-Fella, Yimao Wan, Thomas Allen, Di Yan, Daniel Macdonald, Stefaan De Wolf, Aïcha Hessler-Wyser, Andres Cuevas, Ali Javey, "*Lithium fluoride based electron contacts for high efficiency n-type crystalline silicon solar cells"*, Submitted, 2016.
- James Bullock Mark Hettick, Jonas Geissbühler, Alison J. Ong, Thomas Allen, Carolin M. Sutter-Fella, Teresa Chen, Hiroki Ota, Ethan W. Schaler, Stefaan De Wolf, Christophe Ballif, Andrés Cuevas and Ali Javey, "*Efficient c-Si solar cells with* d*opant-free asymmetric heterocontacts"*, Nature Energy, 2, 15031, 2016

Chapter 5 summarises the main achievements and findings of this thesis and suggests some future areas of research.

2. Electron and hole selective contacts on highly doped surface regions

2.1 Foreword

Given the current dominance of dopant-diffused approaches within the *c*-Si photovoltaic community, a sensible initial stepping stone is to develop enhanced contact systems in conjunction with light diffusions having optimised dopant profiles. In these 'hybrid' systems carrier-selectivity is achieved collectively via doping in the near-surface region and by passivating the contact interface, combining the benefits of both approaches. Such a technique has the potential to de-emphasise the required trade-off between the contacted and non-contacted regions when choosing an appropriate dopant profile, owing to the lower recombination occurring at the contact interface. This introduces obvious benefits for improving efficiency and process simplicity.

In this chapter a number of such systems are developed for collecting either electrons or holes. Among the alternatives, the *a*-Si:H enhanced MIS structure developed on lightly phosphorus diffused surfaces shows superior contact characteristics and temperature stability. As such, in the final manuscript of this chapter, the *a*-Si:H enhanced MIS approach is applied at the cell level yielding a result of 21% – equivalent to a control high efficiency partial rear contact cell fabricated using a similar procedure. Given below is a brief summary of the different manuscripts in order of their appearance.

Manuscript 1: James Bullock, Di Yan, and Andrés Cuevas, "*Passivation of aluminium–n^+silicon contacts for solar cells by ultrathin Al_2O_3 and SiO_2 dielectric layers*", Physica Status Solidi: Rapid Research Letters, 7, No. 11, 946–949, 2013.

This paper documents the development of AlO_x and SiO_x based MIS contacts for phosphorus diffused surfaces. Optimum thicknesses of 22 and 16 Å are found, resulting in ρ_c (mΩcm^2) / J_{0c} (fA/cm^2) combinations of 0.2 / 300 and 2.5 / 600 when applied to ~100 Ω/□ phosphorus diffusions for the AlO_x and SiO_x insulators respectively. Such contacts could result in an increase in open circuit voltage of approximately 15 mV when applied to solar cells.

Manuscript 2: James Bullock, Di Yan, Yimao Wan, Andres Cuevas, Benedicte Demaurex, Aïcha Hessler-Wyser and Stefaan De Wolf, *"Amorphous silicon passivated contacts for diffused junction silicon solar cells"*, Journal of Applied Physics, 115, 163703, 2014.

In this manuscript, *a*-Si:H passivating interlayers are trialled on both boron and phosphorus diffused surfaces as an alternative to conventional MIS structures, which typically use wide energy bandgap insulators. This approach permits thicker interlayer films before the ρ_c increases excessively, due to the relatively small band offsets between *a*-Si:H and *c*-Si. These thicker layers allow dramatic reductions in the surface recombination, with J_{0c} values of 40 and 100 fA/cm^2 attainable on phosphorus and boron diffused regions (including Auger recombination in the bulk of those regions). These are achieved whilst maintaining ρ_c values suitable for full-area contacts. Nevertheless, to avoid interaction between the *a*-Si:H and the overlying metal layer a strict low temperature procedure is required.

Manuscript 3: James Bullock, Di Yan, Andres Cuevas, Benedicte Demaurex, Aïcha Hessler-Wyser and Stefaan De Wolf, *"Amorphous Silicon Enhanced Metal-Insulator-Semiconductor Contacts for Silicon Solar Cells"*, Journal of Applied Physics, 116, 163706, 2014

This paper details the development of a novel method for improving the performance of conventional MIS contacts. This methodology benefits from knowledge gained in the two previous manuscripts. To enhance the performance of *c*-Si(n^+) / SiO_x / Al and *c*-Si(p^+) / AlO_x / Al MIS contacts, *a*-Si:H interlayers are inserted between the insulator and metal layers. This addition provides a source of hydrogen to improve the passivation at the *c*-Si / insulator interface. Following interface passivation, the *a*-Si:H layer is dissolved into the metal to reduce the ρ_c to a value applicable to solar cells. For the *a*-Si:H enhanced *c*-Si(n^+) / SiO_x / Al contact a J_{0c} value of 40 fA/cm^2 is achieved in combination with a ρ_c value of ~3 mΩcm^2. The obtained J_{0c} value is only marginally higher than that of the Auger recombination in the diffused region indicating a very small surface recombination contribution. For the enhanced *c*-Si(p^+) / AlO_x / Al MIS contacts a less impressive improvement to 160 fA/cm^2 and ~28 mΩcm^2 is obtained. Transmission / scanning transmission electron microscopy (TEM/STEM) and energy dispersive x-ray (EDX) spectroscopy are used to show the evolution of the contact formation with annealing. Stability at temperatures up to 350°C is also demonstrated for the electron contact. A complementary first author manuscript is included in the *Appendix: Additional first author manuscripts*, which provides further detail on the optimisation of this contact system. It is omitted here for the sake of brevity (James Bullock, Di Yan, Andres Cuevas, Benedicte Demaurex, Aïcha Hessler-Wyser and Stefaan De Wolf, "*Passivated Contacts to n^+ and p^+ Silicon Based on Amorphous Silicon and Thin Dielectrics*", IEEE Photovoltaic Specialist Conference, 2014.)

Manuscript 4: James Bullock, Andres Cuevas, Christian Samundsett, Di Yan, Josephine McKeon and Yimao Wan, *"Simple silicon solar cells featuring an a-Si:H enhanced rear MIS contact"*, Solar Energy Materials and Solar Cells, Volume 138, Pages 22–25, 2015.

The final paper of this chapter details the integration of the *a*-Si:H enhanced *c*-Si(n^+) / SiO_x / Al MIS structure as a rear contact in an n-type cell. The champion cell in this proof-of-concept structure attains a conversion efficiency of 21%. This result is found to be comparable to a standard n-type cell with partial rear contacts fabricated using a very similar procedure (aside from the rear contact). The equivalence of results, given the significantly simpler procedure required for the *a*-Si:H enhanced MIS cell, highlights the potential of such an approach as an alternative to the partial rear contact. Secondary studies conducted on this cell structure are also included in the appendix section of this thesis.

2.2 First author manuscripts

Passivation of aluminium–n$^+$ silicon contacts for solar cells by ultrathin Al_2O_3 and SiO_2 dielectric layers

James Bullock, Di Yan, and Andrés Cuevas

Research School of Engineering, The Australian National University, Canberra, ACT 0200, Australia

Published in: Physica Status Solidi: Rapid Research Letters

Ultra-thin thermally grown SiO_2 and atomic-layer-deposited (ALD) Al_2O_3 films are trialled as passivating dielectrics for metal-insulator-semiconductor (MIS) type contacts on top of phosphorus diffused regions applicable to high efficiency silicon solar cells. An investigation of the optimum insulator thickness in terms of contact recombination factor J_{0_cont} and contact resistivity ρ_c is undertaken on 85 and 103 Ω/□ diffusions. An optimum ALD Al_2O_3 thickness of ~22 Å produces a J_{0_cont} of ~300 fA/cm^2 whilst maintaining a ρ_c lower than 1 mΩcm^2 for the 103 Ω/□ diffusion. This has the potential to improve the open circuit voltage by a maximum 15 mV. The thermally grown SiO_2 fails to achieve equivalently low J_{0_cont} values but exhibits greater thermal stability, resulting in slight improvements in ρ_c when annealed for 10 minutes at 300 °C without significant changes in J_{0_cont}. The after anneal J_{0_cont} reaches ~600 fAcm^{-2} with a ρ_c of ~2.5 mΩcm^2 for the 85 Ω/□ diffusion amounting to a maximum gain in open circuit voltage of 6 mV.

Introduction The metal-silicon interface, required to contact diffused junction silicon solar cells, is known to host a large density of defects within the silicon band gap. These defects promote carrier recombination – an undesirable characteristic for this device. This issue is typically mitigated by employing deep dopant profiles that reduce the surface minority carrier concentration, which in this case is the limiting factor of surface recombination. However, at the same time, the high majority carrier concentration resultant from the dopant profile causes increased Auger recombination. Hence, the lowest achievable metal-contacted diffused region recombination factor J_{0_cont} is ~350 fA/cm^2 for both phosphorus and boron diffusions, and slightly higher for aluminium alloyed p$^+$ regions [1]. To combat these large recombination factors, high efficiency solar cell architectures implement contact fractions of less than 5% and apply passivating dielectric films to the remainder of the surface. The non-contacted regions benefit from lighter diffusions, especially on the sunward side, introducing the need for a compromise between the two regions, contacted and passivated, in terms of dopant profile. This compromise is sometimes circumvented by applying the deep diffusions only locally under the contacts allowing the remainder of the surface to be lightly diffused. The fabrication of this architecture requires alignment of deep dopant diffusions and metallised regions, a complex process to be industrially implemented. A possible improvement is to passivate the metallised surface regions with an ultra-thin dielectric, allowing a lighter (either local or global) dopant diffusion to be used. This dielectric must be sufficiently thin to present negligible resistance to current flow (possibly via quantum mechanical tunnelling) whilst being thick enough to provide appreciable surface passivation. The same ultra-thin layer can be applied to the entire wafer surface with a capping layer applied in the non-metallised regions [2–4]. The application of an ultra-thin dielectric under the contact, commonly referred to as a metal-insulator-semiconductor

(MIS) type contact, has been implemented by research teams in the past. Green *et al.* used a thermally grown ~1.5 nm SiO_2 layer in their metal-insulator n^+p (MINP) type solar cells in the early 80's [5]. Later, Jäger-Hezel *et al.* [6] and Metz *et al.* [7] applied similar thermal oxide structures to their solar cells (a practice that has continued at ISFH [4]). More recently, the Angstrom level of control and excellent surface passivation afforded by atomic-layer-deposited (ALD) Al_2O_3 has been trialled as MIS contacts, both with oxygen plasma [2, 3] and water [8] as oxidising precursors. This Letter presents an investigation of the optimum dielectric thickness and potential benefit of applying MIS contacts to conventional diffused junction silicon solar cells. The recombination factor of the contacted phosphorus diffused region J_{0_cont} and the contact resistivity ρ_c are investigated as the two metrics of importance. Whilst a detailed solar cell simulation is required to analyse the effect of simultaneously altering J_{0_cont} and ρ_c, it can be taken as a general rule that ρ_c will not significantly contribute to the series resistance of most solar cells unless it exceeds ~1 mΩcm^2. At this resistivity a high efficiency front-side metallisation scheme with a 5% fraction will produce a contact resistance R_c of ~40 mΩcm^2 – accounting for ~5% of typical series resistance values.

Thermally grown SiO_2 and thermal ALD Al_2O_3 are trialled as potential dielectrics. Evaporated aluminium, recently shown to be compatible with industrial production [9], is used as the metal in all cases.

Experimental Symmetrical lifetime test structures were prepared using high resistivity 100 Ωcm, (100) oriented, float zone, p-type silicon wafers with a starting thickness of 500 ± 25 μm. The wafers were subjected to a two minute alkaline saw damage etch followed by surface polishing in a HF:HNO_3 solution. Following an RCA clean, the samples were diffused (~800 °C) using $POCl_3$ and driven-in (~950 °C) in a dedicated quartz furnace, producing a sheet resistance of ~50 ± 5 Ω/□. The resultant dopant profile was measured using an electrochemical capacitance voltage profiler (WEP, CVP21) and is shown in Fig. 1. Dopant profiles were then etched back to one of the two points indicated in Fig. 1 using an alkaline etch. The resultant attributes of the two final dopant profiles are detailed in Table 1. At this point samples were coated (on both sides) with varying thicknesses of either ALD Al_2O_3 or thermal SiO_2. The Al_2O_3 was deposited

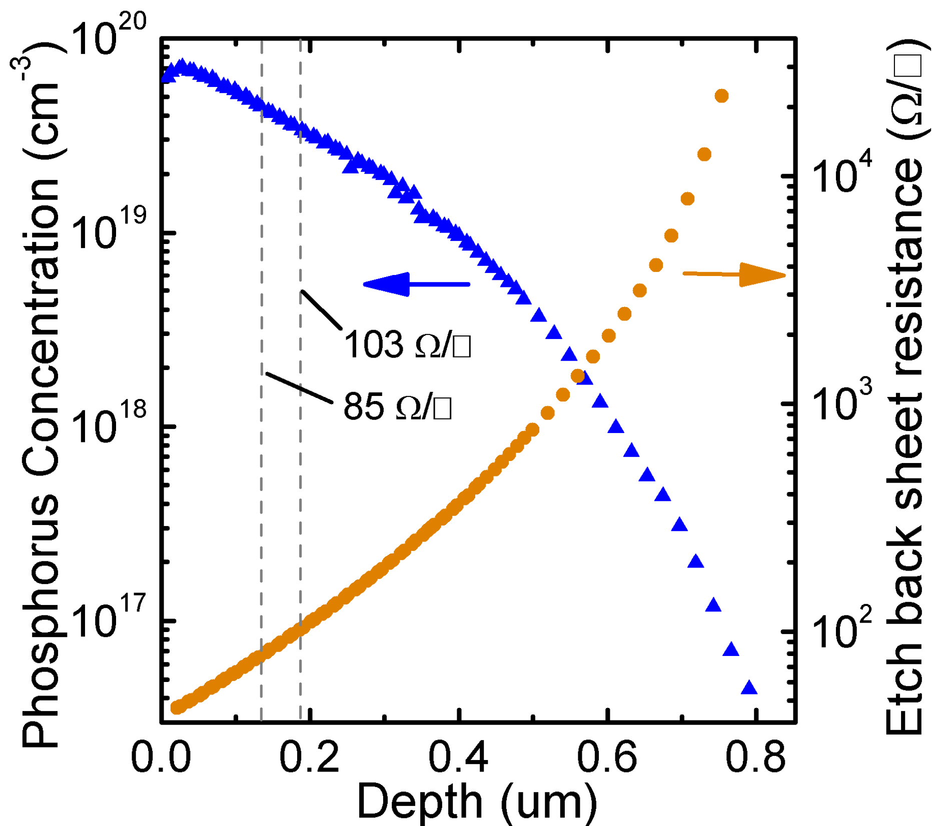

Figure 1 Electrically active phosphorus diffusion profile and associated sheet resistance against diffusion depth. Sheet resistance calculation utilises a model for mobility [10].

at ~200 °C (Beneq TFS200 ALD) using trimethylaluminium and water as alternating precursors. Purge and pulse times were chosen to ensure a self-limiting reaction. No post-deposition anneal was performed on ALD Al_2O_3 coated samples prior to measurement. The thermal SiO_2 dielectrics were grown at 500 °C in O_2. All samples received an RCA clean and HF dip immediately prior to deposition or growth to ensure that native oxides were minimised. A thin (~10 nm) aluminium layer was evaporated on top of the thin passivating layers (on both sides). The thin metal layer replicates the surface condition of the passivated contact, whilst remaining sufficiently thin to allow light through, so that the photoconductance (PC) method can be used. PC measurements of the injection-dependent effective carrier lifetime τ_{eff} were taken with a Sinton WCT 120 instrument, using both the transient and quasi-steady-state (QSS) modes. Recombination factors representative of contact region $J_{_cont}$ were extracted using the Kane and Swanston method, at an injection level ten times that of the base doping, with an intrinsic carrier concentration at 25 °C of $n_i = 8.95\times10^9$ cm^{-3}. Passivated recombination factors J_{0_pass} for the two diffusions sets were measured by depositing ~70 nm of plasma-enhanced-chemical-vapour-deposited (PECVD) SiN_x (Roth & Rau AK 400) – a dielectric known to achieve excellent passivation of n^+ surfaces [11]. The metallised recombination factors J_{0_metal} were obtained by measuring samples with metal directly deposited on the bare silicon surface. These values are included in Table 1.

Table 1 Characteristics of the etched-back n^+ diffusion profiles.

R_{sh} (Ω/□)	N_{surf} (cm^{-3})	x_j (µm)	J_{0_metal} (fAcm^{-2})	J_{0_pass} (fAcm^{-2})
85 ± 5	4(±1)×10^{19}	0.68	1050	55
103 ± 5	3(±1)×10^{19}	0.61	1250	45

* R_{sh} sheet resistance, N_{surf} surface phosphorus concentration, x_j approximate junction depth, J_{0_metal} recombination factor of metallised n^+ region, J_{0_pass} recombination factor of passivated n^+ region.

Transfer length method (TLM) samples were fabricated in an identical manner to the symmetrical lifetime samples described above up until the deposition of passivation layers. At this stage one side of the wafers were coated with passivating dielectrics, following which 1 µm of aluminium was evaporated. A TLM pattern was defined using photolithography and aluminium etching to achieve pad spacings between 10 and 300 µm. Current–voltage measurements were made using a Keithley 2425 Source Meter at 21±3 °C. ρ_c was obtained from an extrapolation of resistance versus pad spacing as described in Ref. [12]. The linear fit used in this extraction consistently produced R^2 statistics of at least 0.99.

Film thickness measurement samples were prepared using single-side mechanically-polished silicon wafers. Due to the dependence of SiO_2 growth on surface dopant concentration, phosphorus diffusion was performed on the SiO_2 thickness samples prior to film growth. Reflectance spectra were obtained using a variable angle ellipsometer (J.A. Woollam M-2000) after growth or deposition of thin passivating films on the polished sides. Indexed optical constants (provided by the device software) for Al_2O_3 and SiO_2 films were used to fit thicknesses.

Results and discussion J_{0_cont} and ρ_c as a function of dielectric thickness for the ALD Al_2O_3 series are shown in Fig. 2. These results were obtained by varying the total number of ALD cycles between 1 and 35. Thickness measurements of samples with 15 to 25 cycles revealed an approximately linear growth rate of ~1.0 Å/cycle which was assumed to be the growth rate for all thicknesses.

For dielectric thicknesses between 1 and 10 Å the J_{0_cont} measurements of both the 85 and 103 Ω/□ were seen to decline only slightly, staying roughly equivalent to directly metallised surfaces. The contact resistivity in this region also remained relatively

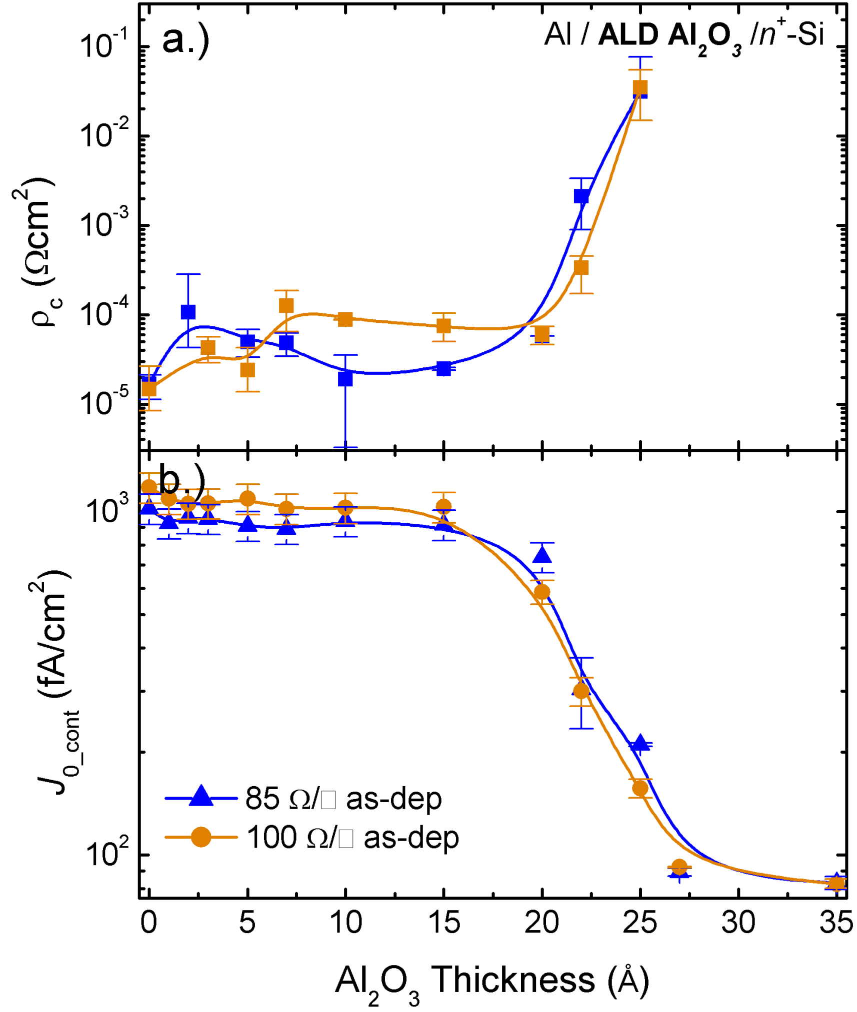

Figure 2 (a) Contact resistivity and (b) contact recombination factor of the ALD Al_2O_3 MIS contacts as a function of the Al_2O_3 thickness. Lines provide a guide to the eyes only. Error bars are based off the measured spread of data and the estimated error of the measurement.

constant. A sharp decrease in J_{0_cont} was observed between 15 and 27 Å for both diffusions, following which J_{0_cont} saturated at ~85 fAcm^{-2}– a low value given the ~3 nm thickness of the layer. The fully passivated (i.e. 70 nm PECVD SiN_x, no metal evaporation) recombination factors were found to be only 30–40 fAcm^{-2} lower (see Table 1). As no post-deposition anneal was used before metallisation it is possible that the negative fixed charge typically associated with ALD Al_2O_3, which may cause increased surface recombination on n^+ Si, is absent or weak. This thickness range also results in a dramatic increase in ρ_c by three orders of magnitude, in agreement with previous observations of

Loozen *et al.* [8]. After 25 Å current-voltage measurements revealed non-linear behaviour and the ρ_c could no longer be extracted accurately. A slight lag between the decreasing J_{0_cont} and increasing ρ_c results in an optimum dielectric thickness of ~22 Å. At this thickness a J_{0_cont}/ρ_c combination of 304 fAcm^{-2}/2 mΩcm^2 is achieved on the 85 Ω/□ diffusion, and 300 fAcm^{-2}/0.3 mΩcm^2 on the 103 Ω/□ diffusion. A significant improvement in surface passivation following the aluminium metal evaporation was observed; the precise nature of this improvement is not yet understood and is the subject of on-going research.

An upper-limit estimate of open circuit voltage gain ΔV_{oc} (relative to the purely metallised surface) as a result of implementing MIS contacts can be calculated, ignoring other sources of recombination and assuming a 5% contacted fraction, according to

$$\Delta V_{oc} = V_t \ln\left(\frac{0.05\times J_{0_metal}+0.95\times J_{0_pass}}{0.05\times J_{0_cont}+0.95\times J_{0_pass}}\right), \qquad (1)$$

where V_t represents the thermal voltage. Using this analysis Al_2O_3 MIS contacts could increase the V_{oc} by up to 15 mV.

To investigate the MIS contact thermal stability both TLM and effective lifetime samples were subjected to a 10 minute, 300 °C, forming gas anneal (FGA). This treatment resulted in a large increase in J_{0_cont} to a level just below the fully metallised surface (not shown). This increase could potentially be explained by either aluminium 'spiking' through the ultra-thin Al_2O_3 or the establishment of a substantial negative fixed charge density leading to increased surface recombination. A large decrease in ρ_c was not seen after thermal treatment, suggesting that significant aluminium spiking has not occurred.

Whilst a similar V_{oc} gain is predicted, both the optimum Al_2O_3 thickness and temperature instability of the MIS contacts outlined above are at odds with cell-level results presented by Zielke *et al.* [2, 3], who found an optimum thickness at 2.4 Å and

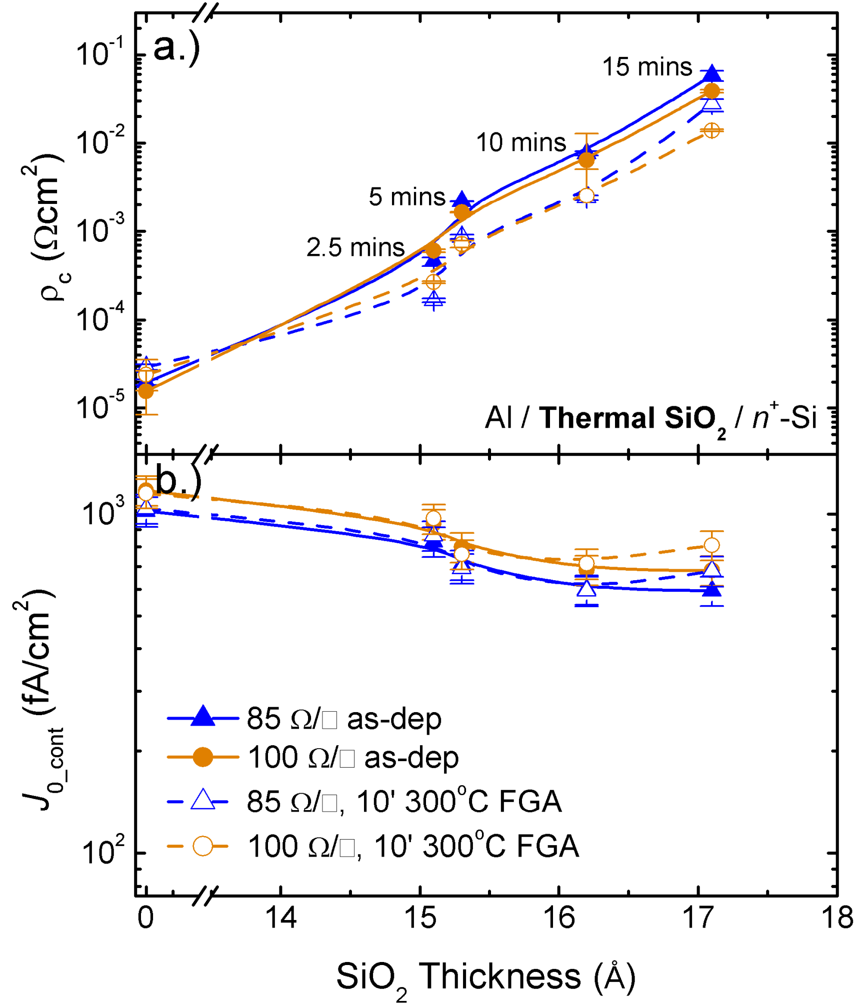

Figure 3 (a) Contact resistivity and (b) Contact recombination factor of the thermal SiO_2 MIS contacts as a function of the SiO_2 thickness. Error bars and lines are based off the same assumptions as in Fig. 2.

improved passivation with annealing. These inconsistencies may be partially explained by differences in the ALD oxidising precursor and surface texturing. A longer time interval between HF dip and ALD deposition could also lead to variation in results due to a thicker native oxide (particularly on an n^+ surface).

Figure 3 provides the J_{0_cont} and ρ_c trends for the SiO_2 passivated contact with increasing SiO_2 thickness. The SiO_2 layers were grown by dry thermal oxidation at 500 °C for 2.5, 5, 10 or 15 minutes. Polished samples, subjected to the same oxidation conditions with the same phosphorus surface concentration, were measured to have thicknesses in the 14–18 Å range. It is inherent, given the small thicknesses and short oxidation times,

that these extracted thicknesses are subject to a significant uncertainty. Again a decrease in J_{0_cont} is seen with increasing insulator thickness, although not to the same degree – the lowest recombination factors were ~595 fAcm^{-2} for the 85 Ω/□ diffusion and 680 fAcm^{-2} for the 103 Ω/□ diffusion. A corresponding increase in ρ_c is seen in the same thickness range. An estimated optimum combination for high efficiency cells is found at an oxide thickness of ~16 Å (10-minute oxidation). At this thickness a J_{0_cont}/ρ_c combination of 600 fAcm^{-2}/7 mΩcm^2 is achieved on the 85 Ω/□ diffusion and 685 fAcm^{-2}/6 mΩcm^2 on the 103 Ω/□ diffusion.

The SiO_2 MIS contact was found to have a greater thermal stability than the Al_2O_3 one. After a 10 minute 300 °C FGA contact resistivity values were more than halved to ~2.5 mΩcm^2 whilst J_{0_cont} remained relatively constant resulting in upper-limit V_{oc} gains of up to 6 mV. This suggests that the aluminium–SiO_2–silicon MIS contact is compatible with cell fabrication procedures that implement thermal processes (eg. PECVD SiN_x) after contact formation, as aluminium spiking is prevented, in alignment with previously published results [4, 6].

It is worth noting that the Al_2O_3 and SiO_2 passivated contacts demonstrated here could also be applied uniformly to the n^+ rear side of a p^+nn^+ solar cell. In that case, the tolerable contact resistivity for a 100% metal contact fraction is far higher than a partial metal grid. The presented results suggest a total rear J_{0_cont} of ~200 fAcm^{-2} could be achieved using a ~2.5 nm Al_2O_3 layer.

Conclusions In this letter we have investigated the contact properties of Al_2O_3 and SiO_2 passivating dielectrics in MIS type contacts on phosphorus diffused regions. In both cases an increasing dielectric thickness leads to a reduction in surface recombination and is accompanied by an increase in contact resistivity. Optimum thicknesses of ALD Al_2O_3 and thermal SiO_2 were found to be ~22 Å and ~16 Å respectively.

The aluminium–Al_2O_3–silicon MIS contacts show an optimum J_{0_pass}/J_{0_cont} combination of 45/300 fAcm^{-2} on a 103 Ω/□ phosphorus diffusion, whilst maintaining a contact resistivity of 0.3 mΩcm^2. This amounts to a maximum potential V_{oc} gain of 15 mV. These gains are found to diminish significantly after a 300 °C anneal. The aluminium–SiO_2–silicon MIS type contacts exhibit a lower maximum V_{oc} gain of 6 mV but greater thermal stability. An after anneal J_{0_pass}/J_{0_cont} combination of 55/600 fAcm^{-2} with a contact resistivity of 2.5 mΩcm^2 on an 85 Ω/□ phosphorus diffusion is achieved for this configuration.

Acknowledgements Financial support by The Australian Solar Institute/Australian Renewable Energy Agency and The Australian Research Council is gratefully acknowledged. Ellipsometer facilities at the Australian National Fabrication Facility were used in this work.

References

[1] R. Woehl et al., *IEEE Trans. Electron Devices* 58, 441 (2011).
[2] D. Zielke et al., *Phys. Status Solidi RRL* 5, 298 (2011).
[3] D. Zielke et al., *Proc. 26th EU PVSEC*, 2011, p. 1115.
[4] J. Schmidt et al., *Progr. Photovolt*. 16, 461 (2008).
[5] M. Green et al., *Proc. 15th IEEE PVSEC*, 1981, p. 1405.
[6] K. Jäger-Hezel et al., *Proc. 13th EU PVSEC*, 1995, p. 1515.
[7] A. Metz et al., *Proc. 26th IEEE PVSEC*, 1997, p. 283.
[8] X. Loozen et al., *Energy Procedia 21*, 75, (2012).
[9] J. Nekarda et al., *Proc. 34th IEEE PVSEC*, 2009, p. 892.
[10] D.B.M. Klaassen, *Solid-State Electron*. 35, 953 (1992).
[11] M. Kerr et al., *J. Appl. Phys*. 89, 3821 (2001).
[12] D.K. Schroder, *Semiconductor Material and Device Characterisation* (Wiley, 2006), p.146

Amorphous silicon passivated contacts for diffused junction silicon solar cells

J. Bullock,[1,a)] D. Yan,[1] Y. Wan,[1] A. Cuevas,[1] B. Demaurex,[2] A. Hessler-Wyser[2] and S. De Wolf[2]

[1]Research School of Engineering, The Australian National University, Canberra, ACT 0200, Australia.

[2]Ecole Polytechnique Fédérale de Lausanne (EPFL), Institute of micro engineering (IMT), Photovoltaics and Thin Film Electronic Laboratory, Maladière 71, CH-200 Neuchâtel, Switzerland.

Published in Journal of Applied Physics

Carrier recombination at the metal contacts is a major obstacle in the development of high-performance crystalline silicon homojunction solar cells. To address this issue, we insert thin intrinsic hydrogenated amorphous silicon [a-Si:H(i)] passivating films between the dopant-diffused silicon surface and aluminum contacts. We find that with increasing a-Si:H(i) interlayer thickness (from 0 to 16 nm) the recombination loss at metal-contacted phosphorus (n^+) and boron (p^+) diffused surfaces decreases by factors of ~25 and ~10, respectively. Conversely, the contact resistivity increases in both cases before saturating to still acceptable values of ~ 50 mΩcm^2 for n^+ and ~ 100 mΩcm^2 for p^+ surfaces. Carrier transport towards the contacts likely occurs by a combination of carrier tunneling and aluminum spiking through the a-Si:H(i) layer, as supported by scanning transmission electron microscopy - energy dispersive x-ray (STEM-EDX) maps. We explain the superior contact selectivity obtained on n^+ surfaces by more favorable band offsets and capture cross section ratios of recombination centers at the c-Si / a-Si:H(i) interface.

Introduction High-efficiency homojunction silicon solar cells have reached a point in their development where carrier recombination at the metal-silicon contact has a significant and sometimes limiting effect on device performance. This is commonly evidenced by relatively low open-circuit voltage values, compared to e.g. silicon-heterojunction (SHJ) solar cells, which do not apply metal directly to the crystalline silicon absorber.[1] This issue has spawned much research in the area of "contact passivation".[2-6]

On homojunction solar cells, contact passivation can be achieved by inserting a thin dielectric interlayer that physically displaces the metal from the crystalline silicon (*c*-Si) surface, in a metal–insulator–semiconductor (MIS) type configuration. This was initially applied at the device level using thermally grown SiO_2,[2] and has more recently been trialed with atomic-layer-deposited Al_2O_3.[3] A modification of this approach is to replace the metal with heavily-doped poly-silicon, or another conductive over-layer, which further improves the selectivity of the contact.[4,5] The efficacy of the MIS type contact scheme is reliant on film-thickness control at the monolayer-level, as a delicate trade-off between increasing contact resistance and decreasing interface recombination exists for both SiO_2 and Al_2O_3.[6] This is directly linked to the wide bandgap of the dielectrics trialed so far, and presents a significant challenge for industrial implementation.

In this article, we propose the use of intrinsic hydrogenated amorphous silicon (*a*-Si:H(*i*)) as an alternative interlayer. This film has a lower bandgap than the previously mentioned dielectrics, and hence may offer a weaker dependence of the contact resistance on thickness. In addition, such films have silicon surface passivation properties on par with the best dielectrics. Both properties are already successfully exploited in the intrinsic buffer layers used in SHJ solar cells, yielding conversion efficiencies as high as 24.7 %,

to date.[7] As with most device structures containing *a*-Si:H(*i*), a strong restriction on the temperature of processing is required, as annealing may irreversibly deteriorate the microstructure and passivation properties of the films. The presence of doped over-layers and metals may place even greater restrictions on the thermal processing of the device. Doped over-layers can lower the defect-creation energy,[8] while many metals induce crystallisation and protrude through *a*-Si:H(*i*) at low temperatures.[9] In particular, the application of aluminum directly to *a*-Si:H(*i*), as is the case in this study, remains a contentious combination in the context of solar cells.[9-11]

The applicability of the *a*-Si:H(*i*) contact interlayer is trialed here on both boron (p^+) and phosphorus (n^+) diffused surfaces, usually employed as the hole and electron collecting regions in traditional silicon solar cells. A simplified representation of the equilibrium energy band diagram of the structures tested in this study is provided in Figure 1. Identical *a*-Si:H(*i*)/Al stacks are used for the boron and phosphorus contacts. The contact resistivity ρ_c and the recombination parameter of the metal-contacted dopant diffusions J_{0c} are taken as the two metrics of importance, where low values are desired for both. The results are examined in terms of increasing *a*-Si:H(*i*) interlayer thickness in an effort to find an optimum value. Scanning transmission electron microscopy (STEM) is used in conjunction with energy dispersive x-ray (EDX) mapping to investigate the nature of the interfaces and the conduction mechanisms.

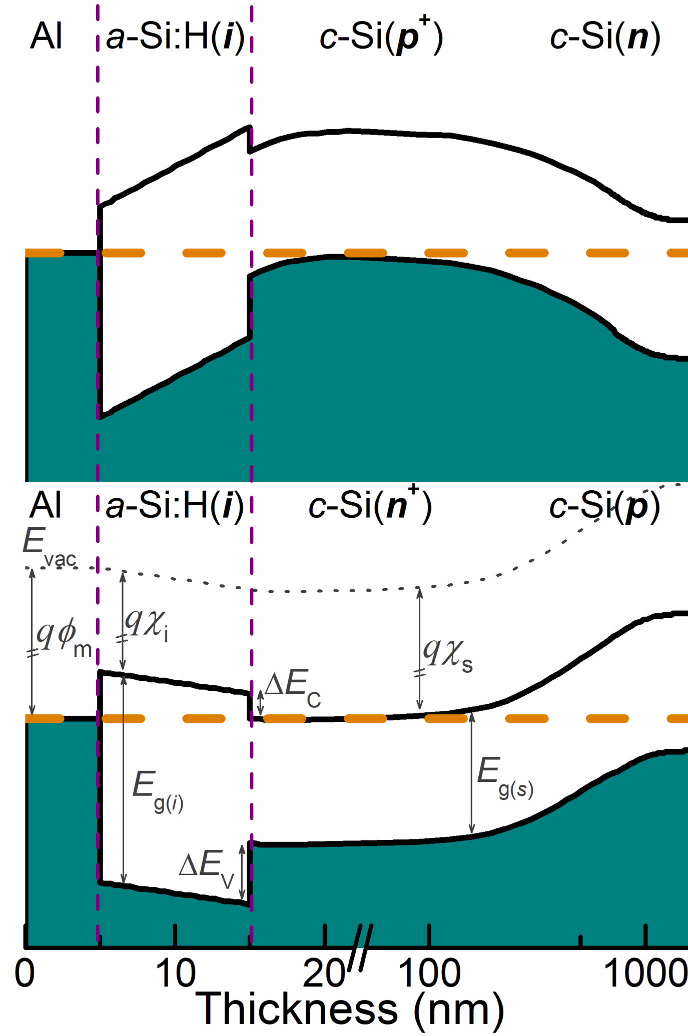

Figure 1. Simplified equilibrium energy band diagrams representative of the hole-selective (top figure) and electron-selective (bottom figure) structures investigated in this study, as simulated by AFORS-HET.[12] Assumed values; Al work function ϕ_m (4.23 V), *a*-Si:H(*i*) electron affinity χ_i (3.8 V), *c*-Si electron affinity χ_s (4.05 V), *a*-Si:H(*i*) mobility band gap $E_{g(i)}$ (1.82 eV),[13] *c*-Si band gap $E_{g(s)}$ (1.12 eV), *a*-Si:H(*i*)/ *c*-Si valence band offset ΔE_V (0.45 eV) and *a*-Si:H(*i*)/ *c*-Si conduction band offset ΔE_C (0.25 eV). [13]

Experimental Methods

Sample preparation Symmetrical test structures were prepared using high resistivity (> 100 Ωcm), (100), FZ, p and n-type silicon wafers. The high resistivity of these wafers simplifies the extraction of recombination parameters. They were subjected to a 2 minute alkaline saw damage etch and their surfaces were chemically polished in a HF:HNO_3 solution. Following a standard RCA clean, the samples were diffused symmetrically in dedicated clean quartz furnaces using a $POCl_3$ source (on p-type wafers) or a BBr_3 source (on n-type wafers) so that in all cases the doping of the substrate and

diffusion were of opposite polarity. Two diffusion recipes were used for each source, the phosphorus diffused samples underwent a further short etch-back process to reduce the surface dopant concentration. The resultant final attributes of the four diffusion sets are given in Table I.

Following another RCA clean, each of the diffusion sets was deposited symmetrically with thicknesses of *a*-Si:H(*i*), in the range of 1–16 nm, using an Oxford PlasmaLab 100 plasma-enhanced-chemical-vapor-deposition (PECVD) instrument. The wafer temperature during deposition was estimated to be ~350°C, which is uncharacteristically high for *a*-Si:H(*i*). At this temperature epitaxial growth of silicon is expected leading to poor quality surface passivation.[14] Despite this, we found this temperature to provide optimum passivation in the as-deposited state, suggesting that no epitaxial growth has occurred. At this point samples were further separated into two groups to be developed into symmetrical lifetime structures (for assessing the contact recombination) or transfer-length-method (TLM) structures (for assessing the contact resistivity).

The lifetime test structures were coated with aluminum on both sides in a vacuum thermal deposition system to a thickness of < 15 nm, which is sufficiently thin to allow light through for photoconductance decay (PCD) measurements to be taken. PCD measurements were performed using a Sinton WCT 120 instrument under both transient and quasi-steady-state modes. The recombination current parameters J_{0c} of the *c*-Si(n^+) / *a*-Si:H(*i*) / Al and *c*-Si(p^+) / *a*-Si:H(*i*) / Al stacks were extracted from the PCD data using an intrinsic carrier concentration of n_i = 8.95×10^9 cm^{-3} (at 25°C) and the well-known Kane and Swanson method.[15] The parameter J_{0c} is a representation of the total minority carrier recombination occurring in the sub-surface diffusion region (predominantly Auger

recombination) and at the diffused surface (predominantly Shockley Read Hall recombination).

Transfer length method (TLM) structures were created by evaporating ~1µm of aluminum onto the *a*-Si:H(*i*) passivated p^+ and n^+ surfaces. Contact pads were photolithograpically defined and isolated using an acidic aluminum etch. A 15 minute 110°C anneal is required to hard-bake the photoresist before the acidic etching. Current – voltage measurements were performed (Keithley 2425 Source Meter) at ~ 297 K on pad spacings in the range of 10–300 µm and ρ_c was extracted as per the description given in Ref. 16. As a point of clarification, in this study the measured ρ_c reflects the average of both bias directions (implicit in TLM), where the resistivity in each direction comprises the resistance through the *a*-Si:H(*i*) as well as across the *a*-Si:H(*i*)/Al and *c*-Si/ *a*-Si:H(*i*) interfaces. It was also assumed that the parallel sheet conductance between pads through the *a*-Si:H(*i*) layer is negligible.

Reference recombination parameters. Included in Table I as a reference are the measured recombination parameters for diffusions covered by either only a metal film (J_{0_metal}) or a high-quality passivation film without a metal over-layer (J_{0_pass}). A thin aluminum layer (< 15 nm) is used to create the directly metallized surface. The high-quality passivation films consisted of ~ 20 nm of plasma-assisted atomic-layer-deposited (PA-ALD) Al_2O_3 (Beneq TFS, 200 ALD instrument) on the boron-diffused surfaces and ~ 75 nm of PECVD *a*-SiN_x:H (Roth & Rau AK 400) on the phosphorus surfaces. The large positive fixed charge density in *a*-SiN_x:H and negative fixed-charge density in Al_2O_3 reduce the minority carrier concentrations at the n^+ and p^+ *c*-Si surfaces, respectively, which results in very low surface recombination even for moderate interface state densities. In comparison, *a*-Si:H(*i*) films exhibit no strong fixed charge, but achieve

a very effective reduction of the density of interface states ($< 10^9$ cm^{-3}),[17] making them ideal candidates for the passivation of both n$^+$ and p$^+$ surfaces.

Given the high quality of passivation obtained by the Al_2O_3 and a-SiN_x:H layers, the J_{0_pass} values provided in Table I can be viewed as an approximate upper-limit for the recombination occurring in the subsurface diffused regions, which is mostly due to the Auger process.

Table I. Dopant diffusion characteristics and recombination parameter of the four diffusion sets

Source	R_{sh} (Ω/□)	N_{surf} (cm^{-3})	J_{0_metal} (fA/cm^2)	J_{0_pass} (fA/cm^2)
$POCl_3$	85 ±5	4(±1)×10^{19}	1050 ±200	55 ±5
$POCl_3$	110 ±10	3(±1)×10^{19}	1200 ±200	41 ±5
BBr_3	110 ±10	1(±1)×10^{19}	1370 ±200	27 ±5
BBr_3	170 ±15	1(±1)×10^{19}	1900 ±200	15 ±5

* R_{sh} sheet resistance, N_{surf} surface phosphorus concentration, J_{0_metal} recombination parameter of metallised n$^+$ region, J_{0_pass} recombination parameter of passivated n$^+$ region.

Photoluminescence analysis. Inherent in the analysis to follow is the assumption that lifetime test structures (aluminum thickness < 15 nm) produce the same carrier recombination as actual (passivated) metal contacts, such as those present in the TLM test structures (aluminum thickness of ~ 1 µm). To verify this assumption a photoluminescence (PL) analysis (BT Imaging LIS-R1) was performed on two symmetrically diffused (n$^+$) and passivated samples with ~ 15 and ~ 30 nm of a-Si:H(i). On the rear side of the two samples, half of the area was evaporated with thin (< 15 nm) and the other half with thick (1 µm) aluminum. Both samples were annealed at 110ºC for 15 minutes before imaging. PL images were taken (rear side down) using a set illumination intensity with and without a short-pass filter of 1000 nm. The images taken without the filter are representative of a broader wavelength range and include longer wavelengths which have a penetration depth greater than the thickness of the wafer. It is therefore expected that the region with the thicker aluminum (greater rear side reflection)

will appear brighter, provided differences in carrier recombination are not significant. The image taken with the filter in place includes only wavelengths with penetration lengths significantly less than the thickness of the wafer – hence if there are no differences in carrier recombination, there should be no visible difference between the thick and thin metal regions. Figure 2 shows the two sets of PL images taken of the same region with and without a short-pass filter, where brighter colours represent a higher PL signal and thus longer effective carrier lifetime. In all cases the above behavior is followed, demonstrating that there are no major differences in carrier recombination between the thin and thick metallisation schemes.

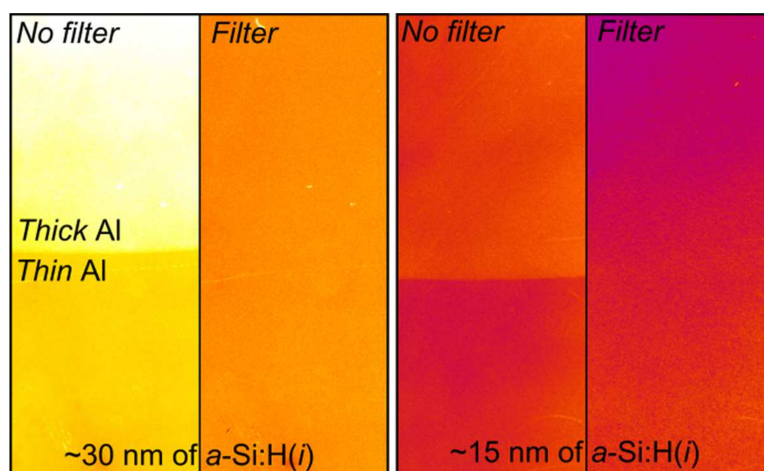

Figure 2. PL images of samples with ~ 30 and ~ 15 nm of *a*-Si:H(*i*) taken with and without a short-pass filter. Without a filter images reveal different rear reflection. With a filter the influence of rear reflection is removed, and the images indicate similar surface recombination for the two thicknesses of aluminum. All four images are scaled individually to highlight contrasts across the imaged region.

Ellipsometry and transmission electron microscopy measurements.

During all *a*-Si:H(*i*) depositions, a single side, mechanically polished wafer was included to monitor film thickness. Reflectance spectra of these samples were measured using a J.A Woolam M-2000 variable angle ellipsometer and thicknesses were obtained using a Tauc-Lorentz material model.[18]

STEM samples were also prepared from single-side mechanically polished wafers. These were deposited with ~ 28 nm of *a*-Si:H(*i*) and ~ 1 μm of aluminum following which they were annealed at 110ºC for 15 minutes. TEM lamellae were prepared by mechanical polishing in a wedge-shape configuration with a Tripod polisher then ion milling with Ar ions (Gatan PIPS). The preparation sequence before imaging required a temperature step at ~130ºC for over 30 minutes. An FEI Tecnai Osiris instrument was used to take bright field (BF) STEM micrographs and high sensitivity EDX maps of aluminum, silicon and oxygen.

Results and Discussion

Interface passivation. The recombination current parameter J_{0c} as a function of *a*-Si:H(*i*) thickness is shown for the two phosphorus diffusions in Figure 3a and for the two boron diffusions in Figure 3b. The quality of the as-deposited surface passivation on the phosphorus diffusion improves dramatically with *a*-Si:H(*i*) thickness and appears to saturate in the 6–8 nm range, consistent with open circuit voltage V_{oc} trends for SHJ solar cells reported in the literature.[19] Beyond these thicknesses excellent passivation is achieved, producing recombination parameter even lower (by about 10 fA/cm^2) than the PECVD *a*-SiN$_x$:H controls listed in Table I, inferring that this value is a more appropriate upper-limit representation of recombination within the bulk of the phosphorus diffusion. An alike sample (not shown) deposited with ~ 30 nm of *a*-Si:H(*i*) produces an identical J_{0c} to that at 10 nm confirming that the passivation is saturated. Whilst an expected slight difference in the magnitude of recombination between the 85 and 110 Ω/□ n$^+$ diffusions is seen, the general behaviour of both n$^+$ diffusions can be well represented by a single trendline, adding to the confidence in the measured results.

Following metallisation a significant increase in J_{0c} was observed for *a*-Si:H(*i*) thicknesses below 10 nm. The spread in measured data and uncertainty in determining J_{0c} values also greatly increase in this region, as indicated by the large error bars in Figure 3. Whilst there were some small increases in recombination evident for samples with *a*-Si:H(*i*) thicknesses above 10 nm, the J_{0c} values remained close to the corresponding pre-metallisation values. To provide a direct comparison to the TLM structures some of the metallised n^+ symmetrical lifetime samples were annealed for 15 minutes at 110ºC as shown in Figure 3a. It can be seen that whilst some additional increase in recombination is caused by the anneal, excellent passivation is still achievable for *a*-Si:H(*i*) thicknesses above 10 nm.

There are four foreseeable causes for the increase in J_{0c} when a metal overlayer is present: *i*) penetration of the *c*-Si minority carrier wavefunctions through the *a*-Si:H(*i*) film to the *a*-Si:H(*i*)/Al interface, where rapid recombination is possible;[20] *ii*) the onset of depletion conditions at the heavily diffused *c*-Si surfaces again caused by the aluminum work function, resulting in a change the recombination statistics at the *c*-Si surface;[21,22] *iii)* a lowering of the Fermi-level within the *a*-Si:H(*i*) film by the aluminum work function, potentially leading to a lower defect formation enthalpy in the *a*-Si:H(*i*) film,[8] or *iv*) partial protrusion of the aluminum through the *a*-Si:H(*i*), possibly making contact with the *c*-Si surface.[9] A low temperature interaction between aluminum and *a*-Si:H(*i*) has been outlined in many previous studies,[9-11] some of which suggest that conditions experienced during aluminum vacuum depositions are sufficient to initiate this interaction. Below we confirm that indeed some aluminum spiking has occurred.

The boron diffused samples in Figure 3b show a more gradual improvement in as-deposited passivation with *a*-Si:H(*i*) thickness and do not achieve as good a level of passivation as the controls listed in Table I. Under these deposition conditions an

additional sample (not shown) with an *a*-Si:H(*i*) thickness of ~ 30 nm produced a recombination parameter of ~70 fA/cm^2 for both p$^+$ diffusions, considerably lower than the 15 nm samples but still well above the controls listed in Table I. Avoiding a post-deposition anneal was a central premise of this work, hence the deposition conditions were chosen to provide the highest as-deposited *a*-Si:H(*i*) passivation. However, in a separate study we have found that the passivation provided by thicker *a*-Si:H(*i*) films (> 12 nm) improved upon annealing, presumably due to a reduction in D_{it} from additional hydrogenation; Therefore lower J_{0c} may be attainable if a re-optimisation of the *a*-Si:H(*i*) films based on annealing was performed. Following metallisation J_{0c} improved for *a*-Si:H(*i*) thicknesses greater than 10 nm, possibly due to a small annealing effect during the thermal evaporation of aluminum. Further annealing at 110°C for 15 minutes resulted in no further improvement, rather in increases in J_{0c}. The higher surface recombination evident on the p$^+$ surface relative to the n$^+$ is potentially due to *c*-Si / *a*-Si:H(*i*) interface defects exhibiting an electron to hole capture cross section area ratio (σ_n/σ_p) greater than unity.[23]

Contact resistivity. The specific contact resistivity ρ_c for the phosphorus and boron diffusions as a function of *a*-Si:H(*i*) thickness are provided in Figure 3c and d respectively. For the phosphorus diffusion the dependence of ρ_c on the thickness of the *a*-Si:H(*i*) interlayer can be separated into two regimes; an approximately exponential increase for the first 10 nm followed by a plateauing of ρ_c. This behavior appears to be largely independent of the underlying doping, as both the 85 and 100 Ω/□ diffusions yield similar trends.

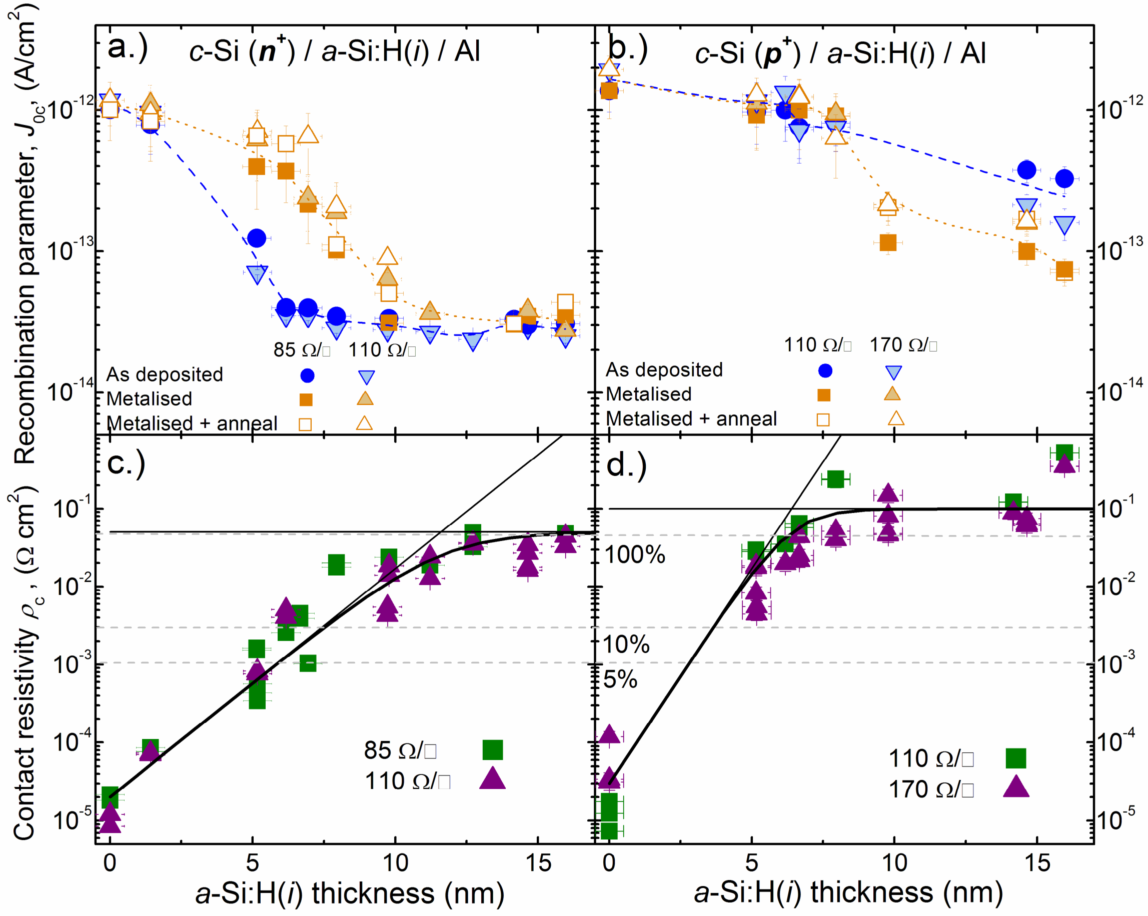

Figure 3. Contact recombination parameter J_{0c} for (a) phosphorus and (b) boron diffused surfaces and contact resistivity ρ_c for (c) phosphorus and (d) boron diffused surfaces as a function of *a*-Si:H(*i*) thickness. The dotted blue and orange lines provide a guide to the eye for the as-deposited (blue) and metallised (orange) results. The dashed lines represent reference values for contacts with a total contact resistance R_c of ~0.05 Ωcm², having areas of respectively 5, 10 and 100% of the wafer surface (see Section III. E). Error bars are based on the measured spread in data or the estimated error of the measurement (whichever was largest).

Both boron-diffused surfaces exhibit a steeper initial increase in ρ_c and plateau at a higher value relative to the n^+ surfaces. A potential explanation for the higher ρ_c on p^+ surfaces may be found in the well-known asymmetry between the conduction and valence band offsets at the *c*-Si / *a*-Si:H(*i*) interface.[13] These offsets contribute to effective barriers for electron and hole transport at the *c*-Si surface, as depicted in Figure 1. A significantly smaller conduction band offset, as compared to the valence band offset has been reported by many studies at this interface which suggest a greater conductivity across the interface for electrons (in n^+ silicon) than holes (in p^+).[13] Studies of window layers in SHJ solar cells equally pointed out that the valence-band offset may hinder efficient hole transport

through passivation stacks.[24] An additional possible explanation is the formation of a large energy barrier at the p^+ *c*-Si surface caused by the low work function of aluminum.[21] An alike barrier forming on the n^+ surface would be smaller owing to a higher *c*-Si surface concentration (compared to the p^+ contact) and a smaller difference between the n^+ *c*-Si Fermi energy and the Al work function.

Structural composition of the layers. STEM-EDX analysis of the contact stack, presented in Figure 4, were taken to better understand the interfacial uniformity and conduction mechanisms. Figure 4a shows the bright field STEM image of a *c*-Si / *a*-Si:H(*i*) / Al (1 µm). Note that the *a*-Si:H(*i*) film was made intentionally thicker (~ 28 nm) than the lifetime and TLM samples for characterisation purposes. Uniform surfaces are seen at both the *c*-Si / *a*-Si:H(*i*) and the *a*-Si:H(*i*) / polycrystalline Al interfaces. As opposed to the polycrystalline Al layer, an absence of diffraction contrast in the *a*-Si:H(*i*) layers suggests that it remains in an amorphous state. The dark line at the *c*-Si / *a*-Si:H(*i*) interface is believed to be a measurement artifact rather than an interfacial species. Figures 4b, c and d provide 2D EDX maps of the local O, Al and Si concentration through the entire depth of the sample (> 100 nm), for the same region as shown in Figure 4a. Figure 4b reveals that both interfaces host a thin unintentional oxide layer, the thicker of which is between Al and *a*-Si:H(*i*) films. The thin oxide at the *c*-Si / *a*-Si:H(*i*) interface may assist in maintaining amorphous growth during the high-temperature deposition, similar to the use of silicon-oxide deposition to prevent epitaxial film growth.[25] Local hemispherical protrusions can be seen originating from the aluminum layer in Figure 4c (which maps the Al concentration), suggesting partial spiking of the Al through the *a*-Si:H(*i*) film, which is supported by corresponding regions of lower silicon concentration in Figure 4d. The higher temperature procedure (130ºC) used for the STEM samples

designate the obtained images as upper-limit representations of the aluminum spiking occurring in the TLM and lifetime samples.

Conduction mechanisms. A lower limit protrusion depth of ~ 20 nm can be estimated from the cross sectional images, implying that direct contact is most likely made to the *c*-Si surface for all thicknesses of *a*-Si:H(*i*) tested in the present study. These findings suggest that some conduction is achieved through a nano-scale partial contact structure. However, this conduction mechanism is unlikely to fully explain the thickness dependent ρ_c behavior observed for both the n^+ and p^+ surfaces. Instead, the results for ρ_c against *a*-Si:H(*i*) thickness suggest that the total conduction is the consequence of both direct contact through the aluminum protrusions, which has no strong dependence with interlayer thickness in the range of 0–15 nm, and a second parallel conduction mechanism with an exponential dependence on *a*-Si:H(*i*) thickness as illustrated in Figure 3. A candidate for the second mechanism, supported also in the literature,[26] is quantum-mechanical tunneling through the *a*-Si:H(*i*) layer; other conduction mechanisms, such as thermionic emission could not easily explain this trend. Starting from very thin *a*-Si:H(*i*) interlayers, a tunneling conduction mechanism could initially dominate the total conduction. The conductivity through this pathway would be expected to exponentially decrease (resistivity would exponentially increase) with increasing *a*-Si:H(*i*) interlayer thickness. At thicknesses of approximately 8 nm, the tunneling current becomes smaller than the direct conduction pathway through the aluminum protrusions, which dominates at thicknesses above this point, explaining the plateauing of ρ_c. It is expected that for *a*-Si:H(*i*) thicknesses greater than the protrusion depth (outside the measured range) the resistivity would be again higher.

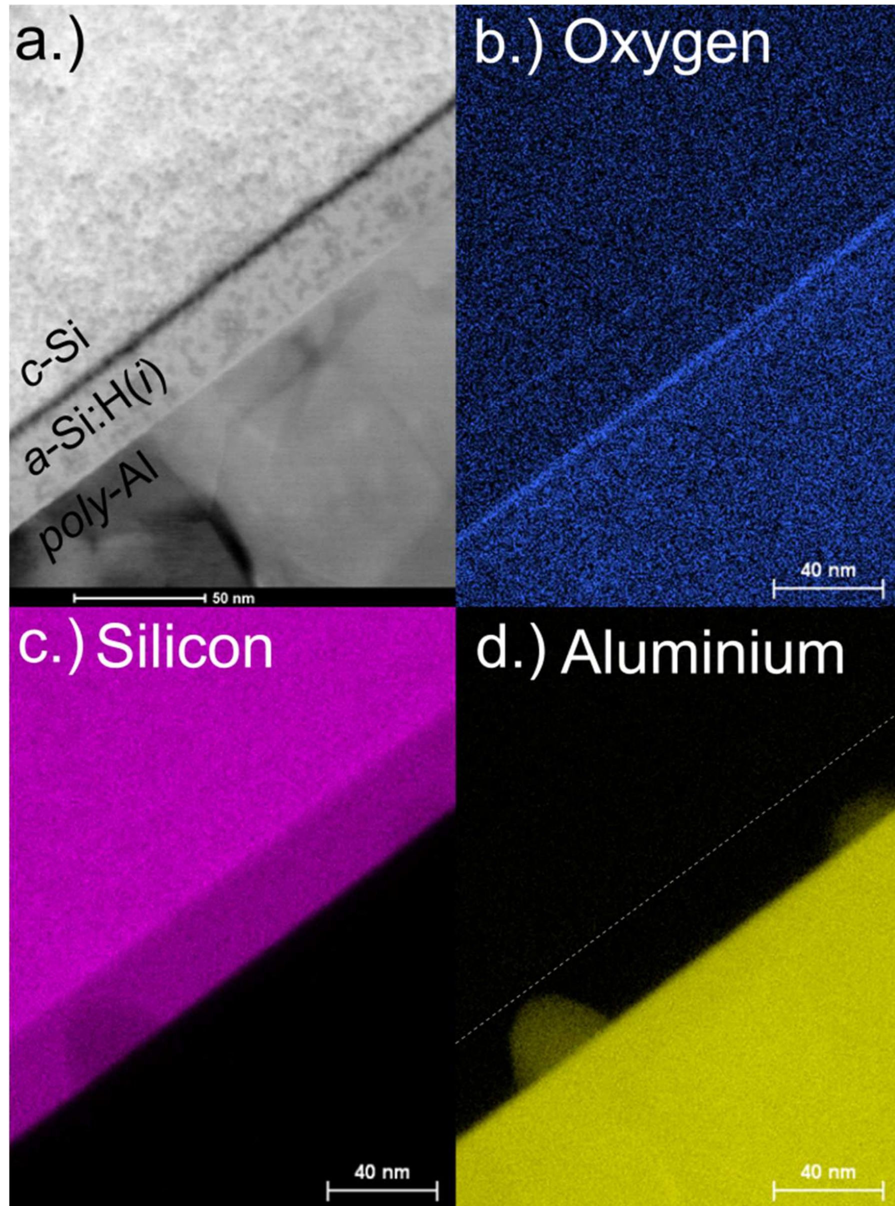

Figure 4. (a) Bright field STEM image of the *c*-Si / *a*-Si:H(*i*) / Al stack. EDX maps of the same region for (b) Oxygen, (c) Silicon and (d) Aluminum. The white dashed line in (d) represents the position of the *c*-Si / *a*-Si:H(*i*)

In an effort to quantify the above suggestion of two parallel conduction pathways, the ρ_c trends in Figure 3c and d were each fitted with the inverse sum of two functions. One is a constant independent of thickness $\rho_{c1}(t) = c$, representative of spiking conduction; and the other function is exponentially dependent on the thickness $\rho_{c2}(t) = a \exp(bt)$, representative of tunneling conduction. The second function $\rho_{c2}(t)$, can

be compared to an approximate analytical expression for the inverse of the tunneling transmission coefficient T through a rectangular potential barrier given by[27]

$$\frac{1}{T(t)} = \exp\left(2t\sqrt{\frac{2m^*_{(e,h)}q\Phi_{eff\,(C,V)}}{\hbar^2}}\right) \propto \rho_c(t)\,, \tag{1}$$

where ρ_c is inversely proportional to the tunneling transmission coefficient T. $m^*_{(e,h)}$ is the tunneling effective electron or hole mass within the a-Si:H(i) layer, $\hbar$ is the reduced Plank constant, q is the elementary charge and $\Phi_{eff(C,V)}$ is the effective barrier presented to conduction band electrons or valence band holes.

By equating the exponents of the modelled contact resistivity $\rho_{c2}(t)$ and Equation (1) it is possible to check if, as stated in Section III.B, the differences in slope observed for the $\rho_c(t)$ trends of the n^+ and p^+ contacts can be accounted for by differences in valence and conduction band offsets. The ratio of the fitted constants b of the p^+ and n^+ contact structures can be related to terms in Equation (1) by,

$$\left(\frac{b^2_{p+}}{b^2_{n+}} = 3.5\right) \approx \frac{m^*_h\Phi_{eff\,(V)}}{m^*_e\Phi_{eff\,(C)}}, \tag{2}$$

which is measured to be 3.5 in the present work. From trusted values in the literature presented in Figure 1, a $\Phi_{eff(C)}$ value of ~0.34 eV is calculated from the average height of the a-Si:H(i) conduction band above the c-Si conduction band. A similar analysis can be performed by comparison of the a-Si:H(i) and c-Si valence bands in Figure 1 to obtain a $\Phi_{eff(V)}$ value of ~ 0.92 eV. The values and validity of using electron and hole effective masses in a-Si:H(i) remain a contentious point,[28] however, if the assumption is made that the electron and hole effective masses are of a similar magnitude, then the calculated ratio in Equation 2 is ~2.7, comparing reasonably well with the measured value of 3.5.

Although the measured exponential dependence of resistivity on thickness strongly suggest that tunneling through the a-Si:H(i) is a contributing mechanism to

conduction, further studies are required to unequivocally confirm its role, given the complex nature of the contact and the aluminum – *a*-Si:H(*i*) interaction and the uncertainties in the band offsets and effective masses.

Consequences for solar cell performance. The above results demonstrate that whilst complete isolation of the aluminum and *c*-Si was not possible under these processing conditions, excellent contact characteristics were still achieved, particularly on the n^+ surface. Included in Figure 3c and d as an approximate guide are lines (horizontal dashed lines) indicating appropriate ρ_c values for 5%, 10% and 100% contact area, chosen in line with a total contact resistance R_c of 0.05 Ωcm^2. For the phosphorus diffused contacts in Figure 3c it can be seen that the ρ_c limit for both the 5% and 10% contact fractions is exceeded in the 5–7 nm range where J_{0c} values still exhibit high recombination of ~ 500 fA/cm^2. This situation can be improved by choosing full-area rear contacts, for which *a*-Si:H(*i*) thicknesses up to 15 nm are acceptable in terms of ρ_c. In this region J_{0c} values of ~ 40 fA/cm^2 are consistently attained for both 85 and 110 Ω/□ n^+ diffusions. Similarly, the boron diffused contacts in Figure 3d suggest that the optimum configuration is again a full area contact, however in this instance J_{0c} values in the 200–700 fA/cm^2 are to be expected – far higher than those on n^+ surfaces.

For an estimation of the V_{oc} gain attained by applying the n^+ contact to a solar cell we introduce a comparison full-area deep phosphorus back surface region which is known to have an optimum recombination parameter of ~ 300 fA/cm^2. Using the optimum post-metallisation J_{0c} value of ~ 40 fA/cm^2 (with ~ 14 nm of *a*-Si:H(*i*)) found in this study, an upper-limit V_{oc} gain of ~ 50 mV is calculated over an optimized full-area heavy phosphorus diffusion, using the method given in Ref 6. A similar analysis for the p^+ surface provides less impressive results.

In summary, the results detailed in this paper present a simple modification to conventional homojunction solar cells which attains a high level of contact passivation. However, the sensitivity of the contact characteristics to temperature presents a technological challenge in ensuring low temperature back-end processing. Values in the literature suggest severe increases in recombination would result from temperatures in the vicinity of 180ºC,[9] and indeed this study has shown that even temperatures as low as 110ºC will affect device performance. The use of other metals with a higher *a*-Si:H(*i*) interaction temperature or an overlying conductive buffer layer may prove beneficial in improving contact stability.

Conclusion. As an alternative to an MIS contact, *a*-Si:H(*i*) was trialed as a passivating interlayer between heavily diffused phosphorus / boron surfaces and aluminum. The contact resistivity and contact recombination parameter were monitored as a function of *a*-Si:H(*i*) thickness in order to find the optimum. For both n^+ and p^+ diffusions a full area rear contact is found to be a suitable practical application of the passivated contact scheme developed in this paper. Superior majority carrier conductivity and surface passivation was found for the *c*-Si (n^+) / *a*-Si:H(*i*) / Al contact with a ρ_c of < 0.05 Ωcm^2 and a J_{0c} of ~ 40 fA/cm^2 for *a*-Si:H(*i*) thicknesses in the 12–15 nm range. These values translate to an upper-limit V_{oc} gain of ~ 50 mV when compared to an optimised phosphorus back surface region. The *c*-Si (p^+) / *a*-Si:H(*i*) / Al contact failed to achieve as low resistivity and recombination results, a larger valence band offset and larger minority carrier capture cross section area of interface defects are possible causes for this difference. STEM EDX analysis reveals that small aluminum protrusions through the *a*-Si:H(*i*) layer may contact the *c*-Si directly, thus contributing to conduction. The exponential trend of contact resistivity on interlayer thickness suggests that quantum-

mechanical tunneling is a second conduction mechanism which dominates at lower *a*-Si:H(*i*) thicknesses.

Acknowledgements. The authors from the ANU acknowledge financial support by The Australian Solar Institute/Australian Renewable Energy Agency as well as access to equipment at the Australian National Fabrication Facility. The authors from EPFL thank the Axpo Naturstrom Fonds, the European Commission (FP7 project Hercules), the EuroTech Universities Alliance and the Swiss Commission for Technology and Innovation for their financial support. The authors thank Danièle Laub (EPFL) for the STEM sample preparation.

References

[1] S. De Wolf, A. Descoeudres, Z. C. Holman, and C. Ballif, *Green* 2, 7 (2012)

[2] M. A. Green, A. W. Blakers, M. R. Willison, T. Szpitalak, E. M. Keller, E. Gauja and P.J. Hart, *Proceedings of the 15th IEEE Photovoltaic Specialist Conference*, Kissimmee, USA, 1981, p. 1405

[3] D. Zielke, J. H. Petermann, F. Werner, B. Veith, R. Brendel and J.Schmidt, *Phys. Status Solidi RRL* 5, 298 (2011).

[4] P. Borden, L. Xu, B. McDougall, C.P. Chang, D. Pysch, P. Voisin and S. W. Glunz *Proceeding of the 23th European Photovoltaic Specialist Conference,* Valencia, Spain, 2008, p. 1149

[5] D. Garcia-Alonso, S. Smit, S. Bordihn and W. M. M. Kessels, *Semicond. Sci. Technol*. 28, 082002 (2013)

[6] J. Bullock, D. Yan and A. Cuevas, *Phys. Status Solidi RRL* 7, 946 (2013).

[7] M. Taguchi, A. Yano, S. Tohoda, K. Matsuyama, Y. Nakamura, T. Nishiwaki, K. Fujita and E. Maruyama, *IEEE J. Photovolt.* 4, 96 (2014).

[8] S. De Wolf and M. Kondo, *J. Appl. Phys*. 105, 103707 (2009)

[9] H. Plagwitz, M. Nerdling, N. Ott, H. P. Strunk and R. Brendal, *Prog. Photovolt: Res. Appl*. 12, 47 (2004)

[10] E Schmich, E. van Kershaver, K. Fisher and P. Basore, *Proceedings of the 28th European Photovoltaic Specialist Conference*, Paris, France, 2013, p. 1271

[11] T. F. Schulze, Ph.D Dissertation, Institut für Silizium-Photovoltaik E-I1, HZB, 2011

[12] R. Stangl, M. Kriegel, M. Schmidt, *Proceeding of the 4th World Conference on Photovoltaic Energy Conversion*, Hawaii, USA, 2006, p. 1350-1353

[13] T. F. Schulze, L. Korte, F. Ruske and B. Rech, *Phys. Rev. B*. 83, 165314 (2011)

[14] H. Fujiwara, and M. Kondo, *Appl. Phys. Lett*. 90, 013503 (2007)

[15] D.E. Kane and R. M. Swanson, *Proceedings of the 18th IEEE Photovoltaic Specialist Conference,* Las Vegas, USA, 1985, p. 578-583.

[16] D. K. Schroder, Semiconductor Material and Device Characterisation (Wiley, Hoboken, 2006), p. 146

[17] S. De Wolf, S. Olibet, and C. Ballif, *Appl. Phys. Lett*. 93, 032101 (2008)

[18] G. E. Jellison Jr. and F. A. Modine, *Appl. Phys. Lett*. 69, 371 (1996)

[19] M. Tanaka, M. Taguchi, T. Matsuyama, T. Sawada, S. Tsuda, S. Nakano, H. Hanafusa and Y. Kuwano, *Jpn. J. Appl. Phys*. 31, 3518 (1992)

[20] S. De Wolf and M. Kondo, *Appl. Phys. Lett.* 91, 112109 (2007)

[21] M. Bivour, C. Reichel, M. Hermle, S. W. Glunz, *Sol. Energ. Mat. Sol. Cells,* 106, 11 (2012)

[22] D. Munoz, T. Desrues, P.-J. Ribeyron, A. Orpella, I. Martin, C. Voz and R. Alubilla, *Phys. Status Solidi C* 7, 1029 (2010).

[23] A. Descoeudres, Z. C. Holman, L. Barraud, S. Morel, S. De Wolf, and C. Ballif, *IEEE J. Photovolt.* 3, 83 (2013).

[24] J.P. Seif, A. Descoeudres, M. Filipic, F. Smole, M. Topic, Z.C. Holman, S. De Wolf, and C. Ballif, *J. Appl. Phys.* 115, 024502 (2014)

[25] H. Fujiwara, T. Kaneko, and M. Kondo, *Appl. Phys. Lett*. 91, 133508 (2007)
[26] A. Kavevce and W. Metzger, *J. Appl. Phys*., 105, 094507 (2009)
[27] S. M. Sze and K. K. Ng, Physics of Semiconductor Devices (Wiley-Interscience, 2007) p.439
[28] R. A. Street, Hydrogenated Amorphous Silicon (Cambridge University Press, 2005) p.142-144

Amorphous Silicon Enhanced Metal-Insulator-Semiconductor Contacts for Silicon Solar Cells

J. Bullock,[1a.)] A. Cuevas,[1] D. Yan,[1] B. Demaurex,[2] A. Hessler-Wyser,[2] and S. De Wolf[2]

[1]Research School of Engineering, The Australian National University, Canberra, ACT 0200, Australia

[2]Ecole Polytechnique Fédérale de Lausanne (EPFL), Institute of micro engineering (IMT), Photovoltaics and Thin Film Electronic Laboratory (PVLab), Maladière 71b, CH-200 Neuchâtel, Switzerland

Published in Journal of Applied Physics

Carrier recombination at the metal-semiconductor contacts has become a significant obstacle to the further advancement of high-efficiency diffused-junction silicon solar cells. This paper provides the proof-of-concept of a procedure to reduce contact recombination by means of enhanced metal-insulator-silicon (MIS) structures. Lightly diffused n^+ and p^+ surfaces are passivated with SiO_2 / a-Si:H and Al_2O_3 / a-Si:H stacks, respectively, before the MIS contacts are formed by a thermally-activated alloying process between the a-Si:H layer and an overlying aluminum film. Transmission / scanning transmission electron microscopy (TEM/STEM) and energy dispersive x-ray (EDX) spectroscopy are used to ascertain the nature of the alloy. Idealized solar cell simulations reveal that MIS(n^+) contacts, with SiO_2 thicknesses of ~1.55 nm, achieve the best carrier-selectivity producing a contact resistivity ρ_c of ~3 mΩcm^2 and a recombination current density J_{0c} of ~40 fA/cm^2. These characteristics are shown to be stable at temperatures up to 350°C. The MIS(p^+) contacts fail to achieve equivalent results both in terms of thermal stability and contact characteristics but may still offer advantages over directly metallized contacts in terms of manufacturing simplicity.

Introduction High-efficiency solar cells require low carrier recombination at their surfaces to ensure high open-circuit and maximum power point voltages. In recent years, focused research into the electronic passivation of *c*-Si surfaces has resulted in the application of a wide range of high quality, industry applicable films for surface passivation, including SiO_2, SiN_x:H, Al_2O_3, *a*-Si:H and stacks of these materials. As a consequence, the issue of surface recombination in the non-contacted surface regions of solar cells has diminished in importance, and recombination in the metallized regions has become one of major limiting factors of high efficiency homojunction solar cells.

In principle, the reduction of recombination at the contact interface can be achieved by the insertion of a thin dielectric interlayer between the silicon surface and the contacting metal, known as a metal-insulator-semiconductor (MIS) structure. The contact resistivity of MIS structures is strongly sensitive to both the thickness and the electronic properties of the dielectric, necessitating very precise control [1]. A simplified theoretical figure-of-merit for comparing MIS contacts with different insulator types and thicknesses is given by [2, 3]

$$f = d\sqrt{m^*_{(e,h)}\Phi_{eff(C,V)}} \,. \quad (1)$$

Where d represents the insulator thickness, and $m^*_{(e,h)}$ and $\Phi_{eff(C,V)}$ are the tunneling effective mass of the collected carrier (electron or hole) and the effective barrier height presented to that carrier. A small value of the parameter f reflects a high tunneling probability and hence a lower contact resistivity. Also to be considered is the resistance presented by the dielectric layer to the other carrier, which should preferably be maximized. Hence an ideal dielectric film would present a low barrier and effective mass to one carrier and a large barrier and effective mass to the other. Unfortunately no such material has been demonstrated to have this attribute whilst simultaneously providing

significant surface passivation. Resultantly, SiO_2 [4-6] and Al_2O_3 [7-9] have typically been used as the dielectric interlayers, as their thicker counterparts (>100 Å) have been successfully implemented for surface passivation in the non-contacted regions. However, given the wide band-gap of these dielectrics and the resultant large barrier heights they present to electrons and holes in *c*-Si, tunnel-able layers are limited to a maximum thickness of ~25 Å in order to permit appreciable current flow. Achieving a high level of surface passivation with a 25 Å thick dielectric (or thinner) remains a difficult task, compromising the benefit of implementing this type of MIS contact.

It has been shown that capping of thin dielectrics (~10 Å) with silicon-based hydrogen-rich films can lead to dramatic improvements in surface passivation [10, 11]. The enhancement is often attributed to the diffusion of atomic hydrogen from the capping film to the *c*-Si / dielectric interface where it deactivates recombination centers. This suggests that plasma-enhanced-chemical-vapor-deposited (PECVD) hydrogenated amorphous silicon (*a*-Si:H), with its high hydrogen content (10 - 20 %) [12], could fulfill the requirements of a capping film.

A second interesting characteristic of *a*-Si:H is its low-temperature interaction with metals, specifically with aluminum [13]. At annealing temperatures well below the Al-Si eutectic temperature (577ºC) silicon will dissolve into aluminum in low concentrations [14]. The rate of dissolution is faster if the silicon is amorphous and faster still if the amorphous film has a high hydrogen concentration [15]. Once dissolved, the silicon atoms can diffuse through the aluminum and crystalize out at nucleation points (defects, surfaces, grain boundaries etc.), most likely with an aluminum doping concentration at the solubility limit [16, 17].

This paper provides a proof-of-concept of a simple procedure for achieving well-passivated MIS-type contacts using the above mentioned two characteristics of *a*-Si:H.

The complete contact structure consists of a lightly doped phosphorus (n^+) or boron (p^+) surface, followed by a tunneling dielectric layer, which is capped with intrinsic *a*-Si:H. Thin Al_2O_3 and SiO_2 layers are implemented as the tunneling dielectrics on p^+ and n^+ *c*-Si surfaces respectively. These combinations are chosen in line with previous results of low surface recombination, assisted at least in part by the accumulation of majority carriers at the surface by the fixed charge density of the Al_2O_3 and SiO_2 films. As the additional intrinsic *a*-Si:H layer presents an impediment to current flow, following deposition it is subsequently alloyed with an overlying aluminum film to create a high conductivity mixed-phase layer. The result is a contact structure that presents a contact resistivity ρ_c similar to that of conventional MIS contacts, together with a much lower recombination current J_{0c}, thanks to interface hydrogenation. Similar processes have previously been exploited for low temperature *pn* junction formation [17] and low resistance metal-silicon contacts (contact formation to *a*-Si:H passivated wafers by means of annealing, "COSIMA") [18]. It is also possible that the hydrogenation provided by the *a*-Si:H over layer could prove beneficial in the passivation of defects within the *c*-Si, for example boron oxygen defects [19] and laser damaged regions [20].

A crucial parameter in the success of the above described *a*-Si:H enhanced MIS contact is the annealing temperature – one must be chosen at which aluminum interacts with the *a*-Si:H but not with the underlying thin dielectric. For the Al / SiO_2 system, the maximum temperature of stability has been estimated to be in the 200-400°C range [21], whilst it is expected that the Al / Al_2O_3 interaction will initiate at lower temperatures [1]. The first part of this paper presents an optimization of the annealing temperature, complemented with transmission / scanning transmission electron microscopy (TEM/STEM) and energy dispersive x-ray (EDX) spectroscopy analysis of changes to the layer composition. Once the fabrication process of the contact system is developed,

the study proceeds to alter the thickness of the dielectric interlayer to find the best combination of contact characteristics.

The efficacy of the contact system, i.e. its selectivity towards electrons and holes, can be monitored by considering its resistive and carrier recombination properties. The contact resistivity ρ_c reflects the (undesired) resistance presented to the collected carrier (contact majority carrier), whereas the recombination current parameter of the contact J_{0c} provides information on the (desired) resistance or 'blocking' action presented to the minority carrier. Whilst it is intuitive that simultaneous minimization of ρ_c and J_{0c} leads to improvements in contact-selectivity, understanding the potential benefits of applying these contacts at the device level is not. Consideration must be made of the physical configuration in which the contacts are to be applied. To address this point, the final section of the paper includes device simulations to determine the optimum ρ_c - J_{0c} combination and corresponding contact configuration.

Fabrication and characterization of the contact structures. To characterize the properties of the contacts, symmetrical test structures were prepared on float-zone, >100 Ωcm resistivity, (100) oriented, p and n-type Si wafers. After saw damage etching and standard RCA cleaning, the wafers were diffused in quartz furnaces with boron (on n-type wafers) or phosphorus (on p-type wafers) so that in all cases the doping of the diffusion and substrate were opposed. A post diffusion alkaline etch was performed on the phosphorus diffusion to lower its surface concentration and increase the sheet resistance. Figure 1 provides the final dopant profiles of the boron (p^+) and phosphorus (n^+) diffusions as determined by electrochemical capacitance voltage measurements (WEP Wafer Profiler).

Following another RCA clean, p⁺ samples were coated symmetrically at 200ºC with between 2 and 25 cycles of thermal atomic-layer-deposited (ALD) Al_2O_3 films (Beneq TFS 200). Alternating cycles of trimethylaluminium and water were used with pulse and purge durations chosen in line with a self-limiting reaction. The ALD growth rate, as measured from thicker films, was found to be ~1 Å/cycle, although for the ultra-thin films used in this study the growth rate cannot be assumed to be perfectly linear [22].

SiO_2 films were grown into the n^+ samples in a clean quartz furnace at either 700ºC or 800ºC in pure oxygen (oxidation times typically less than 60 seconds), resulting

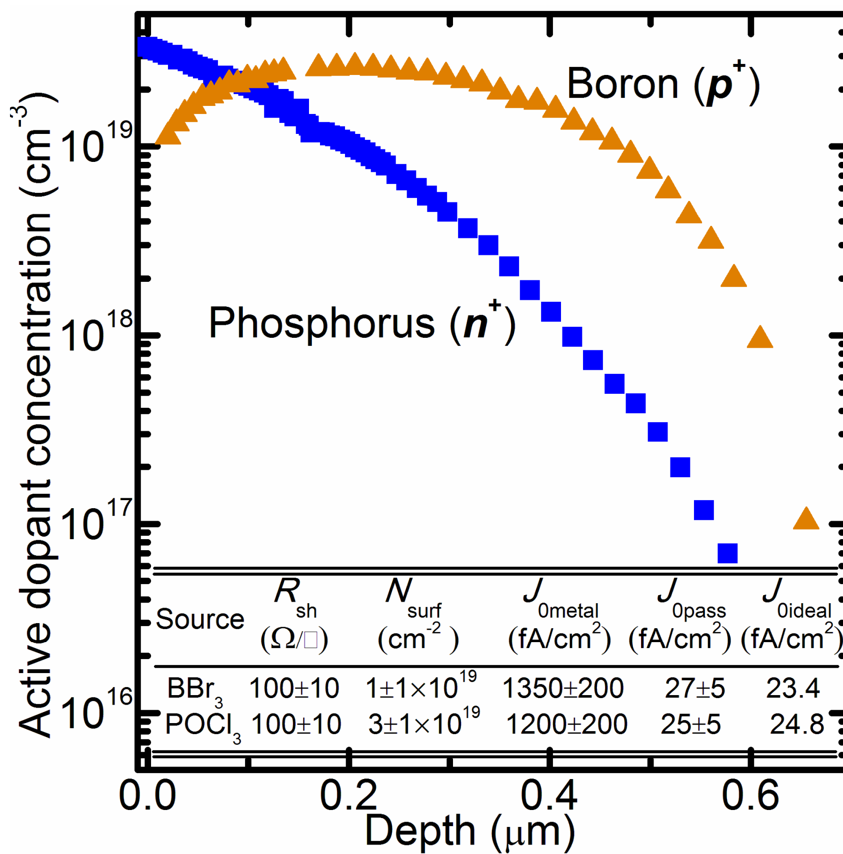

Source	R_{sh} (Ω/□)	N_{surf} (cm^{-2})	J_{0metal} (fA/cm^2)	J_{0pass} (fA/cm^2)	J_{0ideal} (fA/cm^2)
BBr_3	100±10	1±1×10^{19}	1350±200	27±5	23.4
$POCl_3$	100±10	3±1×10^{19}	1200±200	25±5	24.8

Figure 1 Electrically active phosphorus diffusion profile and associated sheet resistance against diffusion depth. Sheet resistance calculation utilises a model for mobility [10].

in film thicknesses between 1.3 and 2.0 nm. Following the deposition/growth of dielectrics, the samples were symmetrically capped with PECVD *a*-Si:H. Interestingly, different optimum capping *a*-Si:H films (deposited by different PECVD tools) were

found for the p^+ and n^+ samples. The p^+ samples were coated with ~30 nm of *a*-Si:H at a deposition temperature of ~200°C (Oxford PlasmaLab 100) and subsequently annealed for 15 minutes at 400°C in forming gas ambient to activate the passivation. The n^+ samples were coated with ~30 nm of *a*-Si:H at ~300°C (Roth & Rau AK400) and required no post-deposition anneal to activate the passivation. Aluminum was then evaporated symmetrically onto all samples to a thickness of ~10 nm to mimic the metal contacts whilst allowing sufficient light through, in order to use the photoconductance decay (PCD) method to measure the effective minority carrier lifetime. PCD measurements were taken using a Sinton WCT120 instrument, and contact recombination factors J_{0c} were extracted using the Kane and Swanson technique [23] with an intrinsic carrier concentration n_i=8.6×10^9 cm^{-3} (at 297 K).

Included in the inset of Figure 1 are reference values of the optimally passivated J_{0pass}, directly metalized J_{0metal}, and simulated ideal J_{0ideal} recombination factors of the p^+ and n^+ dopant profiles used in this study. The J_{0pass} represents the lowest recombination factor that has been achieved experimentally for the p^+ and n^+ dopant diffusions, and is representative of non-contacted regions with state-of-the-art surface passivation. The J_{0pass} values were obtained in a separate study via PECVD *a*-Si:H (~30nm) for the n^+ surface and ALD Al_2O_3 (~20nm) for the p^+ surface, in-line with previously reported low surface recombination results on these doped surfaces [13, 24]. The metallized recombination parameters J_{0metal} were measured on samples with ~10 nm of aluminum evaporated directly onto the diffused surfaces. These values are representative of the recombination factor in the contacted regions if metallization is applied directly to the *c*-Si. The ideal recombination factors J_{0ideal} were simulated from the measured dopant profiles using Boltzmann statistics and the assumptions of no surface recombination (Auger recombination [25], mobility [26] and band gap narrowing [27, 28] models were

utilized in this simulation) [29]. These values represent the theoretical minimum recombination factors that can be achieved with the dopant profiles in Figure 1. It is worth noting that the measured J_{0pass} recombination factors are, within measurement error, approximately equal to the simulated J_{0ideal} values, indicating that surface recombination has been almost completely suppressed in the optimally passivated references.

Transfer-length-method (TLM) samples were fabricated on the same substrates, and using an identical procedure to the lifetime test samples up until the aluminum evaporation, which was instead deposited to a thickness of ~1μm on only one side. The TLM contact pad patterns were photolithographically defined and isolated using an acidic metal etch. Pad spacings of 10-300 μm were used in this study. Current–voltage measurements were performed at ~297 K (Keithley 2425 Source Meter) and ρ_c was extracted as per the description given in [30].

STEM samples were prepared on single-side polished silicon wafers. Thermal SiO_2 / *a*-Si:H / Al contact structures were deposited on the polished surface, following which TEM lamellae were prepared by mechanical tripod polishing and ion milling. An FEI Tecnai Osiris instrument was used to take bright field (BF) and high angle annular dark field (HAADF) STEM micrographs and high sensitivity EDX maps of local aluminum, silicon and oxygen concentrations. Contact structures with an Al_2O_3 tunnel layer were not analyzed by STEM and EDX micrographs due to ambiguity in the aluminum EDX signal.

Film thicknesses were monitored by fitting polarized reflectance data (J.A. Woolam M2000 ellipsometer) of single side polished silicon wafers deposited alongside lifetime and TLM samples. Given the dependence of SiO_2 growth on dopant concentration, the SiO_2 thickness samples were subjected to a phosphorus diffusion prior to oxidation to create an alike surface concentration.

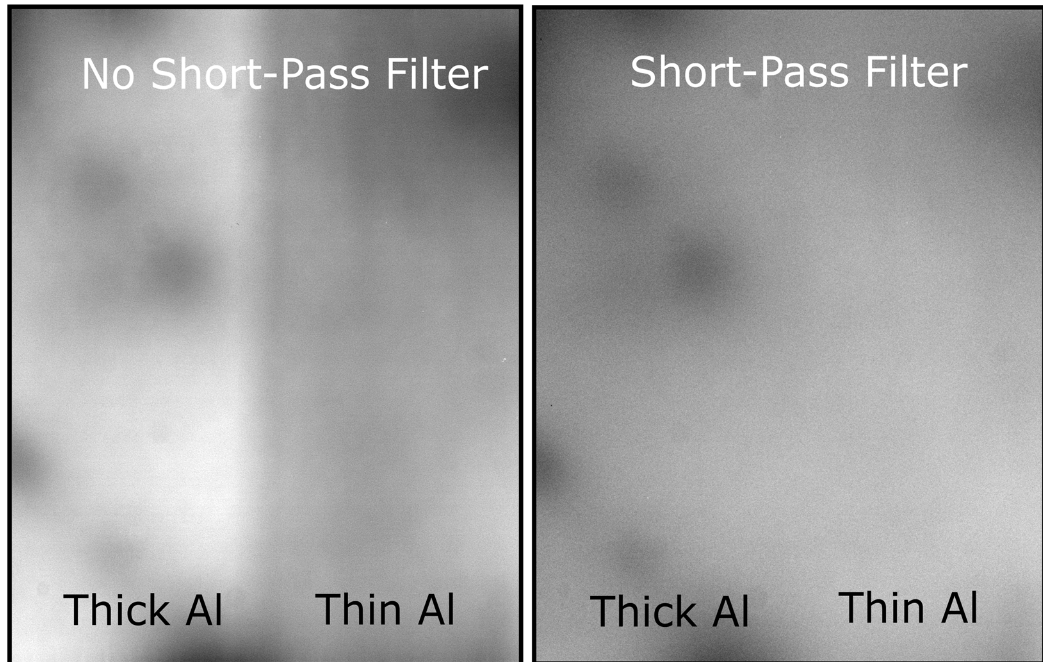

Figure. 2.PL images of an Al / *a*-Si:H / SiO_2(~1.6 nm) / *c*-Si(n^+) sample taken with and without a 1000 nm short-pass filter. The two images are scaled individually to enhance contrast.

Implicit in this study is the assumption that lifetime samples (with ~10 nm of aluminum) and TLM samples (~1 μm of aluminum) behave identically in terms of contact recombination. To explore the validity of this assumption, photoluminescence (PL) images were taken (BT Imaging LIS-R1) of a symmetrically passivated *c*-Si(n^+) / SiO_2(1.6 nm) / *a*-Si:H sample. On the rear side of this sample half the area was covered with thick aluminum (1 μm) and the other half with thin aluminum (~ 10 nm). Figure 2 provides PL images of the sample taken with and without a 1000 nm short pass (SP) filter, after a 40 minute 250°C anneal step (see Section IIIA). Without the SP filter, greater rear-side reflection from the thick aluminum results in contrast between the two regions. With the filter, the effect of rear-side reflection is removed due to a penetration depth shallower than the thickness of the sample. An absence of contrast between the thick and thin

aluminum regions in this image suggests that in both regions the carrier density profiles are very similar, and hence so are their respective surface recombination characteristics.

Optimization of the aluminum-amorphous silicon intermixing

Temperature Dependence of the Characteristic Contact Parameters. A significant component in the implementation of the proposed contact structure is the low-temperature interaction between *a*-Si:H and aluminum. To investigate the lowest temperature at which the Al / *a*-Si:H interaction will commence, Al / *a*-Si:H / Al_2O_3 / *c*-Si(p^+) (referred to hereafter as MIS(p^+)) and Al / *a*-Si:H / SiO_2 / *c*-Si(n^+) (referred to hereafter as MIS(n^+)) TLM structures were fabricated and annealed at different temperatures and ρ_c was monitored as a function of annealing time. Figure 3 shows the dependence of ρ_c on annealing time for the two contact structures, annealed at 200°C and 250°C. In this particular instance the MIS(n^+) and MIS(p^+) structures had insulator thicknesses of ~1.6 nm. It should be noted that the ρ_c values ≥ 1 Ωcm^2 were extracted from current-voltage measurements that deviated from pure Ohmic behavior and, as such, they represent a lower-limit ρ_c. As a reference, the directly metallized ρ_c values measured for the n^+ and p^+ surfaces are also provided in Figure 3. A slight reduction in ρ_c over the 40 minute period is seen for the 200°C anneal, however the reduction in ρ_c is prohibitively slow. Instead, annealing at 250°C provides an acceptable ρ_c for solar cell contacts after 20 minutes, for both the MIS(p^+) and MIS(n^+) contacts. Additional annealing reduces ρ_c only slightly, after which ρ_c appears to saturate to a value of ~10 mΩcm^2, which is still 3 orders of magnitude higher than for the directly metallized case. The saturation of ρ_c after 40 minutes of annealing suggests that the conductivity of the previously *a*-Si:H is layer is no longer the limiting factor of conduction, and that now the tunneling interlayer dominates the measured resistivity. As demonstrated in the following subsection, the final

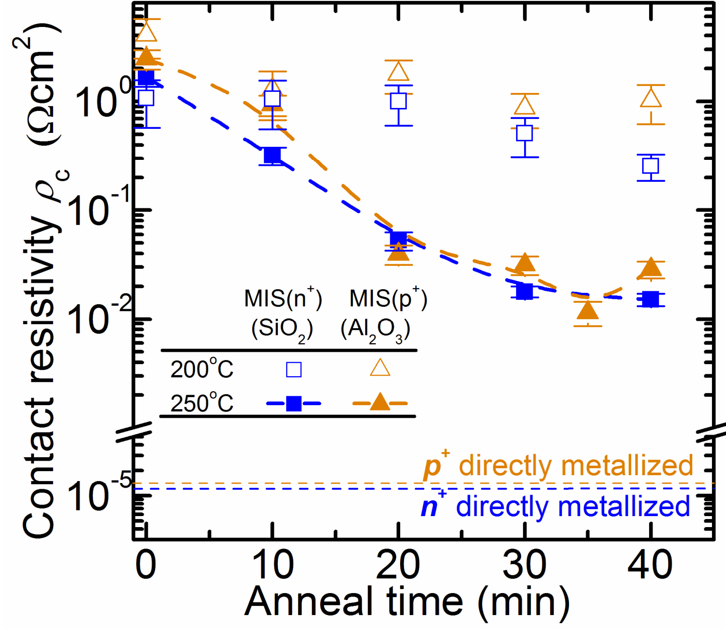

Figure. 3. Anneal time dependent ρ_c for MIS(p$^+$) and MIS(n$^+$) contacts with ~1.6 nm dielectric layers. Lines provide a guide to the eyes only and error bars are based on the estimated measurement error. Dotted horizontal lines represent directly-metallized ρ_c values for the n$^+$ and p$^+$ diffusions.

saturated ρ_c values are strongly dependent on the dielectric thickness, suggesting that further optimization is possible.

As shown in Section IV A below, the J_{0c} attainable with the *a*-Si:H enhanced MIS structures is significantly lower than that of basic MIS type contacts (without the *a*-Si:H capping) and that both structures show a strong J_{0c} dependence on the dielectric layer thickness. In the case of a ~1.6 nm film, as used in Figure 3, the J_{0c} prior to the alloying step were ~40 and 90 fA/cm^2 for the *a*-Si:H enhanced MIS(n$^+$) and MIS(p$^+$), respectively. Over the 40-minute 250ºC alloying anneal the J_{0c} of the MIS(n$^+$) contact did not change significantly, remaining within the margins of measurement uncertainty. The J_{0c} of the MIS(p$^+$) contact increased by approximately a factor of two under these conditions, from 90 to ~160 fA/cm^2.

The annealing conditions described above reflect the lowest temperature at which the *a*-Si:H / Al interaction, and hence contact formation, will occur. Some conventional

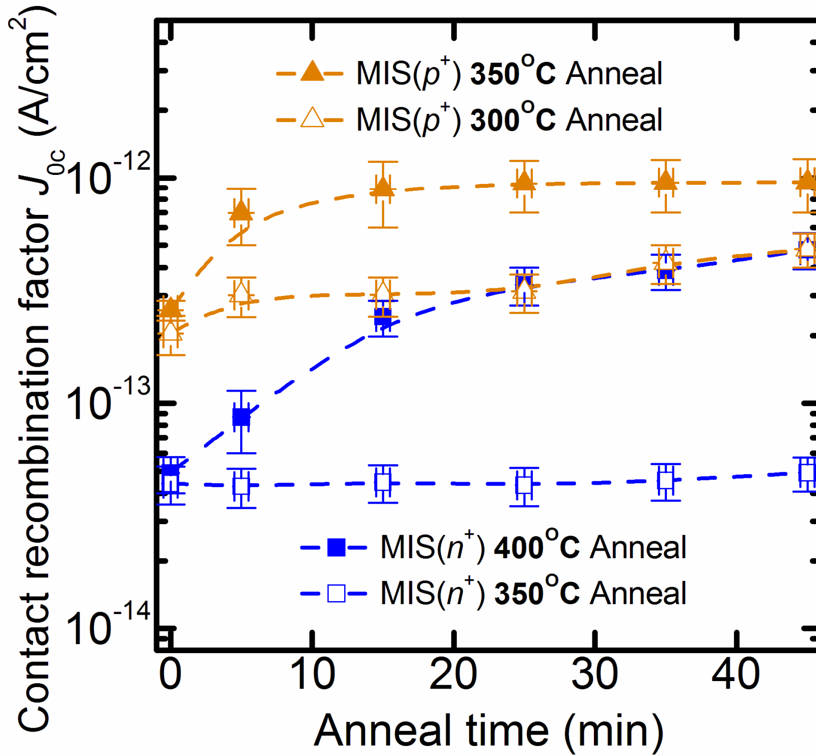

Figure. 4. Temperature stability of MIS(p^+) and MIS(n^+) as assessed by changes in J_{0c}. Lines provide a guide to the eyes only, error bars are based on the estimated measurement error.

solar cell processing steps, such as the application of PECVD *a*-SiN_x:H passivation and antireflection coating, require temperatures of up to 400ºC. Hence it is of interest from a processing perspective to know the stability of J_{0c} at those temperatures as well. Provided in Figure 4 are the J_{0c} values for the MIS(p^+) and MIS(n^+) contacts as a function of anneal time for annealing temperatures between 300ºC and 400ºC. All samples received a 40 minute 250ºC anneal prior to the commencement of the higher temperature annealing. The J_{0c} of the MIS(n^+) exhibits no significant increase after 45 minutes at 350ºC; however, at 400ºC the J_{0c} underwent a 10 fold increase over the same time period. This is in alignment with temperatures reported in the literature for the initiation of the SiO_2 / Al interaction [21], suggesting that aluminum may be moving through the oxide layer.

The MIS(p^+) exhibited a poorer stability at 350ºC, increasing to over ~1000 fA/cm^2 – close to the directly metallized J_{0metal} value of ~1350 fA/cm^2 given in Fig. 1. Nevertheless, a reasonable stability was observed for the MIS(p^+) at 300ºC, with a final J_{0c} of ~500 fA/cm^2 after 45 minutes of annealing, a value well below the directly metallized case.

Contact resistance measurements taken after higher temperature annealing revealed small reductions in ρ_c but remained orders of magnitude above the directly metalized case – again supporting the conclusion that ρ_c is now dominated by tunneling through the dielectric layer.

Temperature Dependent Compositional Analysis. To investigate the compositional changes responsible for the above discussed thermal dependence of the contact characteristics, STEM analysis and accompanying EDX mapping of local Al, Si and O concentrations were performed on MIS(n^+) contacts. As a baseline from which to compare annealed samples, an Al / *a*-Si:H (~30 nm) / SiO_2 (~2 nm) / *c*-Si contact structure was imaged before the alloying anneal. Figure 5a provides a HAADF STEM image and corresponding EDX line-scans of the local Al, Si and O distribution of the un-annealed contact. Evident in the HAADF STEM image are the SiO_2, *a*-Si:H and Al layers on *c*-Si, with an additional unintentional interlayer between the *a*-Si:H and SiO_2 layers. No evidence of significant interaction between the Al and *a*-Si:H layers is seen in the STEM image, as supported by the EDX line scans which show a sharp decline in Al accompanied by a sharp increase in Si concentration at the Al / *a*-Si:H interface. These line scans also suggest that the intermediate layer between the SiO_2 and *a*-Si:H layers is a sub-stoichiometric oxide species ($SiO_{x<2}$). Additional high-resolution (HR) TEM micrographs (not shown here) of the *a*-Si:H layer revealed no sign of crystallization.

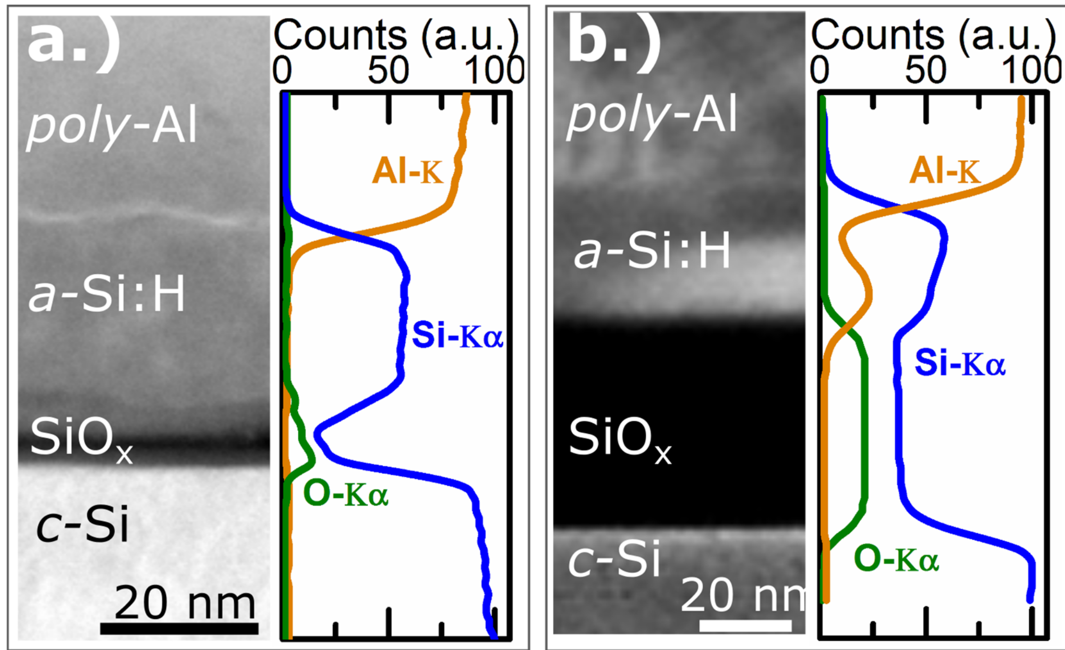

Figure. 5. HAADF STEM and EDX line scans of local Al, O and Si distribution for a.) an Al / *a*-Si:H (~30 nm) / SiO_2 (~2 nm) / *c*-Si contact in its as-deposited state, and b.) an Al / *a*-Si:H (~30 nm) / SiO_2 (~50 nm) / *c*-Si contact after 40 minutes alloying at 250ºC. The line-scans account for the differences in both composition and density of the different films.

To inspect the compositional changes at 250ºC, STEM imaging and EDX mapping and line scans of an Al / *a*-Si:H (~30 nm) / SiO_2 (~50 nm) / *c*-Si structure after a 40 minute 250ºC anneal were undertaken. A thicker SiO_2 layer was used in this instance to obtain a clearer distinction between interfaces. Figure 6a shows the HAADF STEM image and corresponding Al, Si and O EDX mappings of the annealed contact structure. In contrast to the un-annealed sample, the Al mapping in Figure 6a shows a local protrusion of Al through the previously deposited *a*-Si:H layer, with an Al accumulation at the SiO_2 surface. This is supported by a corresponding low Si concentration in the same region as seen in the Si EDX mapping. It appears that the SiO_2 layer limits any significant movement of Al further towards the *c*-Si at this annealing temperature. The EDX line scans included in Figure 5b illustrate the compositional variation through one of these local Al rich regions and show accumulation of Al at the SiO_2 surface. Localized atomic composition analysis reveals a small silicon concentration (~1 at.%) in the Al layer,

indicating partial dissolution of Si into Al. More significantly, Al concentrations of up to 40 at.% are detected in the underlying *a*-Si:H film. These concentrations, which are well above the doping solubility limit, suggest that the previously *a*-Si:H layer is now semi-metallic and hence highly conductive. The saturation in ρ_c seen in Figure 3 is therefore likely dominated by carrier tunneling through the still intact thin dielectric layer. The region of high Al concentration within the *a*-Si:H layer is seen to be correlated with a region of contrast in the HAADF STEM image. HR TEM micrographs of the same region reveals lattice fringes indicative of the presence of crystallites, as shown in Figure 7.

Additional thermal treatment for 15 minutes at 400°C results in aluminum completely replacing the previously *a*-Si:H layer, with a compositional concentration close to 100%, as seen in Figure 6b which shows the EDX mapping after this anneal step. Also evident in this figure is that the SiO_2 layer is acting as a barrier to further Al diffusion. The preservation of the SiO_2 layer is consistent with the results for MIS(n^+) in Figure 4, which indicate that after 15 minutes at 400°C the J_{0c} is ~250 fA/cm^2, still much lower than the corresponding value for the directly metallized surface. A HR TEM image, shown in Figure 7, reveals extensive crystallization (of aluminum-rich regions) in the previously *a*-Si:H layer.

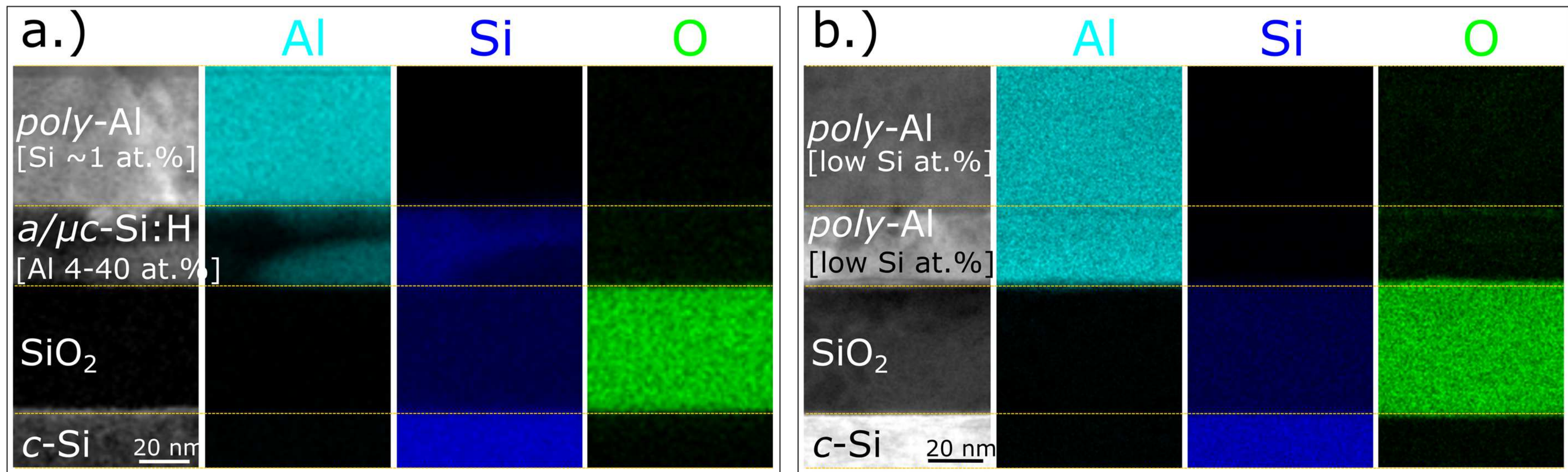

Figure. 6. HAADF STEM and EDX mappings of the local Al, O and Si concentrations for an Al / *a*-Si:H (~30 nm) / SiO_2 (~50 nm) / *c*-Si contact a.) after 40 minutes annealing at 250ºC and b.) after an additional 15 minutes annealing at 400ºC.

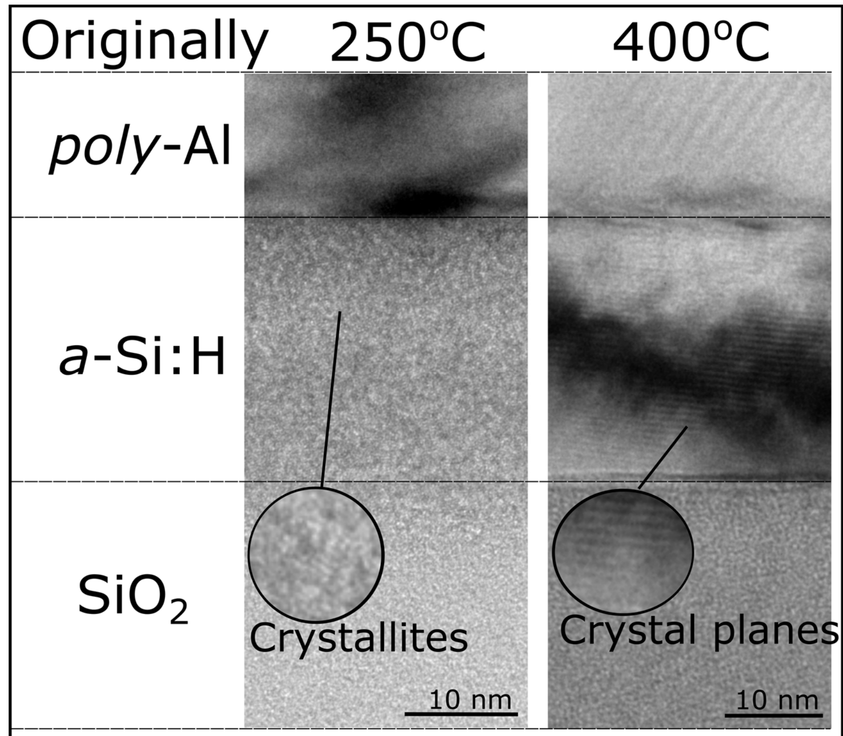

Figure. 7. HR TEM micrographs showing signs of crystallization in the *a*-Si:H layer for Al / *a*-Si:H (~30 nm) / SiO_2 (~50 nm) / *c*-Si contact structures annealed at 250ºC for 40 minutes (left) and at 250ºC for 40 minutes with an additional 15 minutes at 400ºC (right).

The trade-off between recombination current and contact resistance

Dependence of Contact Characteristics on Insulator Thickness. Using the 40-minute 250ºC anneal identified in Section IIIA as optimal, the contact characteristics of MIS(n^+) and MIS(p^+) structures with differing insulator thicknesses were measured. As a baseline from which to compare these results, a set of reference MIS samples were also prepared on identical dopant diffusions, without the *a*-Si:H capping step (referred to hereafter as basic MIS). Figure 8a and b provide the ρ_c and J_{0c} dependence on SiO_2 thickness, for the *a*-Si:H capped MIS(n^+) contact, alongside the corresponding basic MIS(n^+) reference samples. Also included in these plots are horizontal dotted lines corresponding to the directly metallized ρ_c and J_{0metal} and the optimally passivated J_{0pass}. In agreement with the theoretical probability for quantum-mechanical tunneling, a strong increase in ρ_c is observed as a result of increasing

dielectric thickness – spanning more than three orders of magnitude for a 5 Å difference in SiO_2 thickness. Over the range measured, it can be seen that there is no significant difference in the thickness dependence of ρ_c between the *a*-Si:H capped and basic MIS structures. This further supports the conclusion that following the alloying step, the passage of current through the *a*-Si:H capped MIS(n^+) is, like the basic MIS(n^+) structure, limited only by carrier tunneling through the dielectric layer.

Coupled with the increasing ρ_c as a function of dielectric thickness, is a decreasing J_{0c}. The *a*-Si:H capped and basic MIS(n^+) structures both offer a significant reduction in recombination, as compared to the directly metallized case. In addition, it can be seen that for both structures, converse to the ρ_c trend, J_{0c} decreases with increasing insulator thickness. Most significantly, it can be seen that the J_{0c} of the *a*-Si:H capped MIS(n^+) is consistently almost an order of magnitude lower than the basic MIS(n^+). A dielectric thickness of 1.7 nm is sufficient to achieve the lower limit (optimally passivated) recombination factor of ~25 fA/cm^2, but at the expense of a high ρ_c. This value is approximately identical to that corresponding to Auger recombination within the n^+ region, which suggests that even lower recombination factors may be attainable by reducing the dopant dose of the underlying diffusion. The 700 and 800°C oxides exhibit similar ρ_c and J_{0c} trends; a slightly earlier transition to lower J_{0c} and higher ρ_c for the higher temperature oxide may reflect differences in the density of the two SiO_2 films.

An analogous set of results for the MIS(p^+) contact characteristics as a function of the number of ALD Al_2O_3 cycles is provided in Figure 8c and d. Similar to the trend seen for the MIS(n^+) structures, both the *a*-Si:H capped and basic MIS(p^+) structures exhibit alike contact resistance dependences on thickness. Structures which were fabricated with more than 15 ALD cycles (~1.5 nm) were measured to produce large ρ_c values and general nonlinear current-voltage behavior. The rapid onset of high resistance

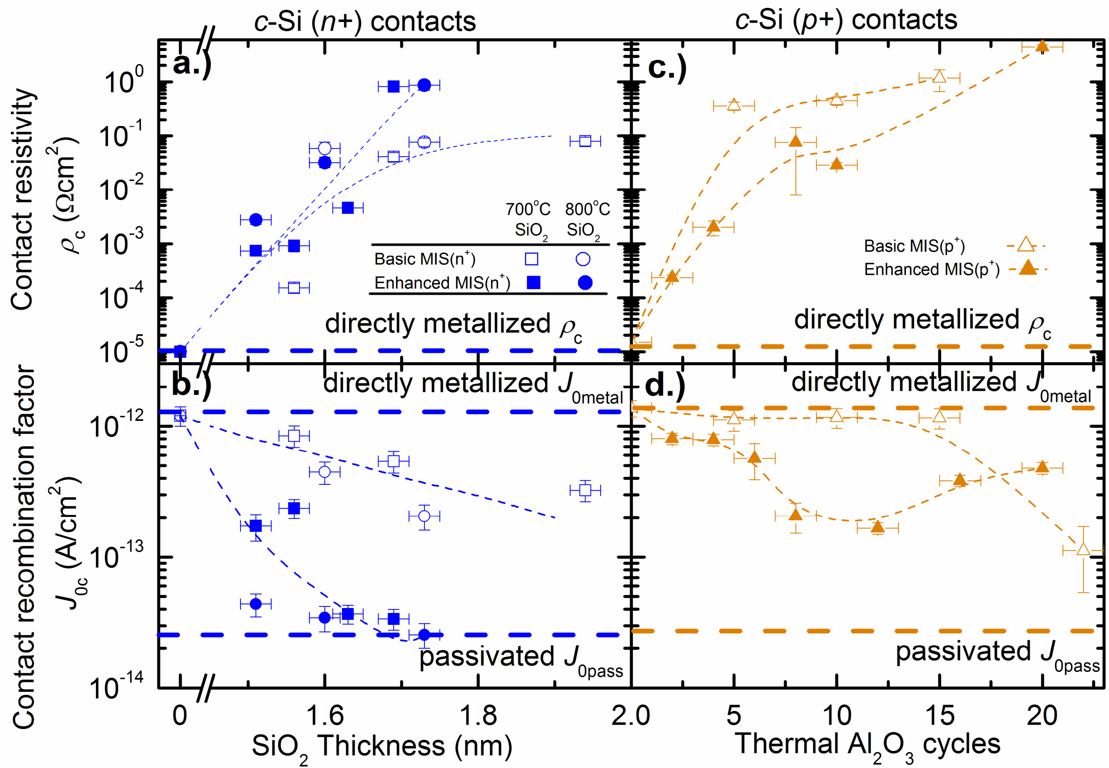

Figure. 8. Contact resistivity ρ_c of a.) MIS(n^+) and c.) MIS(p^+) structures and contact recombination factor J_{0c} for b.) MIS(n^+) and d.) MIS(p^+) structures as a function of insulator thickness. Lines provide a guide to the eyes only, error bars are based off the estimated error in measurement. The above plot includes some data which has previously been presented elsewhere [35].

contact behavior seen for both MIS(p^+) structures is attributable to the large valence band offset between the *c*-Si and Al_2O_3 [31] and the corresponding high value of *f* (Equation 1).

In terms of recombination, again both the *a*-Si:H capped and basic MIS(p^+) structures produce lower recombination factors than the directly metallized case, with the *a*-Si:H capped structures producing the lowest recombination factors within the dielectric thickness range of relevance. However, the level of passivation is consistently less than that provided by the MIS(n^+) structures – reaching at best ~150 fA/cm^2 – which is significantly higher than the optimally passivated case, but still approximately an order of magnitude lower than the directly metallized p^+ surface. The passivation quality of the

a-Si:H enhanced MIS(p^+) appears to stop improving after 10 cycles of Al_2O_3 – producing a local minimum.

The lower level of surface passivation could be associated with a minority/majority capture cross-section ratio σ_n/σ_p greater than unity, which is expected for the recombination active defects present at the Al_2O_3 / *c*-Si interface [32]. In addition, the relatively low work function of aluminum may induce downwards band bending increasing the minority carrier concentration at the *c*-Si surface. A metal with a higher work function which also interacts with *a*-Si:H at low temperatures may prove to be more appropriate for the MIS(p^+), for example nickel [33] or gold [34].

Significance to Solar Cells. The trends presented in the previous section are revealing in themselves, showing the diverging behavior of contact passivation and conductivity with the dielectric layer thickness. This opposing behavior highlights the difficulty in determining the best ρ_c – J_{0c} combination. The simplest application of the contact structures described in the previous sections would be as a full area contact on the rear side of solar cells. But, as it is well known, it is also possible to form the contact only in part of the rear surface, either as dots or lines. In a device design with partial rear contacts, the remaining surfaces can by passivated by an appropriate dielectric film. This design implies that carrier flow towards the contacts is geometrically constricted [36, 37], thus adding an element of resistance, for both majority and minority carriers, to the specific contact characteristics ρ_c and J_{0c}. Therefore, to properly evaluate a given contact system, it is necessary to consider the geometric configuration in which the contact is to be applied. The latter is globally represented by the fraction of the rear surface occupied by the contact m_f.

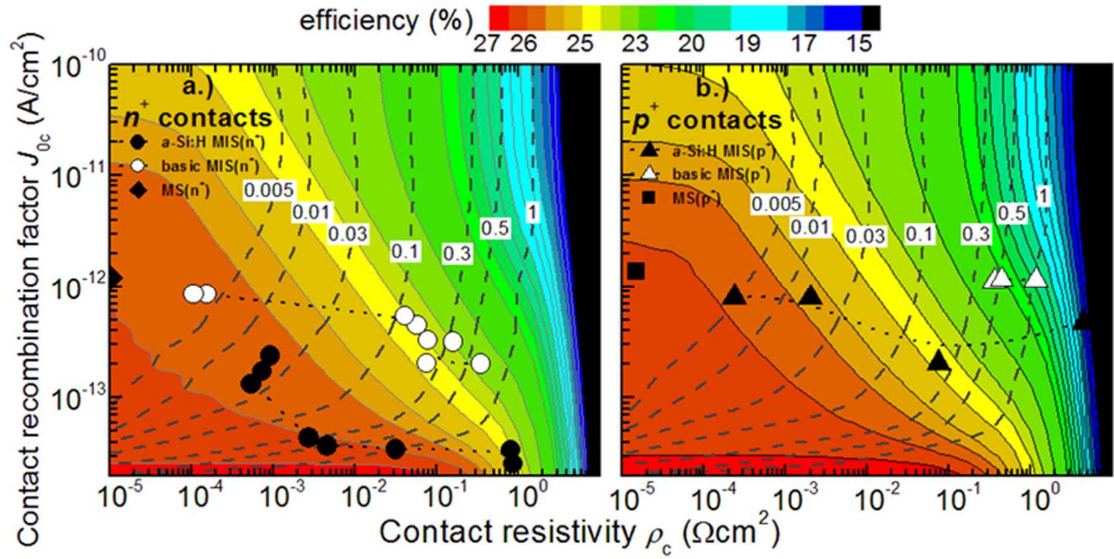

Figure. 9.Simulated optimum contact fraction m_f (dashed lines) and resultant idealized efficiency (contour plot) as a function of rear contact ρ_c and J_{0c} for a.) n^+ contacts and b.) p^+ contacts presented in this paper. All values to the right of the 100% contact fraction lines were simulated with full area contacts. Directly metalized, basic MIS and *a*-Si:H capped MIS data points are superimposed on top of the contours to reflect their relative carrier-selectivity. The varied parameter in the MIS contact data trends is the insulator layer thicknesses.

To compare contact structures, we have modelled an idealized solar cell structure with partial rear contacts using the freeware solar cell simulation program Quokka2 [38]. In these simulations losses due to front surface recombination, resistance and shading have been reduced to a minimum or removed completely in order to emphasize the influence of the rear contact. The rear contact is simulated with a variable ρ_c and J_{0c}; for every ρ_c – J_{0c} combination an optimum contact fraction m_f is calculated (dashed lines) – and from this configuration an idealized efficiency is obtained (contours). These results are presented in Figure 9a and b for the contacts on n^+ and p^+ diffusions respectively. Assumptions used in the simulations are detailed in Table C. Both simulations show almost identical results, this is attributable to the very similar resistivity and recombination characteristics of the n^+ and p^+ diffusions used in this study.

By superimposing the experimentally measured thickness dependent ρ_c - J_{0c} trends (presented in Figure 8) on these plots, the insulator thickness which provides the

optimum ρ_c - J_{0c} configuration is identified as the point which falls within the region of highest efficiency. It can be seen that the trends in efficiency are parallel with the concept of carrier-selectivity described in the introduction. That is, reductions in the majority carrier resistivity and minority carrier recombination, lead to improvements in carrier-selectivity and hence efficiency

Similarly, the trends in optimum m_f provide information on the ease of fabrication for a particular contact, with larger m_f values being easier to fabricate. It is worth mentioning that no technological constraints are placed on the width of the rear fingers used in these simulations. Hence real-world realization of contacts with simulated small optimum m_f values, are likely to result in larger m_f values with lower corresponding efficiencies to those seen in Figure 9.

Included in Figure 9a are data points which reflect the contact characteristics of the directly metallized n^+ contact MS(n^+), the basic MIS(n^+) and the *a*-Si:H capped MIS(n^+). This comparison reveals that in this particular instance, the only benefit gained in using the basic MIS(n^+) over the directly metallized MS(n^+) contact is the ability to use larger contact fractions at the expense of relatively modest decreases in device efficiency. Integrating the *a*-Si:H capping step however, is shown to improve the carrier-selectivity (hence efficiency) whilst simultaneously increasing the optimum m_f value. The highest idealized efficiencies of ~26.1%, are obtained on *a*-Si:H capped MIS(n^+) structures with a ~1.55 nm SiO_2 film which produce a ρ_c - J_{0c} combination of ~3 mΩcm^2 and ~40 fA/cm^2. These values are simulated with an optimum m_f value between 30 - 50 % - a fraction easily achievable using today's industrial processes.

.

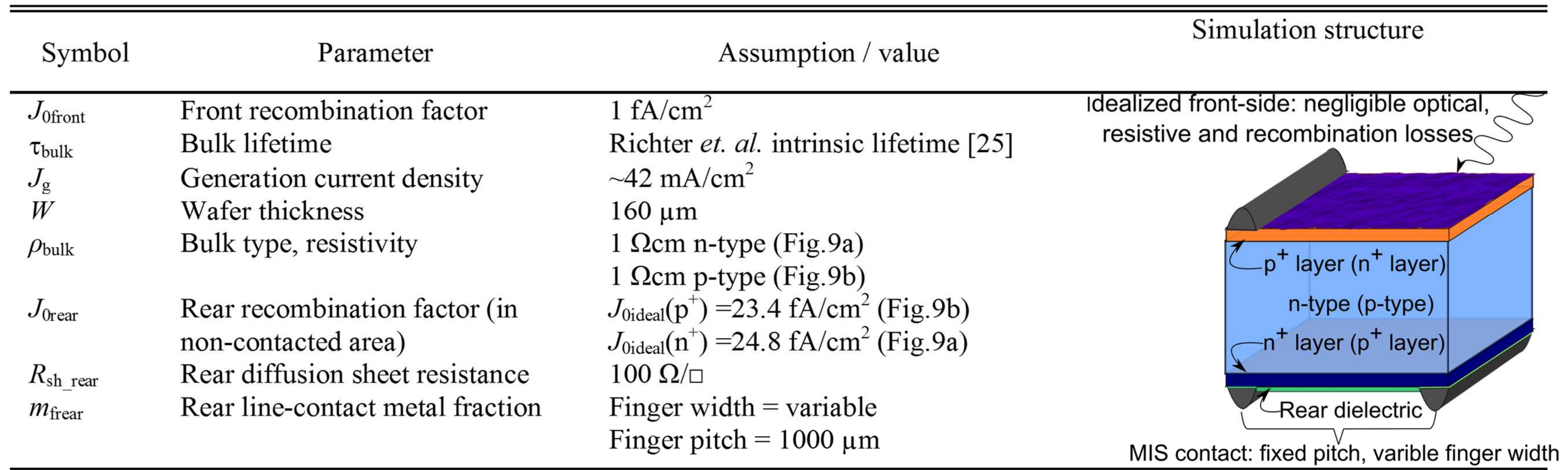

Symbol	Parameter	Assumption / value	Simulation structure
J_{0front}	Front recombination factor	1 fA/cm^2	
τ_{bulk}	Bulk lifetime	Richter *et. al.* intrinsic lifetime [25]	
J_g	Generation current density	~42 mA/cm^2	
W	Wafer thickness	160 μm	
ρ_{bulk}	Bulk type, resistivity	1 Ωcm n-type (Fig.9a) 1 Ωcm p-type (Fig.9b)	
J_{0rear}	Rear recombination factor (in non-contacted area)	$J_{0ideal}(p^+)$ =23.4 fA/cm^2 (Fig.9b) $J_{0ideal}(n^+)$ =24.8 fA/cm^2 (Fig.9a)	
R_{sh_rear}	Rear diffusion sheet resistance	100 Ω/□	
m_{frear}	Rear line-contact metal fraction	Finger width = variable Finger pitch = 1000 μm	

Table. 1. Parameters, assumptions and structure used in the idealized cell simulations

An alike evaluation of the p^+ contacts presented in figure 9b reveals a significant loss in carrier-selectivity as a result of transitioning from the directly metallized MS(p^+) to the basic MIS(p^+). This is due primarily to a larger ρ_c. The *a*-Si:H capped MIS(p^+) also shows small losses in efficiency over the directly metalized case when both are applied in their optimum m_f, with corresponding optimized efficiencies of ~25.9 and ~26.0 % respectively. It can be summarized that the only benefits associated with using either MIS(p^+) contacts is that the lower recombination factors allow the contact to be applied in a larger fraction. The MIS results on p^+ surfaces might be improved by choosing an alternative to Al_2O_3 with a lower figure of merit f (Equation 1) and a metal with a larger work function.

Conclusion. A fabrication procedure for carrier-selective MIS contacts that utilizes an *a*-Si:H capped dielectric tunneling layer has been presented. Lightly diffused (~100 Ω/□) MIS(p^+) and MIS(n^+) structures, employing Al_2O_3 and SiO_2 dielectric layers, respectively, have been shown to greatly reduce recombination, while still permitting majority carrier transport. STEM and EDX analysis reveal that the alloying between the *a*-Si:H capping layer and the Al over-layer is a crucial mechanism in the successful formation of the contact structure.

Based on solar cell device simulations, SiO_2 thicknesses in the 1.5–1.65 nm range are found to be optimum for the MIS(n^+)contacts, resulting in ρ_c - J_{0c} combinations of ~3 m Ωcm^2 and ~40 fA/cm^2. These simulations suggest that the MIS(n^+) contacts can be applied in large area fractions and hence also offer advantages over established high efficiency silicon solar cell approaches in terms of process simplicity. The thermal stability of the MIS(n^+) contacts at 350°C has also been demonstrated, suggesting that they can be integrated with a standard PECVD *a*-SiN_x:H process.

The MIS(p^+) contacts revealed poorer characteristics than MIS(n^+) contacts both in terms of thermal stability and ρ_c - J_{0c} combinations, but still offer advantages over conventional approaches based on selective dopant diffusions.

Acknowledgements. The authors wish to thank Dr. Andreas Fell for his assistance with the Quokka2 simulations. The authors from the ANU acknowledge financial support by The Australian Solar Institute/Australian Renewable Energy Agency as well as access to equipment at the Australian National Fabrication Facility. The authors from EPFL thank the Axpo Naturstrom Fonds, the European Commission (FP7 project Hercules), the EuroTech Universities Alliance and the Swiss Commission for Technology and Innovation for their financial support. The authors thank Daniele Laub (EPFL) for the STEM sample preparation.

References

[1] J. Bullock, D. Yan and A. Cuevas, "Passivation of aluminium n^+ silicon contacts for solar cells by ultrathin Al_2O_3 and SiO_2 dielectric layers", *Phys. Status Solidi RRL* 7, 946 (2013).
[2] S. M. Sze and K. K. Ng, Physics of Semiconductor Devices, Wiley, 3rd Edition, 2007.
[3] Y-C. Yeo, T-J. King and C. Hu, "Direct tunneling leakage current and scalability of alternative gate dielectrics", *Appl. Phys. Lett.* 81, 2091 (2002)
[4] M. A. Green, A. W. Blakers, M. R. Willison, T. Szpitalak, E. M. Keller, E. Gauja and P.J. Hart, "The MINP solar cell – a new high voltage, high efficiency silicon solar cell" *Proceedings of the 15th IEEE Photovoltaic Specialist Conference*, Kissimmee, USA, 1981, p. 1405
[5] J. Schmidt, A. Merkle, R. Brendel, B. Hoex, M. C. M. van de Sanden, and W. M. M. Kessels, "Surface Passivation of High-efficiency Silicon Solar Cells by Atomic-layer-deposited Al_2O_3", *Prog. Photovoltaics* 16(6), 461 (2008).
[6] K. Jäger-Hezel, W. Schmidt, W. Helt, and K.D. Rasch, "Improved Large Area MIS-Contacted Silicon Solar Cells", *Proc. 13th EU PVSEC*, 1995, p. 1515.
[7] D. Zielke, J. H. Petermann, F. Werner, B. Veith, R. Brendel and J.Schmidt, "Contact passivation in silicon solar cells using atomic-layer-deposited aluminum oxide layers" *Phys. Status Solidi RRL* 5, 298 (2011).
[8] X. Loozen, J. Larsen, F. Dross, M. Aleman, T. Bearda, B. O'Sullivan, I. Gordon and J. Poortmans "Passivation of a metal contact with a tunneling layer", *Proc. 3rd Workshop Metallization Crystalline Silicon Sol. Cells,* p.25 -26, 2011
[9] J. Deckers, E. Cornagliotti, M. Debucquoya, I. Gordona, R. Mertensa, J. Poortmans, "Aluminum oxide-aluminum stacks for contact passivation in silicon solar cells", *Proc. 4th International Conference on Silicon Photovoltaics,* 2014.
[10] A. Richter, J. Benick, M. Hermle and S. W. Glunz, "Excellent silicon surface passivation with 5 Å thin ALD Al_2O_3 layers: Influence of different thermal post-deposition treatments" *Phys. Status Solidi RRL* 5, 202 (2011).

[11] W. Liang, K. Weber, A. Thomson, "Effective SiN_x:H capping layers on 1nm Al_2O_3 for p^+ surface passivation", *J. Appl. Phys.* (2014)
[12] A. A. Langford, M. L. Fleet, B. P. Nelson, W. A. Lanford, and N. Maley, "Infrared absorption strength and hydrogen content of hydrogenated amorphous silicon", *Phys. Rev. B* 45, 13367, 1992
[13] J. Bullock, D. Yan, Y. Wan, A. Cuevas, B. Demaurex, A. Hessler-Wyser and S. De Wolf, "Amorphous silicon passivated contacts for diffused junction silicon solar cell" *J. Appl. Phys,* 115, 163703 (2014)
[14] J. L. Murray and A. J. McAlister, "The Al-Si (Aluminum-Silicon) system", *Bull. Alloy Phase Diagrams*, 5 74 (1984)
[15] M. S. Haque, H. A. Naseem, and W. D. Brown, "Interaction of aluminum with hydrogenated amorphous silicon at low temperatures", *J. Appl. Phys*. 75, 3928 (1994)
[16] O. Nast and S. R. Wenham, "Elucidation of the layer exchange mechanism in the formation of polycrystalline silicon by aluminum-induced crystallization", *J. Appl. Phys*. 88, 124 (2000).
[17] B-Y. Tsaur, G. W. Turner and J. C. C. Fan, "Efficient Si Solar cells by low-temperature solid-phase epitaxy", *Appl. Phys. Lett*. 39, 749 (1981)
[18] H. Plagwitz, M. Nerdling, N. Ott, H. P. Strunk and R. Brendal, "Low-Temperature Formation of Local Al Contacts to *a*-Si:H passivated Si wafers", *Prog. Photovolt: Res. Appl*. 12, 47 (2004)
[19] B. J. Hallam, P. G. Hamer, S.R. Wenham, M. D. Abbot, A. Sugianto, A. M. Wenham, C. E. Chan, GQ Xu, J. Kariem, J. Degoulange and R. Einhaus, "Advance Bulk Defect Passivation for Silicon Solar Cells", *IEEE J. Photvolt.,* 4 88, 2014.
[20] B. J. Hallam, A. Sugianto, L. Mai, GQ Xu, C. E. Chan, M. D. Abbot, S.R. Wenham, A. Uruena, E. Cornagliotti and M. Aleman, "Hydrogen Passivation of Laser-Induced Defects for Laser-Doped Silicon Solar Cells", *IEEE J. Photvolt.,* 2014.
[21] A. Bierhals, A. G. Aberle and R. Hezel, "Improved understanding of thermally activated structural changes in Al/SiO_x/p-Si tunnel diodes by means of infrared spectroscopy", *J. Appl. Phys.* 83, 1371 (1998)
[22] R. L. Puurunen, W. Vandervorst, W. F. A. Besling, O. Richard, H. Bender, T. Conard, C. Zhao, A. Delabie, M. Caymax, S. De Gendt, M. Heyns, M. M. Viitanen, M. de Ridder, H. H. Brongersma, Y. Tamminga, T. Dao, T. de Win, M. Verheijen, M. Kaiser and M. Tuominen, "Island growth in the atomic layer deposition of zirconium oxide and aluminum oxide on hydrogen-terminated silicon: Growth mode modeling and transmission electron microscopy" *J. Appl. Phys.* 96, 4878 (2004)
[23] D.E. Kane and R. M. Swanson, "Measurement of the emitter saturation current by a contactless photoconductivity decay method", *Proceedings of the 18th IEEE Photovoltaic Specialist Conference*, Las Vegas, USA, 1985, p. 578-583.
[24] B. Hoex, J. Schmidt, R. Bock, P. P. Altermatt, M. C. M. van de Sanden and W. M. M. Kessels, "Excellent passivation of highly doped p-type Si surfaces by the negative-charge-dielectric Al_2O_3", *Appl. Phys. Lett.* 91, 112107 (2007)
[25] A. Richter, S. W. Glunz, F. Werner, J. Schmidt, and A. Cuevas, "Improved quantitative description of Auger recombination in crystalline silicon," *Physical Review B*, vol. 86, p. 165202, 2012
[26] D. B. M. Klaassen, "A unified mobility model for device simulation – I. Model equations and concentration dependence", Solid-State Electron. 35, 953 (1992).
[27] D. Yan and A. Cuevas, "Empirical determination of the energy band gap narrowing in highly doped n^+ silicon", *J. Appl. Phys*., 114, 044508, 2013
[28] D. Yan and A. Cuevas, "Empirical determination of the energy band gap narrowing in p^+ silicon heavily doped with boron", *J. Appl. Phys.,* 2014.
[29] A. Cuevas, R. Merchan and J. C. Ramos, "On the systematic analytical solutions for minority-carrier transport in non-uniform doped semiconductors: application to solar cells", *IEEE Trans. Electron Devices,* 40, 1181, 1993.
[30] D. K. Schroder, Semiconductor Material and Device Characterization (Wiley, Hoboken, 2006), p. 146.
[31] J. Robertson, Band offsets, "Schottky barrier heights, and their effects on electronic devices", *J. Vac. Sci. Technol. A* 31, 050821 (2013)
[32] L. E. Black and K. R. McIntosh, "Modeling recombination at the Si-Al_2O_3 interface", *IEEE J. Photvolt.*, 3 936, 2013.
[33] Z. Jin, G. A. Bhat, M. Yeung, H. S. Kwok and M. Wong, "Nickel induced crystallization of amorphous silicon thin films", *J. Appl. Phys.,* 84, 194, 1998.
[34] L. Hultman, A. Robertsson, H. T. G. Hentzell, I. Engstrom and P.A. Psaras, "Crystallization of amorphous silicon during thin film gold reaction", *J. Appl. Phys.,* 62, 3647, 1987.

[35] J. Bullock, A. Cuevas, D. Yan, B. Demaurex, A. Hessler-Wyser and S. De Wolf, "Passivated Contacts to n^+ and p^+ Silicon Based on Amorphous Silicon and Thin Dielectrics" *Proceedings of the 40th IEEE Photovoltaic Specialist Conference*, Denver, USA, 2014.
[36] A. Cuevas, "Physical model of back line-contact front-junction solar cells," *J. Appl. Phys*., 113, 164502, 2013.
[37] A. Cuevas, "Geometrical Analysis of Solar Cells with Partial Rear Contacts", *IEEE J. Photovolt*., p.485 – 493, 2012.
[38] A. Fell, "A free and fast 3D/2D solar cell simulator featuring conductive boundary and quasi-neutrality approximations," *IEEE Trans. Electron Devices*, 60 , 733, 2012.

Simple silicon solar cells featuring an *a*-Si:H enhanced rear MIS contact

James Bullock[a.)], Andres Cuevas, Christian Samundsett, Di Yan, Josephine McKeon and Yimao Wan

Research School of Engineering, The Australian National University, Canberra, ACT 2601, Australia

Published in Solar Energy Materials and Solar Cells

This letter presents the experimental demonstration of silicon solar cells that incorporate an enhanced MIS passivated contact scheme on a phosphorus diffused surface. By depositing intrinsic a-Si:H on an ultrathin SiO_x layer and alloying with an overlying aluminium layer, the interface passivation has been vastly improved over that of conventional MIS contacts, whilst maintaining a low contact resistance. This paper focuses on the optimisation of the Al / a-Si:H alloying process and the influence of the tunnelling SiO_x layer thickness. A conversion efficiency of 21.0 % has been achieved for n-type cells fabricated with a front boron diffusion and a full area rear MIS passivated phosphorus diffusion. The cells exhibit a moderate V_{oc}=666 mV and FF=0.805, whereas J_{sc} 39.3 mA/cm^2 is relatively low due to a non-optimal antireflection coating and back surface reflector, and hence will be subject to further improvement.

Introduction. Steady progress in the understanding of dopant diffused regions in crystalline silicon (*c*-Si) and of the technologies used to electrically passivate them has advanced the simple p^+nn^+ solar cell to very high conversion efficiencies. Well-passivated, moderately-doped phosphorus and boron diffusions with corresponding recombination current parameters J_0 of less than 10 fA/cm^2 can now be reproduced consistently [1, 2]. It is straightforward to verify that such surface boundary conditions, together with the assumptions of intrinsic bulk lifetime [3] and negligible optical losses, can permit efficiencies in excess of 26%. However as soon as the metal contact, required to extract carriers from the cell, is placed on a moderately doped diffusion, the recombination parameter increases to values above 1000 fA/cm^2. This means that, even if the metal contact fraction is kept very small, recombination at the metal contacts tends to dominate the total surface recombination current, thereby limiting the cell efficiency of directly metalized devices.

These numbers show the importance of developing passivated contacts, that is, of achieving a low contact recombination parameter J_{0c} without incurring prohibitive resistive losses. The benefits of this philosophy have been demonstrated at the cell level by a number of research groups and companies [4, 5, 6, 7, 8]. Previous studies have explored metal-insulator-semiconductor (MIS) structures and found that they can permit the passage of electric current with an acceptable contact resistivity, if the thickness of the insulator (SiO_x in the cases discussed in this paper) is less than ~1.8 nm [9, 10, 11]. But achieving good surface passivation with such a thin dielectric is difficult and the corresponding J_{0c} values are typically in the range of 350-800 fA/cm^2 [9, 10]. A recently developed strategy to improve this passivation involves the deposition of a hydrogen-rich *a*-Si:H capping-layer on top of the tunnel insulator. This strategy has been shown to reduce the J_{0c} by an order of magnitude. The *a*-Si:H layer is then alloyed at low

temperatures with an overlying aluminium layer. The resultant alloyed film is comprised of up to 4 - 40 atomic % aluminium and is conductive enough to present no significant impediment to carrier flow [12, 9].

Table I indicates that the recombination parameter J_{0c} is reduced ~30 fold for an n^+ region with the *a*-Si:H enhanced MIS contacts compared to the standard metal-contacted n^+ region. This means that the *a*-Si:H enhanced MIS approach offers an attractive alternative for full-area passivated contacts on the rear-side of silicon solar cells, promising an increase of up to 50 mV in device voltage. This letter presents the first experimental demonstration of such a contact structure at the device level. In particular, the influence of the anneal conditions (anneal temperature and time) and the tunnelling SiO_x thickness on the cell efficiency are examined.

Contact system	ρ_c (mΩcm^2)	J_{0c} (fA/cm^2)
c-Si(n^+) / Al	0.03	1200
c-Si(n^+) / SiO_2 / Al	40	400
c-Si(n^+) / SiO_2 / *a*-Si:H / Al	10	40

Table I. Measured contact resistivity ρ_c and recombination current parameter J_{0c} for different passivated contact systems that incorporate moderately doped phosphorus diffusions, taken from refs. [9, 12].

Device fabrication. Given that the MIS structure is opaque, the simplest way in which to demonstate it's capabilities is to apply it as a full area rear contact. A series of small (4 cm^2) cells are fabricated using Czochralski grown, 1.9 Ω.cm n-type, 180 µm *c*-Si substrates. The cell structure, as shown in the inset of Figure 3, consists of a boron diffused region on a textured front-side and a phosphorus diffused region at the planar rear-side. The sheet resistance of both diffusions is approximatly 110 Ω /□. The front-side passivation and antireflection stack consists of ~18 nm of Al_2O_3 film deposited at

~175 ^{o}C via plasma assisted atomic layer deposition (ALD, Beneq TFS 200) capped with ~60 nm of SiN_x deposited at ~400 ^{o}C by plasma assisted chemical vapor deposition (PECVD, Oxford PlasmaLab 100). The *a*-Si:H enhanced-MIS rear-side contacts were formed by sequentially growing a thin oxide layer, depositing an *a*-Si:H film and evaporating a thick aluminium layer. The tunneling SiO_x is created by rapid thermal oxidation (< 60 seconds) of the phosphorus diffused surface at 800 ^{O}C in pure oxygen. The oxidation time is varied to produce a range of SiO_x film thicknesses between 1.5 and 1.7 nm as measured by spectroscopic ellipsometry (J.A. Woolam M2000 ellipsometer). It should be noted that given the inherent difficulties with uniformly growing and measuring such thin films we estimate an uncertainty of ±1 Å, which is significant given the range of thicknesses. This oxidation step was found to be sufficient to activate the Al_2O_3 / SiN_x stack passivation of the boron diffused surface. Following the oxidation, ~30 nm of intrinsic *a*-Si:H was deposited at ~300 ^{o}C via PECVD (Roth and Rau AK400). At this point the pre-metallization implied voltage iV_{oc} could be measured via the photoconductive decay (PCD) method (Sinton WCT 120) before the cells were capped with ~1 μm of thermally evaporated Aluminium. Next, a front metal grid (~3% of the front surface area) is formed by photolithography, vacuum metal evaporation (Cr ~30 nm, Pd ~30 nm, Ag ~40 nm) and Ag electroplating. Finally, the entire cell structure is annealed at temperatures between 300 and 425 ^{o}C to sinter the front contacts and alloy the rear Al / *a*-Si:H stack. The quality of the front-side passivation stack was found to be relatively stable for these annealing temperatures. As shown below, the thickness of SiO_x film and the thermal budget of the alloying step are critical to the achievement of a good fill factor *FF* without compromising the open-circuit voltage V_{oc}.

As a comparison, alike cells were fabricated which utilise a partial rear contact (PRC) scheme rather than a full area MIS contact. The rear-side of these reference cells

were passivated with a ~100 nm PECVD SiN_x film, following which a Ag rear contact with a ~1 % fraction was photlithographically defined and evaporated. For these cells a standard anneal step of 400 ºC for 30 minutes is used to sinter the contacts and activate the front surface passivation. Aside from the abovementioned differences, the two cells structures were essentially identical.

The solar cell I-V characteristics were measured under standard one sun conditions (~1000 W/m^2, ~25 °C, AM 1.5 global spectrum) using a solar simulator (Photo Emission Tech, model SS150). The light intensity was calibrated using a certified reference cell from Fraunhofer ISE Cal lab. A 2 × 2 cm apperture mask was used to avoid possible lateral collection of carriers generated in the periphery of the device. We estimate that the potential error in the efficency measurement is ± 1 % absolute.

The contribution of the different cell regions to the total recombination was monitored via control silicon test structures which were processed alongside the cells. The carrier lifetime of these samples was measured using the photoconductance decay (PCD) method (Sinton WCT 120) and recombination current parameters were extracted using both low and high injection extraction techniques [13, 14]. Different test samples were prepared to characterize the front metalized and passivated p^+ regions, the post-processing bulk lifetime of the silicon wafer and the rear MIS n^+ contact.

a-Si:H/aluminium MIS contact optimisation. To optimise the MIS contact structure, we have measured the cell performance as a function of the SiO_x thickness and the thermal budget of the Al / *a*-Si:H alloy process, focusing in particular on the impact to the open-circuit voltage (V_{oc}) and fill-factor (FF). Based on previous work, the best combination of J_{0c} and ρ_c should be obtained for an oxide thickness of ~1.6 nm, an *a*-Si:H layer thickness of 30 nm, and an Al thickness of > 1 μm [9]. It was also found that

annealing at temperatures in the range of 250-350 ºC for 30 minutes was adequate to sufficiently reduce the resistivity of the *a*-Si:H layers so that carrier tunnelling across the thin SiO_x was the major impediment to current flow. However, as shown below, the optimum temperature range for contacts at the cell level is higher.

Impact of the SiO_x thickness. Figures 1a-d show the dependence of the V_{oc}, short circuit current J_{sc}, FF and efficiency η, on the thickness of the SiO_x layer. For this set of experiments the time of the annealing step was kept at 30 minutes, while three different temperatures were explored; 300 ^{O}C, 400 ^{O}C, and 425 ^{O}C.

As shown in Figure 1a, for SiO_x thicknesses in the range of 1.5 - 1.7 nm, the V_{oc} remains approximately constant at 660–666 mV for all the annealing temperatures. Reference lines for an iV_{oc} of 682±3 mV before front and rear metalisation (as inferred from PCD measurements of the pre-metalised cells) and a lower limit iV_{oc} of < 620 mV (inferred from PCD measurements of the unpassivated rear n^+ diffusion), are included in Figure 1a. The comparison of the measured cell V_{oc} with these two reference lines suggests that a high level of surface passivation is attained at the rear surface. Initial studies on this contact structure showed a strong dependence of the iV_{oc} on oxide thickness, which suggests that for these cells the bulk or the front surface of the cell may be limiting the V_{oc}. Control samples used to monitor the recombination of the front surface metalised and passivated regions (accounting for their relative surface converage) as well as the post-processing bulk recombination revealed that these regions contribute a J_0 of ~35, ~45 and ~100 fA/cm^2 respectively.

Figure 1c shows that an increasing SiO_x thickness has a strongly negative impact on the FF, in-line with the theoretical exponential decrease in tunnelling probability with insulator thickness. Such reduction can be observed for all the annealing temperatures,

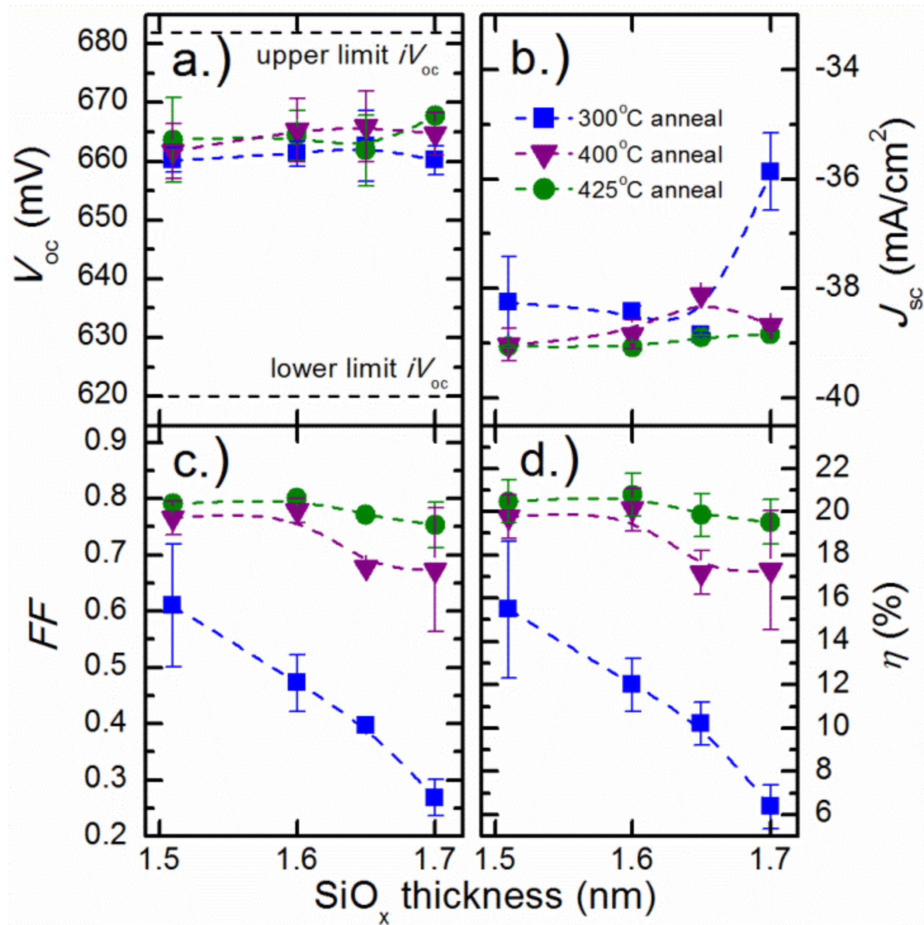

Figure 1.a.) V_{oc}, b.) J_{sc}, c.) FF and d.) η as a function of SiO_x thickness for a series of cells featuring an a-Si:H enhanced MIS rear contact. Error bars are based off the measured spread in data (most points are an average of at least 2 cells) or the estimated error measurement – whichever is largest. Lines provide a guide to the eyes only.

especially below 400 ^{O}C. When the temperature is too low, 300 ^{O}C, the Al / *a*-Si:H alloying process is not sufficiently well formed through the *a*-Si:H layer and across the whole area of the device. This results in a low $FF \approx 0.60$ even for the thinnest oxide, as the resistance caused by tunneling through the SiO_x is compounded with a resistive impediment created by a residual *a*-Si:H layer. The trend corresponding to this low temperature shows that the *FF* strongly decreases as the SiO_x thickness is increased to 1.6 nm and above. At thicknesses greater than 1.6 nm, even J_{sc} is adversely affected as is seen in Figure 1b.

The efficiency trend plotted in Figure 2d is seen to be mostly dominated by changes in the *FF*. The highest results for the cells annealed at both 400 and 425 °C occurs when an oxide thickness of ~1.6 nm is used – in agreement with our previous studies [10, 9].

Impact of the Al / *a*-Si:H alloy time and temperature. Figures 2 a-d provide trends in the solar cell parameters as a function of the Al / *a*-Si:H alloying thermal budget. For this set of experiments, the tunnelling oxide had a fixed optimum thickness of ~1.6 nm. We have explored annealing temperatures of 300 °C, 400 °C and 425 °C, and varied the annealing time between 10 and 60 minutes. Before any annealing, the *a*-Si:H and Al layers remain intact, and the contact exhibits a rectifying, rather than Ohmic behaviour. As a consequence, the *FF* is extremely low at 0.2, and J_{sc} is affected by the very high series resistance; the partly rectifying contact also causes a reduction of V_{oc}, which only reaches 590 mV, a value even lower than the 620 mV that can be estimated for this solar cell with a directly metalized rear n^+ surface. It is likely at this point that the front contact, which is yet to receive a sintering step, is also highly resistive and hence also contributes to the poor cell characteristics.

Annealing at 300 °C for just 10 minutes greatly reduces the series resistance, lifting the V_{oc} up to 660 mV, and allowing for the optically-limited J_{sc} of 38 mA/cm^2 to be measured. Nevertheless, the *FF* remains slightly below 0.50, even if the anneal time is prolonged to 60 minutes. This is at odds with our previous experiments on contact structures, where 300°C was sufficient to produce a low contact resistivity [9]. It can be concluded that differences in the fabrication procedure of the test structures and cells leads to a different range of optimum annealing temperature.

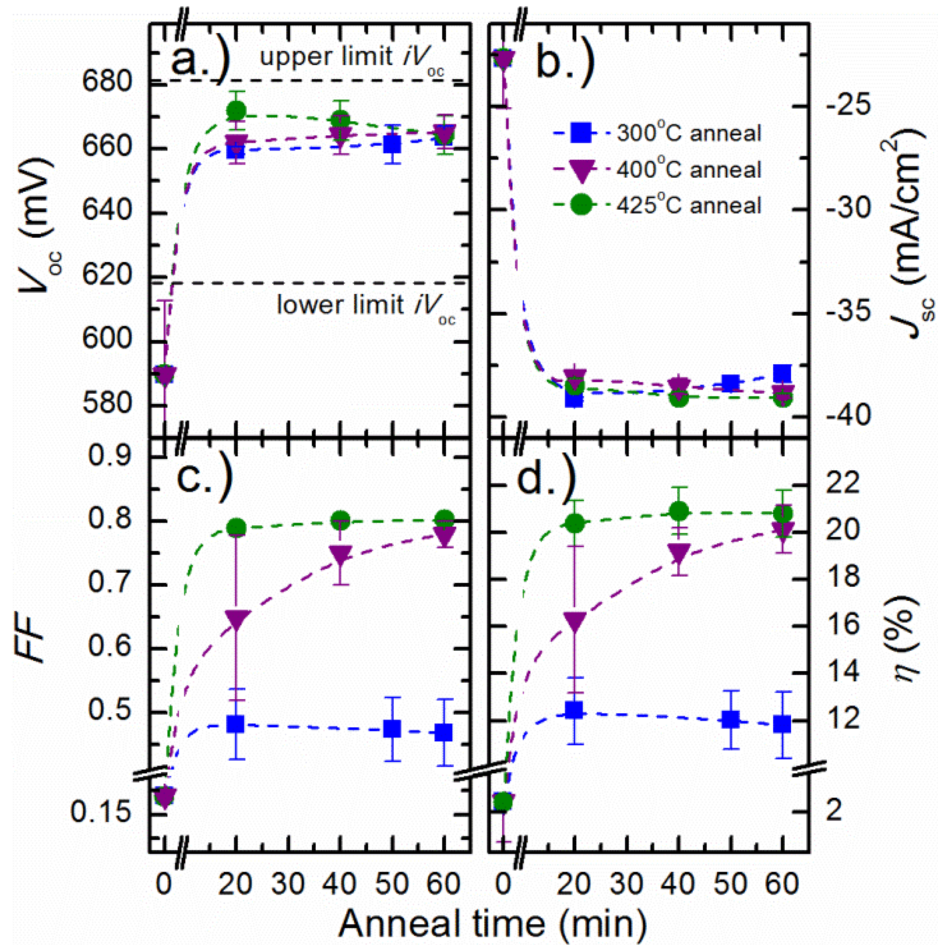

Figure 2.a.) V_{oc}, b.) J_{sc}, c.) FF and d.) η as a function of anneal time for a series of cells featuring an a-Si:H enhanced MIS rear contact. Error bars are based off the measured spread in data (most points are an average of at least 2 cells) or the estimated error measurement – whichever is largest. Lines provide a guide to the eyes only.

Increasing the annealing temperature to 400 ºC improves the alloying process, but as can be seen in the evolution of the *FF* with annealing time, the process is slow, and takes ~60 minutes to complete. Only then the *FF* reaches 0.79 with a corresponding efficiency of ~20 %. A temperature of 425 ºC is optimal for contact formation; after 20 minutes of annealing the alloying process has progressed sufficiently that the initial a-Si:H layer, now converted to a conductive mixed Al – Si layer, presents no impediment to carrier flow. After these 20 minutes, the V_{oc} reaches its maximum value of 672 mV and then it drops-off very slowly, presumably due to a small degradation in surface

passivation due to dehydrogenation or partial disintegration of the SiO_x layer. The *FF* takes a bit longer, ~40 minutes, to reach a maximum of 0.805; this time also corresponds to a maximum conversion efficiency of 21.0 %, even though it remains above 20 % for annealing times between 10 and 60 minutes.

Comparison to a conventional high efficiency solar cell. Figure 3 presents a comparison between the champion MIS passivated contact cell and a reference cell having an alike structure, but with partial rear contacts (PRC) formed on the phosphorus diffusion by photolithographically patterning a silicon nitride layer (rear contact fraction ~1 %). The inset of this figure provides representative diagrams of the two structures as well as values for V_{oc}, J_{sc}, *FF* and η of the two cells. A conversion efficiency of 21.0 % has been achieved for the MIS contact device, with excellent V_{oc} = 666 mV and *FF* = 0.805. Both are comparable to the parameters of the reference cell, evidencing the good characteristics of the passivated contact both in terms of recombination and transport.

The short-circuit current, J_{sc}=39.3 mA/cm^2 is significantly lower than the 40.2 mA/cm^2 of the PRC reference cell, and this explains the 0.5 % lower efficiency. The difference is attributed primarily to better rear reflection characteristics for the PRC cell, which has been confirmed by reflectance and quantum collection measurements [15]. These measurements also revealed slightly better front antireflection and shading properties for the PRC cell, which further contribute to the difference in current. It is expected that the optical properties of the *a*-Si:H / Al alloy are similar to that of the Al alloyed region commonly implemented as the rear contact in industrial *c*-Si solar cells. It can be envisioned that a higher J_{sc} may be achieved by restricting the MIS contact to a

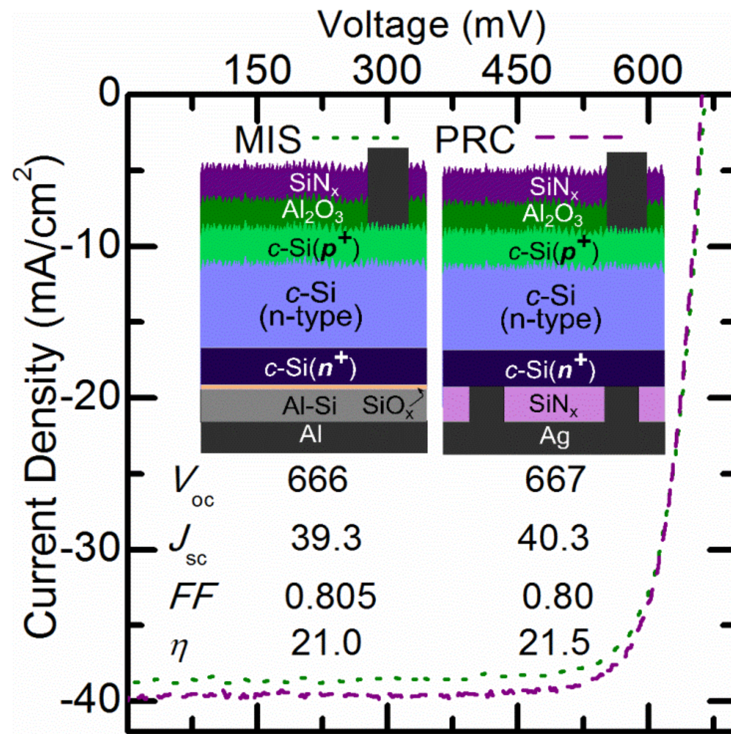

Figure 3: Light I-V comparison of alike n-type cells with an a-Si:H enhanced MIS rear contact and directly metalized partial rear contact.

smaller fraction of the rear surface, and perhaps by replacing the aluminium with silver as an alloy metal [16].

Conclusion. A novel passivated contact technology based on enhancing an MIS structure with PECVD *a*-Si:H has been demonstrated, with the achievement of 21.0 % efficient solar cells that present both a high V_{oc}=666 mV and FF=0.805. These results are realised using a ~1.6 nm SiO_x tunnel film and a 425ºC alloying step. Further improvements should be possible by optimising the optics and the front side of the device. The simplicity in fabrication and high potential in cell performance make the enhanced MIS contact of great interest to the silicon photovoltaic industry.

Acknowledgements. The authors wish to thank Thomas Allen for fruitful discussions. This project has been supported by the Australian Government through The

Australian Renewable Energy Agency (ARENA). Facilities at the Australian National Fabrication Facility was utilised for this project.

References

[1] B. Hoex, J. Schmidt, R. Bock, P. P. Altermatt, M. C. M. van de Sanden and W. M. M. Kessels, “Excellent passivation of highly doped p-type Si surfaces by the negative-charge-dielectric Al2O3,” *Applied Physics Letters,* vol. 91, no. 11, pp. -, 2007.

[2] M. J. Kerr, J. Schmidt, A. Cuevas and J. H. Bultman, “Surface recombination velocity of phosphorus-diffused silicon solar cell emitters passivated with plasma enhanced chemical vapor deposited silicon nitride and thermal silicon oxide,” *Journal of Applied Physics,* vol. 89, no. 7, pp. 3821-3826, 2001.

[3] A. Richter, S. W. Glunz, F. Werner, J. Schmidt and A. Cuevas, “Improved quantitative description of Auger recombination in crystalline silicon,” *Phys. Rev. B,* vol. 86, p. 165202, Oct 2012.

[4] M. A. Green, A. W. Blakers, Z. R. Willison, T. Szpitalak, E. M. Keller, E. Gauja and P. J. Hart, “The MINP solar cell - A new high voltage, high efficiency silicon solar cell,” in *Proceedings 15th Photovoltaic Specialists Conference, Kissimmee, FL*, 1981.

[5] J. Heng, J. Fu, B. Kong, Y. Chae, W. Wang, Z. Xie, A. Reddy, K. Lam, C. Beitel, C. Liao, C. Erben, Z. Huang and Z. Xu, “>23% High-Efficiency Tunnel Oxide Junction Bifacial Solar Cell With Electroplated Cu Gridlines,” *Photovoltaics, IEEE Journal of,* vol. PP, no. 99, pp. 1-5, 2014.

[6] F. Feldmann, M. Bivour, C. Reichel, M. Hermle and S. W. Glunz, “Passivated rear contacts for high-efficiency n-type Si solar cells providing high interface passivation quality and excellent transport characteristics,” *Solar Energy Materials and Solar Cells,* Vols. 120, Part A, no. 0, pp. 270-274, 2014.

[7] J. Schmidt, A. Merkle, R. Brendel, B. Hoex, M. C. M. v. de Sanden and W. M. M. Kessels, “Surface passivation of high-efficiency silicon solar cells by atomic-layer-deposited Al2O3,” *Progress in Photovoltaics: Research and Applications,* vol. 16, no. 6, pp. 461-466, 2008.

[8] D. Zielke, J. H. Petermann, F. Werner, B. Veith, R. Brendel and J. Schmidt, “Contact passivation in silicon solar cells using atomic-layer-deposited aluminum oxide layers,” *physica status solidi (RRL)“ Rapid Research Letters,* vol. 5, no. 8, pp. 298-300, 2011.

[9] J. Bullock, A. Cuevas, D. Yan, B. Demaurex, A. Hessler-Wyser and S. De Wolf, “Amorphous silicon enhanced metal-insulator-semiconductor contacts for silicon solar cells,” *Journal of Applied Physics,* vol. 116, no. 16, 2014.

[10] J. Bullock, D. Yan and A. Cuevas, “Passivation of aluminium n+ silicon contacts for solar cells by ultrathin Al2O3 and SiO2 dielectric layers,” *physica status solidi (RRL) Rapid Research Letters,* vol. 7, no. 11, pp. 946-949, 2013.

[11] D. Pulfrey, “MIS solar cells: A review,” *Electron Devices, IEEE Transactions on,* vol. 25, no. 11, pp. 1308-1317, Nov 1978.

[12] J. Bullock, D. Yan, A. Cuevas, B. Demaurex, A. Hessler-Wyser and S. De Wolf, “Passivated contacts to n+ and p+ silicon based on amorphous silicon and thin dielectrics,” in *Photovoltaic Specialist Conference (PVSC), 2014 IEEE 40th*, 2014.

[13] A. Cuevas, “The effect of emitter recombination on the effective lifetime of silicon wafers,” *Solar Energy Materials and Solar Cells ,* vol. 57, no. 3, pp. 277-290, 1999.

[14] D. Kane and R. Swanson, “Measurement of the Emitter Saturation Current by a Contactless Photoconductivity Decay Method,” in *Proc of the 18th IEEE Photovoltaic Specialists Conference*, 1985.

[15] Y. Wan, J. Bullock, A. Cuevas, C. Samundset and D. Yan, "p+nn+ Silicon Solar Cell with a Full-Area Rear MIS Passivated Contact," in *5th International Conference on Crystalline Silicon Photovoltaics*, 2015.

[16] B. Bian, J. Yie, B. Li and Z. Wu, "Fractal formation in a-Si:H/Ag/a-Si:H films after annealing," *Journal of Applied Physics,* vol. 73, no. 11, pp. 7402-7406, 1993.

3 Molybdenum oxide hole-selective contacts for *c*-Si solar cells

3.1 Foreword

Within the wider photovoltaics community, particularly organic photovoltaics, the high work function transition metal oxides (MoO_x, VO_x and WO_x) have been widely used in hole selective contacts. Among the major benefits of these films are high transparency, with a band gap of ~3.3 eV, and simplicity of deposition, commonly being deposited by thermal evaporation or liquid phase deposition. The use of these films in *c*-Si solar cells is, however, is a relativly new development, with most work being conducted in the last two years.

In this chapter, thermally evaporated sub-stoichiometric MoO_x films are explored as hole contacts on p and n-type *c*-Si. The contact recombination and resistive properies of the direct *c*-Si / MoO_x interface are investigated as a function of MoO_x thickness via a series of ρ_c test structures. With this knowledge, novel MoO_x partial rear contact structures and full-area SiO_x/MoO_x heterocontacts are trialled as hole contacts in proof-of-concept cells, resulting in efficiencies greater than 20% in the former case. Given below is a brief summary of the different manuscripts presented in this chapter in order of their appearance.

Manuscript 1: James Bullock, Andres Cuevas, Thomas G. Allen, Corsin Battaglia, *"Molybdenum Oxide MoO_x: A Versatile Hole Contact For Silicon Solar Cells"* Applied Physics Letters, 105, 232109, 2014.

This paper examines the use of MoO_x films to assist in hole collection on lightly and heaviliy doped p-type *c*-Si, as well as lightly doped n-type *c*-Si. It is found that, even with very thin MoO_x films, recombination current factors of 200 and 300 fA/cm^2 can be obtained on p- and n-type *c*-Si surfaces, respectivly. These recombination factors are found to be largely independent of the wafer doping. The optimum ρ_c on p-type and p$^+$ surfaces is found to be ~1 and 0.2 mΩcm^2, respectivly, with a thickness of ~10 nm. On the n-type surface a ρ_c of ~30mΩcm^2 is extracted. This results indicate that MoO_x could be a good alternative to metal-contacted boron diffusions.

Manuscript 2: James Bullock, Di Yan, Andres Cuevas, Yimao Wan and Christian Samundsett, *"n- and p-type silicon solar cells with molybdenum oxide hole contacts"* Energy Procedia, Volume 77, Pages 446–450, 2015.

In this manuscript simple n- and p-type *c*-Si cells implementing MoO_x based hole contacts are trialled. The n-type cell, referred to as *moly-poly,* utilises a *poly*-Si(n$^+$) rear contact and a front SiO_x / MoO_x / ITO contact. These proof-of-concept cells achieve a power conversion efficiency of 16.7% for a 3×3 cm^2 cell. The p-type cell design utilises a standard phosphorus doped front electron contact and a rear full-area MoO_x / Ag hole contact, to attain a conversion efficiency of 16.4%. Both cells utilise very simple un-optimised fabrication procedures with only ~10 steps, and a crude front metal grid. Nevertheless, they serve to prove that MoO_x does indeed function as a hole-selective contact, both on p-type and n-type wafers.

Manuscript 3: James Bullock, Christian Samundsett, Andrés Cuevas, Di Yan, Yimao Wan and Thomas Allen, *"Proof-of-concept p-type silicon solar cells with molybdenum oxide partial rear contacts"* IEEE Journal of Photovoltaics, vol. 5, no. 6, 2015.

In this paper, knowledge gained in the first paper of this chapter and via three dimensional simulations are combined to design and fabricate a novel p-type partial rear contact (PRC) cell. This cell structure utilisies a ~ 5% rear MoO_x contact to collect holes in combination with a standard phosphorus doped front electron contact. A power conversion efficiency of 20.4% is attained from this cell structure, a promising result given the infancy of this approach.

3.2 First author manuscripts

Molybdenum Oxide MoO_x: A Versatile Hole Contact For Silicon Solar Cells

James Bullock[1,a.)], Andres Cuevas[1], Thomas Allen[1] and Corsin Battaglia[2].

[1]*Research School of Engineering, The Australian National University, Canberra, ACT 0200, Australia*

[2]*Empa, Swiss Federal Laboratories for Materials Science and Technology, 8600 Dübendorf, Switzerland*

Published in Applied Physics Letters

This letter examines the application of transparent MoO_x ($x<3$) films deposited by thermal evaporation directly onto crystalline silicon (c-Si) to create hole-conducting contacts for silicon solar cells. The carrier-selectivity of MoO_x based contacts on both n- and p-type surfaces is evaluated via simultaneous consideration of the contact recombination parameter J_{0c} and the contact resistivity ρ_c. Contacts made to p-type wafers and p^+ diffused regions achieve optimum ρ_c values of 1 and 0.2 $m\Omega{\cdot}cm^2$, respectively, and both result in a J_{0c} of ~200 fA/cm^2. These values suggest that significant gains can be made over conventional hole contacts to p-type material. Similar MoO_x contacts made to n-type silicon result in higher J_{0c} and ρ_c with optimum values of ~300 fA/cm^2 and 30 $m\Omega{\cdot}cm^2$, but still offer significant advantages over conventional approaches in terms of contact passivation, optical properties and device fabrication.

The spatial separation of light-generated electron-hole pairs is critical to the functionality of all photovoltaic devices. The segregation of electrons and holes towards their respective contact regions requires the formation of pathways of asymmetric electron and hole conductivity [1]. The majority of crystalline silicon (*c*-Si) solar cells achieve this by introducing a high concentration of dopants (usually phosphorus, aluminium or boron) in the near-surface regions of the *c*-Si wafer. The dopant species increase the concentration of (and hence, conductivity for) one charge carrier whilst having the opposite effect for the other. This approach is particularly advantageous for directly metalized silicon contacts as the metal-silicon interface suffers from both large majority carrier resistance (due to potential barriers at the interface) and high minority carrier recombination (due to a high concentration of interface defect sites), both of which can be reduced by heavy surface doping. However, the high majority carrier concentration within the doped regions also causes significant Auger recombination, introducing a fundamental limit on the possible reduction of recombination. The lowest recombination parameters for heavily doped, metal-contacted regions have experimentally been found to be ~300 fA/cm^2 for phosphorus [2], ~400 fA/cm^2 for boron [3], and higher still for aluminium alloyed [4] regions[1]. This limitation has prompted the development of device designs with small contact fractions where the total minority carrier recombination can be reduced at the expense of increased majority carrier resistance – a trade-off which is usually permissible given their relative impact on solar cell performance. However, difficulties associated with the transferral of small contact fractions to industrial pilot lines have led to research into alternative means of separating carriers and contacting solar cells.

[1] The given J_0 values have been adjusted in accordance with the intrinsic carrier concentration used in this letter ($n_i = 8.6\times10^9$ cm^{-3}).

An alternative strategy to achieving carrier-selectivity is via the application of thin layers of materials on the *c*-Si absorber that provide an asymmetry in carrier conductivity. Cell architectures utilising such materials have recently demonstrated world record efficiencies on *c*-Si [5, 6], outperforming their dopant diffused counterparts. Not surprisingly, research into suitable electron and hole collecting layers on *c*-Si is currently a popular topic, with some groups transferring layers commonly used for the same purpose from non *c*-Si based solar cells. For example organic polymer [7, 8], transition metal oxide [9, 10, 11, 12] and transparent conductive oxide [13, 14] based contacts, which are standard in other photovoltaic technologies, have recently been demonstrated on *c*-Si. Among these contacting schemes, the use of sub-stoichiometric molybdenum oxide MoO_x ($x<3$) stands out as particularly attractive given its ease of deposition and already demonstrated performance on *c*-Si [9, 10]. This letter examines the application of MoO_x directly to *c*-Si to create a hole-transporting contact for *c*-Si solar cells.

Molybdenum trioxide MoO_3 is a wide band-gap material (~3 eV) with an exceptionally large electron affinity (~6.7 eV) and ionisation energy (~9.7 eV) [10, 15]. When deposited by vacuum evaporation from a solid MoO_3 source, as is the case in this letter, a slightly sub-stoichiometric ($MoO_{x,\ x<3}$) amorphous film results [9, 16]. The reduced Mo oxidation state results in the formation of a defect band below the conduction band and provides the film with a semi-metallic, n-type character [10, 15, 16]. The conductivity of MoO_x films has been shown to vary by more than ten orders of magnitude in transitioning from the insulating MoO_3, with reported conductivities as low as 10^{-7} S/cm, to the semi-metallic MoO_2 which exhibits conductivities in the range of 10^4 S/cm [15, 17]. Gains in conductivity are typically weighed against transparency and work function – both of which are found to decrease with a decreasing oxidation state [15, 18].

The most significant characteristic of thermally evaporated MoO_x films is their large chemical potential of up to ~6.9 eV – much higher than that of the elemental metals, a characteristic that they share with two other sub-stoichiometric transition metal oxides: VO_x and WO_x. Amongst these three oxides, MoO_x has the additional advantage of a low melting point, which assists in maintaining a high oxidation state and a low thermal budget when evaporating.

When MoO_x is applied to *c*-Si, the large chemical potential difference between the two materials induces a balancing electrostatic potential which falls partially across both materials and, if Fermi-level pinning is present, across the interface. Whilst Fermi-level pinning is pervasive at elemental metal / *c*-Si interfaces, it is still unknown to what extent it affects the MoO_x / *c*-Si interface, and it has recently been suggested that MoO_x can partially alleviate this effect for transition-metal dichalcogenides [17]. In the event of weak or no Fermi-level pinning at the MoO_x / *c*-Si interface, a hole accumulation layer on p-type *c*-Si and a hole inversion layer on n-type *c*-Si would be expected - facilitating low resistance hole transport out of the *c*-Si absorber.

In this letter the application of MoO_x to *c*-Si is investigated to form simple hole contacts in three different configurations. These are categorised as 'accumulation' type contacts to *i)* lightly doped p-type silicon (referred to hereafter ***pSi/***MoO_x contact) and *ii)* heavily boron doped silicon (referred to hereafter as ***p⁺Si/***MoO_x contact), and *iii)* an 'inversion' type contact to low resistivity n-type silicon (referred to hereafter as ***nSi/***MoO_x contact).

The efficacy of the the ***pSi/***MoO_x, ***p⁺Si/***MoO_x and ***nSi/***MoO_x hole contacts, that is, their selectivity towards holes, is assessed via their recombination and resistive properties. The contact recombination parameter J_{0c} (as determined from carrier lifetime

test structures) provides information on the undesired 'conductivity' presented to electrons towards the *c*-Si / MoO_x interface, whilst the contact resistivity ρ_c (as determined from contact resistance test structures) indicates the detrimental resistance to holes. Improved hole-selectivity is achieved via simultaneous minimisation of J_{0c} and ρ_c.

All test structures were fabricated on (100) oriented, float-zone, *c*-Si substrates. The wafer resistivities of the ***pSi/***MoO_x and ***nSi/***MoO_x structures were ~2.1 Ωcm and ~4.2 Ωcm respectively, whilst the ***p⁺Si/***MoO_x contact structures were fabricated on 100 Ωcm n-type wafers with front and rear surface boron diffusions (surface concentration N_{surf} ~1×10^{19} cm^{-3}, sheet resistance R_{sh} ~110 Ω/□). Test structures were RCA cleaned and immersed in a 1% HF solution immediately prior to MoO_x deposition. MoO_x films of 3 - 80 nm thickness were thermally evaporated at a rate of ~1 Å/s from a MoO_3 powder source (99.95% purity) with a base pressure of < 7×10^{-7} Torr.

Lifetime test structures were prepared by depositing MoO_x on both wafer surfaces. A thin palladium (Pd) (< 10 nm) over-layer was evaporated onto the MoO_x to mimic a device contact, whilst still allowing sufficient light transmission for the injection dependent carrier lifetime to be measured by the photoconductance decay technique. The J_{0c} values were extracted from the measured effective carrier lifetimes using the Kane and Swanson technique [19] with an intrinsic carrier concentration of $n_i = 8.6\times10^9$ cm^{-3} (at 25°C). This technique, originally applied to characterise dopant diffused wafer surfaces (like the ***p⁺Si/***MoO_x contact), has been shown to also be valid for undiffused wafers with strongly inverted or accumulated surfaces [20], as is expected for the ***pSi/***MoO_x and ***nSi/***MoO_x contacts.

Contact resistance test structures were made by depositing MoO_x on one side of a *c*-Si sample, following which a Pd (40 nm) / Aluminium (1 μm) metal stack was

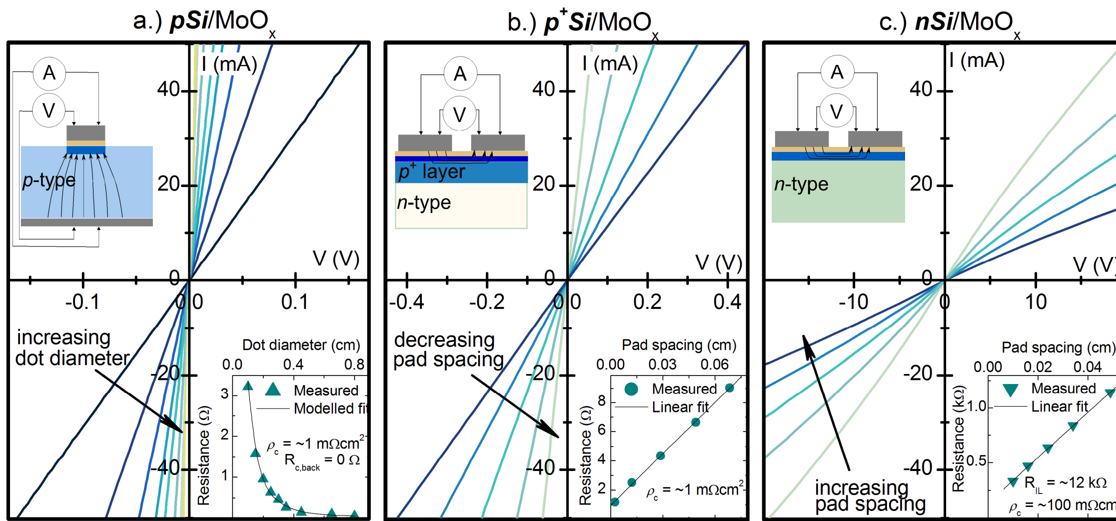

Figure 1. Current-voltage measurements and ρ_c extractions for a) ***pSi***/MoO$_x$, b) ***p$^+$Si***/MoO$_x$ and c) ***nSi***/MoO$_x$ contact structures with a fixed MoO$_x$ interlayer thickness of ~10nm.

evaporated on top through a shadow mask to create the desired contact structure pattern. For the ***nSi***/MoO$_x$ and ***p$^+$Si***/MoO$_x$ contact structures, a transfer-length-method (TLM) contact pad array was used to measure ρ_c. Whilst the use of the TLM procedure on heavily diffused surfaces is well accepted [21], its application to low resistivity wafers with a surface inversion layer has only been explored briefly [22, 23]. In this approach we have assumed that current flows are confined to the inversion layer. The sheet resistance of this inversion layer is also measurable by the TLM method.

For the ***pSi***/MoO$_x$ contacts, ρ_c was measured using the method devised by Cox and Strack [24]. For this measurement an Ohmic rear contact, formed by evaporated aluminium, was assumed to contribute negligibly to the total measured resistance; rendering the extracted ρ_c an upper limit for the ***pSi***/MoO$_x$ ρ_c. All current voltage (I-V) measurements were taken in the dark using a Keithley 2425 source-meter at ~23°C. The ρ_c values presented here are without a sintering step.

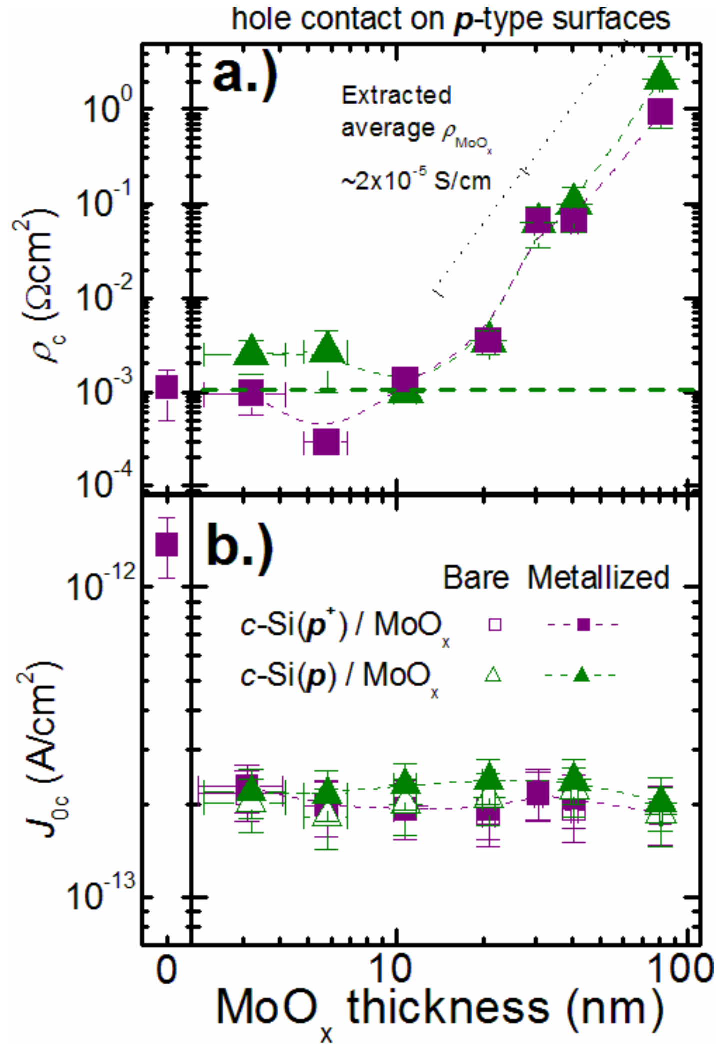

Figure 2. Dependence of a) ρ_c and b) J_{0c} on MoO_x interlayer thickness for the two accumulation type contacts. The straight horizontal line reflects the measurement resolution of the Cox and Strack method for the wafer thickness and resistivity used. Trend lines provide a guide to the eyes only.

It should be noted that in all contact structures used in this study the extracted ρ_c comprises the resistance of the MoO_x / *c*-Si and MoO_x / Pd interfaces as well as the MoO_x bulk resistivity. In addition, whilst Pd was used in this instance, less extensive tests revealed similar results using evaporated Ni and sputtered indium-tin-oxide (ITO) layers.

Representative I-V measurements and ρ_c extractions for the three contact structures are provided in Figure 1. It can be seen that all contacts exhibit Ohmic I-V

behaviour allowing accurate extractions of ρ_c. The correlation of the linear fits to data used in the TLM extraction of ρ_c was high, with R^2 values typically greater than 0.99.

Figure 2a) presents the measured dependence of ρ_c on MoO_x thickness for the 'accumulation' type contacts - ***pSi/***MoO_x and ***p⁺Si/***MoO_x. The ρ_c values corresponding to un-annealed, directly-metalized ***pSi/***Pd and ***p⁺Si/***Pd contacts are ρ_c = 10 mΩ·cm^2 and ρ_c = 1 mΩ·cm^2, respectively. Both the ***p⁺Si/***MoO_x and ***pSi/***MoO_x, contacts show similar ρ_c trends with MoO_x thickness – an initial decrease in ρ_c relative to the directly metalized surface followed by a gradual increase for thicker MoO_x films – with a local minimum ρ_c of 1 and 0.2 mΩ·cm^2 for ***pSi/***MoO_x and ***p⁺Si/***MoO_x structures with ~10 and 5 nm of MoO_x, respectively. The similarity between the two ρ_c numerical values and trends, despite the use of different contact test structures, supports the accuracy of both measurement methods. The minimum ρ_c value for the ***pSi/***MoO_x contact is at the resolution of the measurement technique, shown in Figure 2a) as a horizontal green line. Therefore, we cannot with certainty conclude that ρ_c is lower for the ***p⁺Si/***MoO_x than for the ***pSi/***MoO_x.

A comparison between the ρ_c values measured here and the MoO_x / Pd interface resistivity (measured to be ~0.2 mΩcm^2 in other studies [17]), suggests that, particularly in the case of the ***p⁺Si/***MoO_x, the total resistivity may be dominated by the MoO_x / Pd interface.

The initially decreasing ρ_c seen for both 'accumulation' contacts could potentially be a result of partial MoO_x surface coverage for the thinner films, as island growth (Volmer-Weber nucleation) is common for thermal evaporation. The increase in ρ_c for MoO_x thickness above 20nm is likely a consequence of the MoO_x bulk resistivity dominating the total ρ_c. From the measured ρ_c of the thicker structures (30 – 80 nm of MoO_x) we extract an average dark conductivity σ_{dark} for the MoO_x film of ~2×10^{-5} S/cm,

which falls towards the lower end of the range reported in the literature, indicating that the film is only slightly sub-stoichiometric. This value is comparable to that of phosphorus or boron doped *a*-Si:H films implemented in silicon heterojunction (SHJ) solar cells [25].

An analogous plot of the measured J_{0c} dependence on MoO_x thickness for the 'accumulation' type contacts is shown in Figure 2b). It can be seen that both MoO_x coated p-type surfaces produce a J_{0c} of ~200 fA/cm^2 irrespective of *i)* the MoO_x thickness; *ii)* the surface dopant concentration (***pSi/***MoO_x ~6.8×10^{15} cm^{-3} and ***p***$^+$***Si/***MoO_x ~1×10^{19} cm^{-3}); and *iii)* the application of an overlying Pd layer. The similar J_{0c} values obtained for the two p-type surfaces, despite their vastly different surface dopant concentrations, is consistent with the presence of a strong surface accumulation layer. This point is also supported by the similarities in ρ_c dependence on MoO_x thickness seen for the ***p***MoO_x and ***p***$^+MoO_x$ contacts in Figure 2a). Regardless of the underlying mechanisms, the almost identical J_{0c} and ρ_c behaviour presented above for the ***pSi/***MoO_x and ***p***$^+$***Si/***MoO_x contacts demonstrates that the MoO_x layer removes the necessity of the boron diffusion.

Figures 3a) and b) show the measured dependence of ρ_c and the (dark) inversion layer sheet resistance R_{IL} on MoO_x thickness for the ***nSi/***MoO_x 'inversion' type contact. A ρ_c value for the directly metalized surface could not be measured by the TLM technique due to the absence of a surface inversion layer, however it is known that making direct metal contact to n-type *c*-Si of moderate resistivity is technologically challenging. Similar to the ρ_c trend in Figure 2a), an initial decrease in ρ_c with MoO_x thickness is observed, again potentially associated with Volmer-Weber nucleation. After this strong initial reduction, ρ_c decreases slowly from ~150 m$\Omega\cdot$cm^2 to 30 m$\Omega\cdot$cm^2 before increasing in

the thickness range of 40 - 80 nm to a similar ρ_c to that seen for the ***pSi***/MoO_x and ***p⁺Si***/MoO_x contacts.

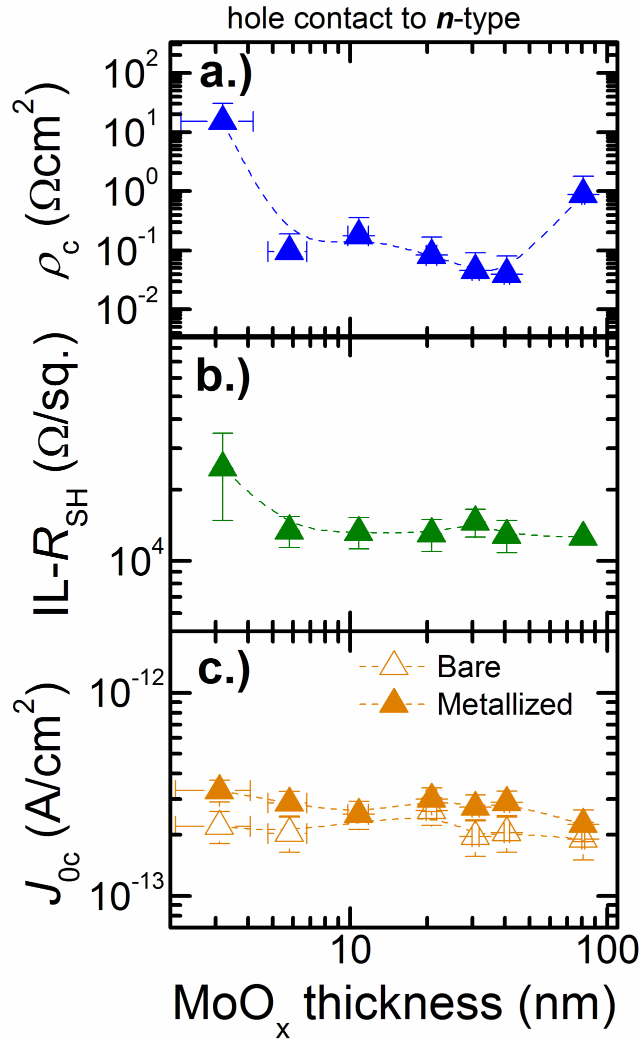

Figure 3. Dependence of a) ρ_c, b) R_{IL} and c) J_{0c} on MoO_x interlayer thickness for the ***nSi***/MoO_x inversion type contact. Trend lines provide a guide to the eyes only.

As shown in Figure 3b) the magnitude of R_{IL} initially decreases with MoO_x thickness, consistent with partial surface coverage, before saturating at ~12 kΩ/□. This sheet resistance is approximately two orders of magnitude higher than the sheet resistance of the n-type Si wafer (~150 Ω/□), which confirms that the current flow is confined to the inversion layer by the carrier depletion region formed between it and the n-type substrate, hence supporting the applicability of using the TLM method to measure this contact. The

R_{IL}~12 kΩ/□ measured here is lower than values reported for inversion layer solar cells, suggesting a higher concentration of holes near the surface [22, 23].

An equivalent inversion layer charge can be calculated from R_{IL} using an average surface hole mobility of 80 cm^2/V, taken from previous studies on MOSFET devices [26]. From this charge a corresponding potential at the *c*-Si surface ψ_s can be calculated by assuming Fermi-Dirac statistics. Under these assumptions ψ_s is calculated to be –0.92 V, with a corresponding hole surface concentration of ~8.6×10^{19} cm^{-3}.

The J_{0c} measurements for the ***nSi/***MoO_x contact as a function of the MoO_x thickness shown in Figure 3c) follow a similar trend to those in Figure 2b): J_{0c} is approximately independent of the MoO_x thickness. The non-metalized ***nSi/***MoO_x structures achieve a minimum J_{0c} of ~200 fA/cm^2, which increases to ~300 fA/cm^2 after Pd deposition.

To contextualise these results, it is illustrative to compare them with conventional aluminium and boron p^+ hole contacts. The Al alloyed p^+, formed by rapid melting and recrystallization of the *c*-Si / Al interface, is typically applied as a rear contact to a p-type wafer and hence is comparable to the ***pSi/***MoO_x contact. The relatively low Al dopant concentration (limited by a solid solubility of ~3×10^{18} cm^{-3} [27]) and the formation of recombination active point defects within the Al doped region generally limit the J_{0c} to between 600 and 900 fA/cm^2 [4, 28], although lower values have been reported [29]. Corresponding ρ_c values of 1 to 50 mΩ·cm^2 have been measured for this hole contact [30, 31]. The ***pSi/***MoO_x produces lower J_{0c} values for a wide range of MoO_x thicknesses and matches the best reported Al alloyed ρ_c values. The results in this study are especially significant given the moderate doping level of the wafers used for the ***pSi/***MoO_x contacts - suggesting that it may be possible to achieve a low ρ_c on wafers with an even lower

doping level, thus mitigating issues such as light-induced bulk lifetime degradation [32]. Improved optical performance, reduced process thermal budget and the ease by which partial contacts can be applied are all further possible advantages of the ***pSi/***MoO_x contact structure.

The boron p^+ contact, typically formed by high temperature (>900ºC) thermal diffusion and subsequent metallization, is the standard hole contact for n-type *c*-Si solar cells and hence can be compared to the ***nSi/***MoO_x contacts presented in this study. Optimised J_{0c} - ρ_c combinations of 400 fA/cm^2 and ~0.1 mΩ·cm^2 can been achieved for metal-contacted heavily doped boron diffused p^{++} contacts [3, 33]. In comparison, the optimal J_{0c} obtained for the ***nSi/***MoO_x contact is lower, J_{0c}~300 fA/cm^2, but the ρ_c value of ~30 mΩ·cm^2 is considerably higher. Despite that, the ***nSi/***MoO_x contact is still adequate for large-area contacts. We have tested such ***nSi/***MoO_x contact via a rudimentary ITO / MoO_x / *c*-Si (n) / *poly*-Si(n^+) device with a planar front surface and coarse front contact grid – achieving an open-circuit voltage of ~640 mV measured by the Suns-V_{oc} technique [34], which is consistent with the J_{0c} value given above. The obtained results for the ***p***$^+$***Si/***MoO_x also suggest that a partial MoO_x contact could be applied on a light boron diffusion to supersede the selective p^{++} contact approach with improved recombination characteristics and simplified processing.

A remaining challenge is the temperature stability of J_{0c}, which degrades at low temperatures, similar to that found for silicon heterojunction cells. This stability can be improved by the addition of an interlayer, which has also been shown to further improve surface passivation [10].

In conclusion, thin films of MoO_x deposited by thermal evaporation form excellent hole-selective contacts on both p-type and n-type *c*-Si. The passivation quality

of the contacts is independent of the MoO_x thickness, with J_{0c} values of ~200 and ~300 fA/cm^2 for p and n-type surfaces, respectively. Conversely, ρ_c is found to be strongly dependent on MoO_x thickness. Upper-limit ρ_c values of 1 and 0.2 mΩ·cm^2 have been demonstrated on p and p$^+$ surfaces respectively. The ρ_c on n-type surfaces is higher, with an optimum value of ~30 mΩ·cm^2, though still applicable to *c*-Si solar cell designs. It is clear that MoO_x films can play a significant role in the development of selective-contacts both in terms of versatility and performance.

Acknowledgments. The authors wish to thank Lachlan Black and Bénédicte Demaurex for fruitful discussions. This project was partially funded by The Australian Renewable Energy Agency. Equipment at the Australian National Fabrication Facility was utilised for this project.

References

[1] U. Würfel, A. Cuevas and P. Würfel, “Charge Carrier Separation in Solar Cells,” *IEEE Journal of Photovoltaics,* **5** ,1*,* 2015.

[2] D. Yan and A. Cuevas, “Empirical determination of the energy band gap narrowing in highly doped n+ silicon,” *Journal of Applied Physics,* vol. 114, no. 4, 2013.

[3] D. Yan and A. Cuevas, “Empirical Determination of the Energy Band Gap Narrowing in p+ Silicon Heavily Doped with Boron,” *accepted for publication, Journal of Applied Physics,* 2014.

[4] P. Altermatt, S. Steingrube, Y. Yang, C. Sprodowski, T. Dezhdar, S. Koc, B. Veith, S. Herrman, R. Bock, K. Bothe, J. Schmidt and R. Brendel, “Highly predictive modelling of entire Si solar cells for industrial applications,” in *Proc. 24th European Photovoltaic Solar Energy Conference*, 2009.

[5] M. Taguchi, A. Yano, S. Tohoda, K. Matsuyama, Y. Nakamura, T. Nishiwaki, K. Fujita and E. Maruyama, “24.7% Record Efficiency HIT Solar Cell on Thin Silicon Wafer,” *IEEE Journal of Photovoltaics,* vol. 4, no. 1, pp. 96-99, Jan 2014.

[6] K. Masuko, M. Shigematsu, T. Hashiguchi, D. Fujishima, M. Kai, N. Yoshimura, T. Yamaguchi, Y. Ichihashi, T. Mishima, N. Matsubara, T. Yamanishi, T. Takahama, M. Taguchi, E. Maruyama and S. Okamoto, “Achievement of More Than 25%; Conversion Efficiency With Crystalline Silicon Heterojunction Solar Cell,” *IEEE Journal of Photovoltaics,* no. 6, pp. 1433-1435, Nov 2014.

[7] D. Zielke, A. Pazidis, F. Werner and J. Schmidt, “Organic-silicon heterojunction solar cells on n-type silicon wafers: The BackPEDOT concept,” *Solar Energy Materials and Solar Cells ,* vol. 131, pp. 110-116, 2014.

[8] J. Schmidt, V. Titova and D. Zielke, “Organic-silicon heterojunction solar cells: Open-circuit voltage potential and stability,” *Applied Physics Letters,* vol. 103, no. 18, 2013.

[9] C. Battaglia, X. Yin, M. Zheng, I. D. Sharp, T. Chen, S. McDonnell, A. Azcatl, C. Carraro, B. Ma, R. Maboudian, R. M. Wallace and A. Javey, “Hole Selective MoOx Contact for Silicon Solar Cells,” *Nano Letters,* vol. 14, no. 2, pp. 967-971, 2014.

[10] C. Battaglia, S. M. de Nicolas, S. De Wolf, X. Yin, M. Zheng, C. Ballif and A. Javey, "Silicon heterojunction solar cell with passivated hole selective MoOx contact," *Applied Physics Letters,* vol. 104, no. 11, 2014.

[11] S. Avasthi, W. E. McClain, G. Man, A. Kahn, J. Schwartz and J. C. Sturm, "Hole-blocking titanium-oxide/silicon heterojunction and its application to photovoltaics," *Applied Physics Letters,* vol. 102, no. 20, 2013.

[12] J. Jhaveri, S. Avasthi, K. Nagamatsu and J. Sturm, "Stable low-recombination n-Si/TiO2 hole-blocking interface and its effect on silicon heterojunction photovoltaics," in *IEEE 40th Photovoltaic Specialist Conference (PVSC)*, 2014.

[13] G. G. Untila, T. N. Kost, A. B. Chebotareva, M. B. Zaks, A. M. Sitnikov, O. I. Solodukha and M. Z. Shvarts, "Bifacial low concentrator argentum free crystalline silicon solar cells based on ARC of TCO and current collecting grid of copper wire," *AIP Conference Proceedings,* vol. 1556, no. 1, pp. 106-109, 2013.

[14] G. Untila, T. Kost, A. Chebotareva and M. Timofeyev, "Optimization of the deposition and annealing conditions of fluorine-doped indium oxide films for silicon solar cells," *Semiconductors,* vol. 47, no. 3, pp. 415-421, 2013.

[15] J. Meyer, S. Hamwi, M. Kroger, W. Kowalsky, T. Riedl and A. Kahn, "Transition Metal Oxides for Organic Electronics: Energetics, Device Physics and Applications," *Advanced Materials,* vol. 24, no. 40, pp. 5408-5427, 2012.

[16] S. McDonnell, A. Azcatl, R. Addou, C. Gong, C. Battaglia, S. Chuang, K. Cho, A. Javey and R. M. Wallace, "Hole Contacts on Transition Metal Dichalcogenides: Interface Chemistry and Band Alignments," *ACS Nano,* vol. 8, no. 6, pp. 6265-6272, 2014.

[17] S. Chuang, C. Battaglia, A. Azcatl, S. McDonnell, J. S. Kang, X. Yin, M. Tosun, R. Kapadia, H. Fang, R. M. Wallace and A. Javey, "MoS2 P-type Transistors and Diodes Enabled by High Work Function MoOx Contacts," *Nano Letters,* vol. 14, no. 3, pp. 1337-1342, 2014.

[18] M. T. Greiner, L. Chai, M. G. Helander, W.-M. Tang and Z.-H. Lu, "Transition Metal Oxide Work Functions: The Influence of Cation Oxidation State and Oxygen Vacancies," *Advanced Functional Materials,* vol. 22, no. 21, pp. 4557-4568, 2012.

[19] R. Swanson and D. Kane, "Measurement of the Emitter Saturation Current by a Contactless Photoconductivity Decay Method," in *In proceedings of 18th IEEE Photovoltaic Specialists Conference*, 1985.

[20] K. R. McIntosh and L. E. Black, "On effective surface recombination parameters," *Journal of Applied Physics,* vol. 116, no. 1, 2014.

[21] S. S. Cohen, "Contact resistance and methods for its determination," *Thin Solid Films,* vol. 104, no. 3, pp. 361-379, 1983.

[22] M. Grauvogl and R. Hezel, "The truncated-pyramid MIS inversion-layer solar cell: a comprehensive analysis," *Progress in Photovoltaics: Research and Applications,* vol. 6, no. 1, pp. 15-24, 1998.

[23] F. Werner, Y. Larionova, D. Zielke, T. Ohrdes and J. Schmidt, "Aluminum-oxide-based inversion layer solar cells on n-type crystalline silicon: Fundamental properties and efficiency potential," *Journal of Applied Physics,* vol. 115, no. 7, 2014.

[24] R. Cox and H. Strack, "Ohmic contacts for GaAs devices," *Solid-State Electronics ,* vol. 10, no. 12, pp. 1213-1218, 1967.

[25] M. Tucci, L. Serenelli, S. De Iuliis, M. Izzi, G. de Cesare and D. Caputo, "Contact Formation on a-Si:H/c-Si Heterostructure Solar Cells in Physics and Technology of Amorphous-Crystalline Heterostructure Silicon Solar Cells," W. G. J. H. M. van Sark, L. Korte and F. Roca, Eds., Springer, 2011, pp. 331-376.

[26] S. Sze and K. Ng, Physics of Semiconductor Devices, John Wiley & Sons, 2006.

[27] P. Lolgen, W. Sinke, C. Leguijt, A. Weeber, P. Alkemade and L. Verhoef, "Boron doping of silicon using coalloying with aluminium," *Applied Physics Letters,* vol. 65, no. 22, pp. 2792-2794, Nov 1994.

[28] J. Muller, K. Bothe, S. Gatz, H. Plagwitz, G. Schubert and R. Brendel, "Contact Formation and Recombination at Screen-Printed Local Aluminum-Alloyed Silicon Solar Cell Base Contacts," *IEEE Transactions on Electron Devices,* vol. 58, no. 10, pp. 3239-3245, Oct 2011.

[29] R. Woehl, P. Gundel, J. Krause, K. Ruhle, F. Heinz, M. Rauer, C. Schmiga, M. Schubert, W. Warta and D. Biro, “Evaluating the Aluminum-Alloyed p+ -Layer of Silicon Solar Cells by Emitter Saturation Current Density and Optical Microspectroscopy Measurements,” *IEEE Transactions on Electron Devices,* vol. 58, no. 2, pp. 441-447, Feb 2011.

[30] A. Rohatgi, S. Narasimha and D. S. Ruby, “Effective Passivation of the Low Resistivity Silicon Surface by a Rapid Thermal Oxide/PECVD Silicon Nitride Stack and Its Application to Passivated Rear and Bifacial Si Solar Cells,” in *In proceedings of the 2nd World Conference on Photovoltaic Solar Energy Conversion*, 1998.

[31] E. Urrejola, K. Peter, H. Plagwitz and G. Schubert, “Al-Si alloy formation in narrow p-type Si contact areas for rear passivated solar cells,” *Journal of Applied Physics,* vol. 107, no. 12, 2010.

[32] J. Schmidt and K. Bothe, “Structure and transformation of the metastable boron- and oxygen-related defect center in crystalline silicon,” *Physics Review B,* vol. 69, p. 024107, Jan 2004.

[33] C. Mader, J. Muller, S. Eidelloth and R. Brendel, “Local rear contacts to silicon solar cells by in-line high-rate evaporation of aluminum,” *Solar Energy Materials and Solar Cells ,* vol. 107, pp. 272-282, 2012.

[34] R. Sinton and A. Cuevas, “A quasi-steady-state open-circuit voltage method for solar cell characterization,” *16th European Photovoltaic Solar Energy Conference,* vol. 25, 2000.

n- and p-type silicon solar cells with molybdenum oxide hole contacts

James Bullock, Di Yan, Andres Cuevas, Yimao Wan and Christian Samundsett

The Australian National University, Canberra, 0200, Australia

Published in Energy Procedia

This paper provides an experimental proof-of-concept for simple solar cell designs on n- and p-type crystalline silicon (c-Si) substrates which utilise sub-stoichiometric MoO_x ($x < 3$) films to collect holes. The n-type cell design (referred to as 'moly-poly') features a planar rear SiO_x / poly-Si(n^+) stack with a planar front SiO_x / MoO_x / ITO stack. We demonstrate an un-optimised conversion efficiency of ~16.7±1% for a 3 × 3cm cell using a simple 10-step fabrication procedure. The p-type cell design (referred to as 'moly-BSR') is comprised of a simple SiN_x passivated, textured, front phosphorus diffusion with a rear MoO_x / Ag hole contact. A conversion efficiency of ~16.4±1% is achieved for 2 × 2cm using an 11-step fabrication procedure. Beyond the proof-of-concept results achieved, a number of future improvements are also outlined.

Introduction. A central premise of a photovoltaic device is the separation of photo-excited electrons and holes at opposite contacts. The present paper focuses specifically on the anode, or hole collecting contact of crystalline silicon (c-Si) solar cells. Table 1 compares the best cell-level results for a wide variety of c-Si solar cells featuring different types of full-area hole contacts. The top three entry types all utilize p^+ doped silicon layers to collect holes. These structures have received considerably more attention from the silicon photovoltaic community and have demonstrated much higher device efficiencies, assisted, at least in part, by knowledge inherited from the silicon microelectronics industry. However, these contact types are still limited by issues such as parasitic absorption, fundamental recombination losses and high temperature processing. This has prompted continued research into alternative hole contacting structures.

The lower half of the table reflects less explored cell structures which utilize non-silicon based materials to promote hole collection. Amongst these, structures utilizing sub-stoichiometric molybdenum oxide MoO_x, offer the additional benefits of ease of fabrication and favorable optical properties for photovoltaic applications. The very high work function of MoO_x has proven beneficial in the collection of holes on a number of solar cell absorber materials and has only recently been transferred to c-Si [1-3], with measured contact resistivities on the order of 1 mΩ cm^2 for moderate silicon doping [3]. It has also been recently demonstrated that when thermally evaporated in a controlled manner this film can provide surface passivation to c-Si with corresponding recombination parameters J_0 between 200 and 300 fA/cm^2 [3]. If these values can be effectively transferred to solar cell designs then MoO_x hole contacts will offer significant gains over conventional approaches in terms of recombination, thermal budget and simplicity. This paper explores the use of full area MoO_x contacts to collect holes on simple n- and p-type c-Si solar cells.

Device structure and fabrication. Figure 1 shows the structure and fabrication procedure for the n- and p-type cells utilizing MoO_x hole contacts. The n-type cells (referred to henceforth as the 'moly-poly' cells) were fabricated using planar, ~1 Ωcm, FZ, 250 µm, n-type wafers. A thick SiO_x layer was grown on the surfaces, via wet oxidation, to act as a protective mask in subsequent steps. This oxide was removed from the rear-side of the wafer using HF fuming and an SiO_x / poly-Si (n^+) stack was deposited to form the rear electron contact, as described in ref. [4]. Following this step the front oxide was removed using dilute HF. The cells were then cleaned using a standard RCA procedure; the thin oxide formed during this process was intentionally left on. A MoO_x (~15 nm) / indium-tin-oxide (ITO, ~50 nm) stack was then deposited on top of the thin chemical oxide layer. The MoO_x was deposited by thermal evaporation (Angstrom Engineering ÅMOD) from a high purity powder source at a rate of ~1 Å/sec using a base pressure of $< 7 \times 10^{-7}$ mTorr. The ITO was deposited via RF sputtering (AJA International, ATC Orion) and had a sheet resistance of ~ 120 Ω/□. A silver fingered grid (~10% contact area) and a silver full area contact were then deposited via thermal evaporation on the front and the rear of the cell, respectively. Finally, the cell area was defined by laser cutting; no attempt was made to reduce the effects of laser induced edge recombination in these proof-of-concept cells.

Table 1. Comparison of open circuit voltage (V_{oc}), fill factor (FF) and efficiency (*η)* for a variety of full-area hole contacts implemented in c-Si solar cells. (T.W. denotes this work.)

Full area hole contact type	Hole contact structure	Holes in the absorber	V_{oc} (mV)	FF (%)	*η* (%)	Ref.
Aluminum alloyed homojunction	c-Si (*p*) / c-Si(Al-p^+)	Majority	648	80.6	20.1	[5]
Amorphous silicon heterojunction	c-Si (*n*) /a-Si:H(*i*) / a-Si:H(p^+) / TCO *	Minority	750	83.2	24.7	[6]
Semiconductor-insulator-semiconductor	c-Si(*n*) / SiO_x / poly-Si(p^+) / Ag	Minority	693	81.5	17.9	[7]
	c-Si (*n*) / SiO_x / a-Si:H(p^+) *	Minority	739	80.45	23.12	[8]
Metal-insulator-semiconductor	c-Si (*n*) / SiO_x / Au	Minority	550	72	9	9]
Silicon / organic hybrid	c-Si(*n*) / PEDOT:PSS	Minority	653	67.2	17.4	[10]
Silicon / carbon nanotube	c-Si(*n*) / carbon nanotube	Minority	530	74.1	11.2	[11]
Silicon / graphene	c-Si(*n*) / Graphene	Minority	552	48	10.3	[12]
Silicon / metal oxide	c-Si(*n*) / MoO_x	Minority	580	65	14.3	[1]
	c-Si(*n*) / a-Si:H (*i*) / MoO_x	Minority	711	67.2	18.8	[2]
Silicon / metal oxide	**c-Si(*n*) / MoO_x**	**Minority**	**637**	**75**	**16.7**	T.W.
	c-Si(*p*) / MoO_x	**Majority**	**616**	**72**	**16.4**	T.W.

**The exact structures of these cells are not known*

The p-type cells (referred to henceforth as ‘moly-BSR’) were fabricated on planar, ~2 Ωcm, FZ, 250 µm, p-type wafers. Following wet oxidation, the front oxide was removed via HF fuming and the exposed surface was textured using an alkaline based etch solution. After an RCA cleaning step, a heavy phosphorus diffusion (~20 Ω/□) was performed. An Al metal grid (~10% metal fraction) was then evaporated on the front-side and the diffusion was etched back to ~100 Ω/□ in the non-metalized regions, as described in ref [13]. A ~75 nm SiNx passivation and antireflection coating was then deposited via plasma enhanced chemical vapor deposition (PECVD, Roth and Rau AK 400). The rear protective oxide was removed by HF fuming and a MoOx (15 nm) / Ag (2 µm) stack was deposited by thermal evaporation (for both the MoOx and Ag layers). Both the moly-poly and moly-BSR cells utilize a coarse front metal grid formed by thermal evaporation through a shadow mask; hence no photolithography steps were used in the fabrication procedure.

Illuminated IV cell characteristics were measured under standard 1-sun conditions (~1000 W/m^2, ~25 °C, AM 1.5 G spectrum) using a solar simulator (Photo Emission Tech, model SS150) which was calibrated using a certified reference cell from Fraunhofer ISE CalLab. We estimate and absolute efficiency uncertainty of ± 1%.

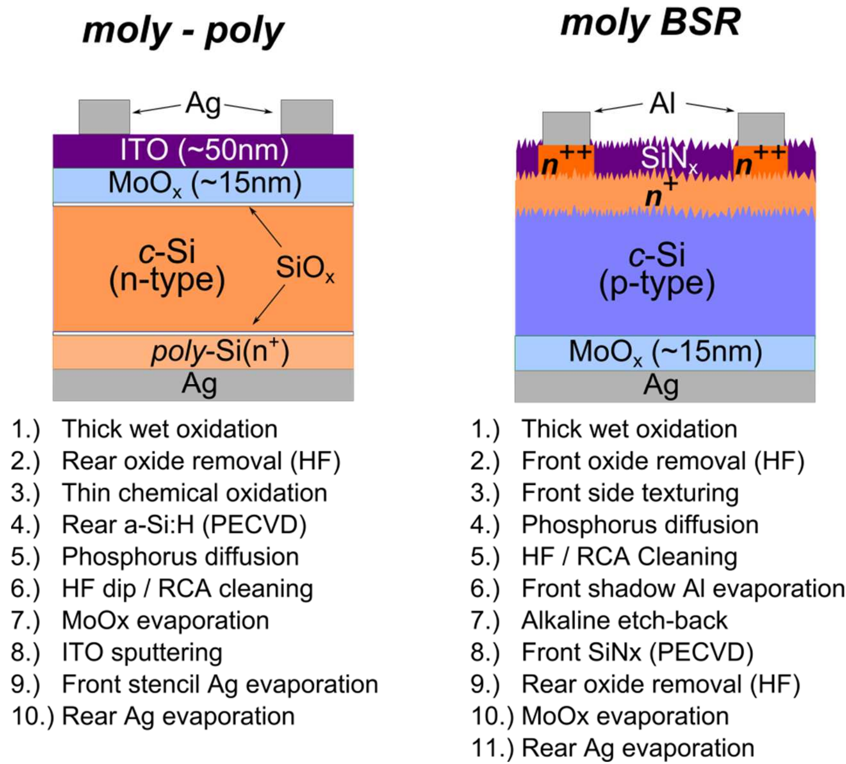

Figure 1 – Representative schematic of the proof-of-concept moly-poly and moly-BSR cell architectures. The major fabrication steps are listed below the schematics

Device characterization. Figure 2 a and b provide representative light IV characteristics (open circuit voltage V_{oc}, short circuit current J_{sc}, fill factor FF and efficiency η) for the moly-poly and moly-BSR cells, respectively. For the moly-poly cell a V_{oc} of 637 mV is slightly higher than typical values for industrial screen printed Al-p$^+$ solar cells. The main losses stem from the low current density (due to the planar front surface and coarse front metal grid) and fill factor (also partly attributable to the thin metal of the front grid). It is envisioned that a significant increase in current density (up to ~4 mA/cm^2) could be achieved by using a finer front metal grid and surface texturing. In addition, the insertion of an interlayer which provides better interface passivation has already been demonstrated to vastly improve the device voltage in n-type c-Si devices [2].

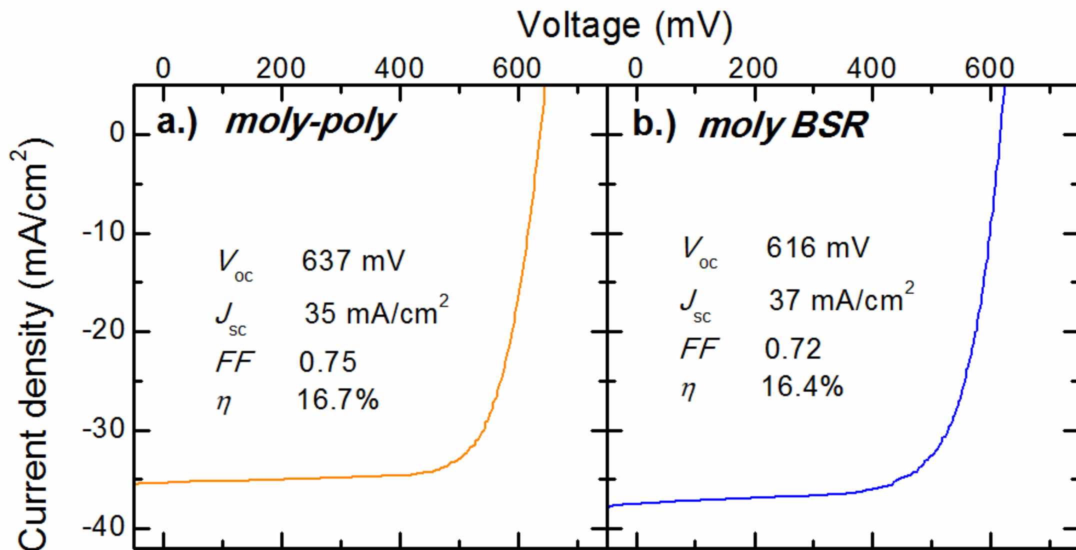

Figure 2 – Representative light IV characteristics and curves for a.) 3 x 3 cm moly-poly and b.) 2 x 2 cm moly BSR cell architectures.

The V_{oc} of the moly-BSR cells is significantly lower, at ~616 mV, whereas J_{sc} is higher, courtesy of the front surface texturing. This device did not have the thin chemical SiOx layer present in the moly-poly cell, but even without it a recombination current density of ~200 fA/cm^2 is expected as inferred from previous studies on simplified test structures [3]. Unfortunately, as can be seen from the obtained device V_{oc}, the previously measured low recombination level has not been achieved at the cell level in these initial attempts.

As a way forward, previously reported measurements of the contact resistivity of MoO_x on p-type silicon [3] suggest that smaller area contacts (for example 5% contact fraction) would not significantly increase the total cell series resistance. This would allow the use of a partial rear MoO_x contact on a p-type cell, with the remainder of the surface being passivated with a high quality passivation layer (for example Al_2O_3).

Conclusion. The two proof-of-concept devices presented here demonstrate the use of SiO_x / MoO_x (on n-type silicon) and MoO_x (on p-type silicon) contacts to c-Si solar

cells. Efficiencies of 16.7% (3 x 3 cm) and 16.4% (2 x 2 cm) are achieved on n and p-type substrates respectively. Although modest in terms of performance, the results show that reasonable passivation and good transport can be simultaneously achieved with MoO_x and MoO_x/SiO_x structures. Indeed they demonstrate that MoO_x could act as a suitable alternative to Al-alloyed and B-diffused p^+ regions.

Acknowledgements. This work has been supported by the Australian Government through the Australian Renewable Energy Agency (ARENA). Facilities at the Australian National Fabrication Facility were utilized for this project.

References

[1] C. Battaglia, X. Yin, M. Zheng, I. D. Sharp, T. Chen, S. McDonnell, A. Azcatl, C. Carraro, B. Ma, R. Maboudian, R. M. Wallace and A. Javey, Hole Selective MoO_x Contact for Silicon Solar Cells, *Nano Lett.*, 2014, vol. 14, no. 2, pp. 967-971,.

[2] C. Battaglia, S. M. de Nicolas, S. De Wolf, X. Yin, M. Zheng, C. Ballif and A. Javey, Silicon heterojunction solar cell with passivated hole selective MoO_x contact, *Appl. Phys. Lett.*, 2014, vol. 104, no. 11,

[3] J. Bullock, A. Cuevas, T. Allen and C. Battaglia, Molybdenum Oxide MoO_x: A Versatile Hole Contact For Silicon Solar Cells, *Appl. Phys. Lett.,* 2014, 105, 232109

[4] D. Yan, A. Cuevas, Y. Wan, J. Bullock, C. Samundsett, Phosphorus-diffused polysilicon contacts for silicon solar cells, *Sol. Energy Mater.*, Vol. 142., page 75 – 82, 2015

[5] T. Fellmeth, S. Mack, J. Bartsch, D. Erath, U. Jäger, R. Preu, F. Clement, and D. Biro, 20.1% Efficient Silicon Solar Cell With Aluminium Back Surface Field, 2011, *IEEE Electron Device Lett.*, Vol 32, No. 8.

[6] M. Taguchi, A. Yano, S. Tohoda, K. Matsuyama, Y. Nakamura, T. Nishiwaki, K. Fujita, and E. Maruyama, 24.7% Record Efficiency HIT Solar Cell on Thin Silicon Wafer, *IEEE J. Photovolt.*, 2014, Vol 4, No. 1.

[7] F. Feldmann, M. Simon, M. Bivour, C. Reichel, M. Hermle, S. W. Glunz, Efficient carrier-selective p- and n-contacts for Si solar cells, *Sol. Energy Mater.*, 2014, Vol. 131.

[8] J. B. Heng, J. Fu, B. Kong, Y. Chae, W. Wang, Z. Xie, A. Reddy, K. Lam, C. Beitel, C. Liao, C. Erben, Z. Huang, and Z. Xu, >23% High-Efficiency Tunnel Oxide Junction Bifacial Solar Cell With Electroplated Cu Gridlines, *IEEE J. Photovolt.*, Vol 5, 2015, No. 1.

[9] J. P. Ponpon and P. Siffert, Open-circuit voltage of MIS silicon solar cells, *J. Appl. Phys.,* 1976, 47, 3248.

[10] D. Zielke, A. Pazidis, F. Werner, J. Schmidt, Organic-silicon heterojunction solar cells on n-type silicon wafers: The BackPEDOT concept, *Sol. Energy Mater.*, 2014, Vol. 131.

[11] Y. Jung, X. Li, N. K. Rajan, A. D. Taylor, M. A. Reed, Record High Efficiency Single-Walled Carbon Nanotube/Silicon p-n Junction Solar Cells, *Nano Lett.* 2013, 13, 95

[12] Y. Zhang, F. Zu, S.-T. Lee, L. Liao, N. Zhao, and B. Sun, Heterojunction with Organic Thin Layers on Silicon for Record Efficiency Hybrid Solar Cells, *Adv. Energy Mater.*, 2014, Vol. 4, 2.

[13] D. Yan, A. Cuevas, J. Bullock and Y. Wan, Development of a Self-aligned Etch-Back Process for Selectively Doped Silicon Solar cells, *40th IEEE Photovoltaic Specialist Conference (PVSC)*, 2014, 2545-2549.

Proof-of-concept p-type silicon solar cells with molybdenum oxide local rear contacts

James Bullock, Christian Samundsett, Andrés Cuevas, Di Yan, Yimao Wan and Thomas Allen

Research School of Engineering, The Australian National University, Canberra, ACT, 2601, Australia

Published in IEEE Journal of Photovoltaics

This paper explores the application of transparent MoO_x ($x<3$) films as hole-collecting contacts on the rear-side of crystalline silicon solar cells. Two dimensional simulations, which consider experimental contact recombination J_{0c} and resistivity ρ_c values, indicate that the benefits of direct MoO_x based contacts are best exploited by reducing the rear contact fraction. This concept is demonstrated experimentally using simple p-type cells featuring a ~5% rear fraction MoO_x contact. These cells attain a conversion efficiency of 20.4%, a promising result, given the early stage of development for this technology.

Introduction. The selective collection of light-generated electrons and holes at separate contacts is critical to the functionality of all photovoltaic devices. This requires that each contact exhibits a low resistance to the collected carrier whilst suppressing recombination of the other carrier. Unfortunately, direct metallization of crystalline silicon (*c*-Si) results in an interface with a very high rate of minority carrier recombination. When applied to moderately doped (1-5 Ωcm) silicon, a directly metalized surface exhibits a recombination parameter J_{0c} of at least 10^5 fA/cm^2 confined mainly by the speed of carrier diffusion to the interface [1]. Such high J_{0c} values limit the open circuit voltage V_{oc} of devices with full-area contacts to < 600 mV.

Given that an outer metal contact is essential for conventional solar cells, there are three main ways to improve the V_{oc}: *i)* mitigate the influence of recombination sites at the metalized surface by heavily doping the semiconductor under the contact [2]; *ii)* reduce the fraction of the surface which is metalized - forming what are known as 'partial' or 'localized' contacts [3]; and *iii)* apply passivating contact interlayer(s) between the *c*-Si absorber and the outer metal. This paper explores the use of the latter two techniques, applying a molybdenum oxide hole contact partially to the rear-side of a p-type *c*-Si solar cell.

Properties and advantages of MoO_x. Sub-stoichiometric molybdenum trioxide (MoO_x, x<3) has recently been demonstrated as a versatile hole contact on *c*-Si [4,5]. Its ability to form a hole contact is attributable to its large work function (5.7 - 6.7 eV) which, when applied to c-Si, encourages hole accumulation at the adjacent *c*-Si surface. A MoO_x interlayer thickness of ~10 nm has been shown to produce J_{0c} values as low as ~200 fA/cm^2 and contact resistivities ρ_c of ~1 mΩcm^2 on moderately doped p-type surfaces [5] – a combination which is considerably better than the directly metallized surface. Recently, simplified p-type solar cell structures featuring full-area MoO_x based

rear contacts have been demonstrated [6]. Whilst the simplicity of these cells precluded high efficiencies, the proof-of-concept was nonetheless demonstrated. In fact p-type cells fabricated using an almost identical process, differing only by the use of directly metalized boron diffused rear contacts, produced almost identical efficiencies [7]. These results highlight the potential of MoO_x based contacts to supersede both diffused and undiffused directly metalized hole contacts to p-type *c*-Si.

Amongst the most notable benefits of using MoO_x to replace directly metalized contacts is low deposition temperature, and hence cheap processing. This low thermal budget can also bring additional lead on-effects including the preservation of bulk lifetimes and a reduced requirement for cleanliness during cell fabrication. The optical properties of MoO_x also introduce potential light management benefits over metals at both the front and rear sides of solar cells. Finally, the low contact resistivity associated with MoO_x / p-type *c*-Si contacts indicates the possibility of using MoO_x as the hole contact in higher efficiency localized rear contact cell structures. The use of MoO_x films in this application removes the need for complex alignment procedures between local diffused regions and overlying contacts – simplifying the design of such cells.

MoO_x based local rear contacts

Simulations. In order to demonstrate the potential benefits of integrating MoO_x rear contacts into a p-type cell structure we have run idealized cell simulations using Quokka [8] - similar in nature to those of previous studies [9,10]. These simulations, shown in Figure 1, are designed in such a way as to emphasize the influence of the rear contact characteristics. As such, a number of idealized values and assumptions, listed in Table 1, are employed. The rear contact resistivity ρ_c and recombination factor J_{0c} are used as the variable inputs to the simulation. For each ρ_c - J_{0c} combination an optimum rear contact fraction is calculated (dotted lines) with a corresponding maximum efficiency (contours). Experimentally determined values of ρ_c and J_{0c} for a given contact can then

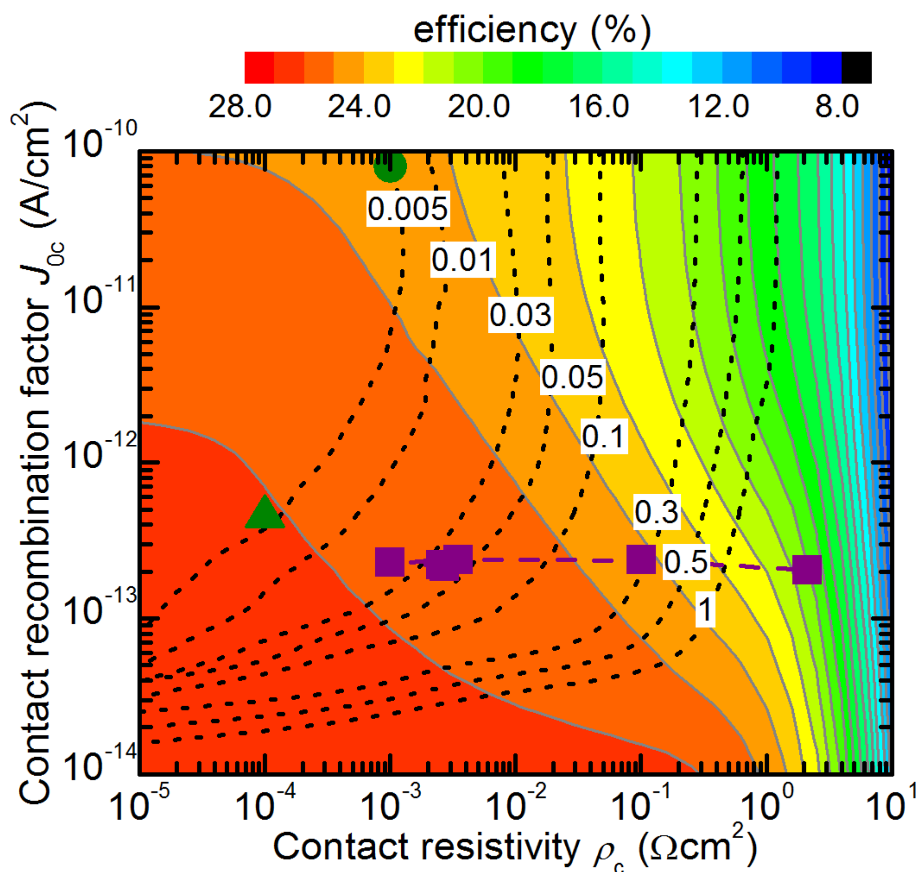

Figure 1. Simulated optimum contact fraction (dotted lines) and resultant efficiency (contours) as a function of rear contact ρ_c and J_{0c}. The green points represent the position of diffused (triangle) and undiffused (circle) directly metalized contacts. The purple circles reflect MoO_x based contacts for a range of MoO_x thicknesses.

Table I: Summary of simulation conditions

Symbol	Parameter	Assumption / value
J_{0front}	Front recombination factor	1 fA/cm^2
J_{0rear}	Rear recombination factor (in non-contacted a	1 fA/cm^2
f_{mrear}	Rear line-contact metal fraction	Finger width = variable Finger pitch = 1000 µm
R_{sh_front}	Front diffusion sheet resistance	10 Ω/□
ρ_b	Bulk type, resistivity	1 Ωcm p-type
W	Wafer thickness	160 µm
J_g	Generation current density	42 mA/cm^2
τ_{bulk}	Bulk lifetime	Richter *et. al.* intrinsic lifetime [12]

be superimposed on this plot to determine the optimum contact configuration and highest attainable efficiency.

As can be seen in Figure 1, the optimum contact fraction for the directly metalized silicon surface is ~0.5% (as represented by the green circle). The addition of a high concentration of p-type dopant species under the contacts simultaneously reduces ρ_c and J_{0c} (green triangle). However, even with optimum underlying doping the ρ_c - J_{0c} combination is still limited to ~0.1 mΩcm^2 [1] and ~500 fA/cm^2 [11], which also correspond to optimum contact fractions less than 0.5%.

Superimposed on the same plot are a series of MoO_x hole contacts (purple squares) to p-type *c*-Si [5]. The data points of this series differ in the thickness of the MoO_x film. The MoO_x data trends demonstrate two concepts: *i.*) a higher optimum efficiency can be achieved compared to directly metalized undiffused contacts; and *ii.*) this higher efficiency occurs at a much larger contact fraction of 3 - 5%, which permits a simpler fabrication process.

The practical implications of the above factors is that MoO_x localized rear contacts effectively remove the difficult components of the localized rear contact design by

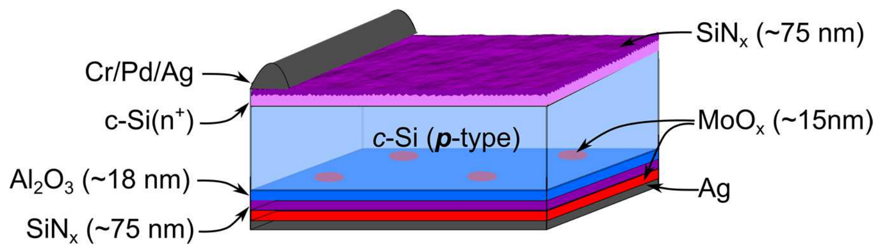

Figure. 2. Representative schematic of MoO_x local rear contact cell structure

eliminating the necessity for both very small contact fractions and aligned localized dopant-diffused regions. This is done whilst preserving the benefits of such an approach, for example, the low absorption and high reflectivity of the rear dielectric stack, which can result in large generation current gains (more than 1 mA/cm^2) over, for example, full-area Al alloyed metal contacts and, to a lesser degree, full-area silicon heterojunction rear contacts. To illustrate this idea we fabricate proof-of-concept p-type cells with a 5% area localized MoO_x rear contact.

Experimental procedure. The proof-of-concept, MoO_x local rear contact cells were fabricated on ~2 Ωcm, FZ, p-type c-Si wafers. Following alkaline based surface texturing and standard RCA cleaning, a phosphorus diffusion was performed in a clean quartz furnace resulting in an n^+ sheet resistance of ~120 Ω/□. This phosphorus diffusion was isolated to the front-side 2 x 2 cm^2 cell area by a subsequent photolithographically defined mesa etch. A plasma enhanced chemical vapor deposited (PECVD) SiN_x (~75nm) single layer and an atomic-layer-deposited Al_2O_3 (~12 nm) / PECVD SiN_x (~75nm) stack were used to passivate the front and rear surfaces, respectively. A front Cr/Pd/Ag metal grid stack was defined photolithographically and thickened using Ag electroplating, resulting in a contact fraction of ~4%. A combined passivation activation and contact sinter step of 400°C for 25 minutes in nitrogen ambient was then performed. Dot openings (~200 μm in diameter, 800 μm apart) totaling ~5% of the surface area were

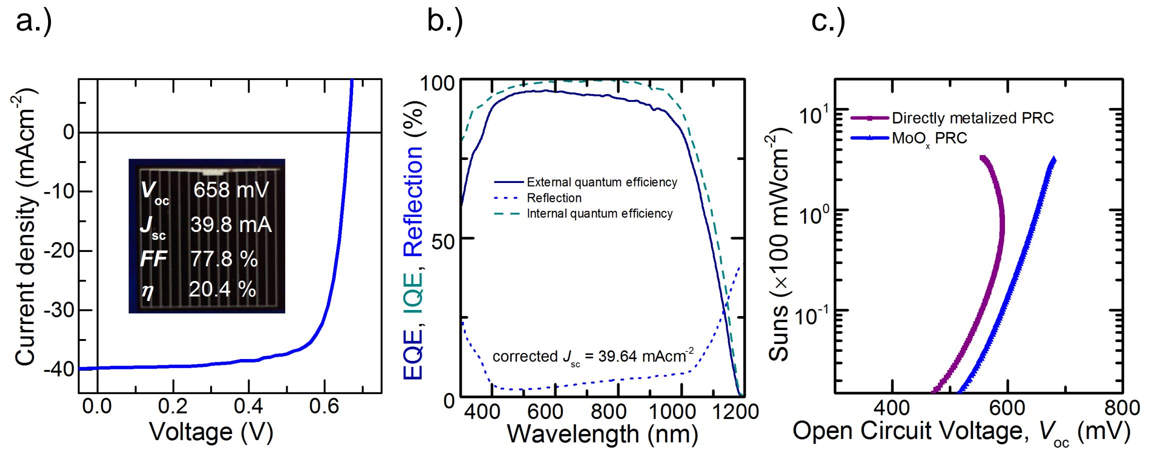

Figure. 3. Representative a.) light *JV* curve and cell characteristics, b.) EQE/IQE analysis for 2 x 2 cm local contact MoO_x *c*-Si solar cells. c.) Suns-V_{oc} of measurements of identical local rear contact structures featuring MoO_x (blue) and directly metalized (purple) rear contacts.

photolithographically defined on the rear side, and a MoO_x (15nm) / Ag (~1µm) stack was deposited over the full surface. The MoO_x films were evaporated from a high purity powder source (4N) at a rate of ~1Å/s with a base pressure < $7x10^{-7}$ mTorr. A representative schematic of the cell structure is provided in Figure 2.

The current-voltage (*JV*) characteristics of the cells were measured using a xenon lamp solar simulator under standard 1-sun conditions (100mW/cm^2, AM 1.5 spectrum, 25°C), which was calibrated using a certified reference cell from Fraunhofer ISE CalLab. We estimate the error of this measurement to be ±1%. The quantum efficiency of the MoO_x local rear contact cell was measured using a Protoflex Corporation QE measurement system (QE-1400-03). These measurements were accompanied by front-side reflectance measurements (taken using a PerkinElmer Lambda 1050 UV/VIS/NIR spectrophotometer with an integrating sphere attachment) to investigate parasitic loses of the cells. Suns-V_{oc} measurements were taken using a Sinton WCT 110 tester to investigate the quality of the rear contact at the cell level.

Results. Figure 3 shows the illuminated *JV* characteristics for the MoO_x local rear contact cell. A conversion efficiency η of 20.4% was achieved for the best device with an open circuit voltage V_{oc}, fill-factor *FF* and short circuit current J_{sc} of 657.5 mV, 77.8 and 39.8 mA/cm^2, respectively. In particular, the obtained *FF* demonstrates effective current transport through the MoO_x, despite the ~5% contact fraction, that is, despite ~20 times higher current density than in a full-area contact. It is also clear that the aforementioned optical benefits implicit to the local rear contact design have been realized at the cell level, resulting in a high J_{sc}.

It is noteworthy that comparison structures using directly metalized local rear contacts did not reach the 20% efficiency level, owing in part to a high rear contact resistance to the ~2 Ωcm p-type substrate. This highlights a further advantage of MoO_x based rear contacts, which exhibit a weaker ρ_c dependence on the substrate doping than direct metal-semiconductor contacts. Suns-V_{oc} measurements of both cell types, shown in Figure 3c, indicated that whilst the directly metalized contacts frequently presented a 'bending' of the Suns-V_{oc} curve at higher illumination intensities indicative of Schottky barrier behavior [13], the addition of a MoO_x interlayer removed this effect, even for bulk resistivities of ~10 Ωcm. This is potentially very significant for the use of p-type CZ grown silicon, considering the detrimental impact of light induced degradation resulting from boron-oxygen related defects can be alleviated by using wafers with a lower boron concentration.

Figure 3d provides a quantum efficiency analysis of the MoO_x local rear contact cell. These measurements confirm good rear-side reflection and recombination characteristics. The estimation of the J_{sc}, made by integrating the product of EQE and the AM1.5 spectrum and correcting for the approximate contact fraction was found to be 39.64 mAcm^{-2}, in good agreement with the measured light *JV* value.

Conclusion. This investigation has confirmed that thin films of MoO_x deposited by thermal evaporation form effective hole contacts on moderate resistivity p-type c-Si. Two dimensional simulations based on experimental results demonstrate that a 3 - 5% contact fraction is optimal for the MoO_x contact – a value which is significantly larger (and hence easier to fabricate) than that for direct metal on silicon contacts. Proof-of-concept cell structures with localized rear MoO_x contacts with a conversion efficiency of 20.4% have been fabricated, directly demonstrating the aforementioned advantages.

Acknowledgements. This project was partially funded by the Australian Renewable Energy Agency.

References

[1] C. Mader, J. Muller, S. Eidelloth, R. Brendel, "Local rear contacts to silicon solar cells by in-line high-rate evaporation of aluminum", Solar Energy Materials & Solar Cells 107 (2012) 272–282.

[2] A. Cuevas, J. G. Fossum and R. T. Young, "Influence of the dopant density profile on minority carrier current in shallow, heavy doped emitters of silicon bipolar devices" *Solid-State Electron*, Vol. 28, p. 247, 1985.

[3] R. M. Swanson, S. K. Beckwith, R. C. Crane, W. D. Eades, Y. H. Kwark, R. A. Sinton, S. E. Swirhun, "Point-contact silicon solar cells," *Electron Devices, IEEE Transactions on*, vol. 31, pp. 661-664, 1984

[4] C. Battaglia, S. M. de Nicolas, S. De Wolf, X. Yin, M. Zheng, C. Ballif and A. Javey, "Silicon heterojunction solar cell with passivated hole selective MoOx contact," *Applied Physics Letters*, vol. 104, no. 11, 2014

[5] J. Bullock, A. Cuevas, T. Allen and C. Battaglia, "Molybdenum Oxide MoOx: A Versatile Hole Contact For Silicon Solar Cells", *Applied Physics Letters,* **105**, 232109, 2014.

[6] J. Bullock, D. Yan, A. Cuevas, Y. Wan and C. Samundsett, "n- and p-type silicon solar cells with molybdenum oxide hole contacts" *Energy Procedia*, **77**, 2015, Pages 446-450

[7] D. Yan, A. Cuevas, J. Bullock and Y. Wan, "Development of a Self-aligned Etch-Back Process for Selectively Doped Silicon Solar cells", *40th IEEE Photovoltaic Specialist Conference (PVSC)*, 2014

[8] A. Fell, "A free and fast 3D/2D solar cell simulator featuring conductive boundary and quasi-neutrality approximations," *IEEE Trans. Electron Devices*, 60, 733 (2013).

[9] D. L. Young, W. Nemeth, S. Grover, A. Norman, H-C Yuan, B. G. Lee, V. LaSalvia, and P. Stradins, "Carrier selective, passivated contacts for high efficiency silicon solar cells based on transparent conducting oxides", *Proc. 4th International Conference on Silicon Photovoltaics*, 2014.

[10] J. Bullock, A. Cuevas, D. Yan, B. Demaurex, A. Hessler-Wyser, and S. De Wolf, "Amorphous silicon enhanced metal-insulator-semiconductor contacts for silicon solar cells", *Journal of Applied Physics* 116, 163706 (2014).

[11] D. Yan and A. Cuevas, "Empirical determination of the energy band gap narrowing in p+ silicon heavily doped with boron", *Journal of Applied Physics* 116, 194505 (2014)

[12] A. Richter, S. W. Glunz, F. Werner, J. Schmidt, and A. Cuevas, "Improved quantitative description of Auger recombination in crystalline silicon," *Phys. Rev. B*, 86, 165202 (2012).

[13] S. Glunz, J. Nekarda, H. Mackel, A. Cuevas, "Analysing back contacts of silicon solar cells by suns Voc measurements at high illumination densities" *22nd European photovoltaic specialist conference*, 2007.

4 Alkali metal salt electron-selective contacts for *c*-Si solar cells

4.1 Foreword

Thin interlayers of alkali and alkaline earth metal salts, for example LiF and $CsCO_3$, are commonly implemented on a range of different electronic devices to enhance electron injection or extraction. The excellent electron injection/extraction behaviour, is typically attributed to a low work function value at the interface between the interlayer and an overlying metal contact layer, usually Al. Despite the widespread use of such materials, their application to silicon solar cells is still incipient.

This chapter focuses on the use of a subcategory of these materials, the alkali metal fluorides, as electron contacts for *c*-Si solar cells. Novel applications are identified for both the direct LiF_x / Al electron contact and an *a*-Si:H / LiF_x / Al electron contact, demonstrated for the first time here. A brief summary of the manuscripts presented in this chapter is detailed below.

Manuscript 1: James Bullock, Peiting Zheng, Quentin Jeangros, Mahmut Tosun, Mark Hettick, Carolin Sutter-Fella, Yimao Wan, Thomas Allen, Di Yan, Daniel Macdonald, Stefaan De Wolf, Aïcha Hessler-Wyser, Andres Cuevas, Ali Javey, *"Lithium fluoride based electron contacts for high efficiency n-type crystalline silicon solar cells"*, Submitted, 2016.

This manuscript is centred on the development of a first-of-its-kind n-type partial rear contact cell which utilises a LiF_x / Al contact rather than relying on heavy phosphorus

doping to collect electrons. Although common for p-type wafers, a partial rear contact architecture was yet to be demonstrated for n-type wafers (without a phosphorus diffusion), given the difficulties in contacting lightly doped n-type silicon. Proof of contact cells featuring a 1% rear LiF_x / Al contact are made, enabling an efficiency greater than 20%—already comparable to a control cell which instead utilises phosphorus doping on the rear.

Manuscript 2: James Bullock, Mark Hettick, Jonas Geissbühler, Alison J. Ong, Thomas Allen, Carolin M. Sutter-Fella, Teresa Chen, Hiroki Ota, Ethan W. Schaler, Stefaan De Wolf, Christophe Ballif, Andrés Cuevas and Ali Javey, *"Efficient silicon solar cells with dopant-free asymmetric heterocontacts"*, Nature Energy, 2, 15031, 2016

This paper focuses on the demonstration of an efficient solar cell with a set of dopant free asymmetric heterocontacts (DASH). A key enabling factor of this cell is the development of an electron contact to complement the MoO_x based hole contact. Initially a direct LiF_x / Al contact is investigated and found to produce a low ρ_c of ~1 mΩcm^2 but very high recombination. To combat the recombination, a passivating *a*-Si:H interlayer is implemented under the LiF_x / Al contact, resulting in a slight increase in ρ_c to 7 mΩcm^2 but a dramatic decrease in recombination, allowing device open circuit voltages above 700 mV. A DASH cell is fabricated using this approach yielding an efficiency of 19.4%, a significant improvement over the state-of-the-art and the first of its kind to demonstrate an efficiency competitive with conventional approaches.

4.2 First author manuscripts

Lithium fluoride based electron contacts for high efficiency n-type crystalline silicon solar cells

James Bullock[1,2,3,†], Peiting Zheng[3,†], Quentin Jeangros[4], Mahmut Tosun[1,2], Mark Hettick[1,2], Carolin Sutter-Fella[1,2], Yimao Wan[3], Thomas Allen[3], Di Yan[3], Daniel Macdonald[3], Stefaan De Wolf[4], Aïcha Hessler-Wyser[4], Andres Cuevas[3*], Ali Javey[1,2*].

[1] Department of Electrical Engineering and Computer Sciences, University of California, Berkeley, California 94720, USA.

[2] Materials Sciences Division, Lawrence Berkeley National Laboratory, Berkeley, California 94720, USA.

[3] Research School of Engineering, The Australian National University (ANU), Canberra, ACT 0200, Australia

[4] École Polytechnique Fédérale de Lausanne (EPFL), Institute of Micro Engineering (IMT), Photovoltaics and Thin-Film Electronic Laboratory (PVLab), Maladière 71b, CH-200 Neuchatel, Switzerland

Abstract. *Low-resistance contact to lightly doped n-type crystalline silicon (c-Si) has long been recognised as technologically challenging, due to the pervasive interfacial Fermi-level pinning effect. This has hindered the development of electronic devices such as n-type c-Si solar cells with partial rear contacts (PRC) made directly to the lowly doped c-Si wafer. Here we demonstrate a simple and robust process for achieving m*Ωcm^2 *scale contact resistivities on lightly doped n-type c-Si via a lithium fluoride / aluminium contact. The realisation of this low-resistance contact enables the fabrication of a first-of-its-kind high-efficiency n-type PRC solar cell. The electron contact of this cell is made to less than 1% of the rear surface area, reducing the impact of its recombination and optical losses, permitting a power conversion efficiency already greater than 20% in the initial proof-of-concept stage. The implementation of the* LiF_x */ Al contact mitigates the need for the costly high-temperature phosphorus diffusion, typically implemented in such a cell design to nullify the issue of Fermi level pinning at the electron contact. The timing of this demonstration is significant, given the on-going transition from p-type to n-type c-Si solar cell architectures, together with the increased adoption of advanced PRC device structures within the c-Si photovoltaic industry.*

Introduction Schottky-Mott theory states that when two materials with different chemical potentials are placed in contact, charge carriers at their interfaces will 'rearrange' to form a perfectly balancing electrical potential, resulting in a flat electro-chemical energy for carriers (Fermi energy). This implies that metals with different chemical potentials could be used to manipulate surface potentials and carrier concentrations of semiconductors – a ubiquitously desirable tool in semiconductor electronics. Unfortunately, such behaviour is seldom seen, owing to the persistent 'Fermi level pinning' (FLP) effect. Resultantly, in most cases a large Schottky barrier to the majority carrier forms at a semiconductor surface when contacted by a metal. This occurs largely independent of the metal's chemical potential – frequently preventing Ohmic contact.[1] A commonly cited example of this, and the one explored in this study, is that of n-type crystalline silicon (*c*-Si) – which typically exhibits a large Schottky barrier of more than 0.65 eV at the *c*-Si interface with a wide variety of outer contact metals.[1,2]

This barrier, amongst other issues, has slowed the development of c-Si solar cell architectures which require low contact resistivity to lightly doped n-type c-Si. The use of n-type, rather than p-type c-Si, is desirable because of the commonly found longer and more stable carrier lifetimes. These arise due to a reduced impact of metallic impurities and surface defects in n-type c-Si (generally defect electron capture-cross sections are larger[3]) as well as the absence of light-activated boron-oxygen complexes,[4] which result in further carrier recombination. These factors have motivated an ongoing trend within the photovoltaics industry to switch from p- to n-type c-Si solar cell architectures.[5] One such n-type cell architecture, which requires a low contact resistivity due to a small contact fraction, is the n-type partial rear contact (PRC) cell. In this structure, by confining the rear contact to a small percentage of the surface area (commonly less than 1%), the effects of high carrier recombination and poor reflectance at the contact interface can be

minimised. However, such an approach is only effective if long carrier diffusion lengths and low contact resistivities are realised. Traditionally, heavy phosphorus doping has been applied underneath the partial contact to circumvent the issue of the Schottky barrier [6]. The large increase in electron concentration (6 orders of magnitude in this case), fixed by the phosphorus doping concentration, decreases the width of the Schottky barrier at the contact allowing carrier tunnelling (via thermionic field emission) across the interface thereby reducing the contact resistivity to acceptably low values. However the heavy phosphorus doping, typically achieved by thermal diffusion, also introduces the requirement of processing temperatures greater than 800ºC,[7] and so the stringent need for cleanliness – greatly increasing the complexity of the n-type PRC cell.

An alternative approach, commonly implemented on organic semiconductor devices,[8-12] but with limited exploration on *c*-Si,[13-15] is the use of alkali and alkaline earth metal salt interlayers between the outer metal electrode and the absorber material. In particular, lithium fluoride (LiF_x) stands out as a promising candidate due to its fabrication simplicity and stability. LiF_x is a wide gap (> 10 eV) material normally deposited via thermal evaporation. In its vapour form, it is composed primarily of monomers, dimers and trimers,[16] and produces slightly sub stoichiometric (LiF_x, $x < 1$) films when deposited on *c*-Si.[15] Typically, only a very thin film (~1 nm) of LiF_x is required under an Al electrode to dramatically improve electron injection / extraction. A number of different mechanisms have been proposed to explain the low resistance to electrons at this contact found across a number of different semiconductor systems. The three most common explanations include (i) Li chemical doping of the underlying semiconductor;[10,12,17–19] (ii) protection/separation of the semiconductor layer from the Al layer;[20,21] and (iii) formation of an exceptionally low work function value localized at the LiF_x/ Al interface.[11,22] This paper investigates the interface properties and

conduction mechanism of the *c*-Si(n) / LiF_x / Al contact and demonstrates, for the first time, the simple fabrication of high efficiency (> 20%) n-type PRC solar cells without the use of heavy n-type doping.

Results and Discussion To investigate the structure and composition of the LiF_x based electron contact, *c*-Si(n) / LiF_x (1.5 nm) / Al structures were fabricated and imaged via scanning transmission electron microscopy (STEM) coupled with energy-dispersive X-ray (EDX) and electron energy-loss spectroscopy (EELS). The small atomic weight of Li increases the difficulty of detection by EDX and EELS at the same time as making it susceptible to severe knock-on effects by the electron beam. These issues are less pronounced for F, which was instead used to assess the LiF_x layer. Figure 1a shows a ~180 nm width high-angle annular dark field (HAADF) STEM image of the interface and Figure 1b provides an accompanying mapping of the local Si, Al and F EDX signal. A uniform F signal between the Al and Si regions is seen within the measured region, further supported by a higher resolution STEM HAADF image with overlying F EDX data shown in Figure 1c. Also included in Figure 1c is an EDX line scan of the local Si, Al, F and O concentrations across the interface, which suggests that there is no significant intermixing of the Al and Si layers. In addition, there is evidence for a sub-oxide species, commonly present at the *c*-Si surface.[23,24] Figure 1d provides a high resolution STEM image and accompanying EELS spectrum image of the *c*-Si(n) / LiF_x / Al interface, confirming again the presence of a continuous F layer confined to a thickness of ~1.5 nm. The apparently continuous F layer is suggestive of a uniform LiF_x film. To further investigate the electrical behaviour of the *c*-Si (n) / LiF_x / Al contact, transfer length method (TLM) test structures are fabricated as shown in Figure 2a. Figure 2b shows the measured temperature dependence of the LiF_x / Al specific contact resistivity ρ_c made to lightly doped n-type silicon (N_D ~5×10^{15}cm^{-3}). A clear thermionic contribution to

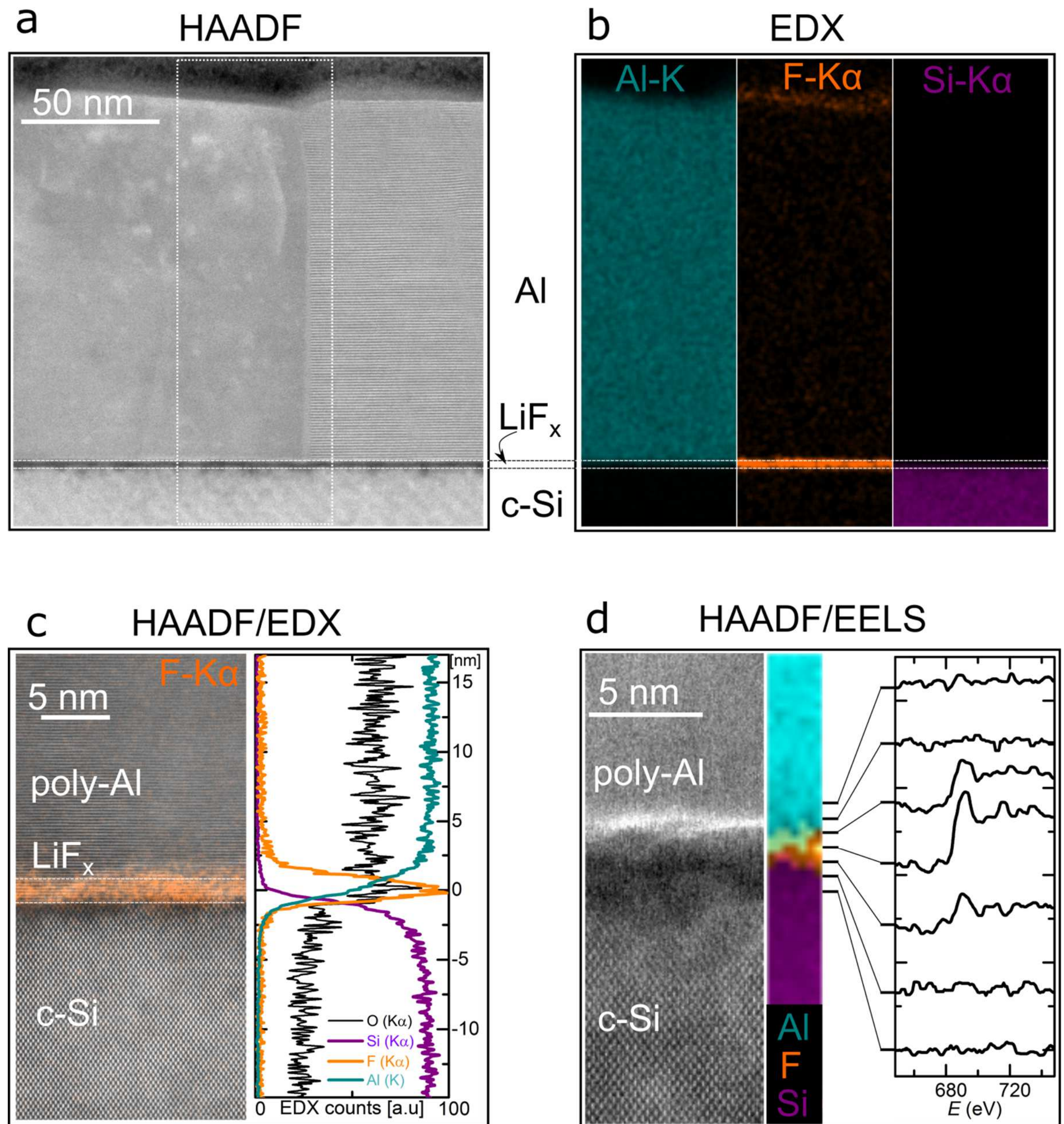

Figure 1: (a) STEM HAADF micrograph of the *c*-Si(n) / LiF_x / polycrystalline Al interface. (b) EDX mapping of Al, F and Si signals of the region highlighted in 1a. (c) STEM HAADF micrograph with an overlying EDX F signal alongside EDX line scan of the Al, F, Si, and O signals. (d) STEM HAADF micrograph and corresponding EELS spectrum image of the Al, F and Si K edges. The depth dependent F K edge evolution is further highlighted in the series of energy-loss spectra shown in the right hand side. The origin of the darker region situated just below the fluorine layer is the subject of ongoing research and could result from thickness variations due to Li removal or could be an artefact of sample preparation.

conduction can be seen at lower temperatures, with the expected exponential increase in ρ_c. However, near room temperature there is little temperature dependence. At 297 K a ρ_c of ~2 mΩcm^2 is obtained, agreeing well with previous results despite the use of a different

ρ_c measurement technique.[15] The inset of Figure 2b shows a high correlation between measured and modelled sheet resistance of the *c*-Si wafer as a function of temperature (resultant from the large decrease in mobility with increasing temperature[25]), supporting the accuracy of the technique. To expand this study to a wider range of dopant concentrations, as might be used in various c-Si device architectures,[6,7,26] Figure 2c shows the room temperature ρ_c as a function of the phosphorus dopant surface concentration N_D in the $10^{13} – 10^{20}$ range (the 10^{20} surface concentration indicated by the star is achieved via a phosphorus surface diffusion). LiF_x based contacts made to all surface concentrations within this range exhibit Ohmic (linear *I-V*) behaviour – a contrast to analogous samples made to wafers without the LiF_x interlayer (See supporting information S1). The clear dependence of ρ_c on N_D suggests that a surface barrier still partially hinders the collection of electrons.

The above information can be used collectively to draw inferences about the mechanism of improved electron transport with the LiF_x interlayer compared to the direct c-Si(n)/Al contact. First, as is evident from the microscopy images of Figure 1, the LiF_x layer appears to provide isolation between the Al and c-Si layers, potentially reducing the Fermi level pinning characteristic at the c-Si surface.[27] Given the wide band gap of bulk LiF, electron transport through this layer to the Al electrode could occur via quantum mechanical tunneling. These points are supported by our previous measurements of the ρ_c dependence on LiF_x thickness.[15] This study showed an initial improvement in ρ_c, which we attribute to the attainment of full surface coverage at $\approx$1 nm, followed by a large increase in ρ_c for thicknesses above 1.5 nm, likely due to the exponential increase in tunneling resistivity with thickness. It is noted that the increase in ρ_c with LiF_x thickness diminishes for films greater than 2.5 nm suggesting conduction via a different pathway, potentially associated with trap states through the LiF_x.[28] It is also apparent from the ρ_c

dependence on N_D shown in Figure 2c that Li chemical doping of the c-Si surface is unlikely to be a significant contributor toward the low ρ_c (Li forms a shallow donor level in silicon).[29] If Li chemical doping of the c-Si was a significant contributor, then ρ_c would be expected to be independent of substrate doping.We note that some of the apparent increase in ρ_c at lower doping densities (< 10^{16} cm^{-3}) can be ascribed to an increasing overestimation in ρ_c inherent in the TLM method. However, this does not change the above conclusion as a large drop in ρ_c is still seen for the heavily doped surface.

Instead, for the case of c-Si, we believe that the dramatic reduction in work function at the contact, previously measured by our group to be ≈2.8 eV in the vicinity of the LiF_x/Al interface,[15] is the most important parameter for the improved electron extraction. This low work function assists in significantly decreasing the surface barrier height compared to that of the direct Al contact.

As a comparison, the modeled $\rho_c(N_D)$ behavior of a typical c-Si(n) metal interface with a barrier height of ≈0.65 eV (a representative value for most metal/c-Si(n) interfaces)[2] is included in Figure 2c. This comparison shows that, despite the perseverance of a small surface barrier, orders of magnitude improvement in ρ_c can be realized by the addition of the LiF_x interlayer for a wide range of wafer doping concentrations, thereby introducing the possibility of using such contacts in n-type PRC solar cell designs without the need for heavy n-type doping.

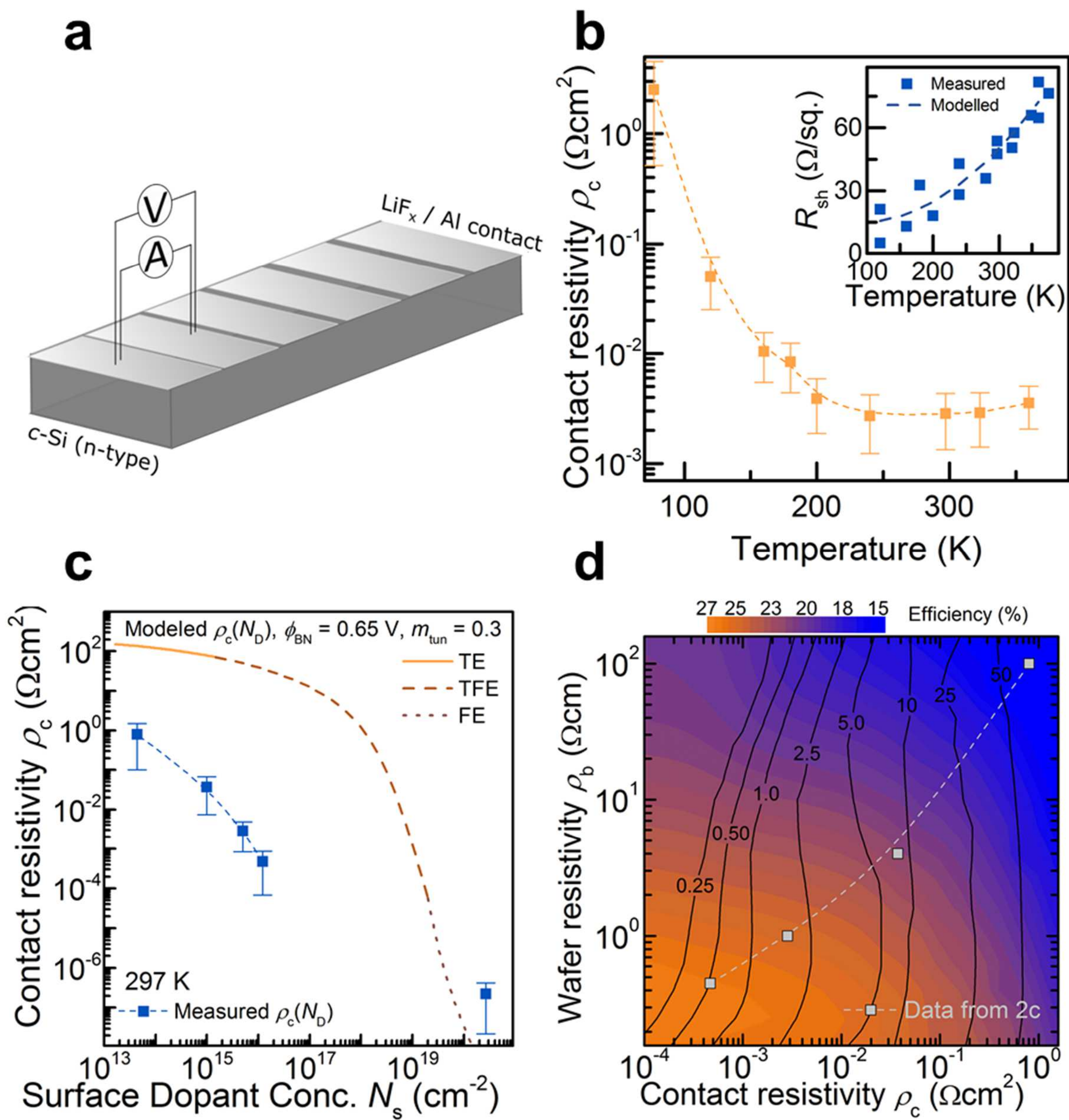

Figure 2: (a) representative schematic of the TLM structure. (b) Contact resistivity of *c*-Si(n) / LiF_x / Al contacts at a range of temperatures from 77 – 360 K. The inset of this plot shows measured and modelled sheet resistance values of the *c*-Si wafer with increasing temperature (also extracted by the TLM procedure). (c) Contact resistivity of LiF_x / Al contacts made to *c*-Si(n) wafers with a range of phosphorus surface concentrations. Shown in the same plot is the modelled contact resistivity as a function of doping concentration using thermionic emission (TE), thermionic field emission (TFE) and field emission (FE) models. These models are constructed with a barrier height of 0.65 V and an electron tunnelling effective mass of 0.3 – both of which are typical for directly metalized n-type silicon surfaces. Error bars in 2b and c reflect the estimated error in measurement. (d) Idealised n-type PRC cell simulations showing optimum contact fraction (dark lines) and idealised efficiency (coloured contours) as a function of the wafer and contact resistivity.

The optimal application of LiF_x / Al contacts in a PRC solar cell architecture is not straightforward. In particular, wafer doping must be carefully selected as it simultaneously affects the ρ_c (as seen in Figure 2c), the bulk carrier lifetime, the internal resistance and the sensitivity to surface recombination velocity (as discussed in supporting information S2). To concurrently consider these effects a two-dimensional idealised PRC cell is simulated with variable bulk resistivity ρ_b and rear ρ_c. For each combination of ρ_b and ρ_c an optimum contact configuration (% indicated by dotted black lines) is found and the resultant idealised efficiency (colour contours) is obtained. For further details on these simulations see supporting information S2. The data presented in Figure 2c can be superimposed on this simulation plot to find the best configuration in which to apply the LiF_x / Al contact. These simulations reveal that a wafer doping of at least 5×10^{15} cm^{-3} is required to make efficient LiF_x / Al PRC cells; lower doping levels produce a prohibitively high ρ_c for these architectures.

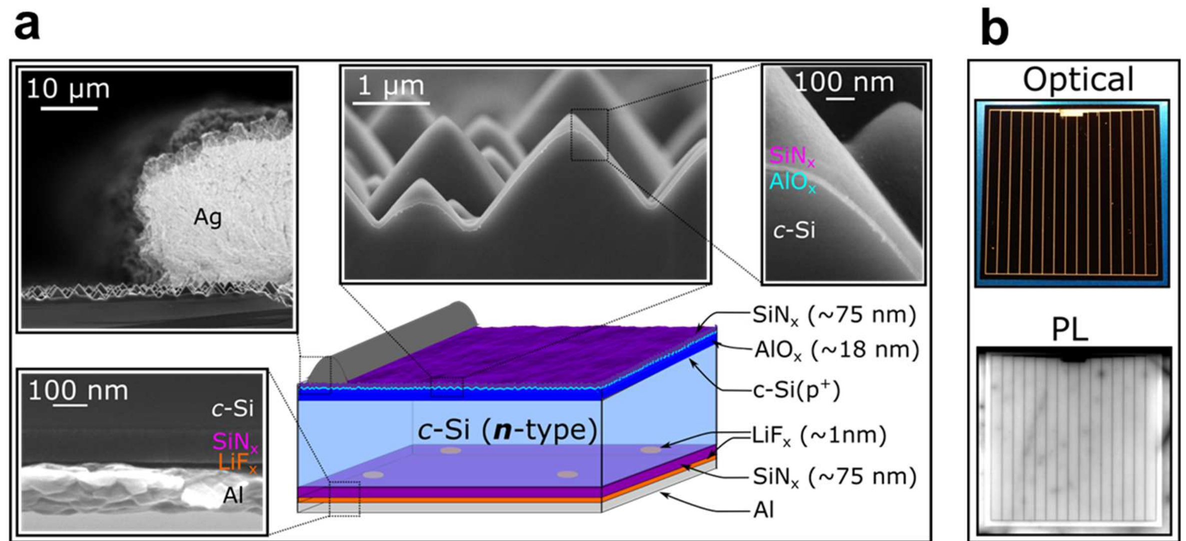

Figure 3: (a) Schematic of LiF_x / Al PRC cell and supporting SEM images of the front Ag plated finger (top left), rear stack in a non-contacted region (bottom left) and front random pyramid texturing on a 1 um (top middle) and 100nm (top right) scale. (b) Optical and photoluminescence (PL) images of the front surface of representative LiF_x / Al PRC cells.

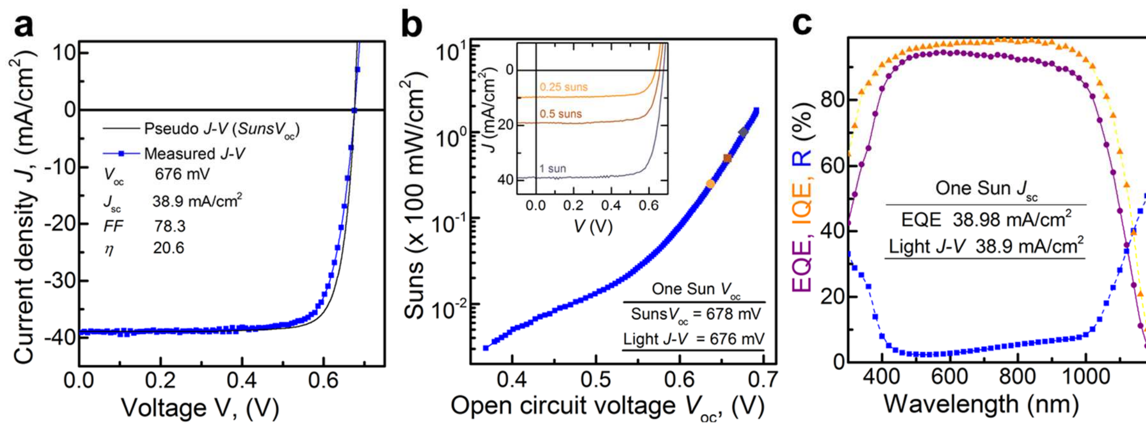

Figure 4: (a) Light *J-V* behaviour under 1 sun conditions of the LiF_x / Al PRC cell (blue squares) with inset cell characteristics alongside a pseudo *J-V* curve (obtained from SunsV_{oc} measurements) reflecting the cells performance in the absence of series resistance. (b) SunsV_{oc} behaviour of the LiF_x / Al PRC cell with a family of light *J-V* curves measured at 1, 0.5 and 0.25 suns. (c) Quantum efficiency analysis of the LiF_x / Al PRC cells showing reflectance (blue squares), external quantum efficiency (purple circles) and internal quantum efficiency (orange triangles).

Using this information, high efficiency 2×2 cm^2 solar cells were fabricated on n-type (N_D ~$5\times10^{15}cm^{-3}$), float-zone grown wafers with ~0.9 % area LiF_x / Al partial rear contacts (for further design and fabrication details see experimental section and supporting information 2). Figure 3a provides a schematic representation of the cell structure, showing cross sectional scanning electron micrographs (SEM) of the cell's front and rear surfaces. The cells feature a random pyramid textured front surface with a boron diffusion passivated by an AlO_x / SiN_x antireflection stack. The boron diffusion is contacted via a Ag plated front metal finger grid with an effective shading fraction of less than 4%. Provided in Figure 3b are optical and photoluminescence micrographs of the front (sunward) side of representative LiF_x / Al PRC cells, showing uniform front surface optics and illuminated excess carrier density over the cell area, necessary conditions for a high power conversion efficiency.

The light *J-V* behaviour of a LiF_x / Al PRC cell is provided in Figure 4a, indicating an efficiency of 20.6% has been attained at the proof-of-concept stage for this technology

–already comparable to alike cells made with a full-area rear phosphorus diffusion which have an optimised efficiency of 21.5%.[30] The open circuit voltage V_{oc} and short circuit current J_{sc}, measured to be 676 mV and 38.9 mA/cm^2, respectively, demonstrate that the recombination and optical benefits of confining the rear contact to a small area have been realised. In addition, a fill factor of 78.3%, despite a contact fraction of less than 1% confirms the low resistivity of the LiF_x / Al interface. Also included in Figure 4a is a pseudo *J*-*V* curve without the effects of series resistance R_s obtained from SunsV_{oc} measurements, the comparison between the two curves revealing that the loss due to R_s is only minor. To analyse the stability of the contact system, light *J*-*V* characteristics are remeasured after a period of 3 months storage in air with no significant change in performance (for details see supporting information S3). The voltage of the cells is also confirmed by SunsV_{oc} measurements, shown in Figure 4b, which include a measured 1 sun V_{oc} of 678 mV. Provided in the inset of the same plot are a family of *J*-*V* curves taken at different illumination intensities, the V_{oc} values of which (indicated by the coloured data points) agree well the SunsV_{oc} trend. To investigate the visible spectrum response, a quantum efficiency analysis included in Figure 4c which shows a high internal collection efficiency > 90% across the 400 - 1000 nm range. A J_{sc} of 38.98 mA/cm^2 was extracted from the integrated external quantum efficiency, confirming the accuracy of the J_{sc} values obtained from light *J*-*V* measurements above. An estimation of the surface recombination velocity (SRV) at the LiF_x / Al contact is made by accounting for recombination in the other areas of the cell via a series of control samples. This analysis, detailed in supporting information S4, suggests that the SRV is significantly reduced with a value of ~5,000 cm/s compared to the directly metallised c-Si surface (~10^6 cm/s).

Conclusion This work demonstrates the general applicability of LiF_x / Al based electron contacts for silicon solar cells. Micrographs and elemental mapping of the *c*-Si(n)

/ LiF_x / Al interface indicate that a ~1.5nm LiF_x layer uniformly separates the Si wafer and the Al layer. This contact system achieves a reduction in ρ_c by several orders of magnitude compared to conventional metal contacts for a range of *c*-Si phosphorus (n-type) doping levels relevant to solar cell production.[7] The efficacy of this contact system is tested in an extreme case by integrating it as a < 1% area contact in a high efficiency n-type PRC solar cell without the use of phosphorus surface diffusions – an architecture which was not previously possible. This simplified proof-of-concept cell structure attained a conversion efficiency of greater than 20% - a value which already demonstrates its competitiveness with conventional high efficiency cell structures.

Experimental section TEM samples were fabricated on mechanically polished, n-type, FZ wafers. A LiF_x (~1.5 nm) and Al (~200 nm) stack was thermally evaporated from high purity sources (> 99.99%) at a base pressure $< 2\times10^{-6}$ mbar. A cross-section of this stack was prepared for TEM observation using the conventional focused ion (FIB) beam lift-out technique in a Zeiss Nvision 40. Final thinning was performed at 5 kV to reduce FIB induced damage. Scanning TEM images were then acquired in combination with either EDX or EEL spectra using a probe and image Cs-corrected FEI Titan Themis operated at 300 kV. Dual EEL spectroscopy of the edges Al $L_{2,3}$ and K (73 and 1560 eV), Si $L_{2,3}$ and K (99 and 1839 eV) and F K (685 eV) was performed with a dispersion of 1 eV/channel. The convergence semi-angle was set to 20 mrad.

Contact resistivity test structures were fabricated on range of n-type, float zone, silicon wafers with surface concentrations in the $10^{13} – 10^{20}$ range. The heavily doped n^+ surface (N_D ~3×10^{20}) is achieved by diffusing phosphorus into the surface from a $POCl_3$ source in a dedicated clean quartz furnace. TLM pads composed of a LiF_x (~1.5 nm) / Al (~200 nm) evaporated stack are defined either via photolithography or a shadow mask. Each TLM set is isolated along its edges to confine the current flow. Dark current voltage

(*I*-*V*) measurements between adjacent pad sets are taken in air (for the doping dependent study) or under vacuum (for the temperature dependent study). The specific contact resistivity is extracted as per the description in Ref[31] .The 'probe to probe' resistance, was measured and subtracted from each TLM pad set measurement.

Proof-of-concept PRC cell test structures were fabricated on lightly phosphorus doped (~5×10^{15}cm^{-3}) n-type, float zone, silicon wafers. Following front surface random pyramid texturing, a full-area boron diffusion with sheet resistance of approximately 120 Ω/□ was performed in a dedicated clean quartz furnace. This boron diffusion was passivated using a ~18 nm atomic layer deposited (ALD) AlO_x and ~75 nm plasma enhanced chemical vapor deposited (PECVD) SiN_x antireflection stack. The undiffused rear surface was passivated using a single PEVCD SiN_x film. The front (10 μm width lines, 1.3mm pitch) and rear (30 μm diameter dots, hexagonal pitch of 300 μm) contact areas were defined photolithographically. The front contact was formed by thermal evaporation of a Cr (~10 nm) / Pd(~10 nm) /Ag (~100 nm) stack which was subsequently thickened using Ag electroplating. The rear contact was formed by evaporating a LiF_x (~1.5 nm) / Al (~200 nm) stack under the same vacuum. The light *J*-*V* behaviour was measured under standard 1 sun conditions (100 mW/cm^2, AM 1.5 spectrum, 25°C) with a 2×2 cm aperture mask using an inhouse system (the cell's bus bar is included within the measured cell area). This system is calibrated with a certified Fraunhofer CalLab reference cell and we estimate the accuracy to be ± 1%. The EQE and reflectance measurements were taken using a Protoflex Corporation QE measurement system (QE-1400-03) and a PerkinElmer Lambda 1050 UV/VIS/NIR spectrophotometer (with an integrating sphere attachment), respectively. SunsV_{oc} and PL measurements were taken using a Sinton SunsV_{oc} tester and a BTImaging luminescence imager, respectively.

Acknowledgments Device design, fabrication, and characterization were funded by the Bay Area Photovoltaics Consortium (BAPVC) and the Australian Renewable Energy Agency (ARENA). Materials characterization was supported by the Electronic Materials Programs, funded by the Director, Office of Science, Office of Basic Energy Sciences, Material Sciences and Engineering Division of the U.S. Department of Energy under (Contract No. DE-AC02- 05CH11231). Work at EPFL was supported by the Office fedéral de l' énergie (OFEN), microscopy was conducted at the Centre for Electron Microscopy (CIME) of EPFL.

References

[1] D. K. Schroder, D. L. Meier, *IEEE Trans. Electron Devices* 1984, 31, 637.
[2] S. M. Sze, K. K. Ng, Physics of Semiconductor Devices, John Wiley & Sons, 2006.
[3] D. Macdonald, L. J. Geerligs, *Appl. Phys. Lett*. 2004, 85, 4061.
[4] J. Schmidt, A. Cuevas*, J. Appl. Phys.* 1999, 86, 3175.
[5] International Technology Roadmap for Photovoltaic (ITRPV), 2014 Results, Revision 1, July 2015, n.d.
[6] J. Benick, B. Hoex, M. C. M. van de Sanden, W. M. M. Kessels, O. Schultz, S. W. Glunz, *Appl. Phys. Lett.* 2008, 92, 253504.
[7] S. W. Glunz, R. Preu, D. Biro, *in Compr. Renew. Energy* (Ed.: A. Sayigh), Elsevier, Oxford, 2012, pp. 353–387.
[8] L. S. Hung, C. W. Tang, M. G. Mason, *Appl. Phys. Lett*. 1997, 70, 152.
[9] X. J. Wang, J. M. Zhao, Y. C. Zhou, X. Z. Wang, S. T. Zhang, Y. Q. Zhan, Z. Xu, H. J. Ding, G. Y. Zhong, H. Z. Shi, Z. H. Xiong, Y. Liu, Z. J. Wang, E. G. Obbard, X. M. Ding, W. Huang, X. Y. Hou, *J. Appl. Phys*. 2004, 95, 3828.
[10] C. Ganzorig, K. Suga, M. Fujihira, *Mater. Sci. Eng. B* 2001, 85, 140.
[11] C. J. Brabec, S. E. Shaheen, C. Winder, N. S. Sariciftci, P. Denk, *Appl. Phys. Lett*. 2002, 80, 1288.
[12] E. Ahlswede, J. Hanisch, M. Powalla, *Appl. Phys. Lett.* 2007, 90, 163504.
[13] S. Kim, J. Lee, V. A. Dao, S. Lee, N. Balaji, S. Ahn, S. Q. Hussain, S. Han, J. Jung, J. Jang, Y. Lee, J. Yi, *Adv. Mater. Charact. Tech. Sol. Cells* 2013, 178, 660.
[14] Y. Zhang, R. Liu, S.-T. Lee, B. Sun, *Appl. Phys. Lett*. 2014, 104.
[15] J. Bullock, M. Hettick, J. Geissbühler, A. J. Ong, T. Allen, C. M. Sutter-Fella, T. Chen, H. Ota, E. W. Schaler, S. De Wolf, C. Ballif, A. Cuevas, A. Javey, *Nat. Energy* 2016, 15031.
[16] M. Yamawaki, M. Hirai, M. Yasumoto, M. Kanno*, J. Nucl. Sci. Technol*. 1982, 19, 563.
[17] Y. Yuan, D. Grozea, S. Han, Z. H. Lu, *Appl. Phys. Lett*. 2004, 85, 4959.
[18] Q.T. Le, L. Yan, Y. Gao, M.G. Mason, D.J. Giesen, C.W. Tang, *J. Appl. Phys*., 2000, 87, 375
[19] E. D. Glowacki, K. L. Marshall, C. W. Tang, N. S., Sariciftci, *Appl. Phys. Lett*. 2011, 99, 043305
[20] H. Ishii, K. Sugiyama, E. Ito, K. Seki, *Adv. Mater*. 1999, 11, 605
[21] S. E. Shaheen, G. E. Jabbour, M. M. Morrell, Y. Kawabe,B. Kippelen, N. Peyghambarian, M.-F. Nabor, R. Schlaf, E. A. Mash, N. R. Armstrong, *J. Appl. Phys*. 1998, 84, 2324.
[22] R. Schlaf, B. A. Parkinson, P. A. Lee, K. W. Nebesny, G. Jabbour, B. Kippelen, N. Peyghambarian, N. R. Armstrong, *J. Appl. Phys*. 1998, 84, 6729.
[23] F. Werner, B. Veith, D. Zielke, L. Kühnemund, C. Tegenkamp, M. Seibt, R. Brendel, J. Schmidt, *J. Appl. Phys.* 2011, 109, 113701.

[24] R. Hezel, *Solid-State Electron*. 1981, 24, 863.
[25] D. B. M. Klaassen, *Solid-State Electron*. 1992, 35, 953.
[26] E. Franklin, K. Fong, K. McIntosh, A. Fell, A. Blakers, T. Kho, D. Walter, D. Wang, N. Zin, M. Stocks, E.-C. Wang, N. Grant, Y. Wan, Y. Yang, X. Zhang, Z. Feng, P. J. Verlinden, *Prog. Photovolt. Res. Appl.* 2014, DOI 10.1002/pip.2556.
[27] J. Robertson, *J. Vac. Sci. Technol.*, A 2013, 31, 050821
[28] B. F. Bory, H. L. Gomes, R. A. J. Janssen, D. M. de Leeuw, S. C. J. Meskers*, J. Appl. Phys*. 2015, 117, 155502.
[29] J. W. Chen, A. G. Milnes*, Annu. Rev. Mater. Sci.* 1980, 10, 157.
[30] J. Bullock, A. Cuevas, C. Samundsett, D. Yan, J. McKeon, Y. Wan, *Sol. Energy Mater. Sol. Cells* 2015, 138, 22.
[31] D. K. Schroder, Semiconductor Material and Device Characterization, John Wiley & Sons, Hoboken, New Jersey, 2006.

Supporting information 1. Contact facilitation

It is known that low resistance contact between lowly doped n-type *c*-Si and Al is difficult, due to the formation of a surface barrier, resulting in rectifying behaviour.[1] This was found to be the case for all contacts made to phosphorus dopant concentrations in the 10^{13} - 10^{16} range. The addition of the thin LiF_x interlayer dramatically improved the contact, resulting in Ohmic behaviour even in the extreme cases of low temperature

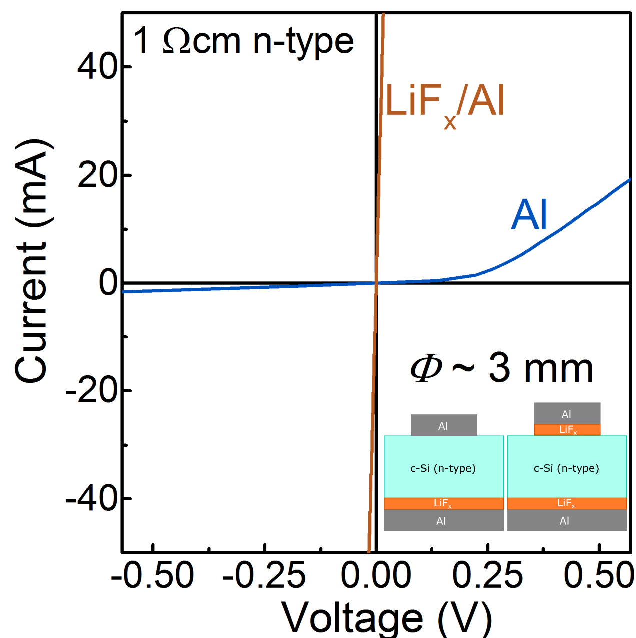

Figure S1: Simple vertical contact structures highlighting the transition from rectifying to Ohmic behaviour as a result the addition of the thin LiF_x layer on n-type ($N_D = 5\times10^{15}$ cm-3) *c*-Si.

(77 K) and low doping ($4\times10^{13}cm^{-3}$). An example of the difference between structures made with and without the LiF_x interlayer is provided for a *c*-Si wafer with a dopant concentration of ~5×10^{15} cm^{-3} in Figure S1. The rectifying behaviour of the direct Al contact prevented an accurate extraction of the contact resistivity, but it is estimated to be greater than 5 Ωcm^2, compared to ~2 $m\Omega cm^2$ for LiF_x / Al contacts. However, Ohmic contact was achieved between the heavily doped *c*-Si(n) surface (N_D ~10^{20} cm^{-2}) and the direct Al contact due to electron tunnelling through the reduced barrier width.

Supporting information 2. Optimisation of LiF_x / Al PRC design

The choice of wafer doping and rear contact configuration for a *c*-Si PRC cell is not straightforward. This is mainly linked to the heavy dependence that many important parameters have on the wafer doping. Among the most important of these are contact

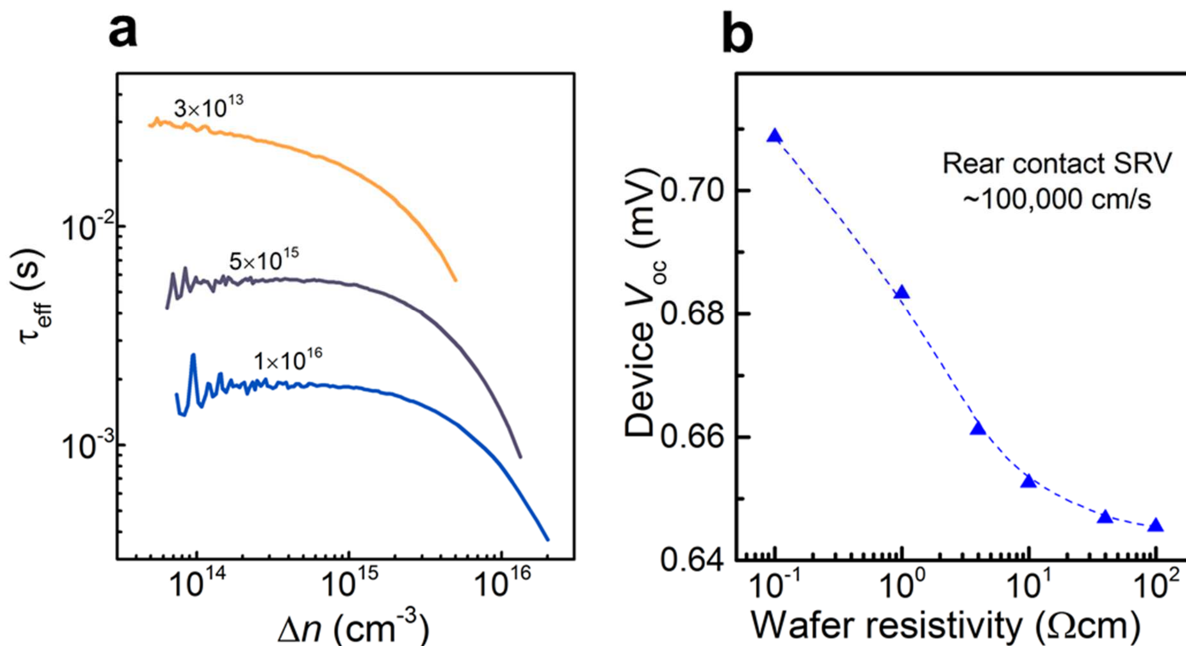

Figure S2: (a) Excess carrier dependent lifetime $\tau_{eff}(\Delta n)$ for c-Si(n) wafers with a range of doping concentrations between 10^{13} – 10^{16} cm^{-3}. To assess the bulk lifetime, state-of-the-art PECVD SiN_x passivation is applied to both wafer surfaces and the lifetime measured via PCD. (b) Simulated idealised PRC device V_{oc} as a function of wafer resistivity when a contact SRV of 10^5 cm/s is assumed. This highlights the increased sensitivity to the SRV for higher resistivity wafers.

resistivity (as shown in Figure 2c of the main text), the bulk lifetime (as shown in Figure S2a), lateral transport and crowding of majority carriers and impact of a given surface recombination velocity (SRV, as shown in Figure S2b). To simultaneously consider all these effects, two dimensional simulations of an idealised n-type PRC cell are run in Quokka.[2] The input parameters of this cell design are given in Table S2 below, and the results are shown in Figure 2d of the main text.

The high efficiency cells detailed in Figures 3 and 4 of the main text utilise a three-dimensional 'dot' PRC structure. It is computationally expensive to simulate such a large ρ_c-ρ_b parameter space and so a two dimensional 'line' contact structure is simulated instead. Whilst the same trends are expected for these two contact systems the optimum fraction for the dot contact will be smaller than that presented in Figure 2d for line contacts, in this case 0.9% is chosen as a suitable contact percentage.

Table S2: Idealised inputs for n-type PRC simulation.

Parameter	Value
Front recombination	1 fA/cm^2
Bulk lifetime	Variable, intrinsic lifetime based on Richter *et. al.* parameterisation[3]
Wafer doping	Variable, 3×10^{13} – 8×10^{16} cm^{-3} phosphorus concentration
Wafer thickness	160 µm
Rear recombination (non-contact)	1 fA/cm^2
Rear line contacts	Contact width (µm) = variable (minimum value 2µm) Contact pitch (µm) = variable

Supporting information 3. Light *J-V* stability.

Historically the alkali metals have been avoided in silicon processing as they are known to diffuse fast in *c*-Si and form energy states within the bandgap. For the case of Li the energy state has been suggested to be a shallow donor.[4] In order to test the stability

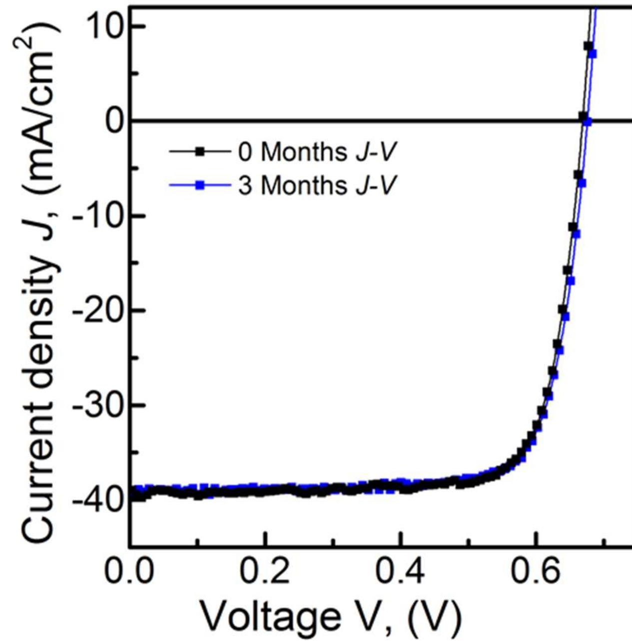

Figure S3: Light *J-V* behaviour measured at 1 sun after fabrication and after an additional 3 months storage

of the LiF_x / Al PRC cell, light *J-V* measurements are taken under identical illumination and temperature conditions after a period of ~3 months storage in air. As can be seen in Figure S3, negligible change is seen over this period, suggesting stability of the contacts, for the duration of the time period investigated.

Supporting information 4. Estimation of the *c*-Si(n) / LiF_x / Al contact surface recombination velocity.

To estimate the contribution that the rear LiF_x / Al contact makes to the total recombination, test structures are fabricated to measure the recombination occurring in different areas of the PRC cell. Schematic diagrams of these test structures are detailed in Figures S4a, c, d and e. Recombination factors J_0, are extracted from the excess carrier dependent lifetime $\tau_{eff}(\Delta n)$ of control test structures measured by photoconductance decay (PCD). J_0 values representing the recombination contribution from the front surface metal and passivated regions as well as the rear passivated regions are included in Figure S4b. In addition, the post-processing bulk τ_{eff} of the silicon wafer, shown in Figure S4c, is

found to be ~1.5ms (at $\Delta n = 10^{15}$ cm^{-3}). The AlO_x, SiN_x and Al layers used in these test structures are deposited at thicknesses of 18 nm, 75 nm and ~10 nm using ALD, PECVD and thermal evaporation, respectively.

These extracted J_0 and τ_{eff} values are used in conjunction with those detailed in Table S4 to simulate the performance of the PRC cell as a function of the rear contact surface recombination velocity (SRV). A quasi-analytical, iterative model of the three-dimensional device geometry,[5] is used to model the output parameters of the solar cell (V_{oc} , J_{sc}, FF and η) as a function of the SRV at the partial rear contact. Figure S4f shows the V_{oc} as a function of the rear contact SRV. A good match between simulated and measured V_{oc} (676 ± 2 mV) is obtained for an SRV of ~5x10^3 cm/s. This is more than two orders of magnitude less than that expected from a directly metallised *c*-Si surface. Figure S4g shows a comparison of the measured light *J-V* and that simulated with a SRV of 5x10^3 cm/s, both giving the same maximum output power and an efficiency of 20.6%.

Table S4. Parameters utilised in the PRC cell simulation

Device property	Parameter	Value
Contact	Front contact fraction	3%
	Rear contact fraction	0.9%
	Rear contact resistivity	2 mΩcm^2
Doping	Base resistivity	1 Ωcm (n-type)
	Boron diffusion sheet resistance	120 Ω/□
	Wafer thickness	160 µm
Recombination	Minority carrier lifetime	1500 µs
	Passivated rear recombination current	3 fA/cm^2
	Front recombination current	72 fA/cm^2
Optics	Front surface shading	3%
	Front antireflection coating on textured surface	~75nm SiN_x
Parasitic resistances	Series resistance	0.75 Ωcm^2
	Shunt resistance	> 10^6 Ωcm^2

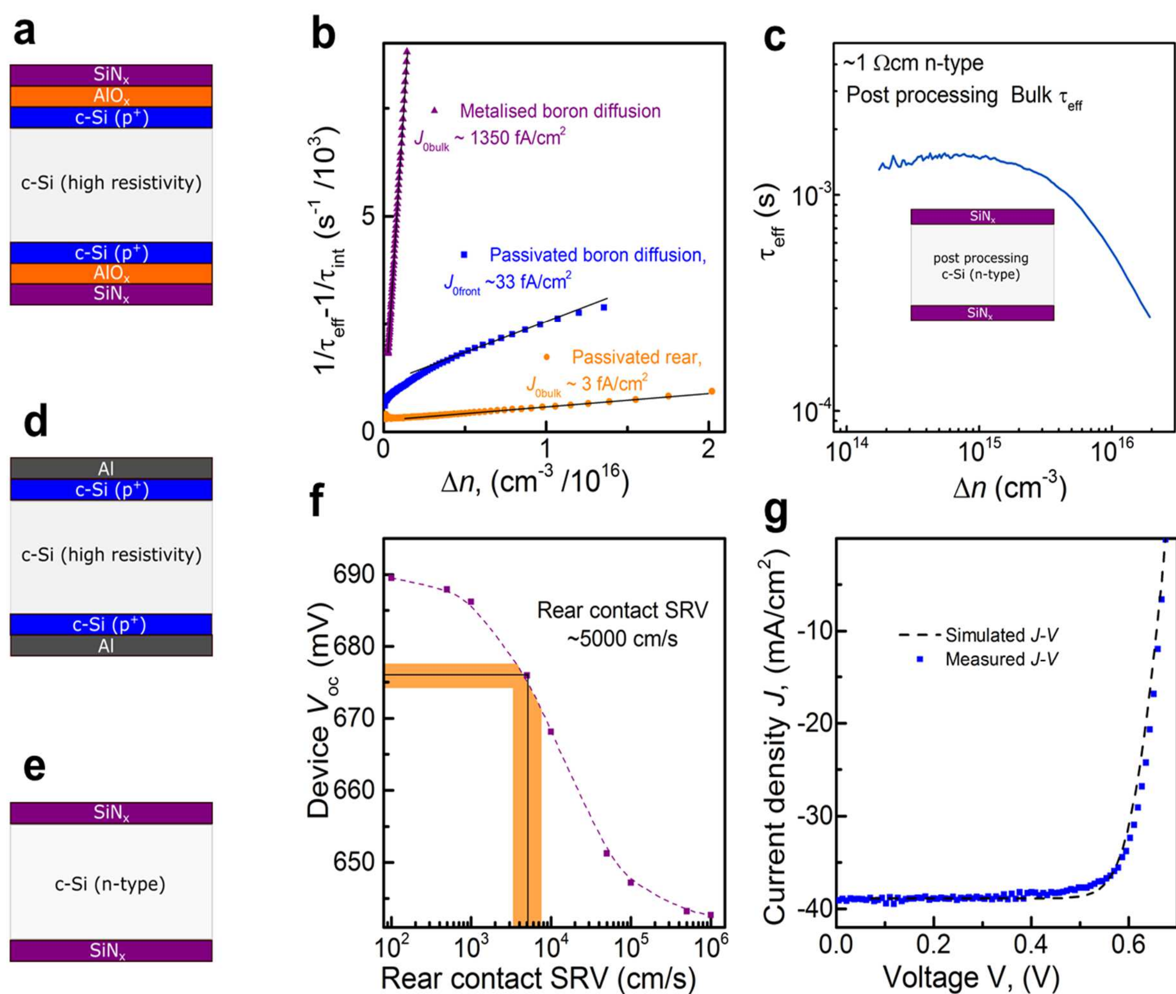

Figure S4: (a) Test structure used to measure the J_0 of the passivated front region. (b) J_0 measurements of the front passivated and metallised regions and the rear passivated region. (c) The post processing bulk lifetime of the LiFx /Al PRC cells. (d) and (e) Test structures used to measure the J_0 of the metalized front and passivated rear samples. (f) Simulated V_{oc} of n-type LiF_x / Al PRC cell ($N_D = 5\times10^{15}$ cm-3) as a function of rear contact SRV showing that a SRV value of ~5000 cm/s agrees well with the measured cell results in Figure 4 of the main text. (g) Comparison between measured and simulated light *J-V* behaviour of n-type PRC cells. A rear contact SRV of ~5,000 cm/s is assumed in the model.

Supplimentory references

[1] D. K. Schroder, D. L. Meier, IEEE Trans. Electron Devices 1984, 31, 637.
[2] A. Fell, Electron Devices IEEE Trans. On 2013, 60, 733.
[3] A. Richter, S. W. Glunz, F. Werner, J. Schmidt, A. Cuevas, Phys. Rev. B 2012, 86, 165202.
[4] J. W. Chen, A. G. Milnes, Annu. Rev. Mater. Sci. 1980, 10, 157.
[5] A. Cuevas, Prog. Photovolt. Res. Appl. 2014, 22, 764.

Efficient silicon solar cells with dopant-free asymmetric heterocontacts

James Bullock[1,2,3,4], Mark Hettick[1,2,3], Jonas Geissbühler[5], Alison J. Ong[1,2,3], Thomas Allen[4], Carolin M. Sutter-Fella[1,2,3], Teresa Chen[6], Hiroki Ota[1,2,3], Ethan W. Schaler[1], Stefaan De Wolf[5], Christophe Ballif[5], Andrés Cuevas[4] and Ali Javey[1,2,3,*].

[1] Department of Electrical Engineering and Computer Sciences, University of California, Berkeley, California 94720, USA.

[2] Berkeley Sensor and Actuator Center, University of California, Berkeley, California 94720, USA

[3] Materials Sciences Division, Lawrence Berkeley National Laboratory, Berkeley, California 94720, USA.

[4] Research School of Engineering, The Australian National University (ANU), Canberra, ACT 0200, Australia

[5] École Polytechnique Fédérale de Lausanne (EPFL), Institute of Micro Engineering (IMT), Photovoltaics and Thin Film Electronic Laboratory (PVLab), Maladière 71b, CH-200 Neuchatel, Switzerland

[6] The Molecular Foundry, Lawrence Berkeley National Laboratory, Berkeley, California 94720, USA.

Published in Nature Energy

A salient characteristic of solar cells is their ability to subject photo-generated electrons and holes to pathways of asymmetrical conductivity—‘assisting’ them towards their respective contacts. All commercially available crystalline silicon (c-Si) solar cells achieve this by utilising doping in either near-surface regions or overlying silicon-based films. Despite being commonplace, this approach is hindered by several optoelectronic losses and technological limitations specific to doped-silicon. A progressive approach to circumvent these issues involves the replacement of doped-silicon contacts with alternative materials which can also form ‘carrier-selective’ interfaces on c-Si. Here we successfully develop and implement dopant-free electron and hole carrier-selective heterocontacts using alkali metal fluorides and metal oxides, respectively, in combination with passivating intrinsic amorphous silicon interlayers, resulting in power conversion efficiencies approaching 20%. Furthermore, the simplified architectures inherent to this

approach allow cell fabrication in only seven low-temperature (≤ 200°C), lithography-free steps. This is a marked improvement on conventional doped-silicon high-efficiency processes, and highlights potential improvements on both sides of the cost-to-performance ratio for c-Si photovoltaics.

The majority of *c*-Si solar cells within both industry and research laboratories utilise doped homojunctions to separate photo-generated electrons and holes. Researchers tasked with optimising these doped homojunctions are faced with a myriad of interrelated optical, carrier transport and recombination based losses, most notably parasitic absorption,[1] Auger recombination and other heavy doping effects[2,3] (for details see Supplementary Table 1). In addition, technological complexities associated with doping, such as high processing temperatures (> 800ºC, with a concomitant necessity for cleanliness), small contact fractions (< 0.5%), dopant glass removal and junction isolation must be considered.[4,5] These issues can be partially alleviated by switching to architectures which instead utilise a set of asymmetric carrier-selective heterocontacts—a strategy that has long been considered a crucial technological step to attaining the intrinsic efficiency limit of *c*-Si.[6] Carrier-selective heterocontacts provide a negligible resistance to the collected carrier (synonymous with a low contact resistivity) whilst simultaneously 'blocking' the other carrier (equivalent to low contact recombination). This can be achieved via a number of possible mechanisms at the heterocontact, for example using surface passivating layers or stacks which provide conductivity asymmetry via band offsets, tunnelling probabilities or band bending when applied to c-Si.[7]

In recent years, the benefits of the asymmetric heterocontact concept have been realised, perhaps most famously by the silicon heterojunction cell architecture (SHJ, sometimes called HIT, 'heterojunction with intrinsic thin-layer'), which has now overtaken its homojunction counterpart in terms of efficiency, claiming the world record for *c*-Si in 2014.[8] Nonetheless, thus far, all competitive demonstrations of asymmetric heterocontacts,[9-11] including the SHJ technology, still rely on doped silicon layers, which introduce complex deposition optimisations and parasitic optical losses.[12-14] A further advancement of the asymmetric carrier-selective heterocontact concept is to completely

replace doped-silicon layers with other materials which do not incur the same fundamental limitations and practical difficulties, as has been realised on amorphous silicon absorber cells previously.[15] Several such carrier-selective materials have now been demonstrated on *c*-Si including transition metal oxides,[16-19] organic films[20-22] and metal-insulator structures (used in metal-insulator-semiconductor inversion layer solar cells),[23-25] many of which were previously implemented in other absorber-type solar cells.[15,26-28] In contrast to the limitations of doped-silicon regions and layers, the use of different carrier-selective materials opens a wider optical and electrical parameter space, decoupling the optimisation of different solar cell components. Furthermore, they can generally be deposited using simpler techniques (evaporation, spin coating, spray pyrolysis etc.), at low temperatures — potentially reducing the cost and complexity of fabrication. Nevertheless, as it currently stands, *c*-Si solar cells implementing a set of dopant-free asymmetric heterocontacts (DASH cells) have been limited to efficiencies less than 14%,[29-32] hindered mostly by carrier recombination losses at the heterointerface with *c*-Si. This paper demonstrates a marked improvement on the state-of-the-art DASH cell, facilitated by dopant-free heterocontacts which implement thin passivating interlayers, the electron contact of which is presented for the first time here. By addressing surface recombination, via passivating interlayers, proof-of-concept cells with open circuit voltages in excess of 700 mV and conversion efficiencies close to 20% have been demonstrated. These developments promote the DASH cell approach into the realm of competitive *c*-Si cell architectures.

DASH cell concept. Figure 1 outlines the conceptual structure of the DASH *c*-Si solar cell explored in this work. In this instance, as in the SHJ cell, thin 'passivating' intrinsic hydrogenated amorphous silicon *a*-Si:H(*i*) films are implemented on both sides

of the wafer. Unlike doped *a*-Si:H films, which result in 100% parasitic absorption, these less-defective intrinsic thin films contribute some current to the solar cell.[12] More importantly these layers greatly reduce the carrier recombination rate at the *c*-Si surface, enabling a high excess carrier concentration under illumination, essential for a high solar cell operating voltage. Such layers must be kept sufficiently thin to avoid excessive resistance and absorption losses.[12] We note these *a*-Si:H(*i*) films are not integral to the DASH concept and could be replaced in the future with other non-absorbing or higher-lifetime organic or inorganic passivating films. On top of the thin passivating layer electron-selective and hole-selective materials are deposited on opposite wafer surfaces. In contrast to the SHJ process, rather than using doped a-Si:H films, in this study transparent materials with extreme work-function values are chosen to achieve carrier-selectivity. Ideally, when a material with a very low work-function is applied to lightly doped *c*-Si, accumulation of electrons (and repulsion of holes) occurs near the surface. This high concentration of surface electrons reduces the heterocontact resistivity and the corresponding low hole surface concentration reduces the probability of Shockley-Read-Hall recombination at the heterocontact interface. The corollary holds for holes and high work-function materials. In this manner, by placing materials with an extreme work-function difference on either side of a *c*-Si wafer, efficient separation of photo-generated carriers can be achieved. Finally, the remaining supporting structures (transparent conductive oxide and metal contacts) are deposited—enabling optimal light coupling into the cell and low resistive losses for photo-generated carriers *en route* to the external circuit.

Central to the DASH cell concept is the functionality of the carrier-selective heterocontacts. For the hole-selective side, we previously developed a a-Si:H(*i*) / molybdenum oxide MoO_x based contact to *c*-Si which owes its hole-selectivity to a very

large work-function of MoO_x.[17,33] Such a structure has recently been demonstrated to be compatible with efficiencies above 22%.[34] However, a dopant-free electron-selective heterocontact with an equivalent level of performance has yet to be demonstrated. A group of proven electron-selective materials, frequently used in organic devices, is that formed by the alkali and alkaline earth metal salts. These materials consist of a metal cation from groups 1 or 2 of the periodic table ionically bonded to different anions, such as carbonate,[35] acetate[36] or halogens.[36-38] Whilst there still exists some contention as to the mechanism of the high electron conductivity across this interface,[35-37] most studies attribute the formation of a low work-function electrode as the most important consequence. Of particular interest within this group of materials are the alkali metal fluorides (AMFs). Thermally evaporated AMFs are explored here as a novel component, complementary to MoO_x, for *c*-Si solar cells. Such a combination has been implemented on other absorber materials previously. Three representative AMFs (LiF_x, KF_x, and CsF_x) are studied to identify which presents the best contact properties to *c*-Si.

Optoelectronic properties of carrier selective materials. As discussed above, the work-function of the carrier-selective materials can play a crucial role in the efficacy of the DASH cell approach. The X-ray photoelectron spectroscopy (XPS) secondary electron cut-off (SEC) analysis presented in Figure 2a shows very low work function values of the LiF_x / Al, KF_x / Al and CsF_x / Al interfaces measured to be 2.86, 2.46 and 2.61 eV respectively. Provided in the same plot is the previously measured value of ~5.7 eV for the high work function material MoO_x,[17] demonstrating the desired extreme work function separation as discussed above.

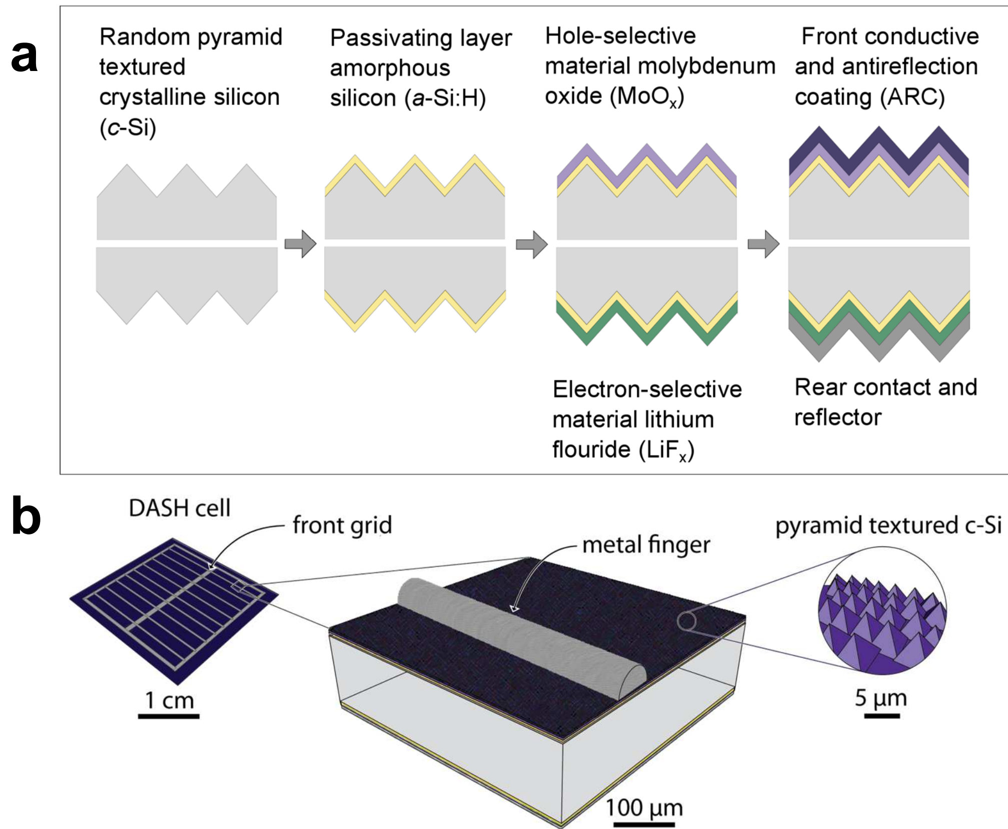

Figure 1: Conceptual structure of the DASH solar cell. a, Cross-section of the DASH cell structure showing the incremental addition of layers. Of notable benefit is the inherent simplicity of the approach requiring no lithography or high temperature processing. b, 3D representation showing the metal grid and texture of the front (sunward) side of the DASH cell.

A unique advantage of dopant-free heterocontacts is the ability to separately tune their optical and electronic impact on the solar cell. A Tauc plot for LiF_x, KF_x, CsF_x and MoO_x, films is provided in Figure 2b, alongside the AM 1.5G spectrum to evaluate the significance of their absorption. Also included in this Tauc plot are trends for phosphorus and boron-doped a-Si:H which are typically implemented as ~10nm films in standard doped-silicon SHJ cells.[39] It can be seen that the MoO_x and AMF films exhibit higher transparency across the spectrum as compared to the conventional doped *a*-Si:H layers. The Tauc energy gap E_{Tauc} of the AMFs is greater than the measurement range (>6.8 eV), resulting in negligible absorption while MoO_x films display an E_{tauc} of ~3 eV, resulting in minor absorption of high-energy light (where the Sun's irradiance is relatively low). Ray tracing simulations reveal that compared to the SHJ cell's doped-silicon

heterocontacts, a reduction in front-film parasitic absorption of ~1 mA/cm^2 could be achieved by switching to an optimised dopant-free heterocontact cell design (see Supplementary Note and Figure 1). In addition, core level and valence band XPS analyses of LiF_x and MoO_x films are shown in Figure 2c. The valence band of the LiF_x is measured to be ~6.6 eV from the Fermi energy and shows no clear sub-band features despite the reduced component suggested by the shape of the Li 1s peaks. The MoO_x valence band and core levels are in alignment with those previously measured for evaporated films, showing the clear formation of a sub-band peak originating from a reduced MoO_x state that has demonstrated importance for its carrier-selective function.[17] Extractions of the film stoichiometry based on core level peak areas also support a slightly reduced cation oxidation state for both LiF_x and MoO_x films.

Electron heterocontact development. Whilst the electrical contact properties of MoO_x based hole-selective heterocontacts on *c*-Si have previously been characterised and shown to be promising for *c*-Si solar cells,[17-19, 33, 34, 40] the application of AMF / Al electron-selective contacts in *c*-Si solar cells remains relatively unexplored.[32, 41] Figure 3a shows that the contact resistivity ρ_c for LiF_x/Al (blue), KF_x / Al (red) and CsF_x / Al (orange) to moderately-doped n-type (N_d ~5×10^{15} cm^{-3}) *c*-Si has a strong dependence on AMF interlayer thickness, with all three materials producing the lowest ρ_c values in the 0.5 – 1.5 nm range. The lowest extracted values of ~1 mΩcm^2 for the LiF_x / Al and CsF_x / Al contacts are at the limit of the measurement resolution, representing an upper limit ρ_c (for details see Supplementary Note 2). Such values are exceptionally low, given the well-known difficulties of contacting moderate resistivity n-type *c*-Si – an issue associated with Fermi level pinning and the position of silicon's

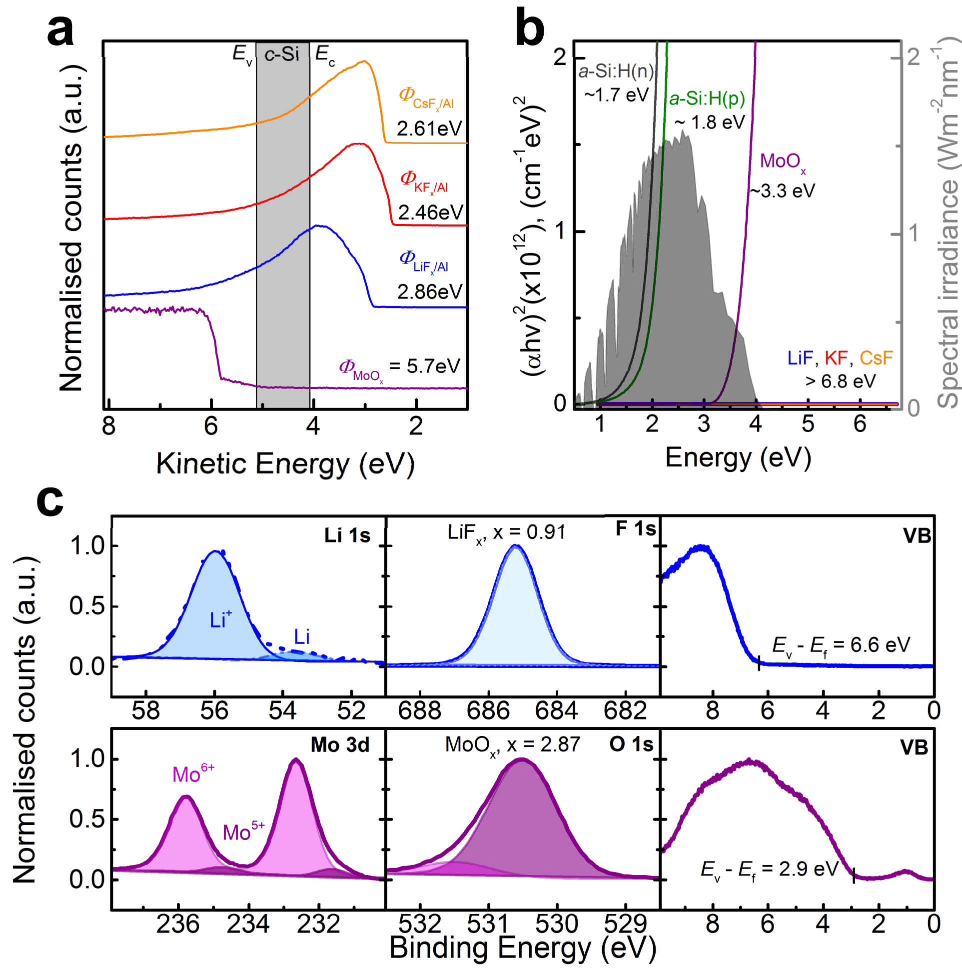

Figure 2: Optoelectronic properties of carrier-selective layers. a, Secondary electron cut-off spectrum yielding low work function Φ values for electron-selective contacts measured at the LiF_x / Al, KF_x / Al and CsF_x / Al interfaces. A spectrum for the high work function Φ hole-selective material MoO_x, developed previously, is also included. The shaded area represents the band position of *c*-Si. b, Tauc plot of carrier-selective materials LiF_x, KF_x, CsF_x and MoO_x. As a reference the AM 1.5G spectrum (which represents the sun's output) is included. These are compared to the highly absorbing phosphorus and boron doped *a*-Si:H films used in SHJ cells. c, Core level and valence band spectrum for LiF_x and MoO_xfilms, fitted with multiple Voigt peaks (shaded areas) to quantify the contribution of different oxidation states. The estimated stoichiometry of the two materials of the two films is also included.

charge neutrality level close to the valence band.[42] This introduces the possibility of previously unattainable cell architectures, for example n-type undiffused partial rear contact cells. The measured stability of these electron-selective contacts in both air (solid markers) and argon (hollow markers) is provided in Figure 3b. An increase in ρ_c for CsF_x and KF_x based contacts is seen within the first 24 hours of air exposure. This increase is slowed by more than an order of magnitude as a result of storing the samples in argon

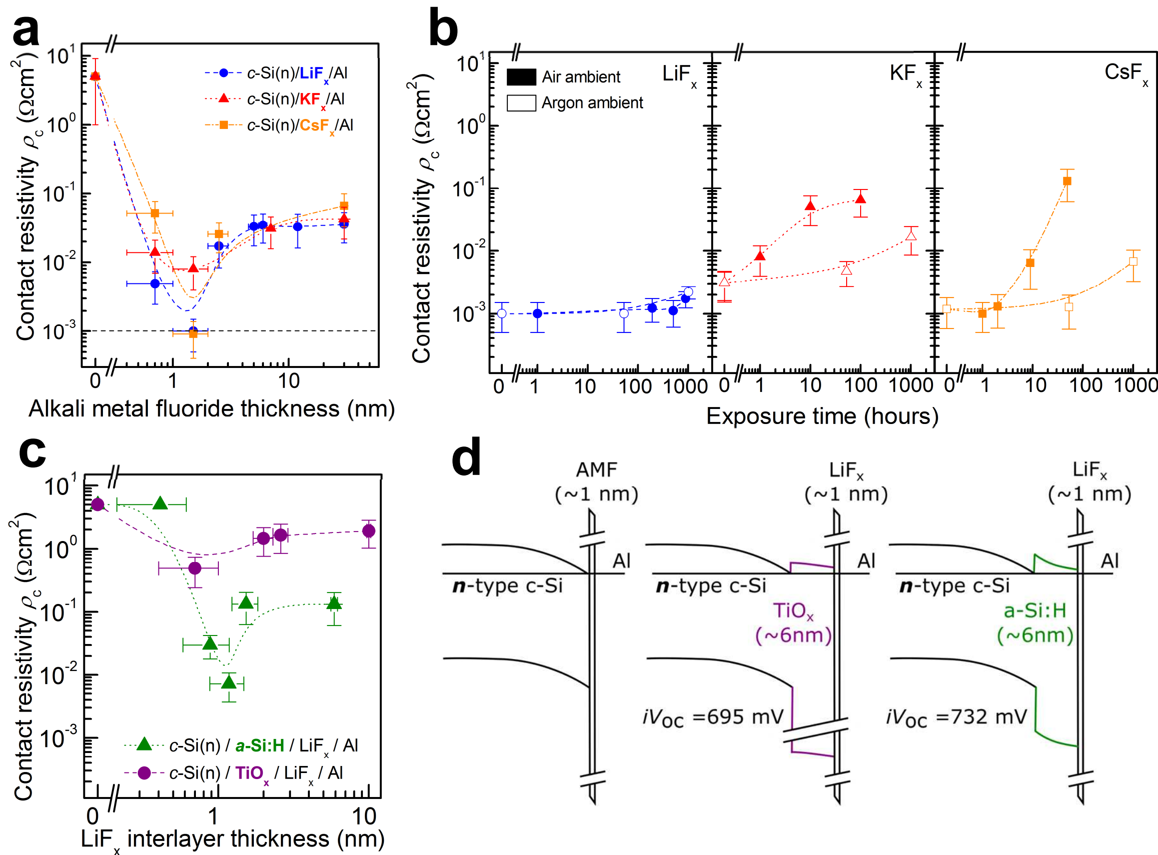

Figure 3: Contact-level analysis of electron-selective contacts. Contact resistivity of LiF_x / Al (blue), KF_x / Al (red) and CsF_x / Al (orange) contacts made to n-type silicon as a function of a, AMF interlayer thickness and b, exposure time to air (solid) and argon (hollow) ambient. The dotted horizontal line in a, represents the estimated resolution of the ρ_c extraction technique (see Supplementary Note 2). c, ρ_c evolution against LiF_x thickness for heterocontacts with TiO_x (purple) and *a*-Si:H(*i*) (green) interlayers. d, schematics of the direct AMF / Al contact as well as heterocontacts implementing TiO_x and *a*-Si:H(*i*) interlayers. The implied open circuit voltage iV_{oc} of the two passivating layers are also included. Error bars are based off the measured spread in data or estimated error in the measurement (whichever is largest). Lines provide a guide to the eyes only.

ambient. The LiF_x electron-selective contact, however, exhibits exceptional longevity with negligible degradation over 1000 hours in both environments and is therefore used in the DASH cells presented in this work.

A high rate of recombination at the *c*-Si / LiF_x interface precludes the direct implementation of full-area LiF_x/Al electron-selective contacts into solar cells (for details see Supplementary Note 2). This issue can be amended by the addition of a thin passivating interlayer between the *c*-Si and LiF_x / Al stack. As shown in Figure 3d two potential candidates for passivating the *c*-Si surface are hydrogenated amorphous silicon

a-Si:H(*i*) (as utilised in the SHJ cell) and titanium oxide TiO_x.[16,30] Both of these films greatly reduce the *c*-Si surface recombination rate allowing high implied open circuit voltage V_{oc} around 700 mV in line with state-of-the-art surface passivation (for details see Supplementary Note 2). Figure 3c shows the ρ_c dependence on LiF_x thickness for n-type wafers passivated with ~6 nm TiO_x (purple) or *a*-Si:H(*i*) (green) films. Clear improvements in electron-selectivity seen with the addition of the LiF_x / Al contact for these disparate passivation strategies highlight the versatility of this approach. Optimum ρ_c values of 500 and 7 mΩcm^2 are found for the TiO_x / LiF_x / Al and *a*-Si:H(*i*) / LiF_x / Al heterocontacts respectively, both with a LiF_x interlayer thickness of ~1 nm. These two values fall at the upper and lower end of an equivalent ρ_c range reported in the literature for doped-silicon based heterocontacts.[43,44] Simulating these contacts within an idealised solar cell, indicate that both systems could be effectively applied as full-area electron heterocontacts and that devices implementing *a*-Si:H(*i*) interlayers will produce higher efficiencies (for details see Supplementary Note 3 and Supplementary Figure 4).

High efficiency proof-of-concept DASH cells. Finally, high-efficiency DASH cells implementing a-Si:H(*i*) / LiF_x / Al and a-Si:H(*i*) / MoO_x heterocontacts were fabricated. Cross-sectional scanning electron micrographs of the top and bottom random pyramid textured surfaces of the DASH cell are included in Figure 4a. Texturing is employed to enhance both the amount of light coupled into the cell and the path length of that light once inside the cell. Of notable benefit in this cell architecture is the fabrication procedure, requiring just seven low-temperature steps without the use of complex alignment or photolithography. This offers a significant simplification over dopant-diffused high-efficiency architectures which involve ~20 steps and a high thermal budget.[45] The simple, room temperature deposition of dopant-free selective layers also potentially introduces benefits over doped *a*-Si:H layers, used in SHJ cells, which are

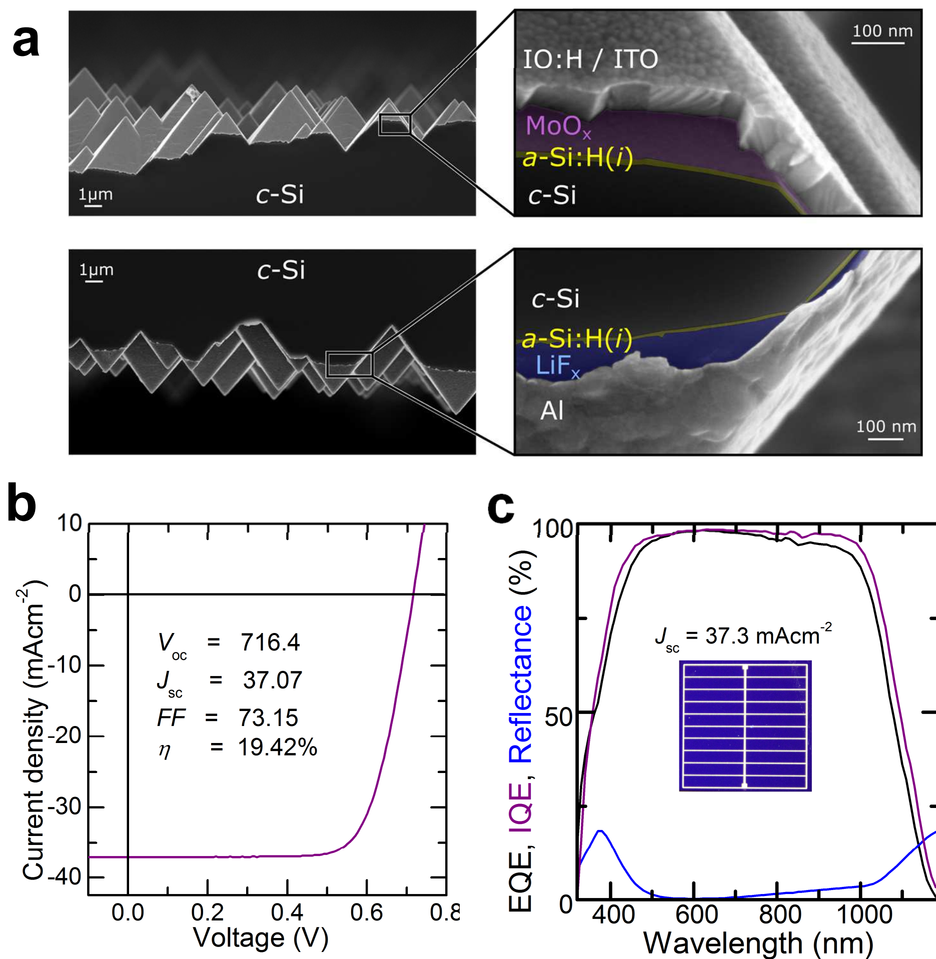

Figure 4: DASH cell level results. a, Micrometre (LHS) and 100 nanometre (RHS) scale cross-sectional scanning electron micrographs of the textured front (sunward side) and back surfaces of the DASH cell. The 100 nanometre scale image is false coloured to highlight the different films on each surface. b, Light *JV* behaviour and cell characteristics of the DASH cell measured under standard 1 sun conditions. c, External (black) and internal (purple) quantum efficiencies alongside the measured reflectance (blue) for the DASH cells. The J_{sc} obtained from the external quantum efficiency, shown above a photograph of the DASH cell, agrees well with that measured from the light *JV* analysis.

typically deposited at ~200°C using toxic gases and require precise condition control to balance trade-offs between J_{sc}, V_{oc} and fill factor based losses.[12-14]

Light *J*-*V* measurements provided in Figure 4b, show that percentage conversion efficiencies η of up to 19.4% have been achieved in the early stages of this DASH cell development, enabled by a V_{oc}, J_{sc} and fill factor of 716 mV, 37.07 mA/cm^2 and 73.15%, respectively. Statistics of the champion cell batch reveal a tight spread in results with an

average efficiency above 19%, a testament to the reproducibility of this DASH cell design (see Supplementary Table 2). An accompanying spectral response analysis, shown in Figure 4c, reveals high quantum collection efficiency over most of the AM1.5G spectrum (see Supplementary Figure 5 and Supplementary Note 4 for further DASH cell characterisation). An enhancement in the rear-side reflection and a reduction in the series resistance of the DASH cell are identified as the two most likely paths towards higher efficiency for this design. An improvement in J_{sc} of ~1 mA/cm^2 could arise by replacing Al with Ag or possibly ITO, and a boost in the fill factor above 79% could occur by further reducing the resistive loses as detailed in the Supplementary Note 4. It is envisioned that future iterations of this DASH approach could be combined with even lower thermal budget processing—integrating amorphous transparent conductive oxides,[46,47] plating metallisation[34] and low-cost, low-temperature back-end processing.[48]

Conclusion. In this work we have demonstrated the DASH cell concept—a simple, low-temperature *c*-Si solar cell featuring dopant-free heterocontacts—with high conversion efficiency. A key enabling factor is the development of a novel *c*-Si / *a*-Si:H(*i*) / LiF_x / Al electron-selective heterocontact to complement the recently developed *a*-Si:H(*i*) / MoO_x hole-selective heterocontact. Proof-of-concept device efficiencies approaching 20% have been achieved, supported by a high V_{oc} and low contact resistance at both heterocontacts. This represents a significant improvement on the state-of-the-art for this approach (from η of ~14% to ~20%) bringing the DASH architecture into the competitive realm of industrially applicable technologies including doped-silicon SHJ and conventional dopant-diffused architectures. The versatility and simplicity of the DASH approach can also potentially benefit more advanced solar cell architectures. In particular, dopant-free interdigitated back contact or dopant-free bifacial (using, for example, LiF_x/

transparent conductive oxide contacts) solar cells are both logical extensions of this work. The advancement past the limitations of single junction *c*-Si cells could also be facilitated using dopant-free carrier-selective contacts for a *c*-Si bottom cell in a monolithic tandem cell structure. Put simply, the above developed DASH system can effectively be viewed as a toolbox for a wide range of *c*-Si solar cell architectures, providing opportunities for facile fabrication of high-efficiency device structures at low temperatures.

Methods. Carrier-selective materials (LiF_x, KF_x, CsF_x, MoO_x) used in this study were deposited via vacuum thermal evaporation from powder sources (>3N purity). Controlled deposition rates of 0.25 - 1 Å/s (as monitored via a crystal oscillator) were used at a base pressure of $< 5\times10^{-6}$ mbar.

For XPS characterisation, thin films of LiF_x, KF_x, CsF_x, MoO_x or Al (or combinations thereof) were deposited on polished *c*-Si wafers. A Kratos AXIS Ultra DLD system with a monochromatic Al Kα X-ray source and a hemispherical analyser was used for the measurements. Secondary electron cut-off and valence band measurements were performed using X-ray excitation, with an added bias to extract the cut-off edge. Linear fits from the respective edges were utilized to extract numerical values for E_f - E_v (at the valence band edge) and the work functions of the AMF / Al interfaces. For the valence band measurements, thin layers of the final implemented contact materials (MoO_x and LiF_x) were characterized as-evaporated directly on *c*-Si substrates, in order to characterize directly the electronic structure near the valence band edge. Work functions were extracted for evaporated AMF / Al bilayers, with the Al thinned down to <5 nm by Ar ion milling (4 kV) in situ to observe the work function modification of the Al contact overlayer by the different AMFs. An Au reference work function at 5.2 eV was measured in the same measurement session confirming the accuracy of measurements. The core level spectra were fitted using the commonly applied Voigtian peak shapes and Shirley

background correction to extract the stoichiometry of the contact layers by the ratio of scaled peak areas. Peak areas were extracted from the background corrected Voigt fits of Li 1s, F 1s, Mo 3d, and O 1s spectra presented in Figure 2, and scaled by their relative atomic sensitivity factors[49] (normalized to F 1s). As expected due to the decomposition of these materials during the evaporation process, the MoO_x contact layer achieves a value of x approximately 2.87 (after accounting for the carbon-related oxygen contaminant peak commonly seen in O 1s levels for MoO_x films[50]), and the LiF_x contact layer is measured to have an x value of approximately 0.91, representing slightly sub-stoichiometric films in both cases. For the LiF_x material, a sub-stoichiometric film is observed due to the presence of a reduced Li(0) peak also observed in previous XPS measurements on LiF_x.[51] The MoO_x Mo 3d level indicates both the 6^+ and 5^+ oxidation states as in previous explorations of evaporated films,[17] a feature attributed to the formation of the defect band in as-evaporated MoO_x films.

Absorbance measurements were performed on transparent substrates with thin films of LiF_x, KF_x, CsF_x and MoO_x on one side (CaF_2 substrates were used for the AMFs and quartz was used for the MoO_x). Measurements were taken using a N_2 purged spectrophotometer (Cary 5000 UV-Vis-NIR spectrophotometer).

The *c*-Si(n) / AMF / Al electron-selective contacts were fabricated on planar, n-type (N_d ~5×10^{15} cm^{-3}), float zone (FZ), *c*-Si wafers with a thickness of ~200 μm. These were subjected to a dilute HF dip prior to evaporation of the contact structures. A full area stack consisting of a ~1.5 nm of AMF/ ~250 nm Al layer was evaporated without breaking vacuum on the rear-side of the contact structures. An array of different diameter circles were evaporated on the front of the test structures by means of a shadow mask. These circles were deposited as a stack of variable thicknesses of AMF capped with ~250 nm

of Al and ρ_c was extracted as described in Supplementary Note 2 and Supplementary Figure 2.

For the interlayer contact study, hydrogenated amorphous silicon films of ~6 nm were deposited via plasma enhanced chemical vapour deposition (PECVD) at ~200ºC on pyramidal textured, FZ, n-type (N_d ~ 1×10^{15} cm^{-3}) c-Si wafers. Titanium oxide films of ~6 nm were deposited on planar, FZ, n-type (N_d ~ 5×10^{15} cm^{-3}), c-Si wafers via atomic layer deposition (ALD) at ~230ºC using alternating pulses of titanium isopropoxide and water (growth rate of ~0.03 nm/cycle). Both sets of samples received standard RCA cleaning and dilute HF dips immediately prior to deposition (see Supplementary Note 2 and Supplementary Figure 3 for details on the passivating interlayers). Contact structures were fabricated and ρ_c was extracted as above. The minor difference in doping concentration is not expected to significantly affect the measured ρ_c.

High efficiency cells (2 × 2 cm^2) were fabricated on double-side pyramidal textured FZ, n-type (N_d ~ 1×10^{15} cm^{-3}) wafers with a thickness of ~240 µm. Following standard RCA cleaning and a dilute HF dip, the cells were passivated on both sides with a ~6 nm intrinsic *a*-Si:H(*i*) layer, grown at 200ºC via PECVD in an Octopus I reactor from INDEOtec SA. On the front-side of the cell, ~10 nm of MoO_x was thermally evaporated, on top of which a bilayer consisting of ~55 nm of hydrogenated indium oxide and ~10 nm of ITO was sputtered (MRC 603) at room temperature through a 2 × 2 cm^2 shadow mask to define the cell area. A screen printed Ag front grid with a corresponding contact fraction of ~5% was printed and baked at ~130ºC. Following this, on the rear-side a ~1 nm LiFx/ ~100 nm Al stack was evaporated without breaking vacuum. Cross sectional scanning electron micrographs were taken on a Zeiss Gemini Ultra-55. Light *J*-*V* characteristics were measured under standard 1 sun conditions (AM 1.5G spectrum, 100 mW/cm^2, 25ºC) with a Wacom solar simulator and EQE was measured using an in-

house built set-up. No bus bar exclusion was made in the current density measurement for the high efficiency DASH cells. Periphery absorption was avoided by using an aperture mask.

Acknowledgements We would like to thank Peter Frischmann for his assistance with *I-V* measurements and Andreas Fell for his suggestions regarding the simulations. Device design, fabrication, and characterization was funded by the Bay Area Photovoltaics Consortium (BAPVC). Materials characterization was supported by the Electronic Materials Programs, funded by the Director, Office of Science, Office of Basic Energy Sciences, Material Sciences and Engineering Division of the U.S. Department of Energy under (Contract No. DE-AC02- 05CH11231). XPS characterization was performed at the Joint Center for Artificial Photosynthesis, supported through the Office of Science of the U.S. Department of Energy under Award Number DE-SC0004993. Work at the Molecular Foundry was supported by the Office of Science, Office of Basic Energy Sciences, of the U.S. Department of Energy (Contract No. DE-AC02-05CH11231). Work at EPFL was supported by the Office fedéral de l' énergie (OFEN). Work at the ANU was supported by the Australian Renewable Energy Agency (ARENA). The authors would like to thank the CSEM PV-centre for wafer preparation and device metallization.

Author contributions J.B. and A.J. conceived the idea. J.B and J.G carried out the device fabrication, electrical characterisation and analysis. A.O, T.A and T.C assisted with device fabrication. M.H, C.S-F, assisted with materials characterisation. H.O and E.S assisted with mask fabrication. A.C, S.D W and C.B discussed the results. J.B wrote the paper and all other authors provided feedback.

References

[1.] Baker-Finch, S. C., McIntosh, K. R., Yan, D., Fong, K. C. & Kho, T. C. Near-infrared free carrier absorption in heavily doped silicon. J. Appl. Phys. 116, 063106 (2014).

[2.] Richter, A., Glunz, S. W., Werner, F., Schmidt, J. & Cuevas, A. Improved quantitative description of Auger recombination in crystalline silicon. Phys. Rev. B 86, 165202 (2012).

[3.] Cuevas, A., Basore, P. A., Giroult-Matlakowski, G. & Dubois, C. Surface recombination velocity of highly doped n-type silicon. J. Appl. Phys. 80, 3370–3375 (1996).

[4.] Zhao, J., Wang, A., Green, M. A. & Ferrazza, F. 19.8% efficient 'honeycomb' textured multicrystalline and 24.4% monocrystalline silicon solar cells. Appl. Phys. Lett. 73, 1991–1993 (1998).

[5.] Goodrich, A. et al. A wafer-based monocrystalline silicon photovoltaics road map: Utilizing known technology improvement opportunities for further reductions in manufacturing costs. Sol. Energy Mater. Sol. Cells 114, 110 – 135 (2013).

[6.] Tiedje, T., Yablonovitch, E., Cody, G. D. & Brooks, B. G. Limiting efficiency of silicon solar cells. Electron Devices IEEE Trans. On 31, 711–716 (1984).

[7.] Wurfel, U., Cuevas, A. & Wurfel, P. Charge Carrier Separation in Solar Cells. Photovolt. IEEE J. Of 5, 461–469 (2015).

[8.] Masuko, K. et al. Achievement of More Than 25%; Conversion Efficiency With Crystalline Silicon Heterojunction Solar Cell. Photovolt. IEEE J. Of, Vol. 4, No. 6,1433–1435, 2014 (November). doi:10.1109/JPHOTOV.2014.2352151

[9.] Taguchi, M. et al. 24.7%; Record Efficiency HIT Solar Cell on Thin Silicon Wafer. Photovolt. IEEE J. Of 4, 96–99 (2014).

[10.] Heng, J. B. et al. >23% High-Efficiency Tunnel Oxide Junction Bifacial Solar Cell With Electroplated Cu Gridlines. Photovolt. IEEE J. Of, Pages 82 – 86, Vol. 5, No. 1, (2015).

[11.] Feldmann, F. et al. Efficient carrier-selective p- and n-contacts for Si solar cells. Sol. Energy Mater. Sol. Cells, 2014 131, 100–104 (2014).

[12.] Holman, Z. C. et al. Current Losses at the Front of Silicon Heterojunction Solar Cells. Photovolt. IEEE J. Of 2, 7–15 (2012).

[13.] Fujiwara, H. & Kondo, M. Effects of a-Si:H layer thicknesses on the performance of a-Si:H/c-Si heterojunction solar cells. J. Appl. Phys. 101, : 054516, (2007).

[14.] Nicolás, S. M. de, Muñoz, D., Ozanne, A. S., Nguyen, N. & Ribeyron, P. J. Optimisation of doped amorphous silicon layers applied to heterojunction solar cells. Proc. SiliconPV 2011 Conf. 1st Int. Conf. Cryst. Silicon Photovolt. 8, 226–231 (2011).

[15.] Ji-Hwan Yang, Sang Jung Kang, Yunho Hong & Koeng Su Lim.Doping-Free Intrinsic Amorphous Silicon Thin-Film Solar Cell Having a Simple Structure of Glass/SnO2/MoO3/i-a-Si/LiF/Al. Electron Device Lett. IEEE 35, 96–98 (2014).

[16.] Avasthi, S. et al. Hole-blocking titanium-oxide/silicon heterojunction and its application to photovoltaics. Appl. Phys. Lett. 102, 203901, (2013).

[17.] Battaglia, C. et al. Hole Selective MoOx Contact for Silicon Solar Cells. Nano Lett. 14, 967–971 (2014).

[18.] Bullock, J., Cuevas, A., Allen, T. & Battaglia, C. Molybdenum oxide MoOx: A versatile hole contact for silicon solar cells. Appl. Phys. Lett. 105, 232109, (2014).

[19.] Bivour, M., Temmler, J., Steinkemper, H. & Hermle, M. Molybdenum and tungsten oxide: High work function wide band gap contact materials for hole selective contacts of silicon solar cells. Sol. Energy Mater. Sol. Cells Volume 142, Pages 34–41 (2015).

[20.] Zielke, D., Pazidis, A., Werner, F. & Schmidt, J. Organic-silicon heterojunction solar cells on n-type silicon wafers: The BackPEDOT concept. Sol. Energy Mater. Sol. Cells 131, 110 – 116 (2014).

[21.] Yu, P. et al. 13% Efficiency Hybrid Organic/Silicon-Nanowire Heterojunction Solar Cell via Interface Engineering. ACS Nano 7, 10780–10787 (2013).

[22.] Shen, X., Sun, B., Liu, D. & Lee, S.-T. Hybrid Heterojunction Solar Cell Based on Organic–Inorganic Silicon Nanowire Array Architecture. J. Am. Chem. Soc. 133, 19408–19415 (2011).

[23.] Hezel, R. Recent progress in MIS solar cells. Prog. Photovolt. Res. Appl. 5, 109–120 (1997).

[24.] Ponpon, J. P. & Siffert, P. Open circuit voltage of MIS silicon solar cells. J. Appl. Phys. 47, 3248–3251 (1976).

[25.] Singh, R., Green, M. A. & Rajkanan, K. Review of conductor-insulator-semiconductor (CIS) solar cells. Sol. Cells 3, 95–148 (1981).

[26.] Chen, L.-M., Xu, Z., Hong, Z. & Yang, Y. Interface investigation and engineering - achieving high performance polymer photovoltaic devices. J. Mater. Chem. 20, 2575–2598 (2010).
[27.] Yin, X. et al. 19.2% Efficient InP Heterojunction Solar Cell with Electron-Selective TiO2 Contact. ACS Photonics 1, 1245–1250 (2014).
[28.] Zhou, H. et al. Interface engineering of highly efficient perovskite solar cells. Science 345, 542–546 (2014).
[29.] Liu, R., Lee, S.-T. & Sun, B. 13.8% Efficiency Hybrid Si/Organic Heterojunction Solar Cells with MoO3 Film as Antireflection and Inversion Induced Layer. Adv. Mater. 26, 6007–6012 (2014).
[30.] Nagamatsu, K. A. et al. Titanium dioxide/silicon hole-blocking selective contact to enable double-heterojunction crystalline silicon-based solar cell. Appl. Phys. Lett. 106, 123906, (2015).
[31.] Zhang, Y. et al. High efficiency hybrid PEDOT:PSS/nanostructured silicon Schottky junction solar cells by doping-free rear contact. Energy Env. Sci 8, 297–302 (2015).
[32.] Zhang, Y., Liu, R., Lee, S.-T. & Sun, B. The role of a LiF layer on the performance of poly(3,4-ethylenedioxythiophene):poly(styrenesulfonate)/Si organic-inorganic hybrid solar cells. Appl. Phys. Lett. 104, 083514, (2014).
[33.] Battaglia, C. et al. Silicon heterojunction solar cell with passivated hole selective MoOx contact. Appl. Phys. Lett. 104, 113902, (2014).
[34.] Geissbühler, J. et al. 22.5% efficient silicon heterojunction solar cell with molybdenum oxide hole collector. Appl. Phys. Lett. 107, 081601, (2015).
[35.] Li, Y. et al. Elucidation of the electron injection mechanism of evaporated cesium carbonate cathode interlayer for organic light-emitting diodes. Appl. Phys. Lett. 90, 012119, (2007).
[36.] Ganzorig, C., Suga, K. & Fujihira, M. Alkali metal acetates as effective electron injection layers for organic electroluminescent devices. Mater. Sci. Eng. B 85, 140 – 143 (2001).
[37.] Helander, M. G., Wang, Z. B., Mordoukhovski, L. & Lu, Z. H. Comparison of Alq3/alkali-metal fluoride/Al cathodes for organic electroluminescent devices. J. Appl. Phys. 104, 094510, (2008).
[38.] Hung, L. S., Tang, C. W. & Mason, M. G. Enhanced electron injection in organic electroluminescence devices using an Al/LiF electrode. Appl. Phys. Lett. 70, 152–154 (1997).
[39.] Descoeudres, A. et al. >21%; Efficient Silicon Heterojunction Solar Cells on n- and p-Type Wafers Compared. Photovolt. IEEE J. Of 3, 83–89 (2013).
[40.] Bullock, J. et al. Proof-of-Concept p-Type Silicon Solar Cells With Molybdenum Oxide Local Rear Contacts. Photovolt. IEEE J. Of 5, 1591–1594 (2015).
[41.] Kim, S. et al. Effects of LiF/Al back electrode on the amorphous/crystalline silicon heterojunction solar cells. Adv. Mater. Charact. Tech. Sol. Cells 178, 660–664 (2013).
[42.] Schroder, D. K. Semiconductor Material and Device Characterization. (John Wiley & Sons, 2006).
[43.] Gogolin, R. et al. Analysis of Series Resistance Losses in a-Si:H/c-Si Heterojunction Solar Cells. Photovolt. IEEE J. Of 4, 1169–1176 (2014).
[44.] Feldmann, F., Bivour, M., Reichel, C., Hermle, M. & Glunz, S. W. Passivated rear contacts for high-efficiency n-type Si solar cells providing high interface passivation quality and excellent transport characteristics. Sol. Energy Mater. Sol. Cells 120, 270 – 274 (2014).
[45.] Franklin, E. et al. Design, fabrication and characterisation of a 24.4% efficient interdigitated back contact solar cell. Prog. Photovolt. Res. Appl. (2014). doi:10.1002/pip.2556
[46.] Demaurex, B. et al. Atomic-Layer-Deposited Transparent Electrodes for Silicon Heterojunction Solar Cells. Photovolt. IEEE J. Of 4, 1387–1396 (2014).
[47.] Morales-Masis, M., De Nicolas, S. M., Holovsky, J., De Wolf, S. & Ballif, C. Low-Temperature High-Mobility Amorphous IZO for Silicon Heterojunction Solar Cells. Photovolt. IEEE J. Of 5, 1340–1347 (2015).
[48.] Dupuis, J. et al. NICE module technology - From the concept to mass production: A 10 years review. in Photovoltaic Specialists Conference (PVSC), 2012 38th IEEE, IEEE, 003183–003186 (2012). doi:10.1109/PVSC.2012.6318254
[49.] Briggs, D. & Seah, P. Practical Surface Analysis, Auger and X-ray Photoelectron Spectroscopy. (Wiley, 1990).
[50.] Scanlon, D. O. et al. Theoretical and Experimental Study of the Electronic Structures of MoO3 and MoO2. J. Phys. Chem. C 114, 4636–4645 (2010).
[51.] Hamrin, K., Johansson, G., Gelius, U., Nordling, C. & Siegbahn, K. Valence Bands and Core Levels of the Isoelectronic Series LiF, BeO, BN, and Graphite Studied by ESCA. Phys. Scr. 1, 277, Pages 277-280, (1970).

Supplementary Note 1. Optical loss simulations. Modelling of the optical losses was performed using freeware ray tracing software hosted by *PV lighthouse*. The generation current J_g losses of four different solar cell structures were analysed; *i.*) the dopant-free *c*-Si solar cell fabricated in this study, *ii.*) a 'standard' *c*-Si heterojunction solar cell utilising doped-silicon layers,[1] and dopant-free *c*-Si solar cells with improved rear optics by substituting *iii.*) Ag and *iv.*) ITO / Ag for Al. A cell schematic and loss analysis is provided for these four cases in Supplementary Figure 1a. The use of LiF_x interlayers with both Ag and (to a lesser extent) ITO for electron contacts has already demonstrated some promise within the organic electronic community,[2,3] suggesting that they might also be viable contacts on *c*-Si. An improvement of nearly 1 mA/cm^2 in J_{sc} is predicted by using Ag instead of Al. The use of ITO over-layers also introduces the added possibility of bi-facial cells. Optical constants for MoO_x and LiF_x films deposited on polished *c*-Si, are measured using an ellipsometer (using a Cody-Lorentz oscillator model, J. A. Woollam M-2000), and provided in Supplementary Figure 1b. Additional optical constants required for the simulations were sourced from the refractive index library hosted by *PV lighthouse*. It is also worth noting that these simulations assume that 100% of the light absorbed in the *a*-Si:H films is lost to recombination in these films. Whilst this assumption has been found to be true for the doped *a*-Si:H layers, the less defective intrinsic *a*-Si:H layers can still contribute ~30% of their absorbed light to the solar cell current.[4] This suggests the benefits of the DASH approach in terms of reduced parasitic absorption percentage could be even greater than the simulations in Supplementary Figure 1 outline. All simulations do not account for the front-contact shading which can be considered constant (as all cells have the same front ITO sheet resistance they will utilise equivalent front-contact patterns).

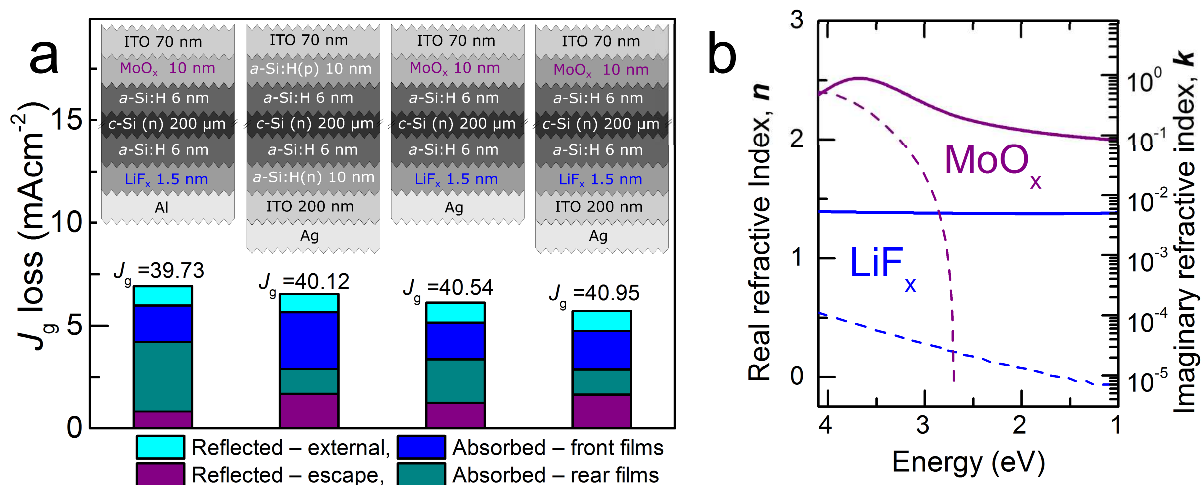

Supplementary Figure 1. Generation current gain analysis. a, Simulations of the loss in generation current for different heterocontact type *c*-Si solar cells. The simulations, conducted using the wafer ray-tracer hosted by *PVlighthouse.com*, assume both surfaces of a 200 μm wafer are random textured and coated with the films as indicated within the figure. The mechanism and location of the current loss in each cell is broken down within each column. b, measured real (solid) and imaginary (dotted) refractive index values for the MoO_x (purple) and LiF_x (blue) films.

Supplementary Note 2. Extraction of the contact resistivity and recombination. Two methods of ρ_c extraction are implemented in this study. The first method, based on the approach introduced by Cox and Strack,[5] involves a series of resistance measurements taken between an array of different diameter front contacts and a full-area rear contact, as shown schematically in Supplementary Figure 2a. The array of different diameter dots was achieved by depositing through a shadow mask. Resistance measurements were taken in the dark at 20 - 25°C using a Keithley 2400 sourcemeter. The resistance versus diameter trend is fitted with a spreading resistance model allowing accurate extraction of ρ_c.[6] The resistance of the measurement setup is also accounted for. An example of this fitting is given in Supplementary Figure 2b. Given the wafer resistivity, thickness and estimated error in the measurement – the lower limit resolution for this technique is estimated at ~1 mΩcm^2.

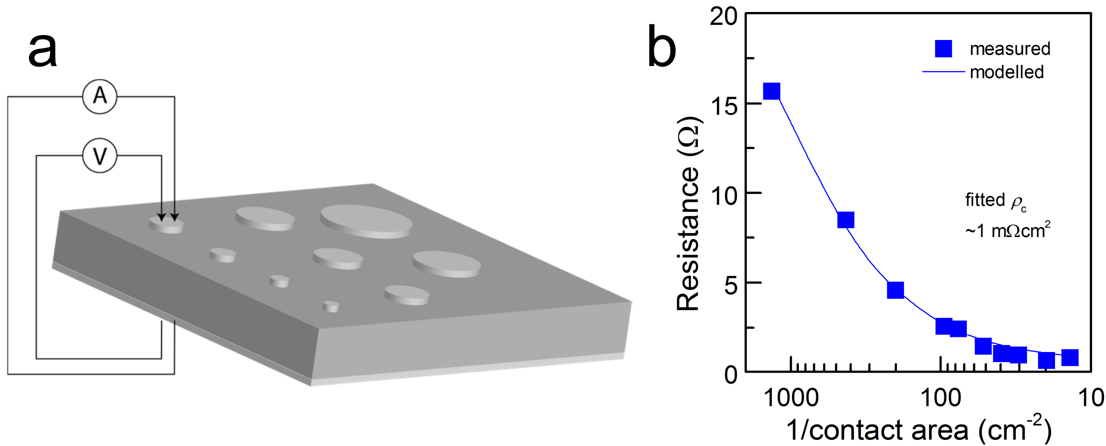

Supplementary Figure 2. Contact resistivity extraction. a, Schematic of the ρ_c test structure. b, Exemplary measured and modelled resistance behaviour of a AMF / Al contact to n-type *c*-Si.

The second, simpler but less accurate method, is used to measure devices with ρ_c values > 0.5 Ωcm^2. The resistance between a full-area rear contact and a ~1.1 mm diameter front circular contact was measured and ρ_c was estimated by accounting for the expected bulk spreading resistance. It should be noted in both of the above contact structures that the extracted ρ_c comprises the interfacial resistivities and bulk resistivities of all layers in-between the *c*-Si and the outer Al layer. Reference samples with only Al contacts (no AMF interlayers) were also fabricated. These contacts exhibited rectifying behaviour when applied both directly and with passivating interlayers (TiO_x and *a*-Si:H), such that ρ_c was prohibitively high for accurate extraction. In this case a lower limit estimation of ~5 Ωcm^2 is made for these contacts.

The recombination at the direct *c*-Si(n) / LiF_x / Al contact was investigated on planar, FZ, n-type (N_d ~ $5\times10^{15} cm^{-3}$) *c*-Si wafers coated symmetrically with a LiF_x ~1.5 nm / Al ~15 nm stack. The Al layer is made thick enough to prevent oxidation of the entire layer at the same time as remaining thin enough to allow sufficient light through and not saturate the conductance signal of a photoconductance decay tester (Sinton WCT 120). The lifetime of these samples was too low for this tool to measure accurately,

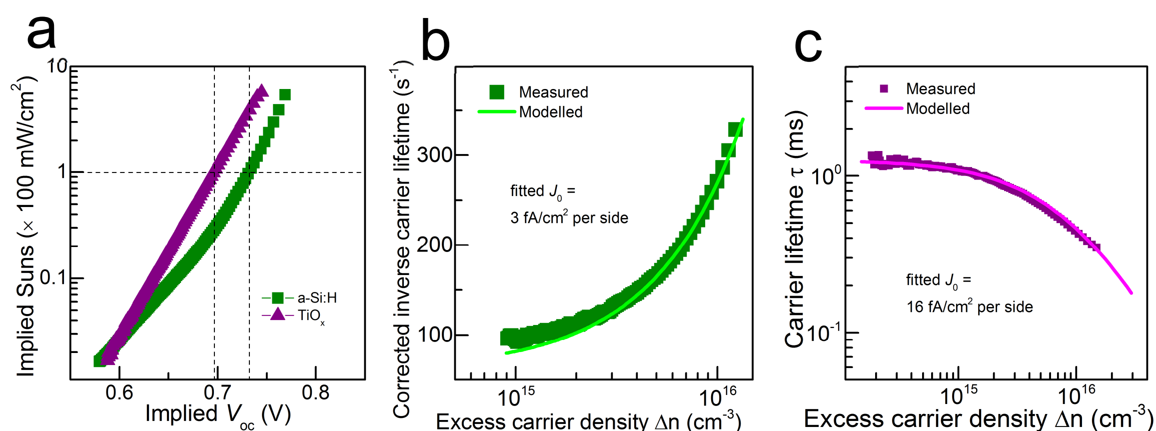

Supplementary Figure 3. *a*-Si:H and TiO_x interlayer passivation details a, Implied Suns V_{oc} behaviour for n-type silicon wafers symmetrically passivated with ~6nm of PECVD *a*-Si:H(*i*) or ALD TiO_x films. The dotted horizontal and vertical lines highlight the implied open circuit voltages at 1 sun. Plots b, and c, show the measured and modelled lifetime behaviour of n-type wafer coated symmetrically with *a*-Si:H(*i*) and TiO_x films, respectively. The models allow the extraction of surface recombination current pre-factors also provided in the plots.

suggesting a high rate of surface recombination. To reduce this rate of surface recombination two candidate passivating layers, suitable for electron-selective heterocontacts when combined with the LiF_x / Al contact. are *a*-Si:H(*i*) and TiO_x films. When applied to *c*-Si both of these films present larger valence band than conduction band offsets potentially assisting in creating a preferential conductivity towards electrons. The Suns-implied V_{oc} behaviour of the two samples are included in Supplementary Figure 3a showing 1 sun implied V_{oc} values of 732 and 695 mV for the wafers coated with *a*-Si:H(*i*) and TiO_x films, respectively (Sinton WCT 120). Due to the difference in wafer resistivity, recombination factors (J_0) were extracted using different techniques[7,8] for the *a*-Si:H(*i*) and TiO_x coated wafers. Plots of J_0 extractions of wafers coated with *a*-Si:H(*i*) and TiO_x layers are included in Supplementary Figure 2b and c, respectively. It should be emphasised that the implied V_{oc} and J_{0c} values represent the recombination before LiF_x / Al deposition and that some changes may occur after contact formation.

Supplementary Note 3. Optimum contact configuration simulations.

Simulations, similar to those in previous studies,[9] are run using the freeware solar cell simulation program *Quokka*.[10] Details of the unit cell characteristics and structure can be found in Supplementary Table 3. The two variables of the simulation are the rear contact ρ_c and J_{0c}. For every input ρ_c and J_{0c} an optimum rear contact configuration is calculated by means of monitoring the device efficiency. Superimposed experimental data points can be matched with the points of these simulations to provide information on the optimum contact fraction and resultant efficiency which can be achieved. The results of this simulation are shown in Supplementary Figure 4. Experimental optimum ρ_c and J_{0c} data for TiO_x / LiF_x / Al (purple triangle) and *a*-Si:H(*i*) / LiF_x / Al (green square) contacts as well as the direct LiF_x / Al (blue circle) contact (a J_0 close to the diffusion limit is assumed[11]) are superimposed on this plot. For the interlayers it can be seen that both contacts are best applied in a 100% contact area and that devices with *a*-Si:H(*i*) interlayers have a higher idealised efficiency. It can also be seen that the direct LiF_x / Al

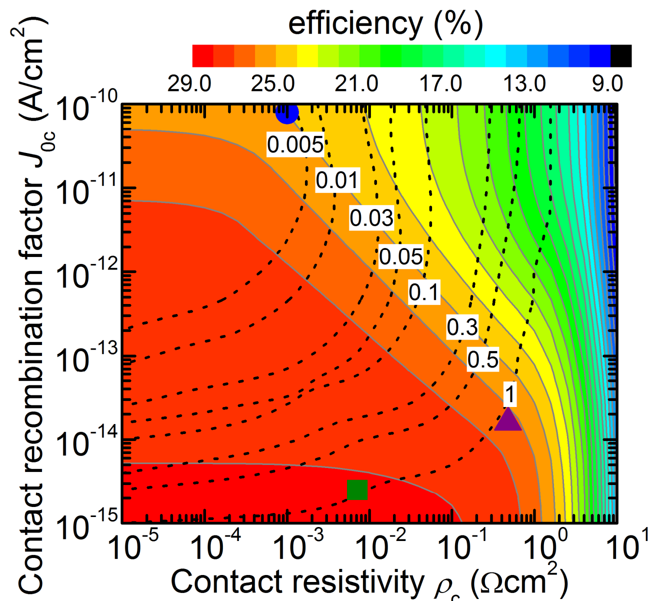

Supplementary Figure 4. Optimum rear contact configuration simulations. *Quokka* simulations of the optimum contact fraction (dotted lines) and resultant idealized efficiency (coloured contours) as a function of the J_{0c} and ρ_c. Values for the direct LiF_x / Al contact (blue circle) as well as the TiO_x / LiF_x / Al (purple triangle) and *a*-Si:H(*i*) / LiF_x / Al contact (green square) are superimposed on the plot.

contact could be effectively applied in localised contacts (0.5% area) – an architecture which was previously not possible, given the aforementioned difficulties of contacting n-type *c*-Si.

Supplementary Note 4. Detailed DASH cell characterisation. The champion cell batch consisted of four 2 x 2 cm^2 DASH cells, the light *J*-*V* results for these cells have been included in Supplementary Table 2, showing an average cell efficiency for the 4 cells above 19%. The small spread in results seen for each parameter is a testament to the exciting potential of this cell structure.

The champion cell was further characterised by measuring its light *J*-*V* behaviour at a range of illumination intensities (see Supplementary Figure 5a) and using the Suns-V_{oc} method (see Supplementary Figure 5b). The V_{oc} values from the three light *J*-*V* curves in Supplementary Figure 5a are superimposed on the Suns-V_{oc} curve showing a good correlation between the two methods. No large 'bending' or inflection points are seen in the Suns-V_{oc} curve at high illumination intensities suggesting that there is no large unwanted Schottky barrier affecting the DASH cell.[12] The Suns-V_{oc} data was further used to construct an ideal pseudo *J*-*V* plot (see Supplementary Figure 5c) which reflects predicted behaviour of the DASH cell without the effect of parasitic series resistance. From a comparison between the cells pseudo and real *J*-*V* curves it can be seen that reducing the series resistance is an obvious path to higher efficiencies. The champion DASH cell light *J*-*V* is well fitted using a simple 'one-diode' model (also shown in Supplementary Figure 5c) with a series resistance R_s ~2.09 Ωcm^2. A reduction of R_s to 1 Ωcm^2 (a typical series resistance value for industrial *c*-Si solar cells) would increase the *FF* and η to above 79% and 21%, respectively.

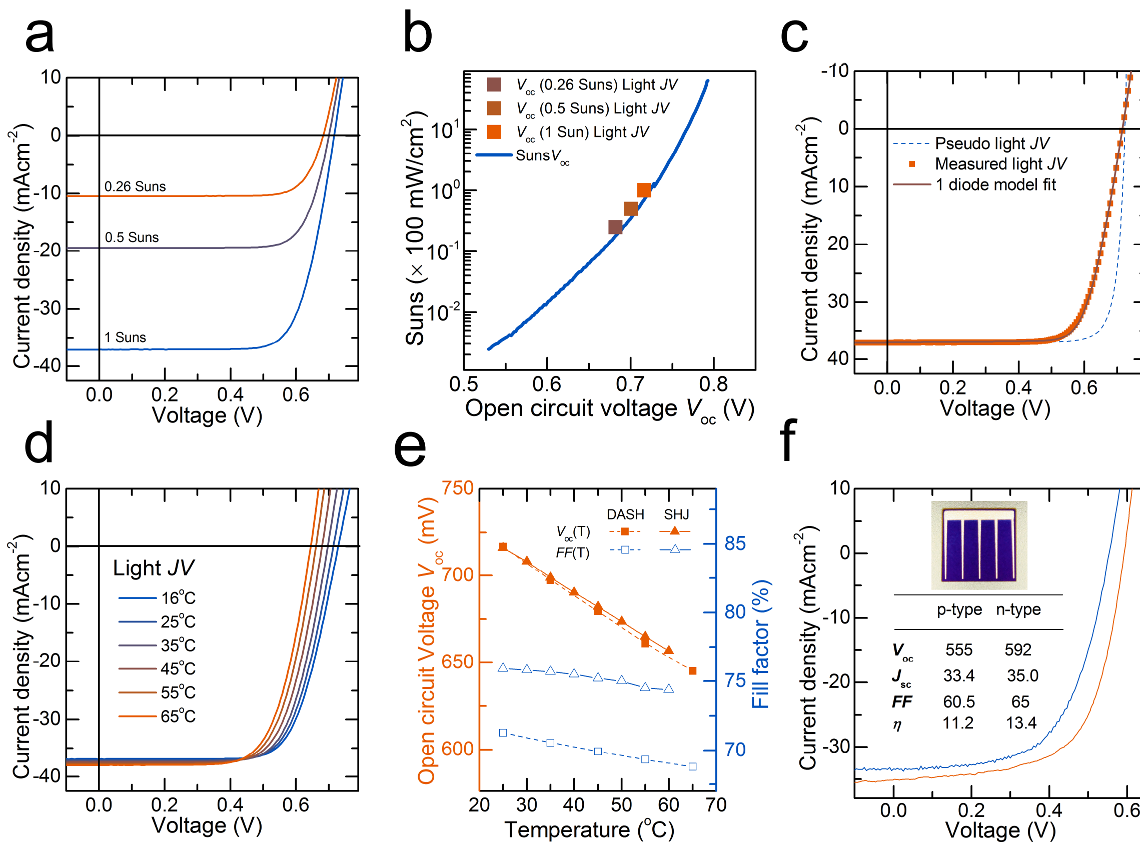

Supplementary Figure 5. Additional solar cell characterisation Light intensity dependent a, *J-V* and; b, V_{oc} behaviour (from Suns-V_{oc}) of the DASH cell. The Suns-V_{oc} is also used to plot an ideal pseudo *J-V* curve for the DASH cell in c, which is compared to the real DASH cell light *J-V* and a simple 'one-diode' fit of the real light *J-V* data. d, shows the temperature dependent (16 - 65°C) light *J-V* behaviour of a standard DASH cell measured under 1 sun conditions; and e, compares the voltage and fill factor temperature dependence of DASH and SHJ type cells. f, Light *J-V* and cell characteristics measured under standard 1 sun conditions of basic n and p-type DASH cells without *a*-Si:H(*i*) passivating interlayers showing that effective carrier separation can be achieved regardless of the base wafer doping.

The light *J-V* behaviour of the DASH cell was further characterised at a range of temperatures (see Supplementary Figure 5d). From these temperature dependent *J-V* curves an analysis of the V_{oc} and *FF* temperature dependence for the DASH cell was conducted (see Supplementary Figure 5e) and compared to the behaviour of a SHJ cell (taken from Ref.[13]). The SHJ and DASH cells show largely similar behaviour exhibiting the expected decrease in V_{oc} with temperature resulting in coefficients of -1.7 and -2 mV/°C, respectively. Similarly the *FF* evolution with temperature for both the SHJ and DASH cells has a negative gradient with values of -0.04 and -0.06 %/°C, respectively.

Such similar temperature dependency of *FF* values suggests that DASH devices perform quite similarly to standard SHJ solar cells in terms of carrier transport.

The light *J*-*V* performance of a representative DASH cell was also measured before and after a ~10 minute, 100ºC anneal without any significant change to the cell performance. This result is important given concerns associated with alkali metal ion incorporation in *c*-Si – centred around both the high mobility of ions and their tendency to form carrier recombination active defect levels within the *c*-Si bandgap.[14] For the latter of these two points Li may be an exception as it has been shown by some authors to form a shallow donor level (even being used as an intentional dopant in some cases[15]). Regardless of this, the stability of the V_{oc} before and after the anneal step suggests that Li incorporation is not an issue at these temperatures. The very high V_{oc} also indicates that the well-known low temperature interaction between Al and *a*-Si:H,[16] is prevented by the thin LiF_x interlayer.

External quantum efficiency (EQE) analysis was also performed on the cells (in-house built set-up) accompanied by front surface reflectance measurements (Lambda 950, Perkin Elmer) to investigate the internal quantum efficiency. An estimation of the J_{sc} is found by integrating the product of the AM 1.5G spectrum (in photons /$cm^{-2}nm^{-1}$) and the EQE in the 310 – 1200 nm wavelength range. A J_{sc} of 39.4 mA/cm^2 is calculated which, after correcting for a 5% reduction due to the contact fraction, agrees well with the light *J*-*V* measured value of 37.07 mA/cm^2.

To test the efficacy of the approach on both wafer doping types, simplified cells (1 × 1 cm^2) without passivating interlayers were fabricated on n-type (N_d ~ 5×10^{15} cm^{-3}) and p-type (N_a ~ 7×10^{15} cm^{-3}), planar, FZ wafers. A 15 nm MoO_x hole contact was thermally evaporated on the front-side. This film was capped with a ~60 nm ITO film and

a ~1 µm Cu front grid, both of which were sputtered (AJA International, ATC 1800 UHV) at room temperature through two different shadow masks to define the 1 × 1 cm^2 cell area and front grid. The rear contact was formed by evaporating ~1.5 nm of LiF_x followed by ~200 nm of Al without breaking vacuum. The light *J*-*V* characteristics of these cells was measured under standard conditions (AM 1.5G spectrum, 100 mW/cm^2, ~25ºC) and are provided in Supplementary Figure 5f. The top bus bar was excluded from the cell area for the current density calculation. Both cells exhibit efficiencies in excess of 10%, clearly indicating effective carrier separation. These results demonstrate the effectiveness of the DASH *c*-Si solar cell concept, irrespective of the substrate doping type (similar behaviour is also obtained for conventional doped *a*-Si:H SHJ cells[1]). This highlights a distinction between the DASH cells and the classic metal-insulator-silicon inversion layer (MIS-IL) cell architectures which also avoid the use of doped-silicon layers. The performance of the archetypal p-type MIS-IL cell is strongly linked to both the silicon wafer dopant type and concentration, mainly due to the need to form an Ohmic rear contact.

Supplementary Table 1 Loss mechanisms associated with doped-silicon.

Limitation	Issue, consequence	Cause	Ref.
Optical	Parasitic free-carrier absorption, reduces J_{sc}	High doping concentration	[17]
	Parasitic window layer absorption, reduces J_{sc}	Using narrow gap window layers (eg. Doped *a*-Si:H and poly-Si)	[4]
Recombination	Auger and radiative recombination, reduces V_{oc}	High doping concentration	[18]
	SRH recombination, reduces V_{oc}	Dopant precipitates (eg. phosphorus clusters)	[19]
		Dopant complexes (eg. Boron-oxygen defects)	[20]
	Surface SRH recombination, reduces V_{oc}	High surface dopant concentration (currently debated)	[21]
	Bulk and surface recombination, reduces V_{oc}	Band gap narrowing, increased minority carrier concentration	[22]
Transport	Resistive losses, reduces *FF* (especially lateral R_s)	Dopant and carrier scattering, low majority carrier mobility	[23]
	Low minority carrier diffusion length, reduces J_{sc}	Dopant and carrier scattering, low minority carrier mobility	[23]

Supplementary Table 2 High efficiency DASH cell results.

	Voc (mV)	Jsc (mA/cm2)	FF	η
Cell1, Champion cell	716.4	37.07	73.15	19.42
Cell 2	716.5	36.97	71.84	19.03
Cell 3	716.7	37.02	71.26	18.91
Cell 4	716.4	37.07	71.1	18.88
Average of 4 cells	716.5	37.03	71.83	19.06

Supplementary Table 3 Assumptions and unit-cell characteristics of simulated cell.

Symbol	Parameter	Assumption / value
J_{0front}	Front recombination factor	1 fA/cm2
τ_{bulk}	Bulk lifetime	Richter et. al. intrinsic lifetime[18]
J_g	Generation current density	~44 mA/cm2
W	Wafer thickness	160 µm
ρ_{bulk}	Bulk type, resistivity	1 Ωcm n-type
J_{0rear}	Rear recombination factor (in non-contacted area)	1 fA/cm2
m_{frear}	Rear line-contact metal fraction	Finger width = variable, Finger pitch = 1000 µm

Supplementary References

[1.] Descoeudres, A. et al. >21%; Efficient Silicon Heterojunction Solar Cells on n- and p-Type Wafers Compared. *Photovolt. IEEE J. Of* 3, 83–89 (2013).

[2.] Wang, X. J. et al. Enhancement of electron injection in organic light-emitting devices using an Ag/LiF cathode. *J. Appl. Phys.* 95, 3828–3830 (2004).

[3.] Sakai, J. et al. Efficient organic photovoltaic tandem cells with novel transparent conductive oxide interlayer and poly (3-hexylthiophene): Fullerene active layers. *Sol.Energy Mater. Sol. Cells* 94, 376–380 (2010).

[4.] Holman, Z. C. et al. Current Losses at the Front of Silicon Heterojunction Solar Cells. *Photovolt. IEEE J. Of* 2, 7–15 (2012).

[5.] Cox, R. H. & Strack, H. Ohmic contacts for GaAs devices. *Solid-State Electron.* 10, 1213– 1218 (1967).

[6.] Cohen, S. S. Contact resistance and methods for its determination. *Thin Solid Films* 104, 361 – 379 (1983).

[7.] D.E. Kane & Swanson, R. M. Measurement of the Emitter Saturation Current by a Contactless Photoconductivity Decay Method. in *Proc of the 18th IEEE Photovoltaic Specialists Conference* 578–583 (1985).

[8.] Cuevas, A. The effect of emitter recombination on the effective lifetime of silicon wafers. *Sol. Energy Mater. Sol. Cells* 57, 277 – 290 (1999).

[9.] Bullock, J. et al. Amorphous silicon enhanced metal-insulator-semiconductor contacts for silicon solar cells. *J. Appl. Phys.* 116, 163706, (2014).

[10.] Fell, A. A Free and Fast Three-Dimensional/Two-Dimensional Solar Cell Simulator Featuring Conductive Boundary and Quasi-Neutrality Approximations. *Electron Devices IEEE Trans. On* 60, 733–738 (2013).

[11.] Mader, C., Muller, J., Eidelloth, S. & Brendel, R. Local rear contacts to silicon solar cells by in-line high-rate evaporation of aluminum. *Sol. Energy Mater. Sol. Cells* 107, 272– 282 (2012).

[12.] Glunz, S. W., Mackel, H., Nekarda, J. & Cuevas, A. Analyzing back contacts of silicon solar cells by Suns-Voc-measurements at high illumination densities. in *22nd European Photovoltaic Solar Energy Conference and Exhibition* (2007).

[13.] Battaglia, C. et al. Silicon heterojunction solar cell with passivated hole selective MoOx contact. *Appl. Phys. Lett*. 104, 113902 (2014).
[14.] Chen, J. W. & Milnes, A. G. Energy Levels in Silicon. *Annu. Rev. Mater. Sci*. 10, 157–228 (1980).
[15.] Wysocki, J. J. Lithium-doped radiation resistant silicon solar cells. in *Electron Devices Meeting, 1966 International* 12, 24–26 (1966).
[16.] Bullock, J. et al. Amorphous silicon passivated contacts for diffused junction silicon solar cells. *J. Appl. Phys.* 115, 163703, (2014).
[17.] Baker-Finch, S. C., McIntosh, K. R., Yan, D., Fong, K. C. & Kho, T. C. Near-infrared free carrier absorption in heavily doped silicon. *J. Appl. Phys.* 116, 063106, (2014).
[18.] Richter, A., Glunz, S. W., Werner, F., Schmidt, J. & Cuevas, A. Improved quantitative description of Auger recombination in crystalline silicon. *Phys. Rev. B* 86, 165202 (2012).
[19.] Min, B. et al. Heavily doped Si:P emitters of crystalline Si solar cells: recombination due to phosphorus precipitation. *Phys. Status Solidi RRL Rapid Res. Lett*. 8, 680–684 (2014).
[20.] Schmidt, J. & Cuevas, A. Electronic properties of light-induced recombination centers in boron-doped Czochralski silicon*.* *J. Appl. Phys.* 86, 3175–3180 (1999).
[21.] King, R. R., Sinton, R. A. & Swanson, R. M. Studies of diffused phosphorus emitters: saturation current, surface recombination velocity, and quantum efficiency. *Electron Devices IEEE Trans. On* 37, 365–371 (1990).
[22.] Yan, D. & Cuevas, A. Empirical determination of the energy band gap narrowing in p+ silicon heavily doped with boron. *J. Appl. Phys.* 116, 194505, (2014).
[23.] Klaassen, D. B. M. A unified mobility model for device simulation: Model equations and concentration dependence. *Solid-State Electron.* 35, 953 – 959 (1992).

5 Conclusion

This thesis has focused on the conceptual and experimental development of novel carrier-selective contacts for *c*-Si solar cells. To assess their carrier-selectivity, the resistive and recombination behaviour of each contact system has been assessed, primarily via the contact resistivity ρ_c and the contact recombination factor J_{0c}. Several promising carrier-selective contact systems were then further developed and integrated into proof-of-concept solar cell structures, many of which exceeded 20% power conversion efficiency. Provided below is a summary of the main findings of each of the three experimental chapters, followed by a table summarising the main contact and cell characteristics achieved in this thesis. The next stage in the development of such technologies is the demonstration of their robustness within manufacturing and operational environments. These factors are discussed in the final section of this thesis as future studies to further the work presented in this thesis.

Electron and hole selective contacts on highly doped surface regions:

- ALD AlO_x (22 Å) and thermally grown SiO_x (16 Å) can be used as passivating interlayers between a 100 Ω/□ phosphorus diffused region and an outer Al contact. These produce contact J_{0c} values of 200 and 300 fA/cm^2, whilst maintaining ρ_c values of 76 and 0.2 mΩcm^2, respectively.

- PECVD *a*-Si:H (100-150 Å) films are effective passivating interlayers on both phosphorus and boron diffused surfaces, producing J_{0c} / ρ_c sets of 40 fA/cm^2 / 50 mΩcm^2 and 100 fA/cm^2 / 100 mΩcm^2, respectively. Such a system, however, requires strict temperature control to avoid interaction of the *a*-Si:H and metal over layers.
- A novel *a*-Si:H enhanced MIS contact process has been developed. In this process the passivation at the *c*-Si(n$^+$) / SiO_x and *c*-Si(p$^+$) / AlO_x interfaces is drastically improved by an *a*-Si:H layer, which provides a source of additional hydrogen to passivate the interface. This *a*-Si:H layer is then dissolved into an overlying metal layer using a low temperature anneal, thus forming a low recombination and low resistance contact.
- This *a*-Si:H enhanced MIS structure has been integrated into an n-type cell as a full-area electron contact, producing a conversion efficiency of 21.0%, comparable to that of an n-type partial rear contact cell fabricated using an alike process (except for the rear contact).

Molybdenum oxide hole selective contacts for *c*-Si solar cells:

- Molybdenum oxide has been found to be an effective hole contact on a number of *c*-Si surfaces, namely lightly doped n- and p-type, and heavily doped p-type. It was found that, even with very thin MoO_x films, recombination factors of 200 and 300 fA/cm^2 can be obtained on p- and n-type surfaces, respectively. The optimum contact resistivity on lightly and heavily doped p-type surfaces was found to be ~1 and 0.2 mΩcm^2 respectively, with a MoO_x thickness of ~10 nm. On the n-type surface a contact resistivity of ~30 mΩcm^2 was extracted.

- Simple n- and p-type *c*-Si cells with full-area MoO_x based hole contacts were trialled. These proof-of-concept cells achieved a power conversion efficiency of 16.7% and 16.4%, respectively, limited mainly by the simplicity of the device architecture and the fabrication process used.
- Simulations revealed that applying the direct MoO_x contact as a partial rear contact in a p-type cell is the best utilisation of such a material. Experimental demonstration of this novel concept (with a ~ 5% rear MoO_x contact percentage) led to a conversion efficiency of 20.4%, a promising result, given the infancy of this approach.

Alkali metal salt electron contacts for *c*-Si solar cells:

- Alkali metal fluorides / Al stacks as electron contacts on moderately doped n-type *c*-Si can achieve $m\Omega cm^2$ scale contact resistivities, significantly lower than contacts made with conventional direct metalization. Lithium fluoride is found to be the most suitable, owing to its excellent contact stability. In addition, a passivating *a*-Si:H interlayer can also be used underneath the LiF_x layer to drastically reduce the recombination, to a level compatible with device open circuit voltages well over 700mV.
- The *a*-Si:H / LiF_x / Al electron contact can be combined with an *a*-Si:H / MoO_x hole contact to fabricate a dopant free asymmetric heterocontact (DASH) cell. A proof-of-concept cell with a power conversion efficiency of 19.4% has been demonstrated, a significant improvement on previous attempts at implementing the DASH type solar cell and the first to demonstrate competitiveness with conventional processes.

- The low resistivity of the LiF_x / Al electron contacts can also be used as partial rear contacts to an n-type cell without the need for heavy phosphorus doping. This has been demonstrated in a first-of-its-kind n-type PRC cell with a conversion efficiency of greater than 20%.

Provided below is a table summarising the main parameters of the carrier-selective contact systems developed in this thesis, as well as the various solar cells made with them.

	Contact resistivity ρ_c (mΩcm^2)	Contact recombination J_{0c} (fA/cm^2)	Cell results	Details
Electron contacts				
c-Si(n$^+$)/Al		1250		Chapter 2
c-Si(n$^+$)/SiO_x/Al	76	200		Chapter 2
c-Si(n$^+$)/AlO_x/Al	0.3	300		Chapter 2
c-Si(n$^+$)/*a*-Si:H/Al	50	40		Chapter 2
c-Si(n$^+$)/SiO_x/*a*-Si:H/Al	3	40	*a*-Si:H enhanced MIS, **21.0%,** 666mV, 39.3mA/cm^2, 80.5	Chapter 2
c-Si(n)/LiF_x/Al	1	~5000 (cm/s)	LiF_x n-type PRC, **20.6%,** 676 mV, 38.9 mA/cm^2, 78.3	Chapter 4
c-Si(n)/*a*-Si:H/LiF_x/Al	7	~716 (mV)	DASH, **19.4%,**716.15 mV, 37.07 mA/cm^2, 73.15	Chapter 4
Hole contacts				
c-Si(p$^+$)/Al	0.015	1370		Chapter 2
c-Si(p$^+$)/AlO_x/Al	360	1100		Chapter 2
c-Si(p$^+$)/*a*-Si:H/Al	100	100		Chapter 2
c-Si(p$^+$)/AlO_x/*a*-Si:H/Al	28	160		Chapter 2
c-Si(p$^+$)/MoO_x	0.2	200		Chapter 3
c-Si(p)/MoO_x	1	200	MoO_x p-type PRC, **20.4%,** 658 mV, 39.8 mA.cm^2, 77.8	Chapter 3
c-Si(n)/MoO_x	30	300		Chapter 3
c-Si(n)/SiO_x/MoO_x			Moly-poly, **16.7%,** 637 mV, 35 mA/cm^2, 75	Chapter 3
c-Si(n)/*a*-Si:H/MoO_x		~716 (mV)	DASH, **19.4%,**716.15 mV, 37.07 mA/cm^2, 73.15	Chapter 3

Suggestions for future work

Given the exploratory nature adopted in this thesis, a number of open questions remain to be addressed before such selective-contact systems could be adopted. A brief description of the main questions is provided below:

- Further optimisation of the *a*-Si:H enhanced MIS process could proceed in two directions: firstly, lightening the underlying dopant diffusion could drastically reduce the J_{0c}, which was limited partially by Auger recombination, without strongly affecting the ρ_c behaviour (provided the surface concentration remains similar). A second front could be to alter the metal which is used. Many metals undergo low temperature interaction with *a*-Si:H, choosing one which also has an appropriate electronic work function may also prove useful in enhancing carrier-selectivity.
- The temperature, humidity and illumination stability of MoO_x and LiF_x based hole and electron heterocontacts remains an open question. The performance of MoO_x based contacts has been shown to be unstable at temperatures around 150°C and the stability of LiF based contacts has not yet been tested. These will need to be tested and if necessary modified to allow device longevity consistent with the 20+ years expected from current *c*-Si solar cells. Such contacts may also require the development of dedicated a low temperature back-end process that prevents exposing the cells to temperatures above 150°C for prolonged periods.
- As it currently stands the application of alkali metal salt based contacts to *c*-Si solar cells has been limited to opaque contacts. A potential future area of research is to instead utilise such an active layer in a transparent electrode

using for example a TCO. Whilst not widespread, some evidence has been seen within organic electronic device literature that such a heterocontact could be possible.

- The solar cell devices presented in this thesis have served as demonstrations of the concepts only and an emphasis was not placed on optimisation. Further optimisation of fabrication sequences should permit higher conversion efficiencies.

6 List of Publications

Journal papers

[1] **James Bullock,** Di Yan, and Andrés Cuevas, "*Passivation of aluminum–n^+silicon contacts for solar cells by ultrathin Al_2O_3 and SiO_2 dielectric layers"*, Physica Status Solidi: Rapid Research Letters, 7, No. 11, 946–949, 2013.

[2] **James Bullock**, Di Yan, Yimao Wan, Andres Cuevas, Benedicte Demaurex, Aïcha Hessler-Wyser and Stefaan De Wolf, "*Amorphous silicon passivated contacts for diffused junction silicon solar cells*", Journal of Applied Physics, 115, 163703, 2014.

[3] **James Bullock**, Di Yan, Andres Cuevas, Benedicte Demaurex, Aïcha Hessler-Wyser and Stefaan De Wolf, "*Amorphous Silicon Enhanced Metal-Insulator-Semiconductor Contacts for Silicon Solar Cells"*, Journal of Applied Physics, 116, 163706, 2014

[4] **James Bullock,** Andres Cuevas, Christian Samundsett, Di Yan, Josephine McKeon and Yimao Wan, "*Simple silicon solar cells featuring an a-Si:H enhanced rear MIS contact*", Solar Energy Materials and Solar Cells, Volume 138, Pages 22–25, 2015.

[5] **James Bullock,** Andres Cuevas, Thomas G. Allen, Corsin Battaglia, "*Molybdenum Oxide MoO_x: A Versatile Hole Contact For Silicon Solar Cells*" Applied Physics Letters,105, 232109, 2014

[6] **James Bullock**, Christian Samundsett, Andrés Cuevas, Di Yan, Yimao Wan and Thomas Allen, "*Proof-of-concept p-type silicon solar cells with molybdenum oxide partial rear contacts*" IEEE Journal of Photovoltaics, vol. 5 no. 6, 2015.

[7] **James Bullock** Mark Hettick, Jonas Geissbühler, Alison J. Ong, Thomas Allen, Carolin M. Sutter-Fella, Teresa Chen, Hiroki Ota, Ethan W. Schaler, Stefaan De Wolf, Christophe Ballif, Andrés Cuevas and Ali Javey, "*Efficient silicon solar cells with dopant-free asymmetric heterocontacts"*, Nature Energy, 2, 15031, 2016

[8] **James Bullock,** Peiting Zheng, Quentin Jeangros, Mahmut Tosun, Mark Hettick, Carolin Sutter-Fella, Yimao Wan, Thomas Allen, Di Yan, Daniel Macdonald, Stefaan De Wolf, Aïcha Hessler-Wyser, Andres Cuevas, Ali Javey, "*Lithium fluoride based electron contacts for high efficiency n-type crystalline silicon solar cells"*, Submitted, 2016.

[9] **James Bullock**, Boris Veith, Andrew Thomson, Ari Karkkainen, Jan Schmidt and Andrés Cuevas, "*Enhanced rear-side reflection and firing-stable surface passivation of silicon solar cells with capping polymer films"*, Physica Status Solidi: Rapid Research Letters, 1-4, 2013.

[10] Xinbo Yang, **James Bullock**, Lujia Xu, Qunyu Bi, Sachin Surve, Marco Ernst, Klaus Weber, "*Passivated contacts to laser doped p+ and n+ region*s", Solar Energy Materials and Solar Cells, 2015.

[11] Xinbo Yang, **James Bullock**, Qunyu Bi, Klaus Weber, "*High efficiency n-type silicon solar cells featuring passivated contact to laser doped regions*", Applied Physics Letters, 2015.

[12] Yimao Wan, **James Bullock**, Andres Cuevas, "*Tantalum oxide/silicon nitride: A negatively charged surface passivation stack for silicon solar cells*", Applied Physics Letters, 2015.

[13] Yimao Wan, **James Bullock**, Andres Cuevas, "*Passivation of c-Si surfaces by ALD tantalum oxide capped with PECVD silicon nitride*" Solar Energy Materials and Solar Cells, 2015.

[14] Xiaojie Xu, **James Bullock**, Laura Schelhas, Elisa Stutz, Jose Fonseca Vega, Mark Hettick, Vanessa Pool, Michael Toney, Xiaosheng Fang, Joel W. Ager, "*Chemical bath deposition of p-type transparent, highly conducting (CuS)x:(ZnS)1-xnanocomposite thin films and fabrication of Si heterojunction solar cells"*, Nano Letters, 2016.

[15] Teck Kong Chong, **James Bullock**, Thomas P White, Martin Berry, Klaus J Weber, "*Nanoporous Silicon produced by Metal-Assisted Etching: A Detailed Investigation of Optical and Contact Properties for Solar Cells*", IEEE Journal of Photovoltaics 2014.

[16] Yimao Wan, Di Yan, **James Bullock**, Xinyu Zhang, and Andres Cuevas, "*Universal surface passivation of c-Si by sub-nm amorphous silicon capped with silicon nitride"*, Applied Physics Letters, 2015

[17] Di Yan, Andres Cuevas, Yimao Wan and **James Bullock**, "*Passivating Contacts for Solar Cells Based on Boron-diffused PECVD Amorphous Silicon and Thin Dielectric Interlayers*", Submitted, 2016

[18] Yimao Wan, Chris Samundsett, **James Bullock**, Mark Hettick, Di Yan, Thomas Allen, Peiting Zheng, Xinyu Zhang, Jie Cui, Josephine McKeon, Ali Javey, and Andres Cuevas, "*Efficient silicon solar cell with magnesium fluoride based electron–selective contact*" Submitted, 2016

[19] Di Yan, Andres Cuevas, **James Bullock**, Yimao Wan, Christian Samundsett, "*Phosphorus-diffused polysilicon contacts for solar cells*" Solar Energy Materials and Solar Cells, Volume 142, November 2015, Pages 75–82, 2015.

[20] Xinyu Zhang, Andres Cuevas, Yimao Wan, **James Bullock**, and Thomas Allen, *"Hole-selective contacts on crystalline silicon via reactively sputtered nitrogen doped copper oxide"*, In prep., 2016

[21] Di Yan, Andres Cuevas, Yimao Wan and **James Bullock**, "*Silicon nitride/silicon oxide interlayers for solar cell passivating contacts based on PECVD amorphous silicon"*, Physica Status Solidi: Rapid Research Letters, 2015.

[22] Kean Chern Fong, Teng Choon Kho, Andreas Fell, Evan Franklin, Ngwe Zin, Andrew W. Blakers, Keith R. McIntosh, Thomas Ratcliff, Matthew Stocks, **James Bullock**, and Er-Chien Wang, "*Contact Resistivity of Evaporated Al Contacts for Silicon Solar Cells",* IEEE Journal of Photovoltaics, Vol. 5, No. 5, September 2015.

[23] Wensheng Liang, Klaus Weber, Dongchul Suh, Jun Yu and **James Bullock,** "*Effect of damp-heat exposure on the degradation of plasma assisted ALD Al_2O_3 based on the application on solar cells"*, Physical Status Solidi A, 2014,

[24] Andrew Thomson, Matthew Gardener, Keith McIntosh, Avi Shalav and **James Bullock**, "*Damp and dry heat degradation of thermal oxide passivation of p^+ silicon"*, Journal of Applied Physics, 2014.

[25] Nicholas Grant, Fiacre Rougieux, Daniel Macdonald, **James Bullock** and Yimao Wan, "*Examining grown-in defects limiting the bulk lifetime of float zone silicon"*, Journal of Applied Physics, 2014.

[26] Avi Shalav, **James Bullock**, Peter Anderson, Simon Ruffell, John White and Robert G. Elliman, "*The Mechanical Photochemical Properties of Titania Coated Silica*", ECS J. Solid State Sci. Technol, 2012

Conference papers

[1] **James Bullock**, Di Yan, Andres Cuevas, Benedicte Demaurex, Aïcha Hessler-Wyser and Stefaan De Wolf, "*Passivated Contacts to n^+ and p^+ Silicon Based on Amorphous Silicon and Thin Dielectrics*", IEEE PVSC, Denver, Colorado, 2014.

[2] **James Bullock**, Di Yan, Andres Cuevas, Yimao Wan and Christian Samundsett, "*n- and p-type silicon solar cells with molybdenum oxide hole contacts*" Energy Procedia, Volume 77, Pages 446–450, 2015.

[3] **James Bullock**, Di Yan, Andrew Thomson and Andrés Cuevas, "*Imaging the recombination current pre-factor J_0 of heavily doped surface regions*", 27th EU PVSEC, Frankfurt, Germany, 2012.

[4] **James Bullock**, Yimao Wan, Mark Hettick, Jonas Geissbühler, Alison J. Ong, Daisuke Kiriya, Di Yan, Thomas Allen, Jun Peng, Xinyu Zhang, Carolin M. Sutter-Fella, Stefaan De Wolf, Christophe Ballif, Andrés Cuevas and Ali Javey, *"Development of Dopant-Free Carrier-Selective Contacts for Silicon Solar Cells"*, submitted to IEEE PVSC, Portland, Oregon, 2016.

[5] Xiaojie Xu, **James Bullock**, Ali Javey and Joel W. Ager, *"High V_{oc} n-Si heterojunctions with p-type transparent (CuS)x:(ZnS)1-x grown by chemical bath deposition"*, MRS spring meeting, Phoenix, 2016.

[6] Yimao Wan, **James Bullock**, Andres Cuevas, Christian Samundset and Di Yan, *"p^+nn^+ Silicon Solar Cell with a Full-Area Rear MIS, Passivated Contact,"* in 5th International Conference on Crystalline Silicon Photovoltaics, 2015.

[7] Di Yan**, James Bullock**, Yimao Wan and Andrés Cuevas, "*Development of a Self-aligned Etch-Back Process for Selectively Doped Silicon Solar cells*", IEEE PVSC, Denver, 2014.

[8] Thomas Allen, **James Bullock**, Andrés Cuevas, Simeon Baker-Finch and Fouad Karouta, *"Reactive Ion Etched Black Silicon Texturing: A Comparative Study"*, IEEE PVSC, 2014.

[9] Yimao Wan, Chris Samundsett, **James Bullock**, Di Yan, Thomas Allen, Peiting Zheng, Xinyu Zhang, Jie Cui, Josephine McKeon, and Andres Cuevas, "*20.1%*

N-type Silicon Solar Cell with MgF_2 Based Electron Contacts", submitted to IEEE PVSC, Portland, Oregon, 2016.

[10] Xinyu Zhang, Andres Cuevas, and **James Bullock**, *"Characterisation of sputtering deposited amorphous silicon films for silicon heterojunction solar cells",* submitted to IEEE PVSC, Portland, Oregon, 2016.

[11] Quentin Jeangros, Jonas Geissbühler, **James Bullock**, Ali Javey, Stefaan De Wolf, Aïcha Hessler-Wyser, Christophe Ballif, "*Advanced TEM characterization of new electrical contacts for high efficiency c-Si solar cells"*, submitted to Microscopy and Microanalysis, Columbus, Ohio, 2016.

[12] Wensheng Liang, Klaus Weber, Dongchul Suh, Jun Yu and **James Bullock**, "*Humidity Degradation and Repair of ALD Al_2O_3 Passivated Silicon"*, IEEE PVSC, 2013.

[13] Andrew Thomson, Teng Kho, Paul Williams, Ari Karkkainen, Leon Kwek, **James Bullock** and Andrés Cuevas, "*Enhanced back-surface reflectance and passivation capping from the application of inexpensive spray/spin on polymer coatings on Thin ALD Al2O3 layers",* 27th EUPVSEC, 2012.

[14] Nicholas Grant**,** Keith. R. McIntosh, **James Bullock**, Yimao Wan and Jason. T. Tan. *"Light enhanced hydrofluoric acid passivation for evaluating silicon bulk lifetimes"*, 28th EUPVSEC, 2013.

[15] Nicholas Grant, Fiacre Rougieux, Daniel Macdonald, **James Bullock** and Yimao Wan, "*Recombination active defects limiting the lifetime of float-zone silicon"*, 24th NREL WCSSC&MMP, 2014.

Appendices

Appendix 1: Carrier-selectivity parameters and simulation details

Carrier-selectivity parameters

For simplicity, the following discussion is arbitrarily focused on the electron-selective or cathode side of the solar cell, an equal (but opposite) discussion is relevant to the hole-selective side.

Electron-selectivity can be intuitively thought of as the ability to maximise the flux of electrons whilst minimising the flux of holes to the contact interface under the maximum power point condition. This flux is governed by the electron and hole conductivities as well as the slope in their electrochemical potential. Let us assume that we have a simple solar cell, the behaviour of which is completely dominated by the recombination J_0 and resistive ρ_c behaviour of the electron-selective side,

$$J = J_g - J_0 \exp\left(\frac{V - J\rho_c}{V_t}\right). \tag{1}$$

All holes that flow to the electron-selective surface do so to recombine. Therefore, we can define the flux of holes through the electron-selective virtual surface, at maximum power point, as:

$$q\Phi_{p,mpp} = J_{p,mpp} = J_0 \exp\left(\frac{V_{mpp}+J_{mpp}\rho_c}{V_t}\right) \quad (2)$$

Similarly, the electron flux through this surface is the collected carriers minus the amount that recombine there, given by

$$q\Phi_{n,mpp} = J_{n,mpp} = J_{mpp} - J_0 \exp\left(\frac{V_{mpp}+J_{mpp}\rho_c}{V_t}\right). \quad (3)$$

And hence the ratio between the two fluxes is given by

$$\frac{q\Phi_{n,mpp}}{q\Phi_{p,mpp}} = \frac{J_{n,mpp}}{J_{p,mpp}} = \frac{J_{mpp} - J_0 \exp\left(\frac{V_{mpp}+J_{mpp}\rho_c}{V_t}\right)}{J_0 \exp\left(\frac{V_{mpp}+J_{mpp}\rho_c}{V_t}\right)}. \quad (4)$$

To extract V_{mpp} and J_{mpp} for a given combination of J_0 and ρ_c we must incorporate a standardised reference value for J_g – a standard value of 43.31 mA/cm^2 is chosen, taken from Richter *et al.* [1]. For J_0 values in the range of 10^{-16} – 10^{-8} A/cm^2 and for ρ_c values between 10^{-3} and 0.6 Ωcm^2 a linear relationship is seen between the $\Phi_{n,mpp}/\Phi_{p,mpp}$ ratio and the obtained efficiency generally confirming its validity as a selectivity metric, as all other components of the cell are idealised.

A similar, but simpler metric could be defined as the carrier-selective contact's 'upper limit' voltage from the combination of the recombination and resistive restrictions on the contact's 'voltage' as the V_{oc} of the contact, minus the approximate shift at maximum power point due to a contact resistivity,

$$V_{UL} = V_t \ln\left(\frac{J_g}{J_0}\right) - J_g\rho_c, \quad (5)$$

where a standard reference value of J_g is used as a proxy for J_{mpp}. Whilst this parameter is unphysical, as it combines open and short circuit components it may act as a suitable approximation to represent trends. The relationship between V_{UL} and efficiency can also be seen to be linear over a wide range of recombination and resistive parameters as shown in Figure 1b.

The above equations are relevant to full-area contacts only, they can be modified to account for a contact fraction, which as discussed in Chapter 1 can intern alter the carrier-selectivity. For example, a simple modification of Equation 5 to approximately account for a reduced contact fraction is given by

$$V_{UL} = V_t ln\left(\frac{J_g}{(m_f J_{0c} + (1-m_f) J_{0p}}\right) - \frac{J_g \rho_c}{m_f} \quad (6)$$

where additional terms for the rear contact fraction m_f and recombination in the non-contacted, surface passivated regions J_{0p} are included. An additional term can also be added to account for intrinsic recombination in the bulk of the wafer.

Reference

[1] A. Richter, M. Hermle, S. W. Glunz, *IEEE J. Photovolt.* **2013**, *3*, 1184

Simulation details

Simulations from Figure 2B Quokka simulation input conditions for a full-area rear contact idealised cell.

Symbol	Parameter	Assumption / value
$J_{0\mathrm{front}}$	Front recombination factor	10^{-17} A/cm^2
ρ_{cfront}	Front contact resistivity	10^{-7} Ωcm^2
τ_{bulk}	Bulk lifetime	Richter *et al.* [1]
J_g	Generation current density	~44 mA/cm^2
W	Wafer thickness	100 µm
ρ_{bulk}	Bulk	Intrinsic

Simulations from Figure 3B Quokka simulation input conditions for a partial area rear contact idealised cell.

Symbol	Parameter	Assumption / value
$J_{0\mathrm{front}}$	Front recombination factor	10^{-17} A/cm^2
ρ_{cfront}	Front contact resistivity	10^{-7} Ωcm^2
τ_{bulk}	Bulk lifetime	Richter *et al.* [1]
J_g	Generation current density	~44 mA/cm^2
W	Wafer thickness	100 µm
ρ_{bulk}	Bulk	Intrinsic
m_f	Rear contact fraction	Pitch = variable
		Width = variable

Reference

[1] A. Richter, S. W. Glunz, F. Werner, J. Schmidt, A. Cuevas, *Phys. Rev. B* **2012**, *86*, 165202.

Appendix 2: Additional first author manuscripts

Passivated Contacts to n^+ and p^+ Silicon Based on Amorphous Silicon and Thin Dielectrics

James Bullock,[1] Di Yan,[1] Andrés Cuevas,[1] Bénédicte Demaurex,[2] Aïcha Hessler-Wyser,[2] and Stefaan De Wolf[2]

[1]Research School of Engineering, The Australian National University, Canberra, ACT 0200, Australia

[2]Ecole Polytechnique Fédérale de Lausanne (EPFL), Maladière 71, CH-200 Neuchâtel, Switzerland

Published in IEEE Photovoltaic specialists conference, 2014

Carrier recombination at the metal contact regions has now become a critical obstacle to the advancement of high efficiency diffused junction silicon solar cells. The insertion of a thin dielectric interlayer – forming a metal-insulator-semiconductor (MIS) contact - is a known approach to reduce contact recombination. However, an insulator thickness less than 25 Å is usually required for current transport, making it difficult to simultaneously achieve good surface passivation. This paper compares standard MIS contacts to a newly developed contact structure, involving hydrogenated amorphous silicon (a-Si:H) over-layers. The contact structures are trialed on both n^+ *and* p^+ *lightly diffused surfaces, with* SiO_2 *and* Al_2O_3 *insulator layers, respectively. In both cases significant improvements in the carrier-selectivity of the contacts is achieved with the addition of the a-Si:H over-layers. Simulations of idealized cell structures are used to highlight the performance and technological benefits of these carrier-selective structures over standard locally diffused contacts.*

Introduction The metal-silicon interface hosts an unavoidably large density of recombination active defects. Carrier recombination occurring at this interface places a significant limitation on the performance of devices which require high minority carrier lifetimes, such as the crystalline silicon (*c*-Si) solar cell. Two approaches have typically been implemented to address this issue: *i.)* the introduction of a heavily doped region immediately beneath the metal contact, and *ii.)* the reduction of the contact fraction to a smaller percentage of the cell surface area.

In the first approach, the addition of a heavy dopant concentration under the contact induces a strong asymmetry in the electron and hole concentrations, hence in their conductivities. By limiting the transport of one carrier (the minority carrier) to the metallized surface, recombination can be greatly reduced. Large reductions in metal-semiconductor contact resistivity can also be realized, as the heavier dopant concentration reduces the width of the potential barrier ubiquitous to the metal-silicon interface thereby increasing the tunneling probability for majority carriers. However, this approach is fundamentally limited by Auger recombination, which increases with increasing dopant concentration. In addition, heavy doping also introduces detrimental effects like reduced carrier mobilities and bandgap narrowing. As such the lowest metallized recombination current parameters J_{0c} achievable by this approach are about 350 fA/cm^2.

The second strategy involves the reduction of the metallized region to a small percentage of the cell area – a method which is essential on the cell's sunward-side given the opacity of metals. With this reduction in contact fraction, carrier flow is constricted so that the conductance towards the metal-silicon interface is reduced [1]. Such a geometrical reduction of the conductance affects majority carriers, causing a higher resistive loss, and minority carriers, leading to a reduced recombination loss. This tradeoff of majority carrier resistance for minority carrier recombination is usually permissible

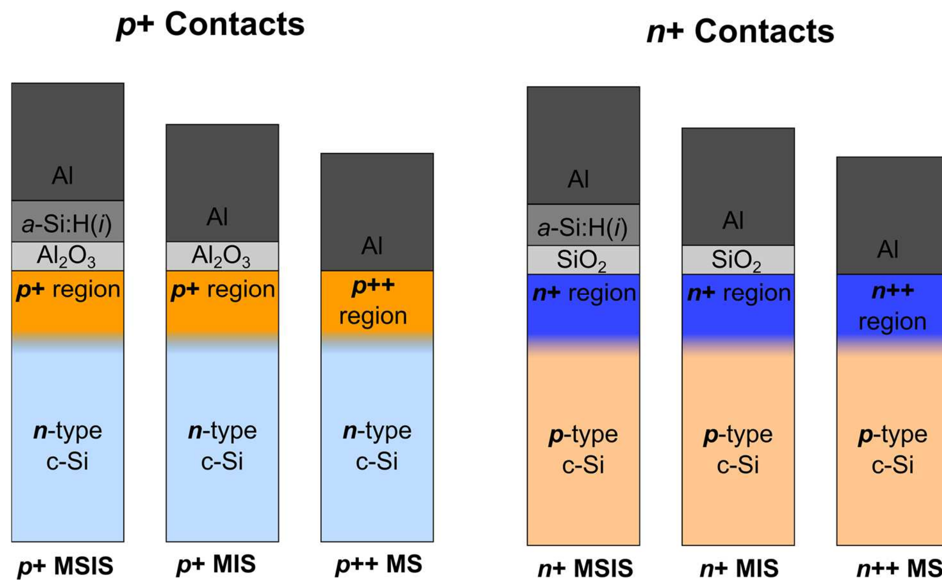

Figure. 1.Contact structures to be compared in this paper. Structures are referenced within the text by the names provided at the bottom. Layer thicknesses are not to scale, images represent the layer structure before annealing (after annealing *a*-Si:H and aluminium will intermix).

given their relative influence on cell performance. However, producing cells with small contact fractions within the industrial environment has proven to be a significant technological challenge, particularly when applied in conjunction with localized heavily doped regions.

The above described fundamental and technological issues associated with metal-silicon contacts have become a roadblock for the advancement of silicon solar cells, prompting much research in the area of passivated contacts. A common approach to achieve passivation of the contacts is to physically displace the metal and silicon surfaces by the insertion of thin passivating interlayers. These contact structures are generally categorized in accordance to the electrical characteristics of the interlayer(s) as metal-insulator-semiconductor (MIS) contacts, semiconductor-insulator-semiconductor contacts, or heterocontacts.

In the context of solar cells, MIS contacts have typically utilized SiO_2 [2-4] and Al_2O_3 [5-8] for the insulators, as their thicker counterparts (>100 Å) have been

successfully implemented for surface passivation in the non-contacted regions. However, the wide band-gap of these dielectrics presents large barrier heights to electrons and holes in the conduction and valence bands of *c*-Si. Hence, effective contacts are limited to a maximum thickness of ~25 Å in order to maintain appreciable current flow through tunneling conduction. Achieving a high level of surface passivation with a 25 Å thick dielectric (or thinner) remains a difficult task, compromising the benefit of implementing such contacts.

A proven pathway to improve the passivation quality of ultra-thin dielectric films is to apply hydrogen rich over-layers which assist in the passivation process [9, 10]. Hydrogenated amorphous silicon (*a*-Si:H) has the unique characteristics of being both an excellent hydrogen rich over-layer and being readily dissolvable in aluminum at low temperatures. With these characteristics in mind, a MIS fabrication procedure can be envisioned in which *a*-Si:H is applied on top of an ultrathin insulator to improve surface passivation, following which it is dissolved into an overlying aluminum layer by means of a low temperature anneal, resulting in the formation of a low resistance and low recombination contact [11].

Table I: Phosphorus and Boron dopant diffusion characteristics

Source	Sample	R_{sh} (Ω/□)	N_{surf} (cm^{-3})	J_{0metal} ($fAcm^{-2}$)	J_{0pass} ($fAcm^{-2}$)
$POCl_3$	n^+MIS, n^+MSIS	100±15	3(±1)×10^{19}	1200±200	25±5
	n^{++}MS	20±5	4(±2)×10^{20}	350±50	N/A
BBr_3	p^+MIS, p^+MSIS	100±15	1(±1)×10^{19}	1370±200	27±5
	p^{++}MS	35±5	2(±2)×10^{19}	520±70	N/A

*R_{sh} sheet resistance, N_{surf} surface dopant concentration, J_{0metal} metallized recombination factor, J_{0pass} passivated recombination factor.

To demonstrate the potential benefits of this process, this paper compares MIS contacts to n^+ and p^+ surfaces both with and without an *a*-Si:H over-layer. Ultrathin

atomic-layer-deposited (ALD) Al_2O_3 and thermally grown SiO_2 insulators are used on p^+ and n^+ surfaces respectively, in line with established best passivation practices for these surfaces. The efficacy of the contacts are described by their resistive and recombination properties as quantified by the contact resistivity ρ_c and contact recombination parameter J_{0c}. Idealized cell structures are simulated to assess the potential of these different approaches and compare them to heavily doped directly metalized surfaces. The different contact structures, and their corresponding abbreviations, are given in Figure 1.

Experimental

Test Structure Fabrication. Accurate J_{0c} and ρ_c values cannot easily be extracted from the same test structures; therefore, pairs of test structures were prepared to be measured via photoconductive decay (PCD) and the transfer-length-method (TLM) measurements. PCD measurements were taken on symmetrical test structures (identical layers / stacks deposited on both wafer faces) whist TLM samples were single side only.

All samples were prepared on FZ, >100 Ωcm resistivity, (100) oriented, p and n-type Si wafers. After saw damage etching and standard RCA cleaning, the wafers were diffused in quartz furnaces with boron (on n-type wafers) or phosphorus (on p-type wafers) so that in all cases the doping of the diffusion and substrate were opposite. Details of the final dopant profile characteristics, as determined by electrochemical capacitance voltage measurements (WEP Wafer Profiler), are given in Table I.

ALD Al_2O_3 layers were deposited at 200^OC (Beneq TFS 200) using alternating cycles of trimethylaluminium and water. Purge and pulse times were chosen as to ensure a self-limiting reaction. A growth-per-cycle of ~ 1Å is measured for this process, extrapolated from thicker Al_2O_3 depositions. All test structures with an Al_2O_3 layer were annealed at 400^OC for 15 minutes immediately prior to metallization, for surface

passivation activiation. SiO_2 layers were grown via rapid thermal oxidation (O_2 ambient) at 700°C in a clean quartz furnace. The *a*-Si:H layers were deposited by plasma-enhanced-chemical-vapor-deposition (PECVD) at a set temperature of either 200°C (p^+MSIS) or 400°C (n^+MSIS) to a thickness of ~ 30 nm.

Aluminum layers were evaporated at low pressure onto samples to a thickness of 1 μm and ~10 nm for the TLM and carrier lifetime test structures respectively (see Section II.B). The p^+ and n^+ MSIS structures require a further annealing step at 250°C to initiate the aluminum *a*-Si:H interaction, a more detailed explanation of the fabrication procedure of these contacts is given in [11].

Included in Table I are the directly passivated J_{0pass} and directly metallized J_{0metal} recombination parameters of the p^+ and n^+ surfaces. The directly passivated recombination parameters have been realized via PECVD *a*-Si:H (~30nm) for the n^+ surface and plasma-assisted-ALD Al_2O_3 (~20nm) for the p^+ surface, in-line with previously reported low surface recombination results on these surfaces [12, 13]. The metallized recombination parameter is measured from samples with ~10 nm of aluminum evaporated directly onto the diffused surfaces.

Characterization. Recombination parameter J_{0c} values were extracted using the Kane and Swanson technique [14] from carrier lifetime measurements taken using a photoconductive decay (PCD) instrument (Sinton WCT 120). An intrinsic carrier concentration of n_i=8.95×10^9 cm^{-3} (at 297 K) was assumed in these extractions. Only thin aluminum layers are used for these samples to ensure that sufficient light passes through the aluminum layer and that the signal from the calibrated conductance tester is not saturated by the additional conductivity of the metal.

Contact resistivity ρ_c measurements are taken using TLM measurements. The TLM contact pad patterns were photolithograpically defined and isolated using an acidic

Al etch. Pad spacings of 10-300 μm are used during this study. Current–voltage measurements were performed using a Keithley 2425 Source Meter (at ~ 297 K) and ρ_c was extracted as per the description given in [15].

Film thicknesses were monitored by fitting reflectance data (J.A. Woolam M2000 ellipsometer) of single side polished silicon wafers deposited alongside carrier lifetime and TLM samples. Given the dependence of SiO_2 growth on the dopant concentration, the SiO_2 thickness samples were subjected to a phosphorous diffusion prior to oxidation to create an alike surface concentration.

Results and Discussion

Contact Characteristics. Figure 2a and b provide the ρ_c and J_{0c} dependence on SiO_2 thickness, for the n^+ contacts. Included in these plots as a reference are dotted lines indicating the position of J_{0metal}, J_{0pass} and the directly metallized ρ_c of the diffusion profile used on the n^+MIS and n^+MSIS structures.

In agreement with the theoretical probability for quantum-mechanical tunneling, a strong increase in ρ_c is observed as a result of increasing insulator thickness for both the n^+MIS and n^+MSIS structures. Both n^+ contact structures exhibit similar resistive behavior for SiO_2 thicknesses in the 1.5 – 1.7 nm range. Above this range the n^+MIS structure appears to maintain a lower ρ_c value than the n^+MSIS structure, with films of 2.2 nm still achieving a ρ_c of ~0.2 Ωcm^2.

Coupled with the increasing ρ_c is a decreasing J_{0c}, which is again seen for both contact structures. For the n^+MSIS structures an order of magnitude reduction in recombination is obtained, as compared to J_{0metal}, for even the thinnest SiO_2 layers. An insulator thickness of 1.7 nm is sufficient to achieve the lower limit recombination factor

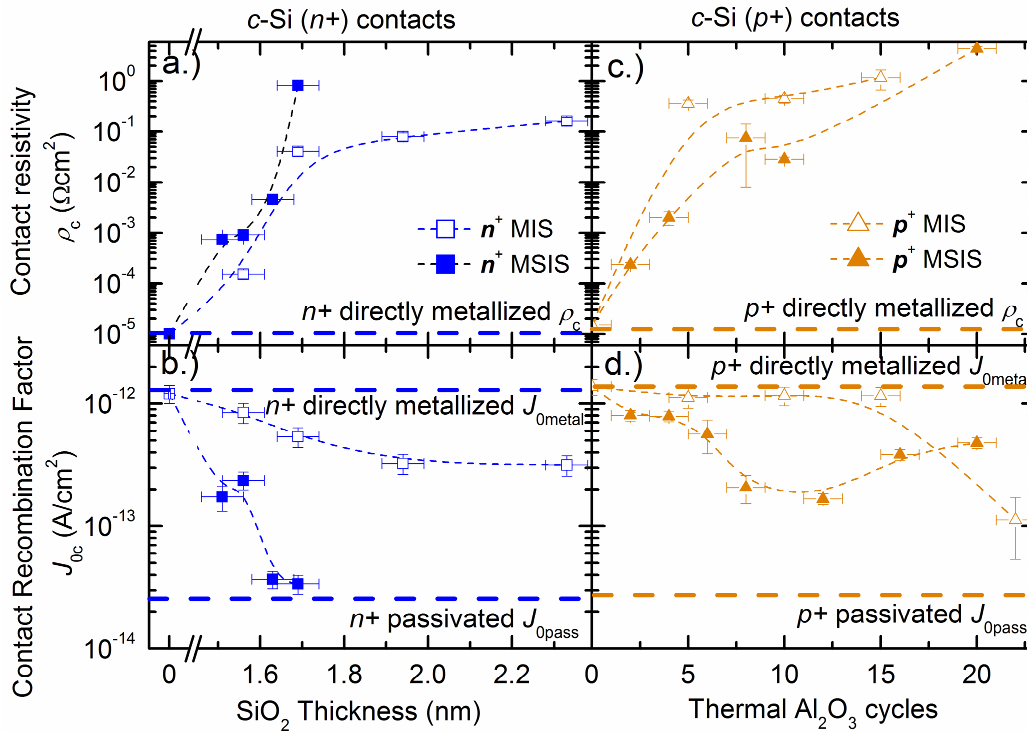

Figure. 2 Contact resistivity ρ_c of a.) n^+ contacts and c.) p^+ contacts and contact recombination factor J_{0c} for b.) n^+ contacts and d.) p^+ contacts as a function of insulator thickness. Lines provide a guide to the eyes only, error bars are based off the estimated error in measurement.

of ~25 fA/cm^2. The n^+MIS structures show a more moderate reduction in recombination but still achieve values of ~300 fA/cm^2 with a 1.9 nm SiO_2 layer.

An analogous set of results for the p^+ contacts as a function of the number of ALD Al_2O_3 cycles is provided in Figure 4c and d. Both p^+MSIS and p^+MIS structures show an increasing ρ_c trend with Al_2O_3 thickness (in this case as number of cycles), although the p^+MSIS structure consistently achieves lower ρ_c values. The improvement in J_{0c} with Al_2O_3 thickness is not as strong as seen for the n^+ contacts – reaching at best ~150 fA/cm^2 for the p^+MSIS structure – which is still approximately an order of magnitude lower than the corresponding J_{0metal}. Interestingly, for the p^+MSIS structure the passivation quality seems to stop improving after 10 cycles of Al_2O_3 – producing a local minimum. The p^+MIS structure exhibits a more gradual reduction in recombination with increasing Al_2O_3 thickness, resulting in no overlap between contact passivation and useful contact

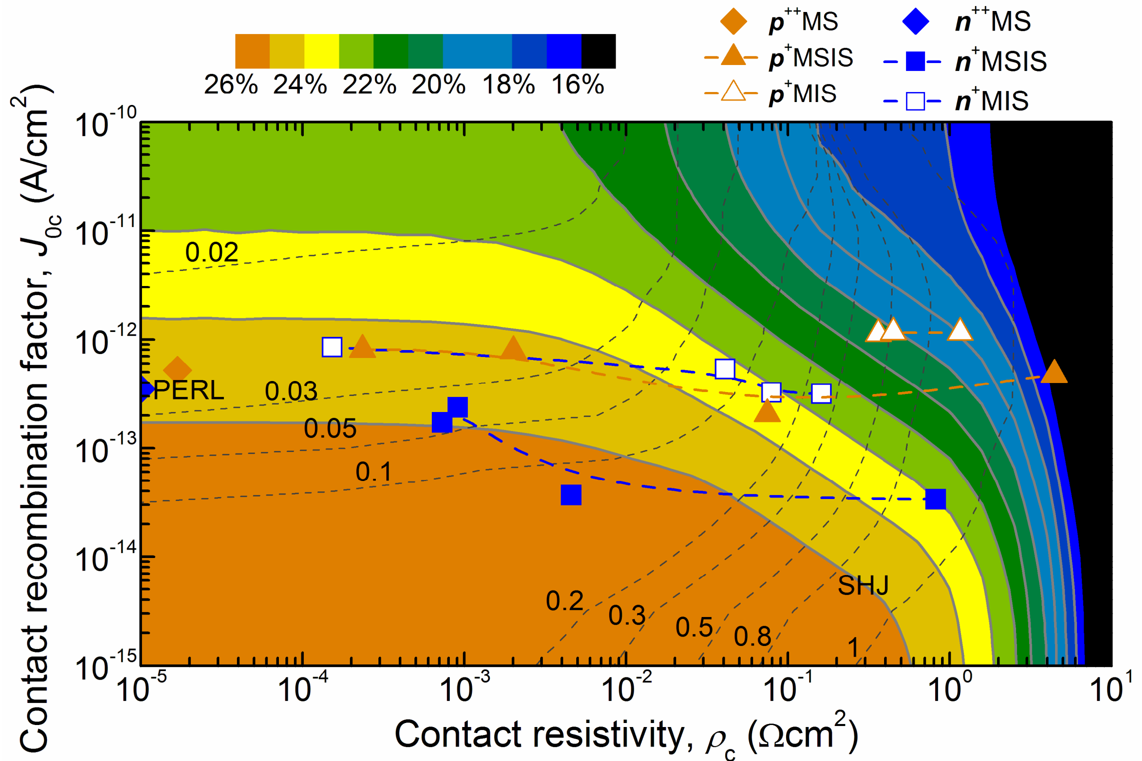

Figure. 3 Simulated optimum contact fraction (dotted lines) and resultant efficiency (contour plot) as a function of rear contact ρ_c and J_{0c}. Results presented in this work are superimposed over the contour plot.

resistances. It should be noted that the ρ_c values of ~1 Ω.cm^2 and above were extracted from contacts that deviated from pure Ohmic behavior and as such they represent a lower-limit ρ_c.

Significance to Solar Cells. In the context of solar cells, the efficacy of the contacts can be described by their carrier-selectivity. The carrier-selectivity of a particular region or contact structure can be generically defined as its ability to perform two separate functions: *i.*) provide a very high conductivity for one carrier type – the collected, or majority carrier; and *ii.*) present a very low conductivity to the other carrier – the minority carrier [16]. These two functions can be well represented by the parameters ρ_c and J_{0c}, respectively. The contact resistivity ρ_c is a measure of the ability to transport majority carriers across the contact interface. A decrease in ρ_c corresponds to an increase in

majority carrier conductivity. The parameter J_{0c} reflects the recombination losses occurring at the contact interface or, more generally, within the complete contact structure, which, for the structures investigated in this paper, includes the recombination in the bulk of the diffused region. The parameter J_{0c} is analogous to the conductivity presented by the contact structure towards minority carriers [17]. A very high J_{0c} means that there is minimal impediment to minority carriers flowing towards the contact, hence it means that there is a high minority carrier conductivity, and vice-versa.

An ideal contact structure should be highly selective, that is, combining very low ρ_c and very low J_{0c}. But in practice, these two properties are difficult to achieve simultaneously, and a trade-off between them needs to be found. The nature of this tradeoff is generally complicated, requiring consideration of the contact architecture. Therefore, a proper discussion of passivated contacts should also include as a third variable the fraction of the solar cell surface where the contact is implemented.

To illustrate the trade-off between ρ_c and J_{0c}, we have simulated an idealized solar cell structure with partial rear contacts (PRC) using a recently developed quasi-analytical model for such a device structure [18, 19], in conjunction with QsCell [20]. The PRC was modelled with a variable ρ_c and J_{0c}, and for each ρ_c - J_{0c} combination an optimum rear contact fraction (dashed lines) is found and the resultant efficiency calculated. Figure 6 presents the results of the simulations. A list of assumptions and values used in the simulation are provided in Table II. Note that we have assumed an homogeneous dopant diffusion on the rear surface, that is, a p^+nn^+ device structure. Such a diffusion helps to transport carriers laterally towards the local contacts, but its presence does not dramatically change the results of the simulations, particularly for larger contact fractions. The results in Fig. 6 are consistent with recent simulations of a similar nature [21].

Fig. 3 shows that there is a relatively broad parameter space in which a high efficiency can be achieved. A low ρ_c permits to afford relatively high J_{0c}, as long as the contact fraction is very small. As an example, the optimized n^{++}MS and p^{++}MS contacts introduced in Figure 1 and Table I are shown on this plot as a blue and orange diamonds respectively. Such a solar cell with localized diffused contacts, frequently referred to as PERL cell, has led to conversion efficiencies up to 25% (note that the efficiency in Fig. 3 is only 24.5% because we have assumed a relatively low photogenerated current density of 40 mA/cm^2).

Table 2: Simulation assumptions and values

Symbol	Parameter	Assumption / value
J_{0front}	Front recombination factor	1 fA/cm^2
J_{0rear}	Rear recombination factor (in non-contacted area)	1 fA/cm^2
R_{sh_front}	Front diffusion sheet resistance	120 Ω/□
R_{sh_rear}	Rear diffusion sheet resistance	100 Ω/□
	Bulk type, resistivity	n-type, 1 Ωcm
W	Wafer thickness	160 µm
J_g	Generation current density	40 mA/cm^2
τ_{bulk}	Bulk lifetime	Richter intrinsic lifetime [22]

On the other extreme, it is possible to also achieve a high efficiency even if ρ_c is relatively high, as long as J_{0c} is very small and the contact fraction is high. Although strictly not applicable to this plot, the position of standard silicon heterojuction (SHJ) contacts, with a J_{0c} of 5 fA/cm^2 and a ρ_c of 0.3 □cm^2, also sits at ~ 25% in line with best results for these structures. To show the significance of the n^+ and p^+ passivated contacts presented in this paper, their corresponding J_{0c} - ρ_c trends are superimposed over the simulated contour plot.

For the n^+MIS contacts the highest efficiencies are seen for the thinnest SiO_2 interlayers, which should be applied in small contact fractions. The addition of the *a*-Si:H

over-layer in the n^+MSIS clearly improves the selectivity of the contact – mostly due to a reduction in the minority carrier conductivity (reduction in J_{0c}). n^+MSIS contacts with an oxide layer of ~1.65 nm produce the optimum tradeoff between J_{0c} and ρ_c with idealized efficiencies of over 25%. A significant advantage of this J_{0c} - ρ_c combination, as compared to the n^{++}MS localized diffusion approach, is that large contact fractions (10 – 30%) are permissible – potentially simplifying the fabrication procedure.

As mentioned in Section III.B, the p^+MIS contact characteristics exhibit no benefit over the corresponding directly metallized case. The addition of the *a*-Si:H over-layer in the p^+MSIS structure is again seen to result in strong improvements in the contact-selectivity. With ~5 cycles of ALD Al_2O_3, the p^+MSIS contact characteristics produce a slightly lower, but similar, idealized cell efficiency to the localized p^{++}MS contacts. Benefits in terms of fabrication simplicity, due to the removal of the local diffusion step, could prove sufficient to outweigh this difference.

Conclusion. This paper has explored the benefits of a newly developed carrier-selective contact, whose fabrication procedure utilizes an *a*-Si:H capping step for MIS contact formation. Passivated contact structures both with (MSIS) and without (MIS) the additional *a*-Si:H over-layer have been trialed on lightly diffused p^+/Al_2O_3 and n^+/SiO_2 structures. These were also compared to optimized n^{++} and p^{++} metal-silicon contacts. The results of the investigation have shown a significant enhancement in carrier-selectivity as a result of the additional *a*-Si:H capping step for both the n^+ and p^+ contacts.

Simulated idealized solar cell structures show that for the n^+MSIS contacts an optimum configuration with a SiO_2 layer of ~1.65 nm produces efficiencies over 25%. These simulations suggest that the n+MSIS contacts can be applied to large area fractions of the rear surface, and hence offer advantages over the traditional localized heavy diffusion approach, both in terms of performance and process simplicity.

The p^+MSIS contacts revealed poorer J_{0c} - ρ_c combinations, with corresponding lower idealized efficiencies, but may still offer advantages over the p^{++}MS contact in terms of process simplicity.

Acknowledgements. The authors from the ANU acknowledge financial support by The Australian Solar Institute/Australian Renewable Energy Agency and facilities at the Australian National Fabrication Facility. The authors from EPFL thank the Axpo Naturstrom Fonds, the European Commission (FP7 project Hercules), the EuroTech Universities Alliance and the Swiss Commission for Technology and Innovation for their financial support.

References

[1] A. Cuevas, “Electrons and holes in solar cells with partial rear contacts,” *Progress Photovoltaics: Res. Appl.,* 2013.

[2] M. A. Green, A. W. Blakers, M. R. Willison, T. Szpitalak, E. M. Keller, E. Gauja and P.J. Hart, “The MINP solar cell – a new high voltage, high efficiency silicon solar cell” *Proceedings of the 15th IEEE Photovoltaic Specialist Conference*, Kissimmee, USA, 1981, p. 1405

[3] J. Schmidt, A. Merkle, R. Brendel, B. Hoex, M. C. M. van de Sanden, and W. M. M. Kessels, “Surface Passivation of High-efficiency Silicon Solar Cells by Atomic-layer-deposited Al_2O_3” *Prog. Photovoltaics* 16(6), 461 (2008).

[4] K. Jäger-Hezel, W. Schmidt, W. Helt, and K.D. Rasch, “Improved Large Area MIS-Contacted Silicon Solar Cells”, *Proc. 13th EU PVSEC*, 1995, p. 1515.

[5] D. Zielke, J. H. Petermann, F. Werner, B. Veith, R. Brendel and J.Schmidt, “Contact passivation in silicon solar cells using atomic-layer-deposited aluminium oxide layers” *Phys. Status Solidi RRL* ***5***, 298 (2011).

[6] X. Loozen, J. Larsen, F. Dross, M. Aleman, T. Bearda, B. O’Sullivan, I. Gordon and J. Poortmans "Passivation of a metal contact with a tunneling layer", *Proc. 3rd Workshop Metallization Crystalline Silicon Sol. Cells*, pp.25 -26 2011

[7] J. Deckers, E. Cornagliotti, M. Debucquoya, I. Gordona, R. Mertensa, J. Poortmans, “Aluminum oxide-aluminum stacks for contact passivation in silicon solar cells”, *Proc. 4th International Conference on Silicon Photovoltaics,* 2014.

[8] J. Bullock, D. Yan and A. Cuevas, “Passivation of aluminium n^+ silicon contacts for solar cells by ultrathin Al_2O_3 and SiO_2 dielectric layers”, *Phys. Status Solidi RRL* ***7***, 946 (2013).

[9] W. Liang, K. Weber, A. Thomson, “Effective SiN_x:H capping layers on 1nm Al_2O_3 for p^+ surface passivation”, *Submitted to Journal of Photovoltaics*, 2014

[10] A. Richter, J. Benick, M. Hermle and S. W. Glunz, “Excellent silicon surface passivation with 5 Å thin ALD Al_2O_3 layers: Influence of different thermal post-deposition treatments” *Phys. Status Solidi RRL* ***5***, 202 (2011).

[11] J. Bullock, D. Yan, A. Cuevas, B. Demaurex, A. Hessler-Wyser and S. De Wolf*, in preparation*, 2014

[12] J. Bullock, D. Yan, Y. Wan, A. Cuevas, B. Demaurex, A. Hessler-Wyser and S. De Wolf, “Amorphous silicon passivated contacts for diffused junction silicon solar cell” *J. Appl. Phys,* 115, 163703 (2014)

[13] B. Hoex, J. Schmidt, R. Bock, P. P. Altermatt, M. C. M. van de Sanden and W. M. M. Kessels, “Excellent passivation of highly doped p-type Si surfaces by the negative-charge-dielectric Al_2O_3”, *Appl. Phys. Lett.* ***91***, 112107 (2007)

[14] D.E. Kane and R. M. Swanson, “Measurement of the emitter saturation current by a contactless photoconductivity decay method”, *Proceedings of the 18th IEEE Photovoltaic Specialist Conference*, Las Vegas, USA, 1985, p. 578-583.

[15] D. K. Schroder, *Semiconductor Material and Device Characterisation* (Wiley, Hoboken, 2006), p. 146

[16] P. Würfel, *Physics of Solar Cells: from Basic Principles to Advanced Concepts*, (Wiley, 2009)

[17] W. Shockley and W. T. Read, “Statistics of the Recombination of Holes and Electrons *Phys. Rev.* 87, 835 (1952)

[18] A. Cuevas, “Physical model of back line-contact front-junction solar cells,” *J. Appl. Phys.*, vol. 113, pp. 164502, 2013.

[19] A. Cuevas, “Geometrical Analysis of Solar Cells with Partial Rear Contacts”, *Journal of Photovoltaics,* p.485 – 493, 2012

[20] A. Cuevas and R. Sinton, "Simple modelling of solar cells", *Proc. 23rd European Photovoltaic Solar Energy Conf., Valencia, September* 2008, pp. 315-319

[21] D. L. Young, W. Nemeth, S. Grover, A. Norman, H-C Yuan, B. G. Lee, V. LaSalvia, and P. Stradins, “Carrier selective, passivated contacts for high efficiency silicon solar cells based on transparent conducting oxides”, *Proc. 4th International Conference on Silicon Photovoltaics*, 2014

[22] A. Richter, S. W. Glunz, F. Werner, J. Schmidt, and A. Cuevas, "Improved quantitative description of Auger recombination in crystalline silicon," *Physical Review B*, vol. 86, p. 165202, 2012

Imaging the recombination current pre-factor J_0 of heavily doped surface regions; a comparison of low and high injection Photoluminescence techniques

J. Bullock, D. Yan, A. Thomson and A. Cuevas

Research School of Engineering, Australian National University, Canberra, ACT 0200, Australia

Published in European Photovoltaics Specialist Conference, 2012

A novel technique for imaging the recombination current pre-factor J_0 of heavily doped surface regions, ubiquitous to mainstream silicon solar cells, is introduced. This technique utilises photoluminescence in a low injection regime, allowing measurement of test structures with low and moderate resistivities, which are unattainable by the conventional Kane and Swanson method [1]. The procedure is fast and simple requiring only one photoluminescence image and no photoconductance measurement (after an initial calibration). The potential of the technique is demonstrated on surface-passivated phosphorus diffusions with sheet resistances in the range of ~15 – 120 Ω/sq. A comparison is made with both high and low injection photoconductance decay (PCD) measurements and a recently proposed high injection J_0 imaging technique (based on Kane and Swanson theory) [2, 3].

Introduction: The recombination current pre-factor J_0, is a useful metric in solar cell characterisation. It provides, after multiplication with the normalised electron hole product, the recombination current flowing into a particular region of, or throughout, a solar cell. As such, J_0 acts as an injection-independent representation of solar cell recombination.

Each individual solar cell can be described in terms of a number of regional J_0 values, representing individual recombination currents in heavily-doped or base-doped regions, and a global J_0 which represents recombination across the entire cell. The heavily doped surface regions of solar cells are of particular importance to their efficacy and generally exhibit large recombination currents. In these regions the recombination current pre-factors can be represented by J_{0n^+} or J_{0p^+} depending on the doping type.

1D measurements of J_{0n^+} and J_{0p^+} have proven invaluable in cell characterisation and optimisation. 2D imaging of J_{0n^+} and J_{0p^+} could provide further benefit in analysing spatial variation across a solar cell. Such an imaging technique would ideally be contactless, non-destructive, applicable to industry doping and have a high accuracy, resolution and throughput. Further benefit could be attained from a process which remains valid when imaging both mono- and multi-crystalline material.

Recently, a number of research groups have developed techniques for imaging of recombination current pre-factors using microwave photoconductance [4] (μPC), electroluminescence [5] (EL) and photolumninescence [2, 6, 7, 8, 3, 9] (PL). However, as of yet these techniques do not satisfy all of the criteria mentioned above, especially with regard to speed of acquisition.

This work introduces two fast and simple J_{0n^+} imaging methods which utilise PL in a low injection regime. Although only the recombination current pre-factors of heavily doped phosphorus surface regions are analysed, the theory and techniques remain applicable to heavily doped p-type regions and hence could be used to acquire images of J_{0p^+} regions under similar conditions. A comparison is made with an adapted high-injection Kane and Swanston [1] method recently demonstrated by both Müller *et al.* [3] and Müller *et al.* [6, 2]. Average J_{0n^+} values obtained from these techniques are compared to single J_{0n^+} values obtained from high [1] and low [10, 11] injection photoconductance decay (PCD) measurements.

Theory

Principle of low injection PL J_{0n^+} imaging. PL intensity I_{ill} shares a proportionality to np-n_i^2 with most of the recombination components found in silicon solar cells. Under certain conditions this linked proportionality allows the removal of injection level Δn consideration when obtaining recombination characteristics, for example J_{0n^+}, from I_{ill}.

In steady state conditions, generation G and recombination U rates in a symmetrically phosphorus-diffused p-type silicon test structure (Structure 1, Figure 1) will be in balance,

$$G = U_{n^+regions} + U_{\text{bulk,SRH}} + U_{\text{bulk,RAD}} + U_{\text{bulk,AUG}} \qquad (1)$$

where $U_{n^+region}$ includes both recombination in the diffused regions and at the diffused surfaces. When considering the above recombination mechanisms only Auger recombination in the bulk does not exhibit proportionality to $np - n_i^2$ [12]. By restricting

this scenario to low injection conditions and assuming an approximately constant Δn profile we can isolate a common dependence on Δn_{av}, given by

$$\frac{J_{\text{ph}}}{q} = \left[\frac{2N_A J_{0n^+}}{qn_i^2} + \frac{W}{\tau_n} + WBN_A + WC_p {N_A}^{1.65}\right]\Delta n_{\text{av}} \qquad (2)$$

where J_{ph} is the photon flux density, N_A the base doping, n_i the intrinsic carrier concentration and q the carrier charge. B and C_p in the above equation are the radiative recombination coefficient and the Auger hole coefficient, both of which are independent of Δn in low injection [12, 13]. τ_n is the Shockley Read Hall electron lifetime.

The relationship between PL intensity and Δn_{av} [14] in low injection can also be written in a similar manner as

$$I_{\text{ill}} = [A_i B N_A]\Delta n_{av}. \qquad (3)$$

where A_i is a linear scaling factor. This factor is a ratio between the amount of photons collected by the detector and the total PL events occurring within the substrate. It is sensitive to the $\Delta n(x)$ profile and the specific measurement setup. A_i can be easily obtained using Equation 3 in conjunction with PL and Δn images from a Quasi-steady-state PC-calibrated PL imager. From Equation 2 we can derive the proportionality between recombination characteristics and PL intensity given by

$$I_{\text{ill}} = A_i B \left[\frac{J_{ph}}{\frac{2J_{0n^+}}{n_i^2} + \frac{Wq}{N_A \tau_n} + WqB + WqC_p {N_A}^{0.65}}\right]. \qquad (4)$$

The extraction of J_{0n^+} from the above equation requires an approximation of the SRH electron lifetime which is often hard to obtain accurately. Two levels of simplification which can be applied when warranted are the assumptions of an intrinsic bulk (only Auger and radiative recombination are significant) or recombination dominance of the heavily doped region (making bulk recombination comparatively negligible). These assumptions produce

$$I_{\text{ill}} = A_i B \left[\frac{J_{ph}}{\frac{2J_{0n^+}}{n_i^2} + WqB + WqC_p {N_A}^{0.65}} \right]. \tag{5}$$

and

$$I_{\text{ill}} = A_i B \left[\frac{J_{ph} n_i^2}{2N_A J_{0n^+}} \right]. \tag{6}$$

respectively. In instances when the above approximations are not warranted the obtained J_{0n^+} value is representative of an upper limit.

The assumption of no significant bulk recombination can be increased in accuracy, albeit sacrificing some signal intensity, by introducing a single-side diffused structure (Structure 2, Figure 1) with a back surface of “infinite” surface recombination velocity S. The previous assumption of constant $\Delta n(x)$ is no longer valid and a simple constant-gradient profile is assumed where Δn_{back} is approximately 0 and $\Delta n_{\text{av}} = 1/2\Delta n_{\text{front}}$. This assumption requires that the base diffusion length is much greater than W. Recombination at the back surface will be limited by the diffusion coefficient of

electrons D_n, which can be assumed constant in low injection [15], the G-U balance can be written in this instance as

$$\frac{J_{ph}}{q} = \left[\frac{N_A J_{0n^+}}{q n_i^2} + \frac{D_n}{W}\right] \Delta n_{\text{front}}. \tag{7}$$

Hence we derive

$$I_{\text{ill}} = A_i B \left[\frac{J_{ph}}{\frac{2J_{0n^+}}{n_i^2} + \frac{2qD_n}{N_A W}}\right]. \tag{8}$$

Comparison to detailed modelling. An analysis of the validity of the simple theory proposed in Equations 5 and 8 is made by comparison with the more complex model for recombination and photoluminescence employed in QSSModelV5 [16]. Structures 1 and 2 with widths of 300µm and base resistivites of 0.5, 1 and 2 Ω-cm, are used for the simulations. Bulk SRH recombination is removed and a monochromatic illumination source with a wavelength of 809nm is used to mimic the PL laser source and ensure the majority of generation occurs at the front side. The simulated photoluminescence intensity I_{ill} is monitored whilst front and back J_{0n^+} values are simultaneously increased in structure 1 and the front J_{0n^+} value is increased in structure 2 (whilst the back is fixed at an S of approximately 10^7 cm/s). I_{ill} is then used as a proxy for an "experimental input" to Equations 5 and 8 in order to determine J_{0n^+}. The results of this exercise are shown in Figure 2. They reflect a high degree of correlation between J_{0n^+} values in the 10-1000 fA/cm^2 range for both structures 1 and 2, proving that in principle a low injection PL method based on either structure should work.

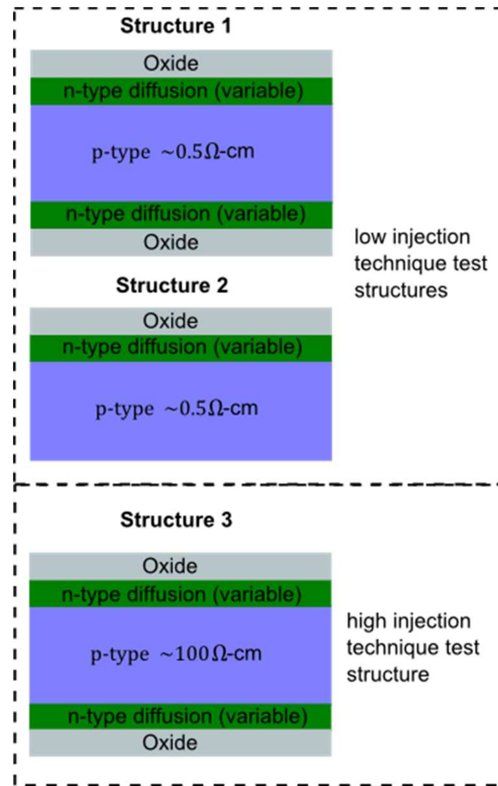

Figure 1: Cross-sectional diagrams of test structures 1-3, used for J_{0n^+} imaging techniques in this paper.

At higher J_{0n^+} values the proposed method decreases in accuracy as the assumption of constant gradient $\Delta n(x)$ becomes invalid due to "bending" of the $\Delta n(x)$ profile from recombination in the surface diffused regions. At lower J_{0n^+} values, diffused region contribution to recombination becomes minute and care should be taken in interpreting results, as a higher weight is placed on the accuracy of parameterisations used to quantify the intrinsic bulk lifetime and the diffusivity.

In the above simulations a new A_i is calculated for every J_{0n^+} input. It would be beneficial in an industrial quality control system to treat this factor as constant removing the need for an inductive coil in the system and reducing the time required to acquire images. Alike simulations performed with a constant A_i reveal a reduction in the valid range for the symmetrically diffused structure (structure 1) to ~10–500 fA/cm^2. No

appreciable reduction in the range of validity was seen with single-side diffused (structure

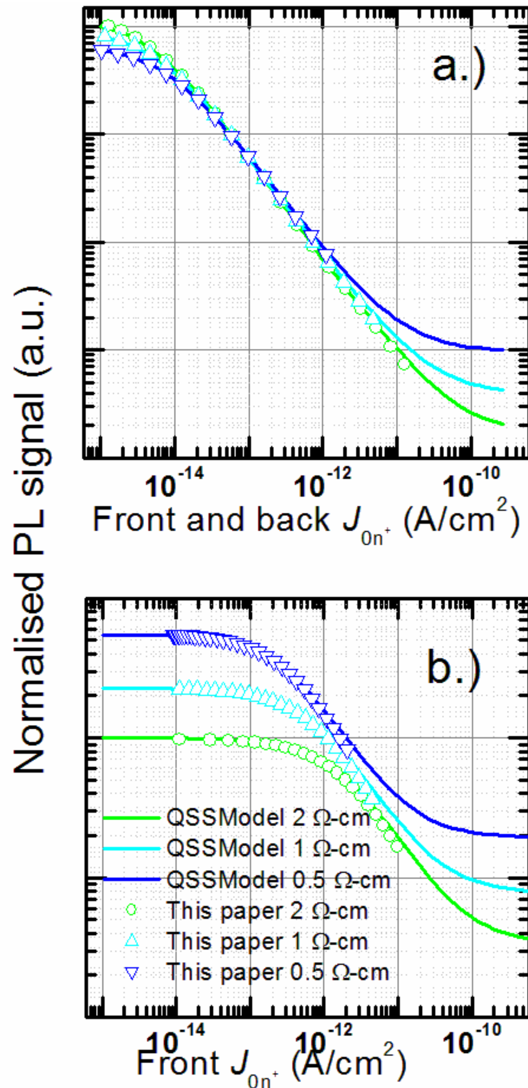

Figure 2: Comparison of $J_{0n^+} - I_{\text{ill}}$ proportionality of the simplified theory in this paper (hollow markers) and the QSSModelV5 [16] (lines). Simulations are shown for symmetrical structure 1 (a.) and asymmtrical structure 2 (b.).

2) simulations due to only a very small change in the $\Delta n(x)$ profile with increasing J_{0n^+}.

The two test structures and accompanying equations described above allow the acquisition of J_{0n^+} images by fast, simple, linear scaling of a *single* I_{ill} image using known test structure characteristics and constants. This method requires no contacts and can be conducted on test structures with low bulk resistivities, representative of industrial solar cells – a possibility sometimes unattainable by the Kane and Swanson

PCD technique. Further, structure 2 resembles a solar cell precursor, hence this technique could be applied as part of an inline quality control system.

One drawback of these techniques is that the J_{0n^+} image depends heavily on the accuracy of test structure width, doping and optical property measurements as well as parameterisations of Auger, radiative and diffusion coefficients.

High injection PL J_{0n^+} imaging. The method of J_{0n^+} extraction pioneered by Kane and Swanston using PCD forms the basis for high injection J_{0n^+} imaging used in this paper. Adapting Equation 1 into an effective lifetime τ_{eff} form yields

$$\frac{1}{\tau_{\text{eff}}} = \frac{2J_{0n^+}(\Delta n_{avg} + N_A)}{qWn_i^2} + \frac{1}{\tau_{\text{bulk,SRH}}} + \frac{1}{\tau_{\text{bulk,RAD}}} + \frac{1}{\tau_{\text{bulk,AUG}}}, \quad (9)$$

assuming a uniform $\Delta n(x)$ and identical front and rear diffusions. The intrinsic bulk recombination components are eliminated using appropriate parameterisations of Kerr *et al.* [12] creating a corrected lifetime τ_{corr}. The separation of recombination components from the heavily doped region and bulk (only SRH) is achieved by their difference in Δn dependence in high injection. This can be utilised by plotting $1/\tau_{\text{corr}}$ against Δn and deriving J_{0n^+} by a simple scaling of the gradient. In this manner multiple high injection PC-calibrated PL τ_{eff} and Δn image sets can be used to calculate a J_{0n^+} value at each pixel location. In practice at least four, preferably more, PL image sets are taken at different illumination intensities (to produce different Δn densities) to acquire sufficient data for reliable J_{0n^+} images.

As this method inherits from the Kane and Swanson technique it is subject to the same measurement range limitations and inaccuracies. It is also worth noting that

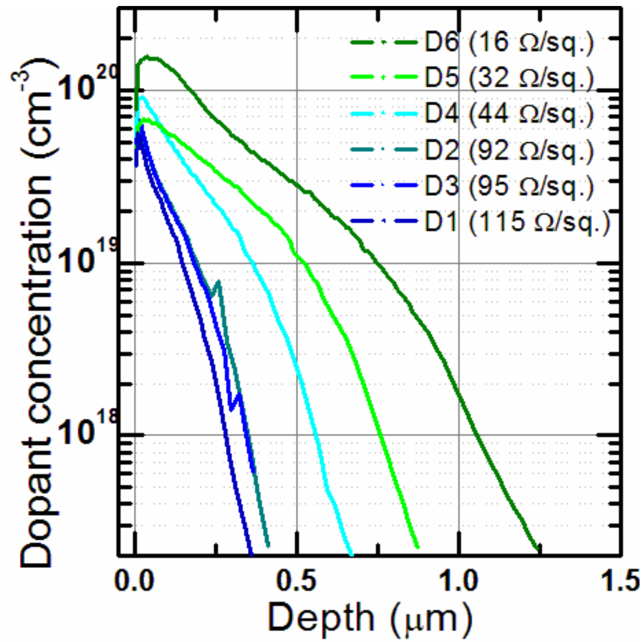

Figure 3: Diffusion profiles and measured sheet resistances (single side) from diffusion processes 1-6.

significant computational power is required to perform linear regression at every pixel – this is especially relevant to high resolution imaging.

Test Structure Fabrication. Test structures implemented in this study were fabricated from float zone (FZ), p-type, (100) silicon substrates. Resistivities of 100 and 0.5 Ω-cm were used to ensure that high and low injection conditions were attainable. Following Si-etching and RCA cleaning samples were subjected to one of six (D1-D6) different symmetrical phosphorus-diffusion and thermal oxide drive-in procedures (phosphorus glass was deglazed and samples re-cleaned between diffusion and oxidation/drive-in steps). Precursors of structures 1-3 were included in each of these six procedures to ensure comparable dopant diffusions. The profiles and sheet resistances (single-side) of the diffusions produced by the six procedures were determined by electrochemical capacitance-voltage (ECV) and contactless conductance measurements, these are shown in Figure 3. Simulated sheet resistances were also obtained from the measured diffusion profile and are included as a comparison in Table 1. The final

fabrication step for test structures 1 and 3 was a 30 minute forming gas anneal (FGA) at 400ºC, known to improve the surface passivation quality of thermal SiO_2. In addition to this, structure 2 required the etching of both the oxide and diffusion from one side. Reactive ion etching (RIE) was used for this process as it is known to result in a surface with an approximately "infinite" SRV.

J_{0n^+} values for structures 1 and 3 were obtained for accuracy comparison using low [10, 11] and high injection [1] PCD measurements (using a Sinton WCT 120 lifetime tester). Quasi-steady-state PC and transient PCD were used to make the low and high injection measurements respectively. Accurate determination of test structure width, doping and optical properties required for J_{0n^+} calculation were obtained by digital micrometre callipers, Sinton conductive instrument and a spectrophotometer with an integrated-sphere, respectively.

J_{0e} Imaging. All PL imaging is performed with a BT-Imaging LIS-R1 QSSPC calibrated PL imager. Low injection J_{0n^+} images of structure sets 1 and 2 are obtained by first finding the relevant A_i values (using I_{ill} and Δn images in conjunction with Equation 3), following which J_{0n^+} images can be obtained by a simple scaling of the I_{ill} image in accordance with Equations 5, 6 or 8. The Δn region in which PL measurements are made must be both in low injection and free of lifetime overestimation artefacts like trapping in multi-crystalline silicon and depletion region modulation in mono-crystalline silicon. In this instance the 5×10^{14} – 1×10^{15} cm^{-3} region was seen to avoid such effects. An acquisition time of less than 0.5 seconds is required to take images. Example images for structure sets 1 and 2 are shown in Figure 4 with diffusions D2, D4 and D6.

For the high-injection imaging, five high-injection (> 1.3×10^{15} cm^{-3}) τ_{eff} and Δn images are taken of structure set 3 at increasing incident photon flux. J_{0n^+} images are

prepared using the simple but computationally-intensive process described in the theory section above. Example high injection J_{0n^+} images are also included in Figure 4 for diffusions D2, D4 and D6.

Some degree of correlation is seen between analogous images collected from the three different techniques. Images acquired by the high injection technique produce J_{0n^+} values consistently lower than those generated via the low injection techniques. This difference is discussed in the PCD comparison section below.

Table I: Comparison of average J_{0n^+} values obtained from high and low injection imaging techniques to corresponding values obtained by PCD, these results are plotted in Figure 5. The values within the brackets are the standard deviations of the measured area.

Measurement	Δn regime	Parameter	D1	D2	D3	D4	D5	D6
PCD		$R_{\mathbf{Sheet}}(\Omega/\mathbf{sq.})$	**115**	**95**	**92**	**44**	**32**	**16**
Simulation		$R_{\mathbf{Sheet}}(\Omega/\mathbf{sq.})$	**143**	**108**	**107**	**47**	**32**	**16**
PCD	High Injection	$J_{0n^+}(\mathrm{fA/cm^2})$	83	115	109	168	180	229
PL (Structure 3)	High Injection	$J_{0n^+,AVG}(\mathrm{fA/cm^2})$	64 (4)	92 (10)	85 (6)	140 (10)	157 (18)	255(9)
PCD	Low Injection	$J_{0n^+}(\mathrm{fA/cm^2})$	76	103	100	196	209	228
PL (Structure 2)(Eq.8)	Low Injection	$J_{0n^+,AVG}(\mathrm{fA/cm^2})$	79 (29)	132 (29)	145(19)	229 (24)	276 (34)	280(27)
PL (Structure 1)(Eq.5)	Low Injection	$J_{0n^+,AVG}(\mathrm{fA/cm^2})$	79 (17)	110 (13)	108 (12)	218 (36)	242 (45)	271 (23)
PL (Structure 1)(Eq.6)	Low Injection	$J_{0n^+,AVG}(\mathrm{fA/cm^2})$	95 (14)	129 (16)	128 (13)	238 (37)	261 (46)	286 (20)

Aside from general differences in magnitude, the images generated by the high injection technique appear more uniform than those produced by the low injection techniques. The greater uniformity is possibly a consequence of the averaging involved in the high injection measurement method, as images are generated from linear regression performed on 5 image sets (5 τ_{eff} and 5 Δn images). The slightly deeper position of the n^+p junction in the high resistivity structures as compared to the low resistivity ones could also increase the uniformity. In addition to this, a longer fabrication procedure was required for structure 2, accounting for some of the very high J_{0n^+} regions seen in these images.

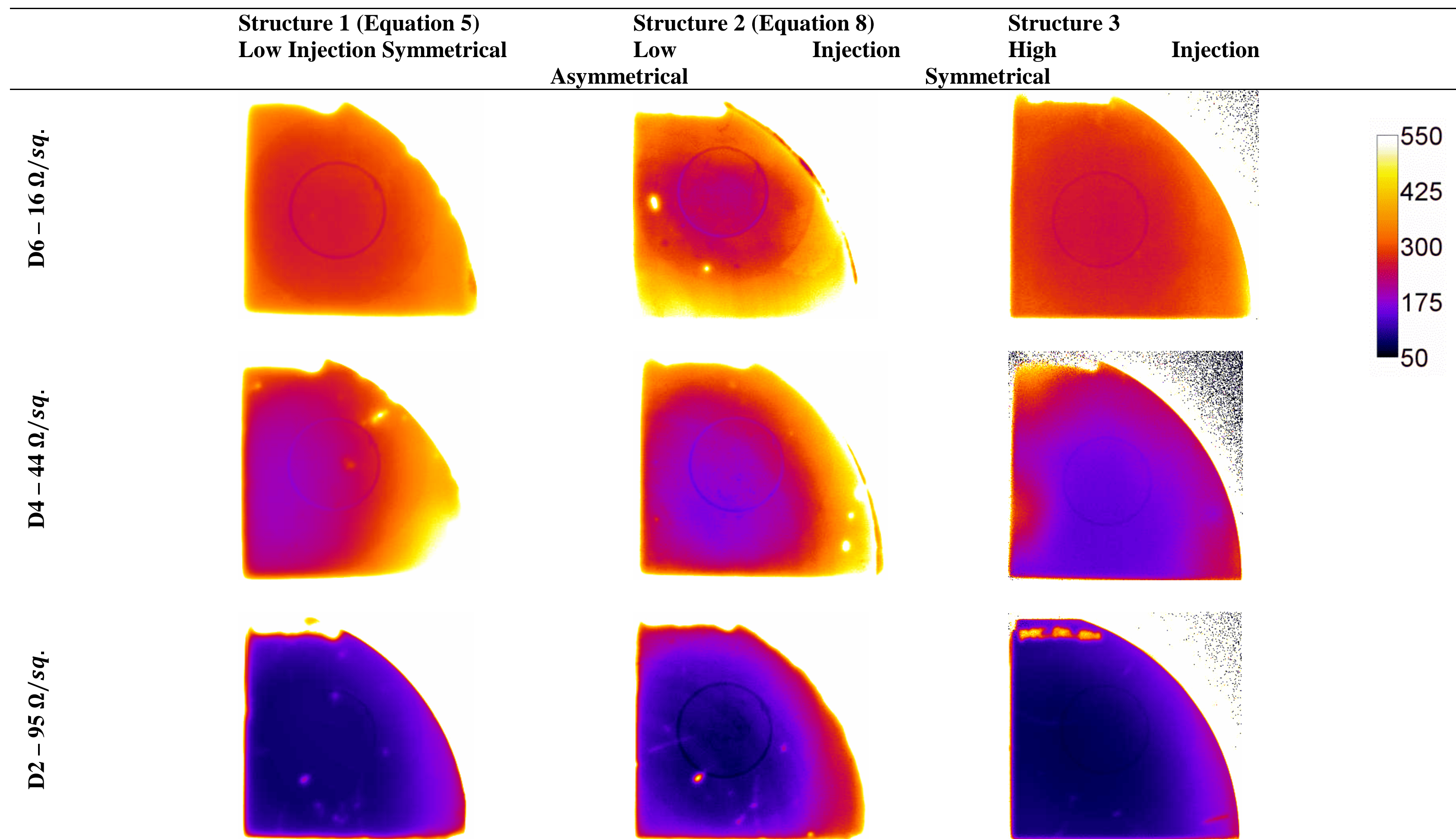

Figure 4: A small selection of J_{0n^+} images obtained from high (structure 3) and low (structures 1 and 2) injection techniques applied to test structures with equivalent diffusion profiles. The scale on the right has units of fA/cm^2.

Worth noting is that on some of the images taken with the low injection techniques, especially on the asymmetrical samples, faint lines following the contour of the outer edge of the test structure are visible. This is not to be confused with the clear ring like structure, seen in almost all images, caused by the underlying inductive coil and housing. These are believed to be caused by deviations in dopant densities arising during the crystal growth procedure [17]. These deviations affect both the diffusivity and PL signal resulting in slight differences in the measured J_{0n^+}.

Comparison with PCD. A comparison between average J_{0n^+}, values determined via the PL imaging techniques described above, and J_{0n^+} values obtained by well-established PCD techniques on analogous structures needs to be undertaken to assess the validity of the former. Individual image averaging was made over the estimated area and location of the coil used in PCD measurements. The results are presented in Table 1 and are plotted in Figure 5. Each data point is further the result of an average of two to four individual wafers. Standard deviations of values around the coils are also included in Table 1 and align with the previous observation of greater uniformity in the images obtained by the high injection technique.

It can be seen that all techniques reveal the same expected dependence of J_{0n^+} on the sheet resistance of the surface-passivated diffusion. That is, a decreasing J_{0n^+} for increasing R_{sheet}. A very high degree of correlation is seen between the low and high injection PCD techniques. Of the imaging techniques, the best agreement with standard high injection PCD is exhibited by the high injection PL imaging technique, which utilizes the same theoretical principle at each pixel location. Although consistently lower it remains within 25% of the high injection PCD values across all measurements.

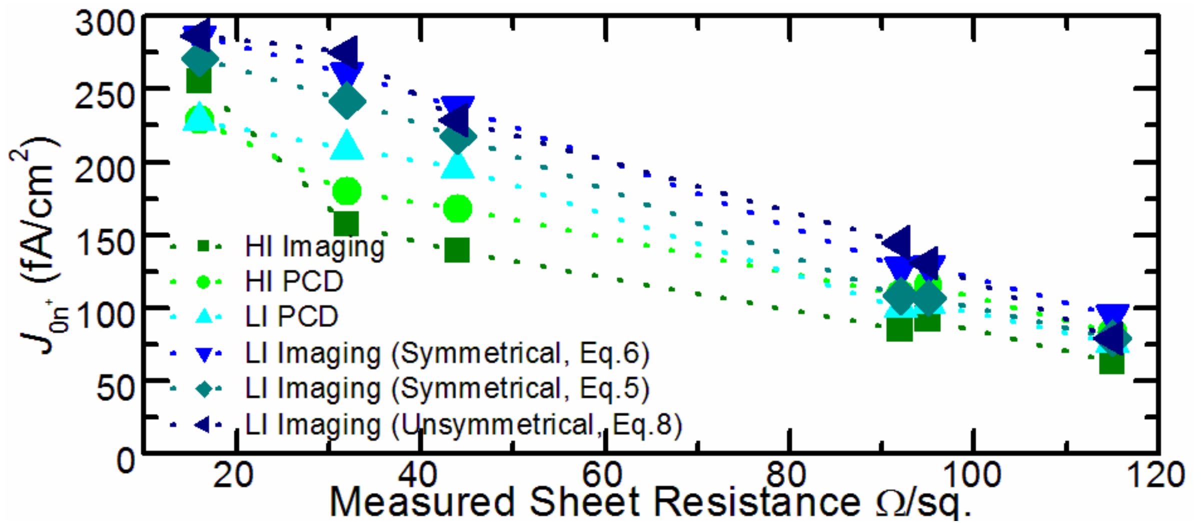

Figure 5: Comparison of obtained average J_{0n^+} (imaging) and J_{0n^+} values (PCD) as a function of measured sheet resistance. The green data sets are those obtained by high injection methods whist those in blue and cyan are low injection techniques. Phosphorus diffusions followed by thermal oxide growth and forming gas anneal.

Low injection imaging techniques generally give higher J_{0n^+} values for a given sheet resistance, especially at lower sheet resistances. This is likely potentially due to a number of contributing factors:

Unaccounted for SRH recombination in the base would result in a larger portion of recombination being attributed to the heavily doped region and hence a higher J_{0n^+}. This same effect would not be expected using the high injection techniques as the base SRH recombination is separated by its different dependence on Δn rather than being subtracted from the recombination total. It is unlikely that the differences seen between the techniques are solely due to this effect as FZ wafers were used and the low injection PCD technique does not exhibit the same high J_{0n^+}. In fact, the deviation is seen to increase with lower sheet resistances, where the dominance of the diffused region recombination over base SRH recombination is strongest.

The differences and particularly the increased deviation from the high injection PCD technique seen at lower sheet resistances could also be explained by the different

conditions of measurement. As the low injection imaging technique utilises QSS conditions a significant proportion of carriers may be injected into the diffusion region and not reach the base. This would lead to an overestimation of J_{ph} and hence J_{0n^+} for a given PL output. The effect would increase with lower sheet resistances, like the trend seen in Figure 5, as the junction is deeper. However, this same effect is not seen clearly for the low injection PCD measurements and high injection imaging technique, both of which are measured in QSS. The high injection PCD technique is impervious to this effect as it is measured using transient PCD where J_{ph} is not used.

Another potential contribution to the differences is the slightly thinner diffusion region width expected for the lower resistivity structures. The difference in diffusion width could result in a change in J_{0n^+}, as the actual base width is now larger (see Equations 5, 6 and 8). However, simulations in EDNA V1.2 [18] of measured diffusion profiles with different background doping suggest that this contribution is very small.

Finally, it is worth noting that as all of the low injection techniques are based around a subtraction of recombination components, a heavy emphasis is placed on the accuracy of parameterisations and test structure measurements.

Even with the above mentioned deviations, the introduced low injection J_{0n^+} imaging techniques show very good agreement with the high injection PCD measurement given the inherent level of error in the experiment. In a separate experiment, a comparison of average J_{0n^+} values of heavily doped regions formed under the same diffusion and drive in conditions revealed deviations of up to 10% which were not factored into this experiment. In addition the error in PCD measurements are not insignificant and could also affect the spread of data and assessment of correlation [19].

Conclusion. A novel, low injection technique which provides a 2D image of the recombination current pre-factor that characterises the surface diffused region has been introduced. This technique is demonstrated over diffusion profiles with an approximate sheet resistance range of 15 – 120 Ω/sq. The validity range of the proposed theory, estimated by comparison with simulated PL results from QSSModelV5, is found to be appropriate for imaging industrial high efficiency solar cells. A comparison with existing dominant PCD based techniques and a high-injection J_{0n^+} imaging technique indicate reasonable correlation between all techniques. A deviation in correlation of J_{0n^+} values between the new, low injection technique and the comparison techniques is seen at lower sheet resistances. Potential contributing factors to this reduced correlation include an overestimation of J_{ph} using QSS conditions, unaccounted for SRH recombination in the base region and general inaccuracies in test structure measurements and parameterisations.

Acknowledgements. The authors gratefully acknowledge the support provided by the Australian Research Council and the Australian Solar Institute.

References

[1] D. E. Kane and R. M. Swanston, "Measurement of the Emitter Saturation Current by a Contactless Photoconductivity Decay Measurement," in *Proceedings of the 18th IEEE Photovoltaic Specialist Conference*, Las Vegas, USA, 1985.

[2] J. Muller, K. Bothe, S. Herlufsen, T. Ohrdes and R. Brendel, "Reverse saturation current density imaging of highly doped regions in silicon employing photoluminescence measurements," *IEEE Journal of Photovoltaics,* 2012.

[3] M. Muller, P. P. Altermatt, K. Schlegel and G. Fischer, "A method for imaging the emitter saturation current with lateral resolution," *IEEE Journal of Photovoltaics, Short Paper,* 2012.

[4] M. Wilson, A. Savtchouk, J. Lagowski, K. Kis-Szabo, F. Korsos, A. Toth, R. Kopecek and V. Mihaietchi, "QSS-uPCD measurement of lifetime in silicon wafers: advantages and new applications," *Energy Procedia 8 Proceedings of the 1st SiliconPV 2011,* vol. 8, pp. 128-134, 2011.

[5] M. Glatthaar, J. Giesecke, M. Kasemann, J. Haunschild, M. The, W. Marta and S. Rein, "Spatially resolved determination of the dark saturation current of silicon solar cells from electroluminescence images," *Journal of Applied Physics,* vol. 105, 2009.

[6] J. Muller, K. Bothe, S. Herlufsen, H. Hannebauer, R. Ferre and R. Brendel, “Reverse saturation current density imaging of highly doped regions in silicon: A photoluminescence approach,” *Solar Energy Materials & Solar Cells,* 2012.

[7] D. Delamarre, L. Lombez and G. J-F, “Contactless mapping of saturation currents of solar cells by photoluminescence,” *Applied Physics Letters,* vol. 100, 2012.

[8] M. Glatthaar, J. Haunschild, M. Kasemann, J. Giesecke, W. Warta and S. Rein, “Spatially resolved determination of dark saturation current and series resistance of silicon solar cells,” *Physica status solidi - Rapid research letters,* vol. 4, pp. 13-15, 2012.

[9] D. Hinken, K. Bothe, K. Ramspeck, S. Herlufsen and R. Brendel, “Determination of the emitter saturation current density of silicon solar cells using photoluminescence and quantum efficiency analysis,” in *Proceedings of 24th European Photovoltaic Solar Energy Conference*, Hamburg, Germany, 2009.

[10] C. Reichel, F. Granek, J. Benick, O. Schultz-Wittmann and S. W. Glunz, “Comparison of emitter saturation current densities determined by injection-dependent lifetime spectroscopy in high and low injection regimes,” *Progress in Photovoltaics: Research and Applications,* 2010.

[11] A. Cuevas, “The effect of the emitter recombination on the effective lifetime of silicon wafers,” *Solar Energy Materials & Solar Cells,* vol. 57, pp. 277-290, 1998.

[12] M. J. Kerr and A. Cuevas, “General Parameterization of Auger recombination in crystalline silicon,” *Journal of Applied Physics,* vol. 91, no. 4, pp. 2473-2480, 2002.

[13] P. P. Altermatt, F. Geelhaar, T. Trupke, X. Dai, A. Neisser and E. Daub, “Injection dependence of spontaneous readiative recombination in crystaline silicon: Experimental verification and theoretical analysis,” *Applied Physics letters,* vol. 88, 2006.

[14] S. Herlufsen, J. Schmidt, D. Hinken, K. Bothe and R. Brendel, “Photoconductance-calibrated photoluminescence lifetime imaging of crystalline silicon,” *Physica status solidi - Rapid research letters,* vol. 6, no. 2, pp. 245-247, 2008.

[15] Klaassen, “A unified mobility model for device simulation,” *IEEE,* vol. 90, pp. 357-360, 1990.

[16] A. Cuevas and R. Sinton, “Simple Modelling of solar cells,” in *Proceedings of 23rd European Photovoltaic Solar energy Conference*, Valencia, 2008.

[17] S. Y. Lim, S. P. Phang, T. Trupke, A. Cuevas and D. MacDonald, “Dopant concentration imaging in crystalline silicon wafers by band to band photoluminescence,” *Journal of Applied Physics,* vol. 110, no. 113712, 2011.

[18] M. K. R and P. P. Altermatt, “A freeware 1D emitter model for silicon solar cells,” in *Proceedings of the 35th IEEE photovoltaics specialist conference*, Honolulu, 2010.

[19] K. R. McIntosh and R. A. Sinton, “Uncertainity in photoconductive lifetime measurements that use an inductive-coil detector,” in *Proceeding of the 22nd European Photovoltaic Solar Energy Conference*, Valencia, Spain, 2008.

Enhanced rear-side reflection and firing-stable surface passivation of silicon solar cells with capping polymer films.

James Bullock [1], Andrew Thomson[1], Andrés Cuevas[1], Boris Veith[2], Jan Schmidt[2] and Ari Karkkainen[3]

[1] *Research School of Engineering*, the Australian National University, Canberra, ACT 0200, Australia

[2] *Institute for Solar Energy Research Hamelin (ISFH)*, Am Ohrberg 1, 31860 Emmerthal, Germany

[3] *Optitune International Pte. Ltd.*, 20 Maxwell Road, #05-08 Maxwell House, Singapore 069113, Singapore

Published in Physica Status Solidi: Rapid Research Letters.

Low refractive index polymer materials have been investigated with a view to form the back surface mirror of advanced silicon solar cells. SiO_x:H or AlO_ySiO_x:H polymer films were spun on top of an ultra-thin (< 10 nm) atomic-layer-deposited (ALD) Al_2O_3 layer, itself deposited on low resistivity (1 Ω cm) p-type crystalline silicon wafers. These double layer stacks were compared to both ALD Al_2O_3 single layers and ALD Al_2O_3 / plasma-enhanced chemical vapour deposited (PECVD) SiN_x stacks, in terms of surface-passivation, firing-stability and rear-side reflection. Very low surface recombination velocity (SRV) values approaching 3 cm/s were achieved with ALD Al_2O_3 layers in the 4-8 nm range. Whilst the surface passivation of the single ALD Al_2O_3 layer is maintained after a standard firing step typical of screen printing metallisation, a harsher firing regime revealed an enhanced thermal stability of the ALD Al_2O_3 / SiO_x:H and ALD Al_2O_3 / AlO_ySiO_x:H stacks. Using simple 2D optical modelling of rear-side reflection it is shown that the low refractive index exhibited by SiO_x:H and AlO_ySiO_x:H results in superior optical performance as compared to PECVD SiN_x, with gains in photogenerated current of ~ 0.125 mA/cm^2 at a capping thickness of 100 nm.

Recently, atomic-layer-deposited (ALD) Al_2O_3 surface passivation has emerged as a promising technology for high-efficiency silicon solar cells. These films provide excellent passivation of c-Si surfaces, including heavily doped p-type surfaces — a feat which was previously considered difficult. Despite the promising prospects of this technology, its industrial implementation is not without significant challenges: the ALD rate is slow, precursor materials can be expensive and hazardous and some evidence exists of a high sensitivity of passivation on the 'firing' processes required for metal contact formation [1, 2]. In addition, a low temperature (400-450°C) thermal step is commonly implemented to fully activate surface passivation [3], increasing the thermal budget of solar cell fabrication using this technology. A potential avenue to address some of these issues is to create a stack system composed of an ultra-thin (< 10 nm) passivating layer of ALD Al_2O_3 and an inexpensive overlying capping layer. This structure decouples surface passivation from other solar cell design considerations allowing freedom to choose a capping material with suitable protective and optical properties. In addition, improvements in deposition time and cost are possible without sacrificing passivation quality. Several groups have investigated this idea with the application of plasma-enhanced chemical vapour deposited (PECVD) SiN_x capping layers [2, 4-6], some reporting excellent passivation and stability results. However, such a stack system is not ideal for enhancing reflection at the rear side of a solar cell, where a lower refractive index (RI) capping layer would be beneficial.

This work focuses on the application of low RI (n ~ 1.5) polymer based spin/spray-on films as capping layers on top of plasma assisted-ALD (PA-ALD) Al_2O_3 films for the rear side of p-type solar cells. Two polymer-based coating materials, produced by Optitune, were selected as the capping layers. The first is SiO_x:H, an amorphous silicon oxide based film with hydrogen constituents and the second is

AlO_ySiO_x:H, an amorphous aluminium oxide / silicon oxide hybrid, again containing hydrogenated compounds. These films have been designed to act as a source of atomic hydrogen, aiding in surface passivation, when annealed in appropriate conditions [7]. Layer thicknesses in the range of 5-250 nm can be achieved by adjusting the viscosity of the liquid polymers and by optimising the deposition parameters using a variety of techniques, such as spin-coating, roller coating or spray coating. In this initial proof-of-concept investigation the surface passivation, firing stability and rear-side optical characteristics of the stack systems are compared to those of a single layer of PA-ALD Al_2O_3 and a PA-ALD Al_2O_3 / PECVD SiN_x stack. Further studies, including the interaction between metal pastes and the stack systems, will be required before integrating the stacks into partial rear contact solar cell devices.

The symmetrical lifetime samples used in this study were fabricated on 1±0.1 Ω cm, (100), FZ p-type wafers with starting thicknesses of 540±10 µm. An alkaline based saw damage etch and RCA clean were implemented to prepare surfaces prior to deposition. PA-ALD Al_2O_3 layers were deposited on both sides of the wafers using a Beneq TFS-200 ALD instrument at a deposition temperature of ~175°C. Trimethylaluminium (TMA) and O_2 plasma were used as alternating precursors, purge and pulse times were chosen as to ensure a self-limiting reaction. SiN_x layers were deposited using a Roth & Rau SiNA. Polymer coatings were deposited via a simple spin coating procedure, following which they were cured at ~200°C for 5 minutes in air. Activation of the surface passivation was performed using either a 15 minute forming gas anneal (FGA) at ~400°C or a firing process in a conveyor belt furnace. Two high temperature processes were investigated to account for variations in firing regimes required for different commercially available screen-printed metal pastes. Firing procedure 1 replicates 'standard' firing conditions with a furnace set temperature of

910°C and a wafer peak temperature of ~810°C. The silicon wafers are subjected to temperatures above 600°C for ~6.5 seconds. Firing procedure 2 represents a 'harsher' firing condition with a lower furnace set temperature of 860°C, resulting in a wafer peak temperature of ~790°C, but holding the samples above 600°C for ~12 seconds. Both firing procedures were performed using a Centrotherm industrial infrared furnace. Photoconductance decay measurements (transient mode) were made with a Sinton Instruments WCT-120 apparatus to extract the effective minority carrier lifetime. The surface recombination velocity (SRV) was extracted from the effective lifetime by assuming an intrinsic bulk carrier lifetime value [8], a procedure that gives an upper limit for the SRV.

Initially, an analysis of the PA-ALD Al_2O_3 thickness required to achieve optimum surface passivation was performed. PA-ALD Al_2O_3 layers of thicknesses in the range of 2-20 nm were deposited. Before activation of the PA-ALD Al_2O_3 layers test structures were separated into three sets; 1) not capped, 2) capped with a ~60 nm SiO_x:H film; and 3) capped with a ~110 nm AlO_ySiO_x:H film. Surface passivation was activated using either a FGA or the standard firing process. Fig. 1 gives the results of this study and reveals that the two activation processes exhibit almost identical behaviour and that there is no requirement for a separate FGA. Saturation of surface passivation was observed for PA-ALD Al_2O_3 layer thicknesses in the 4-8 nm range, corresponding to a SRV of ~5 cm/s. A data point for each of the three groups, with a PA-ALD Al_2O_3 thickness of ~18 nm, is included in the top plot of Fig. 1 to demonstrate that there is no further substantial gain in surface passivation. It is worth noting that application of the SiO_x:H and AlO_ySiO_x:H polymer films results in no significant change to the surface passivation, except perhaps for the thinnest PA-ALD Al_2O_3 layers. Despite the high temperatures of the standard

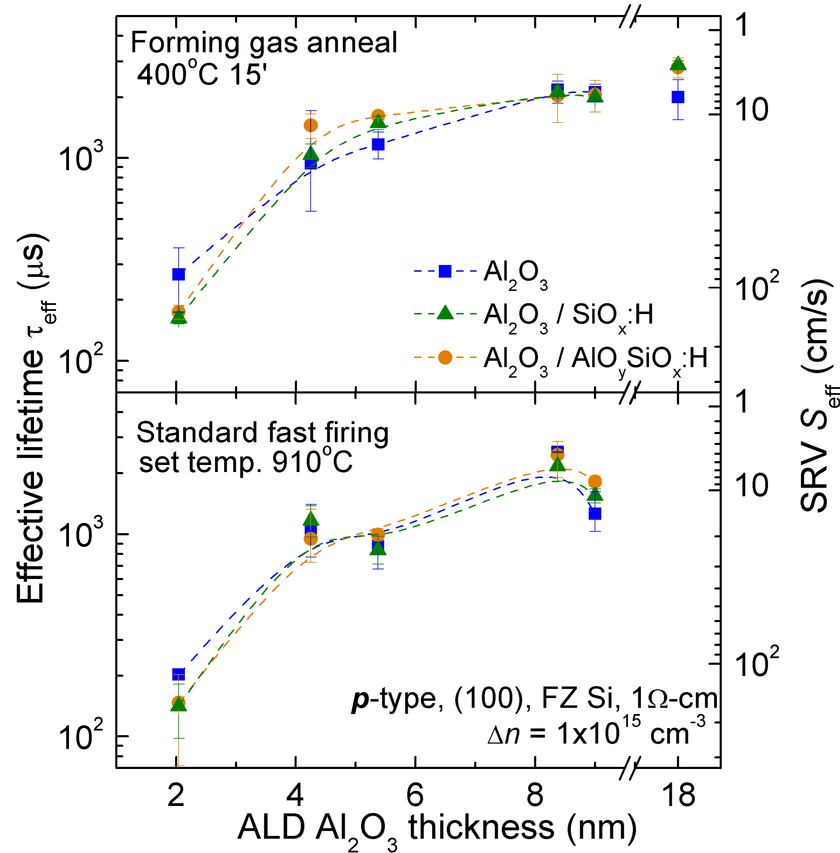

Figure 1 Effective lifetime and SRV values as a function of PA-ALD Al_2O_3 layer thickness. Lines provide a guide to the eyes. Capping film thicknesses: SiO_x:H (~60 nm) and AlO_ySiO_x:H film (~110 nm). Error bars are based on the measured spread of data, each point is an average of at least two test structures.

firing process, no benefit was obtained by capping the ALD Al_2O_3, since the single layer appears to be firing stable for all the thicknesses investigated here.

To further investigate the firing stability of these stack systems and compare them to SiN_x capping, additional test structures were deposited with a fixed PA-ALD Al_2O_3 layer thickness of ~8 nm and separated into four groups; 1) not capped 2) capped with a ~60 nm SiO_x:H film; 3) capped with a ~110 nm AlO_y/SiO_x:H film and 4) capped with a ~100 nm PECVD SiN_x film. Standard or harsh firing regimes were used to activate the PA-ALD Al_2O_3 surface passivation. This comparison, which is presented in Fig. 2a, indicates that under the harsh firing regime the uncapped test structures do suffer a decline in effective lifetime, unlike in the standard firing case. Enhanced firing stability can be

seen for all three capped test structures. Both polymer films produce final SRV values lower than the PECVD SiN_x capped structures. It should be noted that the relatively small gain in firing stability measured for the SiN_x capped films is not in alignment with previously published results of almost identical stack systems [4]. The mechanism of the enhancement contributed by the capping films could be the diffusion of hydrogen or hydrogenated radicals to the interface during the firing, where they assist in surface passivation. No issues of film 'blistering' were encountered before or after firing the capped test structures.

The deposition of Al_2O_3 on p-type surfaces is commonly expected to result in an effective lifetime that is independent of excess minority carrier concentration in low injection [3], but this is not always the case. Fig. 2b presents representative injection dependent lifetime curves of the four test structure sets following the harsh firing procedure, alongside a control sample (8 nm Al_2O_3) which received a 15 minute FGA at ~400°C. A small decline in effective lifetime is seen for all the passivation layers at carrier concentrations below 10^{15} cm^{-3} possibly due to Shockely-Read-Hall recombination in the silicon bulk.

Whilst it is intuitive to expect some rear-side reflectance enhancement by lower RI capping films, the extent to which they can improve solar cell optics is not immediately apparent. To quantitatively assess the potential optical behaviour of the three sets of double layer dielectrics, simple ray tracing simulations were conducted to provide an indication of the enhanced rear-side reflection of near band-gap photons and the resultant gain in photocurrent for each stack system.

To obtain wavelength dependent *n* and *k* values for these simulations, single-side mechanically-polished silicon test structures were coated with PA-ALD Al_2O_3, SiO_x:H, AlO_ySiO_x:H and PECVD SiN_x films and fired under the standard firing procedure.

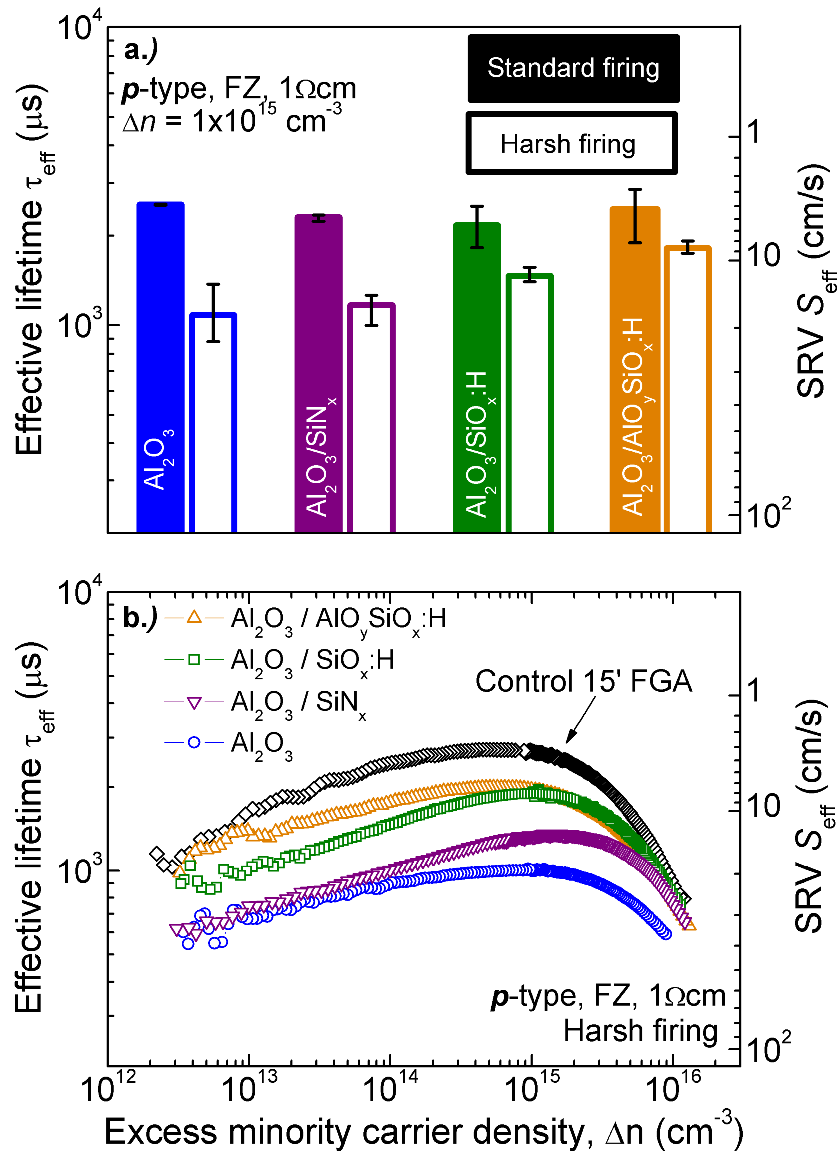

Figure 2 a.) Effective lifetime and upper limit SRV values for standard and harsh firing procedures. 8 nm thick passivating ALD Al_2O_3 layer (all test structures). Capping layer thicknesses: PECVD SiN_x ~100 nm, AlO_ySiO_x:H ~110 nm, SiO_x:H ~ 60 nm. b.) Plots of effective lifetime against excess minority carrier density for the four test structure types after a harsh firing and a control test structure (8 nm Al_2O_3) after a 15 minute FGA.

Reflectance spectra of these test structures, measured using a FilmTek 4000 spectrophotometer, are fitted using the differential power spectral density technique in combination with the Tauc-Lorentz material model [9] to extract the refractive index.

The simulations relied on Macleod's transfer matrix method [10] to calculate reflectance, transmittance and absorption of individual rays as they hit the front and rear sides of a simple solar cell structure. The low absorption rate of near band-gap light in

silicon results in a large number of light bounces between the front and rear surfaces before being absorbed. This process can be computationally expensive to simulate. To reduce simulation time in this instance, ray-tracing was run until 98% of the near band-gap light intensity was accounted for; either being absorbed in the silicon or dielectric films, escaping off (reflected) or through (transmitted) the front-side, or escaping through (absorbed by the metal) the rear-side. The remaining 2%, composed of rays around 1200 nm, are ignored in calculations. All reflections and transmissions were treated as purely specular and free carrier absorption was neglected. The front surface was assumed to be SiN_x coated and pyramidally textured, with characteristics similar to those of common industrial solar cells. A planar rear-side composed of 8 nm of PA-ALD Al_2O_3 / capping film (SiO_x:H, AlO_ySiO_x:H or SiN_x) / 1µm of Aluminium was used to simulate the back surface mirror. The small percentage of rear surface directly contacted with metal in partial rear contact solar cell designs was not included in this simulation. Specific details of the simulation and structure are given in Table 1.

Table 1 Structure and conditions of 2D optical simulation.

Incident spectrum	Perpendicular incidence, only near band-gap light (900-1200 nm), wavelength dependent intensity according to the AM1.5 spectrum (ASTMG 173-03), equal *s* and *p* polarisation intensity.
Front-side	Incident medium: Air (n = 1 and k = 0), Regular texturing: facet height: 3 um, facet angle: 52° [11], Anti-reflection coating: 75 nm of high RI PECVD SiN_x [12] n and k from [13].
Silicon	Thickness 180 mm, planar rear-side, n and k from [14].
Rear-side	First film: PA-ALD Al_2O_3 8 nm (measured RI), Second film: variable material and thickness (measured RI), Metal film: Aluminium, 1 µm, n and k from [15].

The results of the simulation are shown for the three capping layers in Fig. 3. The first (left) y axis depicts the weighted sum of rear-side reflectance, R_b. This sum is obtained by calculating the individual reflection of all light rays hitting the rear-side and summing them in accordance to their incident intensity. The simulations predict a clear

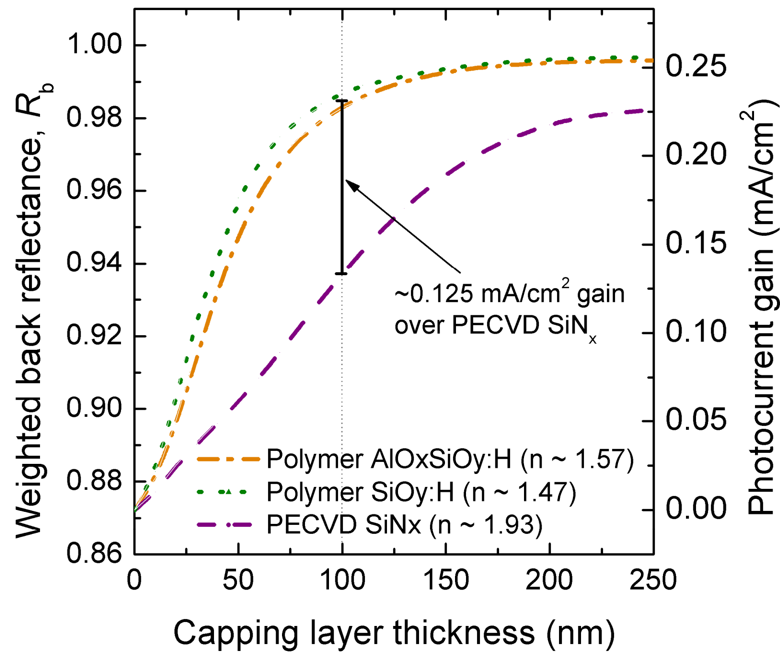

Figure 3 Weighted back reflectance R_b and photocurrent gain (mA/cm^2) as a function of capping layer thickness for the three capping layers investigated. At a capping thickness of 0 nm the values reflect the expected behaviour for an 8 nm PA-ALD Al_2O_3 / 1 µm Al stack without any capping layer in-between.

increase of R_b with the thickness of the capping layers, reaching saturation at ~150 nm for the two polymer films. The increase in R_b results in a longer average path-length of rays through the silicon leading to a larger absorption and photocurrent, as shown on the second (right) axis. A value for the real part of the refractive index at 900 nm is also provided for each capping film in the figure. It is clear from Fig. 3 that both of the low RI capping films outperform the PECVD SiN_x in terms of R_b and hence photocurrent. The latter reaches an R_b value of ~0.98 at a thickness of 250 nm. Both polymer films need only be 100 nm thick to achieve a similar value of R_b. For this thickness of the capping layers, the polymer films can provide an enhancement in photocurrent of ~0.125 mA/cm^2.

In this letter we have shown that the combination of ultra-thin PA-ALD Al_2O_3 passivation layers and inexpensive spin-on polymer capping films can lead to enhanced firing stability and rear-side reflection without compromising c-Si surface passivation. Activation of the PA-ALD Al_2O_3 surface passivation was achieved by the firing process

itself, without incurring any issues of film blistering. PA-ALD Al_2O_3 passivation layer thicknesses of only 4 to 8 nm were sufficient to achieve excellent surface passivation on low resistivity (1 Ω cm) p-type wafers. A harsh firing procedure revealed that all three capping films provide an enhanced firing stability, the two polymer films producing the lowest final SRV values. Optical simulations of rear-side reflection suggest that a polymer capping layer thickness of 100 nm is optimal, producing a photocurrent gain of ~0.125 mA/cm^2 compared to a similar thickness of PECVD SiN_x.

Acknowledgements The authors would like to thank Keith McIntosh for his suggestions regarding the optical modelling. Financial support by The Australian Solar Institute / Australian Renewable Energy Agency and The Australian Research Council is gratefully acknowledged.

References

[1] J. Benick et al., Phys. Status Solidi RRL 3, 233 (2009).
[2] J. Schmidt et al., Phys. Status Solidi RRL 3, 287 (2009).
[3] G. Dingemans et al., Phys. Status Solidi RRL 4, 10 (2010).
[4] B. Veith et al., Energy Procedia 8, 307 (2011).
[5] A. Richter et al., Phys. Status Solidi RRL 5, 202 (2011).
[6] L. Black et al., Proc. 3rd Silicon PV (2013).
[7] A. Thomson et al., Proc. 27th EUPVSEC (2012), p. 1784.
[8] A. Richter et al., Energy Procedia 27, 88 (2012).
[9] G. E. Jellison et al., Appl. Phys. Lett. 69, 371 (1996).
[10] H. A. Macleod, Thin-Film Optical Filters, Institute of Physics Publishing (2001).
[11] S. C. Baker-Finch et al., Progr. Photovolt: Res. Appl. (2012).
[12] S. C. Baker-Finch et al., Progr. Photovolt. 19, 406 (2011).
[13] S. C. Baker-Finch et al., Proc. 35th IEEE PVSC (2010), p. 2184.
[14] M. A. Green, Sol. Energy Mater. Sol. Cells 92, 1305 (2008)
[15] E. D. Palik, Handbook of Optical Constants of Solids, Academic Press, 1985.

Appendix 3: Additional relevant manuscripts

p^+nn^+ silicon solar cell with a full-area rear MIS passivated contact

Y. Wan, J. Bullock, A. Cuevas, C. Samundsett, D. Yan, J. McKeon

[1] *Research School of Engineering*, the Australian National University, Canberra, ACT 0200, Australia

Presented in the Silicon Photovoltaic Conference, Netherlands, 2014

In this paper we compare n-type front-junction silicon solar cells (p^+nn^+) with a full-area rear, metal-insulator-semiconductor (MIS) passivated contact to a reference cell with partial rear contacts that are formed by patterning a silicon nitride layer. A conversion efficiency of 21% has been achieved for the MIS contact device with excellent V_{OC} at 666 mV and FF at 80.3% (both are comparable to the reference cell), evidencing good characteristic of a passivated contact. The low J_{SC} (39.3 mA/cm^2 comparing to 40.2 mA/cm^2 of reference) is attributable to a non-optimal antireflection coating at front and a low surface reflection at rear. The performance of MIS contact cell can be further improved by (i) restricting the MIS contacts to a 10–30% fraction of the rear surface, and (ii) replacing the aluminum with silver as an alloy metal. The simplicity in fabrication and high potential in cell performance make the MIS passivated contact of great interest to silicon photovoltaic industry.

The implementation of two carrier-selective contacts is of fundamental importance for solar cells. In this paper we build on the traditional approach of creating a near-surface doped layer and complement its selectivity by depositing layers that improve the blocking action towards minority carriers, while selectively passing majority carriers. That is, the extra layers minimise recombination at the metal/n^+ silicon interface without incurring a significant resistive loss. As a starting idea, the well-documented metal-insulator-semiconductor (MIS) structure can permit the passage of electric current if the thickness of the insulator (silicon oxide in this case) is less than ~2 nm. Achieving good surface passivation with such a thin dielectric is however difficult. The addition of a hydrogen rich capping layer such as hydrogenated amorphours silicon (a-Si:H) improves the passivation, but if the a-Si:H is undoped, as in our case, it presents a further impediment to the transport of majority carriers. The solution that we have found is to alloy a metal with the a-Si:H, forming a mixed phase that is semi-metallic in terms of conductivity, but still preserves enough hydrogen to passivate the interface between the thin oxide and the mono-crystalline silicon [1]. At the solar cell level, the thickness of SiO_2 and the thermal budget of alloying (in terms of temperature and duration) have been shown to be critical in achieving a good fill factor whithout compromising open-circuit voltage (V_{OC}) [2]. This work compares the n-type front-junction silicon solar cells (p^+nn^+)

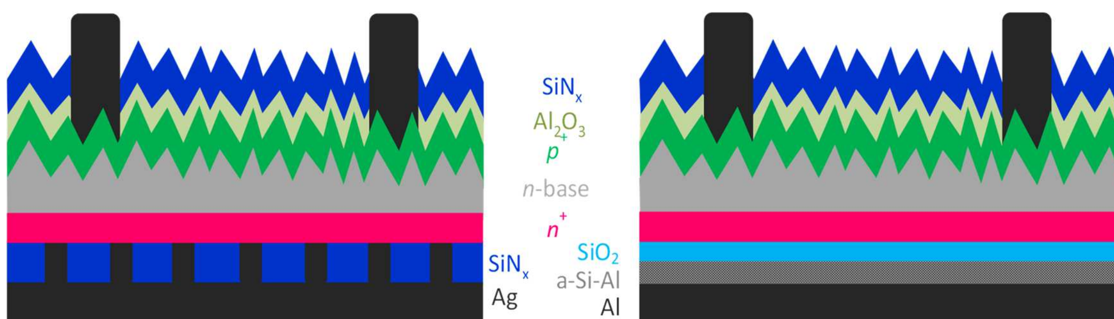

Figure 1 Schematic of p+nn+ devices with (left) partial rear contact, and (right) full-area rear a-Si:H enhanced MIS contact.

Partial rear contact (PRC)	Full-area rear MIS contact
Alkaline texturing	
Boron diffusion	
Phosphorus diffusion	
Front APCVD Al_2O_3 and PECVD SiNx	
Thermal activation of Al_2O_3	Rear thermal SiO_2 (Co-activation of Al_2O_3)
Rear PECVD SiN_x	Rear PECVD a-Si:H
Front dielectric patterning	
Rear dielectric patterning	
Rear thermal evaporated Ag	Rear thermal evaporated Al
Front thermal evaporated and electro-plated Ag	
Sintering	Al/a-Si alloying

Figure 2 Fabrication sequences for p+nn+ devices with (a) partial rear contact, and (b) full-area rear MIS contact.

with the full-area rear, a-Si:H enhanced MIS contact (hereafter referred as MIS cell) to a conventional cell with partial rear contacts (PRC) that are formed by patterning a SiN_x layer (hereafter referred as PRC cell). Surface recombination, spectral response and reflectance measurements are undertaken to provide insight into the physical mechnisms for the difference in cell performance of the two rear contact technologies.

Device structure and fabrication. As Figures 1 and 2 indicate, an advantage of the MIS contact approach is that it makes unnecessary the patterning of the rear dielectric (by photolithography in our lab, but commonly by laser in industry). On the other hand, it requires the formation of a 1.6 nm thick SiO_2 and an anneal at about 425 °C to alloy the Al with a-Si:H.

Device characterisation

Recombination at rear surface. Using test structures, we measured the recombination parameter J_0 that charaterises surface recombination at the rear phosphorus diffusion of both devices. For the PRC cell, the total J_{0back} is made up of ~25 fA/cm^2 corresponding to the 99% of the SiN_x passivated area, plus ~10 fA/cm^2 corresponding to

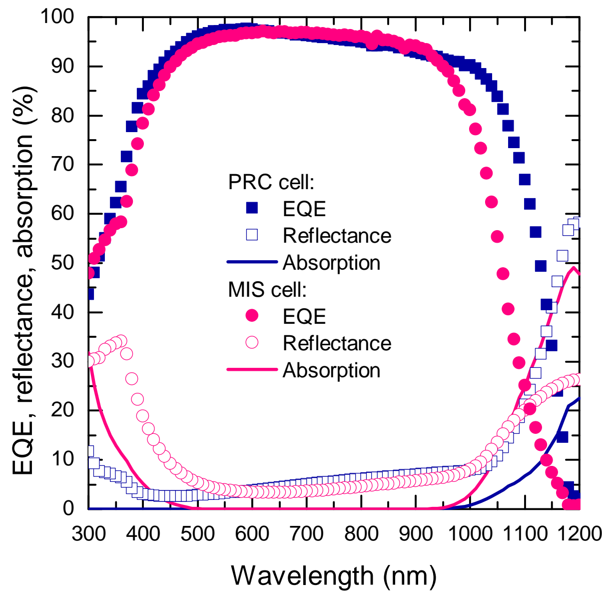

Figure 2 EQE, reflectance and absorption of the partial rear contact device and full-area MIS rear contact device after excessive alloy.

the 1% of the metal-contacted area. For the MIS cell, the lowest J_{0back} that we have measured is ~40 fA/cm^2, which if a full area contact is applied results in a similar rear J_0 to that of the PRC. Therefore, both approaches have, in principle, a similar potential to produce high efficiency solar cells. The MIS contact is fully one-dimensional, but given that a full-area phosphorus diffusion is used in both devices, this does not represent a significant advantage compared to the localised contact case. Presumably, some gain in device voltage may be achieved by combining both approaches, that is, forming a localised MIS contact in the device of Figure 1-(a). This would reduce the contribution of the 1% metal contacted region from ~10 fA/cm^2 to ~0.4 fA/cm^2, leading to a total J_{0back} ~25.4 fA/cm^2.

Solar cell parameters. Table I presents cell results of the two rear contact schemes. An extensive experiment on the effect of Al/a-Si alloy and SiO_2 thickness on cell performance revealed a trade-off between open-circuit voltage (V_{OC}) and fill-factor (FF), has been presented elsewhere [2]. The best cell with optimum alloying time and

SiO_2 thickness has an efficiency of 21%, which is 0.5% lower than the reference PRC cell, mainly attributable to a lower short-circuit current (J_{SC}). Notably, both the V_{OC} and FF are comparable to that of the reference cell, demonstrating a superior characteristic of carrier-selective contact (i.e., low recombination and high transport). Upon an excessive alloying the MIS cell exhibits a 0.2% drop in efficiency, attributable to a degradation in surface passivation, presumably at the rear MIS surface [1].

Table I. Summary of cell results

Cell	V_{OC} **(mV)**	J_{SC} **(mA/cm²)**	***FF*** **(%)**	η **(%)**
PRC (reference)	667	40.2	0.801	21.49
MIS with optimum alloy	666	39.3	0.803	21.03
MIS after excessive alloy	660	39.1	0.806	20.84

Spectral response. To further investigate the differences between the two cell technologies, which are particularly significant in J_{SC}, we performed reflectivity and spectral response measurements. In addition to the external quantum efficiency (EQE) and reflectance Fig. 3 shows the absorption in the front and rear SiN_x layers, for the PRC cell, and in the front SiN_x and rear Al-alloyed region, for the MIS cell. The absorption was simulated using the "Wafer Ray Tracer" available at the PVLighthouse website, using the experimentally determined optical constants $n(\lambda)$ and $k(\lambda)$ for the SiN_x used in these devices. Note that the front SiN_x films used in the two cells were deposited by two different PECVD reactors due to the availability of reactors during cell fabrication. For the Al-alloyed region the assumption has been made that it is optically similar to a traditional p^+ region formed by alloying an Al paste into monocrystalline silicon. This may not be totally correct for the present case of alloying with *a*-Si:H. A strong difference

between the EQE of both cells can be noted in the IR; this is largely attributable to a poor back surface reflectance by the MIS structure, and probably a significant absorption in the Al/a-Si alloyed layer [3]. Nevertheless, this particular MIS device had been annealed beyond the optimum point and its V_{OC} had dropped by 6 mV, indicating a possible degradation of the back surface passivation. In addition, the short-wavelength response is significantly different, mainly due to a non-optimal front SiN_x for this particular MIS cell (high reflectance and absorption). Hence the EQE results are inconclusive, but they do explain that the main reasons for the low J_{sc} of the MIS cell are of an optical, rather than electronic, nature. They indicate that the back surface mirror created by the Al/a-Si based MIS contact is not as good as that provided by the SiN_x/Ag system. Possible solutions are to restrict the MIS contact to a 10–30% of the rear surface or to replace the aluminum with silver as an alloying metal.

References

[1] J. Bullock, A. Cuevas, D. Yan, B. Demaurex, A. Hessler-Wyser, and S. De Wolf, "Amorphous silicon enhanced metal-insulator-semiconductor contacts for silicon solar cells," *Journal of Applied Physics,* vol. 116, pp. -, 2014.

[2] J. Bullock, A. Cuevas, C. Samundsett, D. Yan, J. McKeon, and Y. Wan, "Solar cells featuring a simple passivated rear contact," In preparation.

[3] A. Uruena, L. Tous, F. Duerinckx, I. Kuzma-Filipek, E. Cornagliotti, J. John*, et al.*, "Understanding the Mechanisms of Rear Reflectance Losses in PERC Type Silicon Solar Cells," *Energy Procedia,* vol. 38, pp. 801-806, 2013.